# ADDITIVE MANUFACTURING OF MAGNETOCALORIC MATERIALS FOR MAGNETIC REFRIGERATION

By

KUN SUN

A thesis submitted to the University of Birmingham for the degree of DOCTOR OF PHILOSOPHY

Department of Metallurgy and Materials
College of Engineering and Physical Sciences
The University of Birmingham

March 2023




UNIVERSITY OF BIRMINGHAM

UNIVERSITY OF
BIRMINGHAM

## University of Birmingham Research Archive

### e-theses repository

This unpublished thesis/dissertation is copyright of the author and/or third parties. The intellectual property rights of the author or third parties in respect of this work are as defined by The Copyright Designs and Patents Act 1988 or as modified by any successor legislation.

Any use made of information contained in this thesis/dissertation must be in accordance with that legislation and must be properly acknowledged. Further distribution or reproduction in any format is prohibited without the permission of the copyright holder.

# ACKNOWLEDGEMENTS

First and foremost, I am indebted to the University of Birmingham and the China Scholarship Council for my PhD scholarship.

I want to express my profound appreciation to my supervisor Professor Moataz Attallah for giving me the precious opportunity to undertake the presented research and pursue a PhD at the University of Birmingham. His immense knowledge, excellent research experience, expert guidance, and perpetual encouragement encouraged and influenced me to become a better researcher.

I want to express my sincere gratitude to my supervisors, Dr Richard Sheridan and Dr Abd El-Moez A. Mohamed, for their encouragement, guidance, support, and suggestions throughout these years, without which this work would not have been possible. Thank you all so much.

It is also a pleasure to thank my colleagues and friends for their supportive helps at the University of Birmingham, in particular to Dr Sheng Li, Dr Ranxi Duan, Dr Minki Jeong, Dr Biao Cai, Prof. Yu-Lung Chiu, Dr Kan Ma, Dr Ludwig Schneider, Dr Theresa Morris, Dr Stano Imbrogno, Dr Parastoo Jamshidi, Mr Jake Head, Ms Amy Newell, Mr Francesco Careri, Ms Xue Cao, Ms Emily Rose Lewis, Mr Peter Ibrahim, Mr Tugrul Ersoz, and Ms Anastassia Milleret.

Finally, I would like to express my profound thanks to my parents, my uncle Yinliang Zhu, my brother Tianen Feng, my girlfriend Yu Xiao, and other friends who have always stood by me and given me the strength to pursue this current academic goal. Thank you for always encouraging and supporting me through my most challenging times.

# ABSTRACT

Magnetic refrigeration is a promising environmentally friendly technology that may help address global warming and energy challenges worldwide. Compared with conventional cooling systems, magnetic refrigeration devices emit less mechanical noise and vibrations and theoretically achieve higher energy efficiency (60% of the Carnot cycle). This technique is based on the magnetocaloric effect (MCE), which is a change in the magnetic entropy ($\Delta S$) upon applying/removing an external magnetic field, resulting in a temperature change ($\Delta T$). The magnetocaloric materials (NiMnSn Heusler alloys and LaCe(Fe,Mn,Si)$_{13}$ alloys) are very interesting due to their high MCE. However, the materials also have limited uses due to poor mechanical properties. Laser powder bed fusion (PBF-LB) technology can overcome the disadvantage of hard-to-machine magnetocaloric materials to produce parts with complex shapes and extremely porous magnetocaloric materials with predefined external shapes. This work explores and investigates the possibility of the PBF-LB technique in creating NiMnSn and LaCe(Fe,Mn,Si)$_{13}$ samples. We also examined different post-treatment processes to improve PBF-LBed parts' MCE.

The PBF-LB technology can be used to build NiMnSn Heusler alloys with different shapes, particularly blocks, microchannel (MC) cylinders, lattices, and LaCe(Fe,Mn,Si)$_{13}$ samples. The PBF-LB processing parameters were optimised for these samples' minimum defects, cracks, and maximum densification. It has demonstrated that PBF-LB technology can create a fully dense NiMnSn block and LaCe(Fe,Mn,Si)$_{13}$ samples with a competitive MCE, although it is challenging to make cracks disappear. The low laser powers (60, 70, and 80 W) are more suitable for manufacturing NiMnSn Heusler alloys with MC cylinders and lattices. The appropriate energy density with low laser power, low scanning speed, and low hatch is good

for building $LaCe(Fe,Mn,Si)_{13}$ block samples with the lowest porosity fraction and crack formation. The behaviour and mechanism of different cracks and defects within PBF-LBed NiMnSn alloys and $LaCe(Fe,Mn,Si)_{13}$ alloys were revealed.

The chemical composition of PBF-LBed in-situ NiMnSn alloys is more uniform when the heat treatment time increases. Although the long heat treatment process did not significantly affect the MCE of NiMnSn alloys around the curie temperature. The different PBF-LB process parameters did not significantly affect the $\Delta S_m$ around $T_C^A$. The $\Delta S_m$ for the three PBF-LB samples around $T_C^A$ is approximately 1.0 $Jkg^{-1}K^{-1}$ when applied to the 1 T field. Two different heat treatment processes were used to improve the MCE and change the transition temperature of PBF-LBed $LaCe(Fe,Mn,Si)_{13}$. The heat treatment processes in an argon atmosphere enhance the form of $NaZn_{13}$-type $LaCe(Fe,Mn,Si)_{13}$ phases and improve the MCE. The heat treatment in a hydrogen atmosphere incorporates hydrogen atoms into $NaZn_{13}$-type $LaCe(Fe,Mn,Si)_{13}$ interstitially. This treatment improves the MCE and increases the curie temperature. Moreover, the heat treatment in a hydrogen atmosphere can decrease oxides volume, improving the magnetic properties. At $T_c$ (298 K), the $\Delta S_m$ of HTH $LaCe(Fe,Mn,Si)_{13}$ sample was -3.68 $Jkg^{-1}K^{-1}$ when applied to 1 T field. Compared with the pure Gd and LaFeSi-based alloys reported in other literature, the $\Delta S$ of the second-order phase transition (SOPT) in this work was promising $T_c$ (room temperature, 298 K) found in this study makes the material an ideal choice for realising room-temperature magnetic refrigeration.

In this work, the PBF-LB technology is a promising manufacturing route for producing magnetic refrigerant. Furthermore, the PBF-LBed magnetocaloric materials with a large surface area, such as MC cylinders and lattices, can increase the efficiency of heat exchange and magnetic refrigeration.

# LIST OF PUBLICATIONS

The following sections of this work have been published or submitted to the journals for publication:

Chapter 4: **K. Sun**, A.A. Mohamed, S. Li, M. Jeong, J. Head, M.M. Attallah, (2023). Laser Powder Bed Fusion of the NiMnSn Heusler Alloy for Magnetic Refrigeration Applications. Additive Manufacturing, 103536. https://doi.org/10.1016/j.addma.2023.103536

KS conceived and designed the experiment, performed the experiments, interpreted data, and wrote and reviewed the manuscript. AAM, SL, and MMA reviewed the manuscript, assisted in analysing the data, and provided supervision. MJ provided the help of investigation and methodology. JH assisted with the investigation.

Chapter 5: **K. Sun**, S. Li, A.A. Mohamed, K. Ma, R. Duan, O.P. Brooks, M. Jeong, J. Head, R. Sheridan, M.M. Attallah, The effect of Thermal Post-processing Treatment on Laser Powder Bed Fusion Processed NiMnSn-based Alloy for Magnetic Refrigeration. (Manuscript submitted to Journal of Alloys and Compounds; JALCOM-D-23-03535; Initial Date Submitted: Mar 10, 2023; Current Status: Major revision)

KS conceived and designed the experiment, performed the experiments, interpreted data, and wrote and reviewed the manuscript. AAM, SL, and MMA reviewed the manuscript, assisted in analysing the data, and provided supervision. MJ, KM, RD, and JH provided the help of investigation and methodology.

Chapter 6: **K. Sun**, A.A. Mohamed, M. Jeong, E.R. Lewis, P. Ibrahim, O.P. Brooks, R. Sheridan, M.M. Attallah, On the origin of cracking in laser powder bed fusion processed $LaCe(Fe,Mn,Si)_{13}$, and the impact of post-processing. (Manuscript submitted to Journal of Alloys and

Compounds; JALCOM-D-23-02077; Initial Date Submitted: Feb 12, 2023; Current Status: Under Review.)

KS conceived and designed the experiment, performed the experiments, interpreted data, and wrote and reviewed the manuscript. AAM, RS, and MMA reviewed the manuscript, assisted in analysing the data, and provided supervision. MJ, ERL, and PI provided the help of investigation and methodology.

# TABLE OF CONTENTS

**CHAPTER 1: Introduction ..... 1**

1.1 Additive manufacturing-laser powder bed fusion ..... 1

1.2 Magnetocaloric materials ..... 5

1.3 Aims and objectives of the research ..... 6

1.4 References ..... 8

**CHAPTER 2: Literature Review ..... 10**

2.1 Laser powder bed fusion (PBF-LB) ..... 10

2.1.1 Thermo physical phenomena ..... 10

2.1.2 Process parameters in PBF-LB ..... 19

2.1.3 The defects in PBF-LB ..... 22

2.2 Solidification theory ..... 23

2.2.1 Nucleation ..... 24

2.2.2 Growth ..... 25

2.2.3 Undercooling ..... 26

2.3 Magnetocaloric materials ..... 27

2.3.1 Magnetocaloric materials' history ..... 27

2.3.2 The characterisation of magnetocaloric materials ..... 30

2.3.3 The magnetic refrigeration cycles ..... 32

2.3.4 Magnetic entropy change ($\Delta S$) and adiabatic temperature change ($\Delta T_{ad}$) ..... 34

2.4 Metallurgy of NiMnSn alloy ..... 35

2.4.1 The crystal structure of NiMnSn alloy ..... 35

2.4.2 The martensite phase structure of NiMn-based alloy ..... 38

2.4.3 The magnetic transformation of NiMnSn alloy ..... 41

2.4.4 FOPT and SOPT of NiMnSn alloy ..... 43

2.4.5 The heat treatment process ..... 45

2.5 Metallurgy of LaFeSi-based alloy ..... 47

2.5.1 The LaFeSi alloy ..... 47

2.5.2 The crystal structure and phase transformation ..... 47

2.5.3 The optimisation of MCE ..... 49

2.5.4 The heat treatment process ..... 49

2.6 The manufacturing methods of magnetocaloric materials ..... 51

2.7 Additive manufacturing of the magnetocaloric materials ..... 52

2.7.1 Additive manufacturing of the magnetic materials ..... 52

2.7.2 Magnetocaloric materials ..... 53

2.8 Summary of the literature and areas for further investigation ..... 55

2.9 References ..... 56

**CHAPTER 3: Experimental Methods..... 67**

3.1 Introduction ..... 67

3.2 Materials ..... 67

3.2.1 The details of powders ..... 67

3.2.2 As-received powder particle size distribution measurement ..... 69

3.2.3 Chemical composition analysis ..... 69

3.3 Laser powder bed fusion ..... 70

3.3.1 Machine set-up ..... 70

3.3.2 Scanning strategy ..... 72

3.4 The heat treatment process ..... 73

3.5 Microstructural characterisation ..... 74

3.5.1 Metallurgical samples preparation ..... 74

3.5.2 Scanning electron microscopy (SEM) ..... 77

3.5.3 X-Ray Diffraction (XRD) ..... 81

3.5.4 Transmission electron microscopy (TEM) ..... 83

3.6 Superconducting quantum interference device (SQUID)-Magnetic property measurement system (MPMS) ..... 86

3.7 References ..... 90

**CHAPTER 4: Laser Powder Bed Fusion of the NiMnSn Heusler Alloy for Magnetic Refrigeration Applications ..... 92**

4.1 Abstract ..... 92

4.2 Introduction ..... 93

4.3 Material and methods ..... 95

4.3.1 Powder preparation ..... 95

4.3.2 Sample fabrication and design of experiment ..... 97

4.3.3 Sample preparation and analysis ..... 99

4.4 Results and discussion ..... 102

4.4.1 Microstructure of the as-fabricated samples ..... 102

4.4.2 Microstructure evolution and defects mechanism ..... 103

4.4.3 Influence of thermal quenching post-process on the microstructure ..... 106

4.4.4 Density ..... 109

4.4.5 Influence of thermal quenching post-process on the phase formation ..... 114

4.4.6 Magnetic properties ..... 116

4.4.6.1 Temperature dependence of magnetisation ..... 116

4.4.6.2 Isothermal magnetisation ..... 117

4.4.6.3 Magnetocaloric effect (MCE) ..... 122

4.5 Conclusion ..... 129

4.6 References ..... 130

**CHAPTER 5: The effect of Thermal Post-processing Treatment on Laser Powder Bed Fusion Processed NiMnSn-based Alloy for Magnetic Refrigeration ..... 136**

5.1 Abstract ..... 136

5.2 Introduction ..... 137

5.3 Experimental ..... 138

5.3.1 In-situ powder ..... 138

5.3.2 PBF-LB processing and heat treatment ..... 139

5.3.3 Microstructural characterisation and magnetic measurements ..... 140

5.4 Result and discussion ..... 141

5.4.1 Microstructure ..... 141

5.4.1.1 Influence of HT process on the microstructure and phase formation ..... 141

5.4.1.2 Composition evolution ..... 147

5.4.2 Magnetic properties ..... 149

5.4.2.1 Thermo-magnetisation curves ..... 149

5.4.2.2 Temperature dependence of magnetisation at 1 T magnetic field ..... 151

5.4.2.3 Isothermal magnetisation ..... 154

5.4.2.4 Magnetocaloric effect (MCE) ..... 158

5.5 Conclusions ..... 159

5.6 References ..... 160

**CHAPTER 6: On the Origin of Cracking in Laser Powder Bed Fusion Processed $LaCe(Fe,Mn,Si)_{13}$, and The Impact of Post-Processing ..... 165**

6.1 Abstract ..... 165

6.2 Introduction ..... 166

6.3 Experimental ..... 168

6.3.1 Laser powder bed fusion ..... 168

6.3.2 Powder characterisation ..... 169

6.3.3 Heat-treatment ..... 169

6.3.4. Microstructural characterisation and magnetic measurements ..... 170

6.4 Result and Discussion ..... 171

6.4.1 Characteristics of the pre-alloy powder ..... 171

6.4.2 PBF-LB parameters and flaw characterisation ..... 172

6.4.2.1 The defects within the microstructure ..... 172

6.4.2.2 The relationship between the linear energy density and the hatch ..... 175

6.4.3 Microstructure and crystallographic texture ..... 176

6.4.3.1 Microstructure of the as-fabricated sample ..... 176

6.4.3.2 Microstructure of the heat-treated sample (HTH) ..... 180

6.4.4 Detailed characterisation of cracking modes ..... 182

6.4.4.1 The solidification cracking ..... 182

6.4.4.2 Intergranular liquid film ..... 184

6.4.4.3 Driving force for the initiation and propagation of cracks ..... 185

6.4.5 The solid-state cracking ..... 186

6.4.5.1 The longitudinal crack ..... 186

6.4.5.2 The transverse crack ..... 187

6.4.6 The segregation cracking ..... 189

6.4.7 Magnetic property ..... 190

6.5 Conclusion ..... 196

6.6 References ..... 197

**CHAPTER 7: Conclusion & Future work ..... 202**

7.1 Summary and conclusion ..... 202

7.1.1 Parametrical studies for densification ..... 202

7.1.2 Influence of solution heat treatments ..... 203

7.1.3 The cracking mechanisms ..... 203

7.1.4 The magnetocaloric effect ..... 204

7.2 Future work ..... 205

# LIST OF FIGURES

**Fig. 1.1.** Principle of PBF-LB process. ……2

**Fig. 1.2.** A magnetic refrigeration device's general block diagram. ……..……3

**Fig. 1.3.** The main classification of magnetocaloric materials. ……6

**Fig. 2.1.** Schematic representation of heat transfer. ……...……11

**Fig. 2.2.** Reflection of laser light in powder. ……12

**Fig. 2.3.** Absorptivity of the powder layer for different particle sizes. ……14

**Fig. 2.4.** Absorbed irradiance of powder layers with different powder sizes. ……...…..14

**Fig. 2.5.** The relationship between $E_L$, melt pool depth, and absorption ratio. ……...15

**Fig. 2.6.** The reflection of the laser beam (a) a few reflections, and (b) multiple reflections. 16

**Fig. 2.7.** Schematic representation of possible process by-products. ……..17

**Fig. 2.8.** Melt pool flow dynamics. a, b and c present the global, transverse, and longitudinal views of melt pool flow. The black arrows indicate the velocity vector. The white (interface flow) and yellow (inside flow) arrows indicate the flow pattern. ……18

**Fig. 2.9.** The PBF-LB process and process parameters……..20

**Fig. 2.10.** PBF-LB terminology. ……20

**Fig. 2.11.** Schematic of different scanning strategies. ……21

**Fig. 2.12.** Classification of defects. ……22

**Fig. 2.13.** Temperature gradient G and growth rate R's effect on microstructure's morphology and size. ……26

**Fig. 2.14.** The influence of constitutional supercooling on different structural morphologies.27

**Fig. 2.15.** The schematic representation of the structures of the semi and full-Heusler compounds. ……..……29

**Fig. 2.16.** Schematic representation of the unit cell of $LaFe_{11.6}Si_{1.4}$ (space group Fm-3c). .30

**Fig. 2.17.** Schematic representation of magnetisation (M) concerning temperature. ……31

**Fig. 2.18.** The magnetocaloric cycle. ……...33

**Fig. 2.19.** Four stages of a magnetic refrigeration cycle. ……33

**Fig. 2.20.** Schematic of the relationship between the entropy of magnetocaloric material and temperature. ……..34

**Fig. 2.21.** Schematic representation of the $L2_1$-NiMnSn HA and its components. ……36

**Fig. 2.22.** NiMnSn ternary phase diagrams with Ni content of 50 at.%. ……..36

**Fig. 2.23.** The $Ni_{50}Mn_{50-x}Sn_x$ alloys' XRD results: (a) as-melted samples, (b) annealed samples. ……38

**Fig. 2.24.** The crystal structures of austenite and different martensites in Ni-Mn-In alloys. ..39

**Fig. 2.25.** Crystal structures of 4O martensite. ……39

**Fig. 2.26.** XRD results with varying temperatures for NiMnSn alloys with different e/a. ...40

**Fig. 2.27.** Phase diagrams for $Ni_{50}Mn_{50-x}Ga_x$ (a) and $Ni_{50}Mn_{50-x}Sn_x$ (b) Heusler alloys. ……41

**Fig. 2.28.** Summary of the main relevant forms of magnetism and their features. ...42

**Fig. 2.29.** The effects of different chemical substitutions on the magnetic structure of the austenite phase. a) Unit cell of the $L2_1$ structure (Wyckoff sites 4a, 4b, and 8c are marked by red, yellow, and blue colors, respectively) corresponding to the $X_2MnZ$ (X—late transition element, Z—main group element) composition. The colour of a particular Wyckoff site matches that of the occupying element. d) In case of $Ni_2MnZ$, the parallel Mn–Ni coupling is much weak. e) In the case of $Ni_2Mn_{1+x}Z_{1-x}$, excess Mn randomly substitutes Z atoms in the 4b sites (indicated by mixed-coloured spheres). This leads to the emergence of antiparallel Mn(4a)–Mn(4b) exchange coupling (indicated by the red bonds). ……...43

**Fig. 2.30.** M (T) at H = 5 mT and 5 T. (a)–(j) show ZFC, FC, and FW runs for $Ni_{50}Mn_{50-x}Sn_x$ samples with x=20.3, 16.2, 15.1, 13.0 {(e/a) = 8.11}, 13.0 {(e/a) = 8.12}, 11.4, 11.0, 10.1, 8.9, 7.1, and 5.1, respectively. ……45

**Fig. 2.31.** SEM micrographs of $Ni_{50}Mn_{37}Sn_{13}$ showing the effects of heat treatment at 950 °C followed by water quench: (a) as-cast; (b) 1 h; (c) 2 h; (d) 72 h. ……46

**Fig. 2.32.** Schematic illustrations of the (a) cubic-type, (b) tetragonal-type $LaFe_{13-x}Si_x$ phases with their Wyckoff positions, and (c) Vertical section phase diagram in $La(Fe_{1-x}Si_x)_{13}$ ($0.07 \leq x \leq 0.40$). ……48

**Fig. 2.33.** Backscattering images (BSIs) of the specimens annealed at 1323 K for different annealing times. (a) 0, (b) 25, (c) 50, (d) 100, (e) 200 and (f) 300 h. (The α-Fe and LaFeSi phases are the (A) and (B) phases, respectively. The (C) phase, identified as the $NaZn_{13}$-type phase.). ……50

**Fig. 2.34.** The 3D printing of magnetic refrigerant. ……54

**Fig. 3.1.** Schematic illustration of the powder blending process. ……67

**Fig. 3.2.** The mixed Ni, Mn, and Sn powders. ……68

**Fig. 3.3.** The microstructure of pre-alloy powder. ……...69

**Fig. 3.4.** Photographs showing the main features of the 'Concept Laser M2 Laser Powder Bed'. ……...…..70

**Fig. 3.5.** Experimental flow chart. ……71

**Fig. 3.6.** PBF-LBed NiMnSn blocks, lattices, and microchannel cylinders. ……...……72

**Fig. 3.7.** A schematic illustration shows the three scanning strategies for building block samples in this study. ……...……72

**Fig. 3.8.** (a) The LJD 1500 ℃ furnace, and (b) the tube furnace is filled with hydrogen gas……..……73

**Fig. 3.9.** The electrical discharge machining (EDM). ……..74

**Fig. 3.10.** The whole cutting process. ……....75

**Fig. 3.11.** Density testing equipment. ……76

**Fig. 3.12.** Struers-Tegramin grinding and polishing machines. ……...……77

**Fig. 3.13.** Schematic diagrams for SEM. ……78

**Fig. 3.14.** The Hitachi TM3000 SEM. ……...80

**Fig. 3.15.** The FEI FIB Quanta 3D SEM. ……..80

**Fig. 3.16.** The Jeol 7000 SEM. ……81

**Fig. 3.17.** Schematic representation of θ-2θ configuration for XRD measurements. ……82

**Fig. 3.18.** The Proto AXRD. ……...……..83

**Fig. 3.19.** Schematic diagrams for TEM. ……84

**Fig. 3.20.** Tecnai F20 TEM. ……..…85

**Fig. 3.21.** Quantum design magnetic properties measurements system (MPMS). ……89

**Fig. 4.1.** (a) Schematic illustration of the powder blending process, (b) backscattered electron image and corresponding EDX elemental map of the NiMnSn blended powder, (c) Particle size distribution of the three powders. ……96

**Fig. 4.2.** (a) and (b) PBF-LB-fabricated specimens, (c) Geometry of blocks, lattices, and microchannel cylinders, (d) Details of three different designs. ……...98

**Fig. 4.3.** Three different scan strategies; 90˚ raster, island scan, and chess scan strategies.…98

**Fig. 4.4.** The correlation of $E_L$ and Hatch with the (a) Defects fraction and (b) Crack density of all blocks with 90° raster scan strategy. ……103

**Fig. 4.5.** SEM-BSE micrographs showing the defects in the sample with low energy density……104

**Fig. 4.6.** SEM-BSE micrographs showing the defects in the best sample (No.2-AF) ……105

**Fig. 4.7.** SEM-BSE micrographs showing the defects in the sample with high energy density……106

**Fig. 4.8.** SEM-BSE micrographs showing surface morphologies (X-Y) and microstructure of MC cylinders samples; SEM-BSE micrographs showing surface morphologies (X-Y/Y-Z) and microstructure lattice strut samples. ……109

**Fig. 4.9.** (a) Influence of $E_V$ on density, (b) Influence of laser scan strategy on block density. ……111

**Fig. 4.10**. The relationship of $E_V$, $E_L$, and the relative density of all blocks with 90° raster scan strategy. ……112

**Fig. 4.11.** SEM-BSE micrographs showing surface morphologies (X-Y) and microstructure of cylinders with the microchannels (red circles); SEM-BSE micrographs showing surface morphologies (X-Y/Y-Z) and microstructure lattice strut samples…….113

**Fig. 4.12.** XRD patterns of the heat-treated PBF-LB processed NiMnSn alloys……..…….115

**Fig. 4.13.** XRD patterns of the heat-treated PBF-LB processed NiMnSn alloys at different temperatures (100 K, 200 K, 295 K). ……115

**Fig. 4.14.** Thermo-magnetisation curves of HT PBF-LBed samples in an applied field of 0.01 T……116

**Fig. 4.15.** (a, b, c) Isothermal magnetisation curves of PBF-LB block samples with E = 18.52 J/mm$^3$, 53.33 J/mm$^3$ and 88.89 J/mm$^3$ near the martensitic transition temperature, (d,e,f) Isothermal magnetisation curves of PBF-LB block samples with E=18.52 J/mm$^3$, 53.33 J/mm$^3$, and E=88.89 J/mm$^3$ near the $T_C^A$. ……120

**Fig. 4.16.** Arrott plots of HT PBF-LB block samples with E=18.52 J/mm$^3$, 53.33 J/mm$^3$, and E=88.89 J/mm$^3$ near (a,b,c) the martensitic transition temperature and (d, e, f) near the $T_C^A$……121

**Fig. 4.17.** The value of n around the $T_C^A$ and $T_M$……122

**Fig. 4.18.** (a) Thermal variation of ΔS around FOPT of HT block samples at 1 T, and (b) Thermal variation of ΔS around SOPT of HT block samples at 1 T. ……123

**Fig. 5.1.** (a) The backscattered electron image and the corresponding EDX elemental map of NiMnSn blended powder. (b) The schematic of the powders blending processing. ……...139

**Fig. 5.2.** The scan strategy. ……140

**Fig. 5.3.** SEM-BSE micrographs of the microstructure of (a) the as-fabricated sample; (b) the Mixed EDX map for the as-fabricated sample; (c, d, e) the HT samples; (e) and (f) the Mn segregation (red box in (e))……142

**Fig. 5.4.** XRD patterns of AF and annealed PBF-LB processed NiMnSn alloys. The # peaks fit the MnO phase. Other peaks correspond to the $L2_1$ Heusler phase.…..……...142

**Fig. 5.5.** (a) The SEM picture of the No.3 sample (the inset picture is the EDX line analysis); (b and d) the EBSD Kikuchi pattern from $L2_1$ $Ni_2MnSn$ structure in the No.3 sample; (c and e) the EBSD Kikuchi pattern from MnO structure in the No.3 sample. ……143

**Fig. 5.6.** The SEM micrograph of (a) the FIB lift-out region with Mn segregation in the No.3 sample and (b) TEM samples; (c) STEM bright-field image showing the precipitate-matrix boundary and nano-scale phases within the precipitates with corresponding element mapping by STEM-EDX. (d and e) The TEM image and the selected area electron diffraction (SAED) pattern were collected from the red dotted circle. ……..…..144

**Fig. 5.7.** EBSD analyses of the PBF-LBed NiMnSn alloy (X-Z section) annealed at 940 °C (the SEM picture, corresponding image quality maps, IPF map, and KAM map): (a-d) as-fabricated sample, (e-h) annealed for one week, (i-l) annealed for two weeks, (m-p) annealed for three weeks. ……..147

**Fig. 5.8.** Thermo-magnetization curves in an applied field of 0.01 T for the annealed PBF-LB processed NiMnSn alloys; the inset displays the dM/dT vs temperature for NiMnSn alloys. ……151

**Fig. 5.9.** Thermo-magnetization curves in an applied field of 1 T for the annealed PBF-LB processed NiMnSn alloys. ……...152

**Fig. 5.10.** (a,c,e) Isothermal magnetisation curves of PBF-LBed NiMnSn samples with annealing time of one week, two weeks, and three weeks near the martensitic transition temperature; (b,d,f) Isothermal magnetisation curves of PBF-LBed NiMnSn samples with annealing time of one week, two weeks, and three weeks near the curie temperature of the austenite phase. ……..155

**Fig. 5.11.** Arrott plots of annealed PBF-LBed block samples with annealing time of 1 week, 2 weeks, and 3 weeks near (a,c,e) the martensitic transition temperature and (b,d,f) near the curie temperature. ……..…157

**Fig. 5.12.** The value of n around the $T_c$ and $T_M$. ……158

**Fig. 5.13.** (a) the thermal variation of ΔS around the FOPT of the HTed block samples; (b) the thermal variation of ΔS around the SOPT of the HTed block samples. ……159

**Fig. 6.1.** The chess scan strategy. ……168

**Fig. 6.2.** (a-c) The microstructure of pre-alloy powder. (c-1, …, c-6) The SEM-EDX map of the pre-allow powder in (c). (d-1, …, d-6) The SEM-EDX map of the pre-allow powder in (d). ……..171

**Fig. 6.3.** Defects distribution in SEM images evolution with PBF-LB laser power for 90 W, 100 W, and 125 W. ……173

**Fig. 6.4.** The redeposits during the PBF-LB process. ……174

**Fig. 6.5.** The microstructure of the redeposits. ……...175

**Fig. 6.6.** The linear energy density and hatch influence on the porosity and cracks. …….176

**Fig. 6.7.** The microstructure of the AF sample (a and b) SEM images, (c and d) Euler EBSD image of the microstructure, (e) EBSD band contrast (BC) map, (f) EBSD phases map, (g) SEM image, and (h) the SEM-BSE image. ……178

**Fig. 6.8.** The microstructure of #90-4 sample with higher magnification (a and b) SEM and BSE images, and EDX map, including La, Ce, Fe, Mn, Si, and O elements. ……179

**Fig. 6.9.** The microstructure of the HTH sample: (a and b) SEM and BSE images with low magnification, (c and d) BSE images with high magnification, and (e) EDX map for the microstructure. ……..180

**Fig. 6.10.** XRD patterns of the #90-4 and HTH samples. ……..……181

**Fig. 6.11.** SEM microscopy of hot cracking in #90-4: (a) Hot crack; and (b) The details of hot cracking. ……..……183

**Fig. 6.12.** (a) The inverse pole figure (IPF) along the crack; (b) SEM image showing the crack. ……...183

**Fig. 6.13.** Solid-state cracks observed in #90-4 sample: (a) the SEM image with low magnification; (b) the SEM image with high magnification; (c) the SEM-BSE image with high magnification; (d) the IPF map with low magnification; and (e-f) the IPF map with high magnification. ……187

**Fig. 6.14.** Transverse solid-state cracks: (a) the SEM image with low magnification; (b-c) the image with high magnification. ……188

**Fig. 6.15.** Transverse solid-state cracks: (a) the SEM image; (b) the corresponding IPF map. ……189

**Fig. 6.16.** (a-d) SEM microscopy of the cracking around the La/Ce/Si segregations……190

**Fig. 6.17.** (a) Thermo-magnetisation curves in an applied field of 0.01 T; (b) Isothermal magnetisation curves of the HTH sample near the $T_c$; (c) the relevant induced Arrott plot; and (d) the Thermal variation of $\Delta S$ around the $T_c$ at 1 T. ...……192

# LIST OF TABLES

**Table 2.1.** The absorptance of powders. ……13

**Table 3.1.** Starting powder characteristics. ……68

**Table 4.1.** Starting raw powder characteristics. ……96

**Table 4.2.** The investigated PBF-LB processing parameters for blocks with the 90° raster scan strategy. ……99

**Table 4.3.** The PBF-LB processing parameters for blocks with island and chess scan strategies, MC cylinders and lattices. ( √ : Succeed; × : Failed). ……101

**Table 4.4.** The PBF-LB and heat treatment processing parameters for picked blocks.…107

**Table 4.5.** Average chemical composition analysis in at.% of the HT PBF-LB for the HT block sample using SEM-EDX. ……107

**Table 4.6.** Chemical composition analysis (including oxygen analysis using LECO) in at. % for the HT block sample. ……108

**Table 4.7.** Comparison of the magnetic entropy of the NiMnSn Heusler alloys with those reported in the literature. ……126

**Table 5.1.** The information about powders. ……..139

**Table 5.2.** The investigated PBF-LB processing parameters. ……140

**Table 5.3.** Average chemical composition analysis in at.% of the No.3 sample at different points using SEM-EDX. ……145

**Table 5.4.** The average chemical composition and the composition deviation for PBF-LBed samples with different HT processes. ……149

**Table 5.5.** The characteristic temperature of the magnetic phase transformation at 1 T. ……...……153

**Table 6.1.** The investigated PBF-LB processing parameters for blocks with the chess scan strategy. ……..……..169

**Table 6.2.** The heat-treatment processing. ……169

**Table 6.3.** Chemical composition analysis in wt.% of the pre-alloy powder and as-fabricated and HT samples with $E_V$=250 J/mm$^3$. ……172

**Table 6.4.** Composition at points shown in Fig. 6.8 b obtained via EDX. ……177

**Table 6.5.** Composition at points shown in Fig. 6.10 a and d obtained via EDX. ……..181

**Table 6.6.** The physical parameters are used to calculate the undercooling $\Delta T_{ad}$. ……185

**Table 6.7.** Comparison of the magnetic entropy of the LaFeSi-based alloys with those reported in the literature. ……193

# LIST OF SYMBOLS AND ABBREVIATIONS

| Symbol | Definition |
|---|---|
| AF | As-fabricated |
| AFM | Antiferromagnetic |
| AM | Additive manufacturing |
| AOD | Atomic ordering degree |
| $A_f$ | Austenitic finish temperature |
| $A_s$ | Austenitic start temperature |
| BCC | Body-centred cubic |
| BD | Build direction |
| BSE | Backscattered electrons |
| CAD | Computer-aided design |
| d | The layer thickness |
| EBSD | Electron backscattered diffraction |
| EDM | Electrical discharge machining |
| EDX | Energy dispersive X-Ray spectroscopy |
| $E_L$ | The linear energy density |
| $E_V$ | the volume energy density |
| FC | Field cooling |
| FMA | Ferromagnetic austenite |
| FM | Ferromagnetic |
| FMM | Ferromagnetic martensite |
| FOPT | First-order phase transition |
| FW | Field warming |
| h | The hatch distance |
| HA | Heusler alloys |
| HAGB | High-angle grain boundaries |
| HT | Heat treatment |

| | |
|---|---|
| IPF | Inverse pole figure |
| G | The Gibbs free energy |
| GB | Grain boundary |
| KAM | Kernel averaged misorientation |
| LAGB | Low-angle grain boundaries |
| $L1_0$ | Modulated martensite with on-modulated martensite |
| MCE | Magnetocaloric effect |
| MCMs | Magnetocaloric materials |
| $M_f$ | Martensite finish temperature |
| MPMS | Magnetic property measurement system |
| $M_s$ | Martensite start temperature |
| P | The effective laser power |
| PBF-LBed | Laser powder bed fusion made |
| PM | Paramagnetic |
| PMA | Paramagnetic austenite |
| PMM | Paramagnetic martensite |
| $\overrightarrow{Q_{CD}}$ | The sum of conduction |
| $\overrightarrow{Q_{CV}}$ | The convection losses |
| $\overrightarrow{Q_R}$ | The radiation losses |
| $\overrightarrow{Q_L}$ | The vector heat quantities for the laser flux |
| RT | Room temperature |
| SAED | The selected area of electron diffraction |
| SEM | Scanning electron microscopy |
| SOPT | Second-order phase transition |
| SQUID | Superconducting quantum interference device |
| T | Temperature |
| $T_c$ | The curie temperature |
| TEM | Transmission electron microscopy |

| | |
|---|---|
| $T_M$ | The martensitic transitions |
| $T_C^A$ | Curie temperature of the austenitic phase |
| V | The laser scan speed |
| XRF | X-ray fluoresce |
| ZFCW | Zero-field cooled warming |
| 4O | Modulated martensite with an orthorhombic four-layered |
| 5M | Modulated martensite with a monoclinic five-layered |
| 6M | Modulated martensite with a monoclinic six-layered |
| 7M | Modulated martensite with a monoclinic seven-layered |
| ΔS | Magnetic entropy change |
| $\Delta S_m$ | Maximum magnetic entropy changes |
| $\Delta T_{hys}$ | Thermal hysteresis |
| $\Delta T_{ad}$ | Adiabatic temperature change |

*For the abbreviations used more than three times.

# CHAPTER 1: Introduction

This chapter briefly introduces magnetocaloric materials and laser powder bed fusion (PBF-LB) technology, one additive manufacturing (AM) method. The novelty of the thesis is briefly stated. Finally, the aim of this research is presented.

## 1.1 Magnetocaloric materials (MCMs)

Refrigeration and air conditioning are widely used daily to control environmental temperatures, such as in airports, hospitals, offices, etc. However, the effective use of these machines is a response to high energy consumption and global warming because of the vapour refrigeration system and environmentally polluted freezing medium [1]. Magnetic refrigeration is a promising technology to save energy, improve energy-efficient thermal management, and address global warming. Also, magnetic refrigeration devices can reduce noise and vibration by avoiding gas compression. Magnetic refrigeration can be applied in various thermal management applications, such as air-conditioning, data servers, cooling of vaccines, solar cell panels, and electronic devices [2].

Fig. 1.1 shows a magnetic refrigeration device's general working principle. The apparatus comprises a magnetic refrigeration material, a switched magnetic field source, and two thermal valves. The thermal valve allows thermal contact with the cooled heat load and sinks at isothermal segments of the Carnot cycle. A thermal valve will isolate the working body (magnetocaloric materials) during adiabatic magnetisation and demagnetisation [3]. The magnetisation-demagnetisation can be achieved by switching the current in the magnetic field.

By controlling the magnetic field, magnetocaloric materials can store and release heat due to their magnetocaloric effect (MCE) [4, 5]. And several families of magnetocaloric materials have been studied during the last decade. Franco and Blazquez et al. [5] summarised different magnetocaloric materials' primary information and classified them in terms of crystalline materials and amorphous materials (see Fig. 1.2).

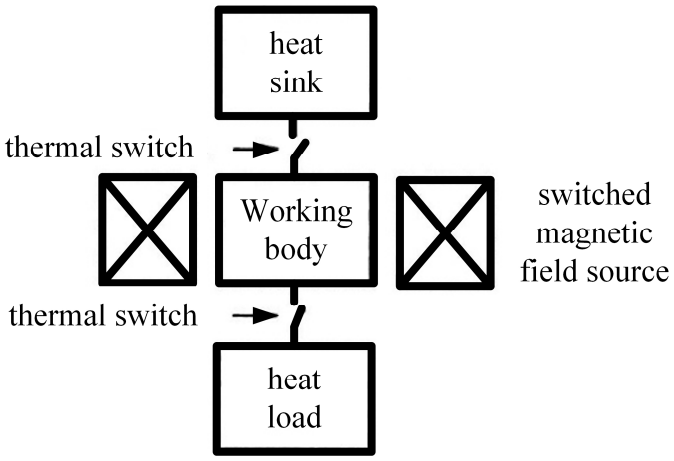



**Fig. 1.1. A magnetic refrigeration device's general block diagram [3].**

The magnetocaloric effect's characteristics are the maximum effect and reversibility near the transition temperature. NiMn-based Heusler alloy (NiMnZ, Z=Ga, In, Sn, Sb) is a new series of ferromagnetic materials. The alloy shows a promising magnetocaloric effect and controllable working temperature of magnetic refrigeration. And NiMn-based Heusler alloy (HA) are cheaper than rare-earth-based magnetocaloric materials [6].

It is possible to control the curie temperature and the phase transition temperature in NiMn-based HA in magnetic refrigeration by adjusting the ratio of alloying elements and adding new compositions (Co, Cr, Si). Magnetic refrigeration can therefore be performed at low, high, and near room temperatures. Designing and inventing new NiMn-based HA with a tremendous magnetic effect and less hysteresis is also possible. Magnetism, mechanical sensing, magnetic

**Fig. 1.2. The primary classification of magnetocaloric materials [2].**

field-induced actuation, and energy harvesting are all potential applications of NiMnSn alloys [7]. The low cost, nontoxic nature, good mechanical properties, and competitive MCE of NiMn-based HA make them attractive [7].

It is also worth mentioning that $La(Fe,Si)_{13}$-based alloys have low costs, low loss of hysteresis, nontoxic effects, and a significant magnetocaloric effect (MCE) [8]. The MCE of $La(Fe,Si)_{13}$-based alloys is attributed to the $NaZn_{13}$-type $La(Fe,Si)_{13}$ phases (the 1:13 phase) [8]. However, the as-cast state $La(Fe,Si)_{13}$-based alloys consist of a large amount of the LaFeSi phases, α-Fe phases, and a small number of other phases. This is because conventional melt/solidification processes do not enable peritectic reactions to occur ($\alpha\text{-Fe}+LaFeSi=La(Fe,Si)_{13}$) [9]. As a result of a long heat-treatment process at high temperatures and quenching, the 1:13 phase volume fraction increases [10]. However, Mayer et al. produced $LaCe(Fe,Mn,Si)_{13}$ pre-alloy powder, which can reach approx 95 wt. % of the 1:13 phase after heat treatment with only one hour at 1373 K [11]. Thus, $LaCe(Fe,Mn,Si)_{13}$ is potential magnetocaloric material.

MCMs have been prepared via different synthesis methods, such as arc melting and powder metallurgy [12], …etc. The main problem of resultant samples from these traditional methods is the lack of shaping to suit a specific application, which is a challenge of being machined after fabrication due to the weak mechanical strength of these materials [13]. Additive manufacturing (AM) technology such as PBF-LB has overcome the challenge of machining by direct part production with the ability to do complex designs, where components are designed using computer-aided design software and then built from a raw powder a layer-by-layer fusion [14]. Thus, the PBF-LB technology can overcome the disadvantage of MCMs being difficult-to-machine and directly producing parts with complex shapes, especially the porous MCMs with predefined external shapes and internal architecture [15].

## 1.2 Additive manufacturing-laser powder bed fusion

A complex structure or geometries can be fabricated by additive manufacturing (AM). The method is widely used in the automotive, aerospace, engineering, medicine, biological systems, and food production industries [16]. PBF-LB is one of the advanced additive manufacturing technologies. Three-dimensional (3D) parts can be built using Computer-aided design (CAD) in a computer then the model is separated into hundreds of layers with about 30μm thickness. During PBF-LB, a high-intensity laser melts defined areas under a protective atmosphere. The scanning optics system steers the laser beam in the x-y plane. A table moves down (z-direction) at the same time. The powder can then be melted, layer by layer, as guided by a digital model, directly to construct complex or customised parts [17]. Compared with conventional manufacturing, PBF-LB is especially advantageous in manufacturing customised parts and has high material utilisation. Fig. 1.3 presents the principle of PBF-LB.

During the PBF-LB process, there are some unavoidable problems. PBF-LB is expensive because of the high cost of machine and powder materials. The support structure needs to be removed after building. Elemental evaporation is also an unavoidable problem as the melt pool's maximum temperature is above the boiling point of metallic elements when there is sufficient energy to boil the liquid [18]. The evaporation of Mn, Sn and rare earth metals is intense because of their low boiling point. The intense element vaporisation disturbs the molten pool's stability by applying recoil pressure to liquid metal [19]. In addition, post-processing is almost necessary for PBF-LBed parts to reduce residual stresses.

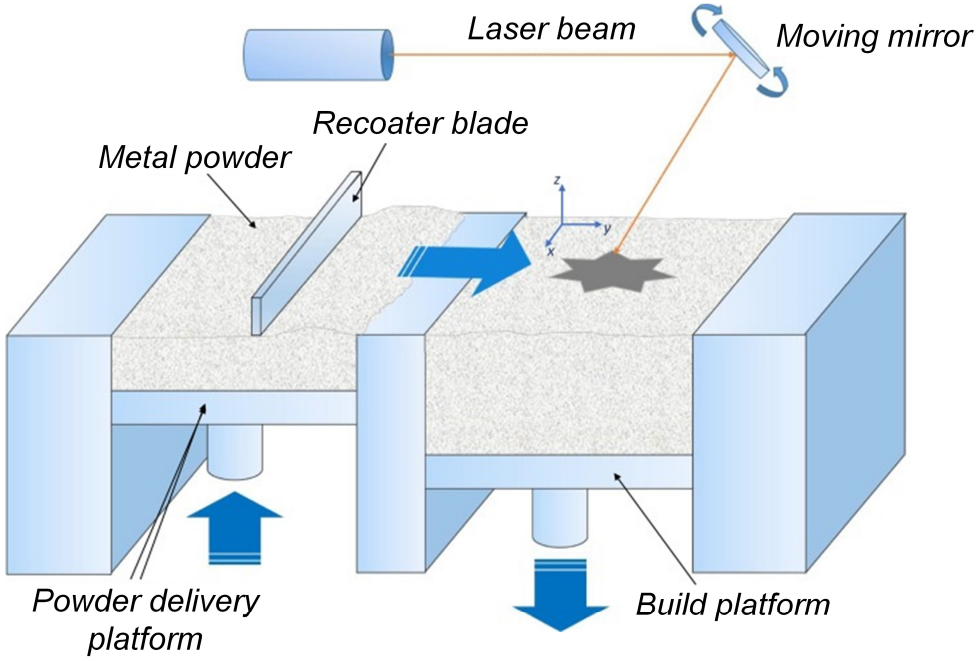



**Fig. 1.3. Principle of PBF-LB process [20].**

## 1.3 Aims and objectives of the research

The study explores the possibility of building different magnetocaloric materials. The in-situ NiMnSn blended powder and pre-alloy $LaCe(Fe,Mn,Si)_{13}$ powder were chosen to build magnetocaloric materials by using PBF-LB. Arc-melted NiMnSn HA is less expensive, environmentally friendly, non-toxic, and has a competitive MCE [6], however, PBF-LBed NiMnSn alloy did not perform good magnetocaloric properties around $T_M$. To PBF-LB magnetocaloric materials with good magnetocaloric properties, the $LaCe(Fe,Mn,Si)_{13}$ pre-alloyed powder was used to PBF-LBed magnetocaloric parts.

The main aim is to develop, process and evaluate high magnetocaloric performance PBF-LBed NiMnSn alloy and $LaCe(Fe,Mn,Si)_{13}$ alloy. The effect of microstructural changes caused by different PBF-LB and heat treatment processes on magnetocaloric properties are studied. The specific objectives are summarised as follows:

- To fabricate NiMnSn bulk samples with the maximum density and minimum defects (cracks and pores) by deriving optimum PBF-LB processing parameters from parametric studies (Chapter 4).
- To understand the mechanisms for pores and cracks formation in PBF-LBed NiMnSn by investigating PBF-LB processing parameters, microstructural features, and residual stresses (Chapter 4).
- To characterise the microstructures of PBF-LBed NiMnSn by observing texture development and grain structures (Chapter 4).
- To maximise heat transfer efficiency and increase the surface-area-to-volume of the component by manufacturing micro-channelled cylinders and lattice strut NiMnSn samples (Chapter 4).
- To investigate the magnetic transition and magnetocaloric properties of the best NiMnSn sample using a Superconducting quantum interference device (SQUID) Magnetic Property Measurement System (MPMS) (Chapter 4).
- To investigate the microstructural development in HT PBF-LBed NiMnSn samples using Scanning Electron Microscopy (SEM), and Transmission Electron Microscopy (TEM) (Chapter 5).
- To investigate the effect of HT on the chemical composition homogeneity using SEM-EDX (Chapter 5).
- To investigate the magnetic transition and MCE of PBF-LBed NiMnSn samples treated with different HT processes using MPMS (Chapter 5).
- To fabricate LaCe(Fe,Mn,Si)$_{13}$ bulk samples with the maximum density and minimum defects by deriving optimum PBF-LB processing parameters from parametric studies (Chapter 6).

- To understand the mechanisms for pores and cracks formation in PBF-Lbed $LaCe(Fe,Mn,Si)_{13}$ by investigating PBF-LB processing parameters, and microstructural features (Chapter 6).
- To study the influence of post-process heat treatments on the microstructures of $LaCe(Fe,Mn,Si)_{13}$ samples (Chapter 6).
- To investigate the magnetic transition and magnetocaloric properties of the best $LaCe(Fe,Mn,Si)_{13}$ sample using MPMS (Chapter 6).

The main findings are shown in chapters 4, 5, and 6. Chapter 7 summarises this thesis and makes recommendations for future research.

## 1.4 References


[1] R.C. Arora, Refrigeration and air conditioning, PHI Learning Pvt. Ltd.2012.

[2] V. Chaudhary, X. Chen, R.V. Ramanujan, Iron and manganese based magnetocaloric materials for near room temperature thermal management, Prog Mater Sci 100 (2019) 64-98.

[3] R. Gimaev, Y. Spichkin, B. Kovalev, K. Kamilov, V. Zverev, A. Tishin, Review on magnetic refrigeration devices based on HTSC materials, International Journal of Refrigeration 100 (2019) 1-12.

[4] V. Franco, J.S. Blazquez, B. Ingale, A. Conde, The Magnetocaloric Effect and Magnetic Refrigeration Near Room Temperature: Materials and Models, Annu Rev Mater Res 42 (2012) 305-342.

[5] V. Franco, J.S. Blazquez, J.J. Ipus, J.Y. Law, L.M. Moreno-Ramirez, A. Conde, Magnetocaloric effect: From materials research to refrigeration devices, Prog Mater Sci 93 (2018) 112-232.

[6] S. Singh, L. Caron, S.W. D'Souza, T. Fichtner, G. Porcari, S. Fabbrici, C. Shekhar, S. Chadov, M. Solzi, C. Felser, Large Magnetization and Reversible Magnetocaloric Effect at the Second-Order Magnetic Transition in Heusler Materials, Adv Mater 28(17) (2016) 3321-3325.

[7] G.H. Yu, Y.L. Xu, Z.H. Liu, H.M. Qiu, Z.Y. Zhu, X.P. Huang, L.Q. Pan, Recent progress in Heusler-type magnetic shape memory alloys, Rare Metals 34(8) (2015) 527-539.

[8] G. Cao, Q. Wang, J. Liu, Y. Zhang, X. Wang, M. Huang, H. Shen, L. Zheng, Enhanced magnetic entropy change and refrigeration capacity of La(Fe,Ni)11.5Si1.5 alloys through vacuum annealing treatment, J Alloy Compd 800 (2019) 363-371.

[9] X.C. Zhong, X.T. Dong, D.R. Peng, S.M. Wu, C.L. Liu, J.H. Huang, H. Zhang, K.W. Long, D.L. Jiao, H. Zhang, W.Q. Qiu, H.Y. Yu, Z.W. Liu, R.V. Ramanujan, Microstructural evolution, magnetocaloric effect, mechanical and thermal properties of hot-pressed LaFe11.6Si1.4/Ce2Co7 composites prepared using strip-cast master alloy flakes, Journal of Magnetism and Magnetic Materials 525 (2021) 167652.

[10] X. Chen, Y. Chen, Y. Tang, The studies of high-temperature and short-time annealing, phase transition process, and magnetic property for LaFe11.7Si1.3 compound, Phase Transitions 85(1-2) (2012) 27-40.

[11] C. Mayer, A. Dubrez, M. Pierronnet, P. Vikner, Towards the large scale production of (La1-zCez)(Fe1-x-yMnySix)13Hn products for room temperature refrigeration, 11(5-6) (2014) 1059-1063.

[12] A.E.-M.A. Mohamed, B. Hernando, Self-assembled impurity and its effect on magnetic and magnetocaloric properties of manganites, Ceram Int 44(14) (2018) 17044-17049.

[13] J.D. Moore, D. Klemm, D. Lindackers, S. Grasemann, R. Träger, J. Eckert, L. Löber, S. Scudino, M. Katter, A. Barcza, K.P. Skokov, O. Gutfleisch, Selective laser melting of La(Fe,Co,Si)13 geometries for magnetic refrigeration, J Appl Phys 114(4) (2013) 043907.

[14] T. DebRoy, H.L. Wei, J.S. Zuback, T. Mukherjee, J.W. Elmer, J.O. Milewski, A.M. Beese, A. Wilson-Heid, A. De, W. Zhang, Additive manufacturing of metallic components – Process, structure and properties, Prog Mater Sci 92 (2018) 112-224.

[15] W. Sun, X. Lu, Z. Wei, Q. Li, Z. Li, Y. Zhang, J. Liu, Multicaloric effect in Ni–Mn–Sn metamagnetic shape memory alloys by laser powder bed fusion, Addit Manuf 59 (2022) 103125.

[16] W. Gao, Y. Zhang, D. Ramanujan, K. Ramani, Y. Chen, C.B. Williams, C.C.L. Wang, Y.C. Shin, S. Zhang, P.D. Zavattieri, The status, challenges, and future of additive manufacturing in engineering, Computer-Aided Design 69 (2015) 65-89.

[17] H. Attar, M. Calin, L.C. Zhang, S. Scudino, J. Eckert, Manufacture by selective laser melting and mechanical behavior of commercially pure titanium, Materials Science and Engineering: A 593 (2014) 170-177.

[18] Y. Lu, Y. Wang, Physics based compressive sensing to monitor temperature and melt flow in laser powder bed fusion, Addit Manuf 47 (2021) 102304.

[19] K. Wei, Z. Wang, X. Zeng, Influence of element vaporization on formability, composition, microstructure, and mechanical performance of the selective laser melted Mg–Zn–Zr components, Mater Lett 156 (2015) 187-190.

[20] V. Griffiths, J.P. Scanlan, M.H. Eres, A. Martinez-Sykora, P. Chinchapatnam, Cost-driven build orientation and bin packing of parts in Selective Laser Melting (SLM), European Journal of Operational Research 273(1) (2019) 334-352.

# CHAPTER 2: Literature Review

This chapter provides a general introduction to PBF-LB processing and magnetocaloric materials. This chapter also details the metallurgy of NiMnSn and LaCe(Fe,Mn,Si)$_{13}$ alloys, with relevant literature regarding them discussed with emphasis on the heat treatment process' effect on the microstructure and MCE. The final section discussed the magnetocaloric materials' different traditional manufacturing methods.

## 2.1 Laser powder bed fusion (PBF-LB)

In L-PBF, Computer-aided design (CAD) files are prepared first, then computer software slices them into two-dimensional (2D) layers. The layer thickness of the slice is one of the PBF-LB process parameters. During the PBF-LB process, the laser beam is incident on a metal powder bed. A relatively high-powered laser entirely melted the layer of metal powder. Then, a new layer of powder is applied after lowering the platform by a predetermined layer thickness. As the cycle repeats, the last sliced layer of components melts. Thus, complex parts are directly built by melting the powder in selected areas layer by layer under the guides of a digital model. The building process was completed in the argon atmosphere ($O_2$<1000 ppm). The oxygen sensor is used to measure the $O_2$.

### 2.1.1 Thermo physical phenomena

During the PBF-LB process, the laser interacts with the powder, a highly complex thermophysical phenomenon [1]. Several complex multi-phenomena are involved in melting and solidifying powders, including laser-powder interaction, spattering, evaporation, melt pool dynamics, and gas bubble dynamics [2-4]. This section introduces the essential thermophysical

phenomena within the powder bed and the melt pool. According to the first law of thermodynamics, the vector heat quantities for the laser flux ($\overrightarrow{Q_L}$) are equal to the sum of conduction ( $\overrightarrow{Q_{CD}}$) happening between the powder bed and substrate, and inside the powder bed, convection losses ($\overrightarrow{Q_{CV}}$) happening between the powder bed and environment, and radiation losses ($\overrightarrow{Q_R}$) happening between the laser beam and powder particles in the closed system (see Eq. 2.1 and Fig. 2.1) [5].

$$\overrightarrow{Q_L} = \overrightarrow{Q_{CD}} + \overrightarrow{Q_{CV}} + \overrightarrow{Q_R} \tag{2.1}$$

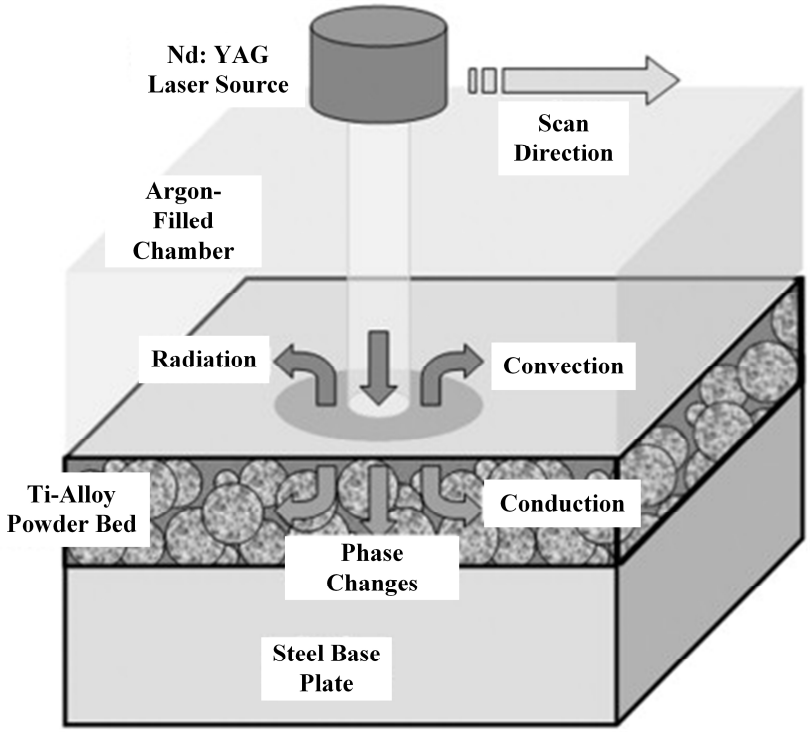



**Fig. 2.1. Schematic representation of heat transfer [5].**

### i. Absorption

When hitting the powder, the laser is absorbed by reflecting multiple times in the oblique surface particles through pores. Then, it scatters into greater depths (see Fig. 2.2). Thus, the photon energy converts into thermal energy and melts the powder [1, 2]. For the PBF-LB

process, the overall absorption and local energy distribution are crucial. Many factors affect them, including laser power, scan speed, wavelength, surface roughness, surface oxidation, and inclusions/impurities. [1, 6, 7].

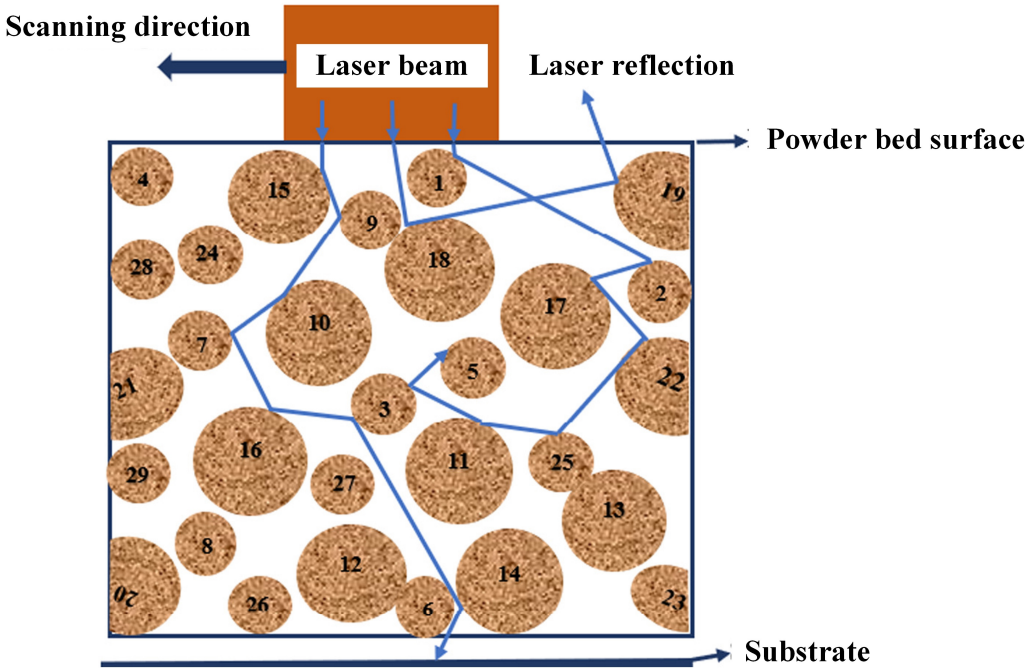



**Fig. 2.2. Reflection of laser light in powder [1].**

Different melt powders have different laser absorption due to their physical and chemical properties. Tolochko et al. measured the absorptance of single-component powder with an Nd-YAG laser (the laser wavelength (λ) =1.06 μm) [8], as shown in Table 2.1. In addition, surface roughness, surface oxidation, and inclusions/impurities change powders' physical and chemical properties. Thus, the three factors also affect the absorption of the powders.

Direct absorption measurements are complex and time-consuming, with the spatial distribution of the absorbed radiation unobtainable. Thus, the numerical investigation approach solves this problem [9].

Besides the powder metal, particle sizes also affect the absorptivity. Zhang et al. [9] studied the relationship between the pure tungsten powder layer absorptivity and particle size. Fig. 2.3 shows the powder layer absorptivity decreased with increased particle sizes. Powder particles exhibit inhomogeneous irradiance distributions. According to Fig. 2.4, the irradiation area falls as particle size increases [9]. Particle size is a key factor in determining the effectiveness of laser irradiation. As particle size increases, the number of powder particles irradiated by the laser beam decreases. This is due to the inhomogeneous distribution of irradiance intensity across the powder particles, which leads to a decrease in the overall laser irradiance. As a result, particle size must be taken into consideration when using lasers for powder processing [9].

**Table 2.1. The absorptance of powders [8].**

| Material | Absorptance: Nd-YAG laser (λ=1.06 μm) |
|---|---|
| Cu | 0.59 |
| Fe | 0.64 |
| Sn | 0.66 |
| Ti | 0.77 |
| Pb | 0.79 |
| Co-alloy (1% C; 28% Cr; 4% W) | 0.58 |
| Cu-alloy (10% Al) | 0.63 |
| Ni-alloy (13% Cr; 3% B; 4% Si; 0.6% C) | 0.64 |

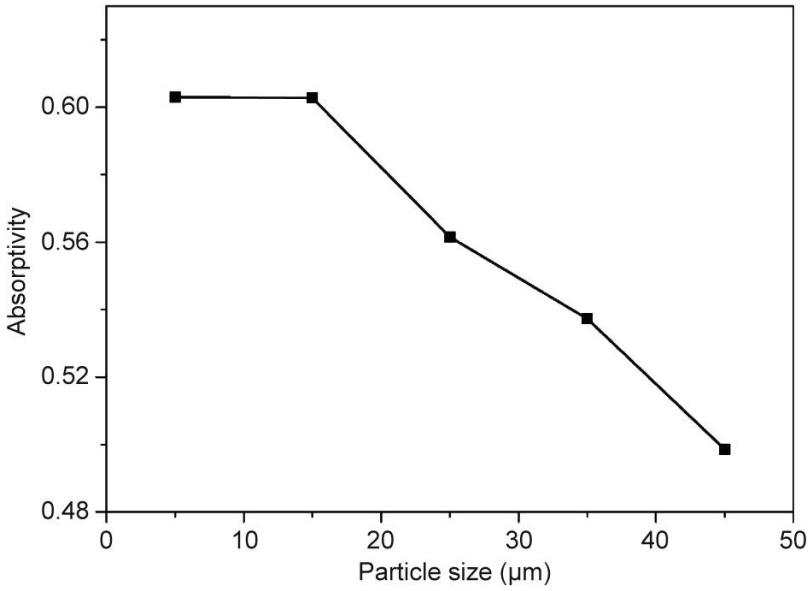



**Fig. 2.3. Absorptivity of the powder layer for different particle sizes [9].**

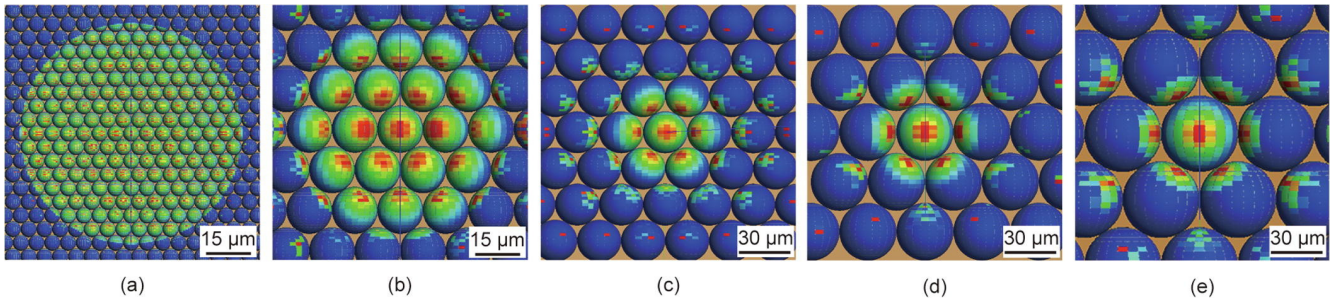



**Fig. 2.4. Absorbed irradiance of powder layers with different powder sizes [9].**

Scime et al. [10] studied the relationship between laser power/scan speed and absorption ratio. They reported the absorption ratio increased with the linear energy density ($E_L$) (see Fig. 2.5) [10]. Khorasani et al. reported a similar trend when they studied the absorption ratio's effect on melt pool features in PBF-LB of IN718 [11].

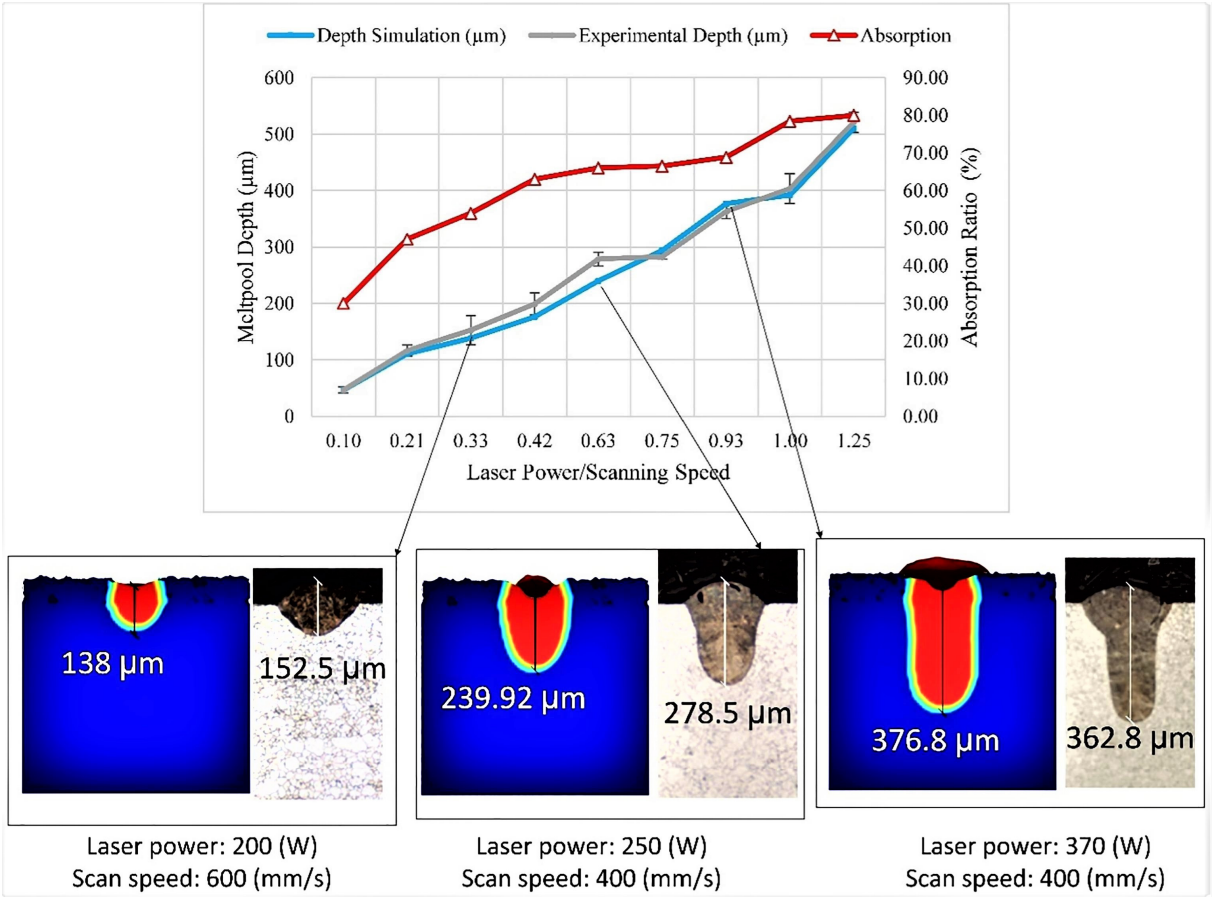



**Fig. 2.5. The relationship between $E_L$, melt pool depth, and absorption ratio [11].**

Low $E_L$ results in shallow melt pools, with high $E_L$ resulting in deep melt pools. In a shallow melt pool, the absorption is low, as the front wall comprises a few reflections of the beam. When the melt pool becomes deep, the absorption is high. Multiple reflections happened between the front and rear keyhole walls. Thus, high energy is induced, and the melt pool becomes more profound, as shown in Fig. 2.6.

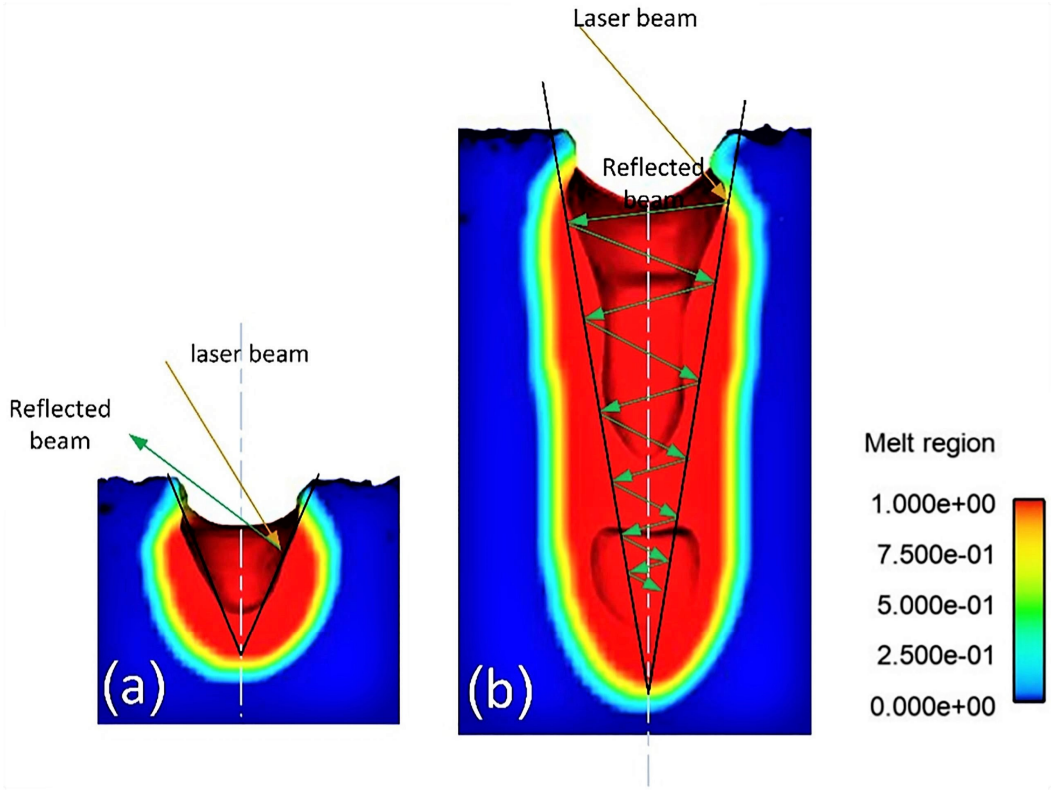



**Fig. 2.6. The reflection of the laser beam (a) a few reflections, and (b) multiple reflections [11].**

### ii. Melt Flow Dynamics

In the PBF-LB process, heat generates as the focused laser beam hits the powder surface and diffuses inward. When it reaches the melting temperature, the deposition heat melts the powder, which results in the phase transition (from solid to liquid); a molten melt pool forms, as shown in Fig. 2.7. The continuous weld bead forms (ideally) when the laser beam keeps moving. One must understand the underlying melt flow dynamics in the PBF-LB process to develop this technology.

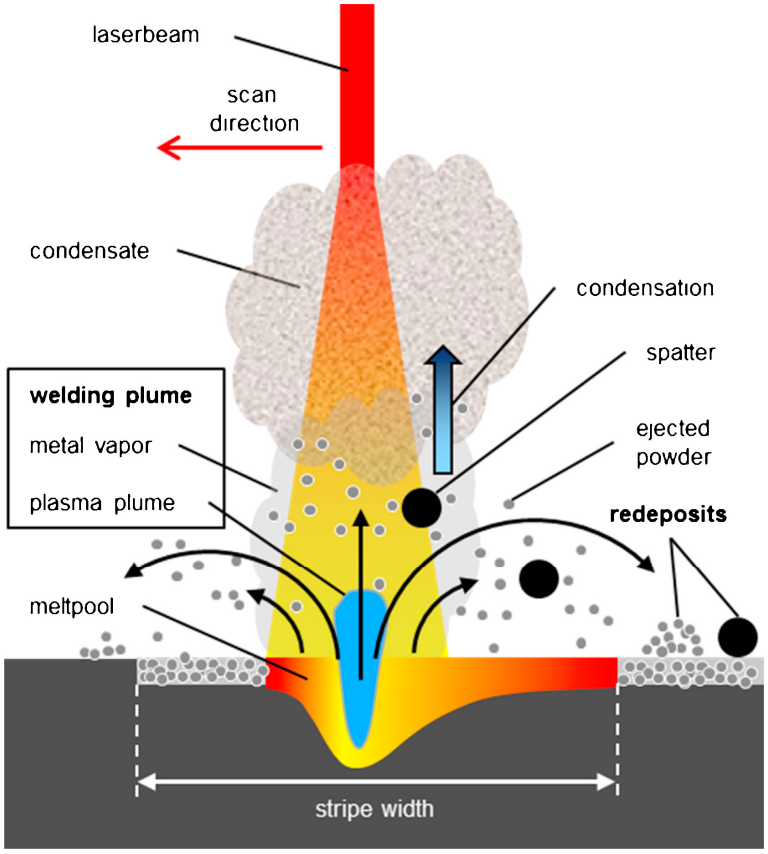



**Fig. 2.7. Schematic representation of possible process by-products [12].**

Qiu et al. [13] reported that the Marangoni and recoil forces are the main factor of melt flow instability. Erlei Li et al. [4] studied the melt pool dynamics using a well-established three-dimensional model. The connection between the forces and liquid flow was built by tracking the melt pool flow pattern's temporal variation.

Fig. 2.8 presents the melt pool's velocity at different times. The flow pattern at 150 μs was analysed and illustrated as an example. The molten liquid shows a centrifugal flow at the top edge of the melt pool. The liquid in front of the laser spot flows forward, the liquid behind the laser spot flows backwards, and the liquid at the side rim and behind the laser spot flows downward (see Fig. 2.8 a). As shown in Fig. 2.8 b and c, the liquid inside the melt pool shows a similar pattern. At the top, the liquid flows back or downward when it impinges on the powder

of the solid region. The turning liquid impinged the powder, and the solid area flowed upward when they met in the melt pool's central part. Thus, two vortices are produced.

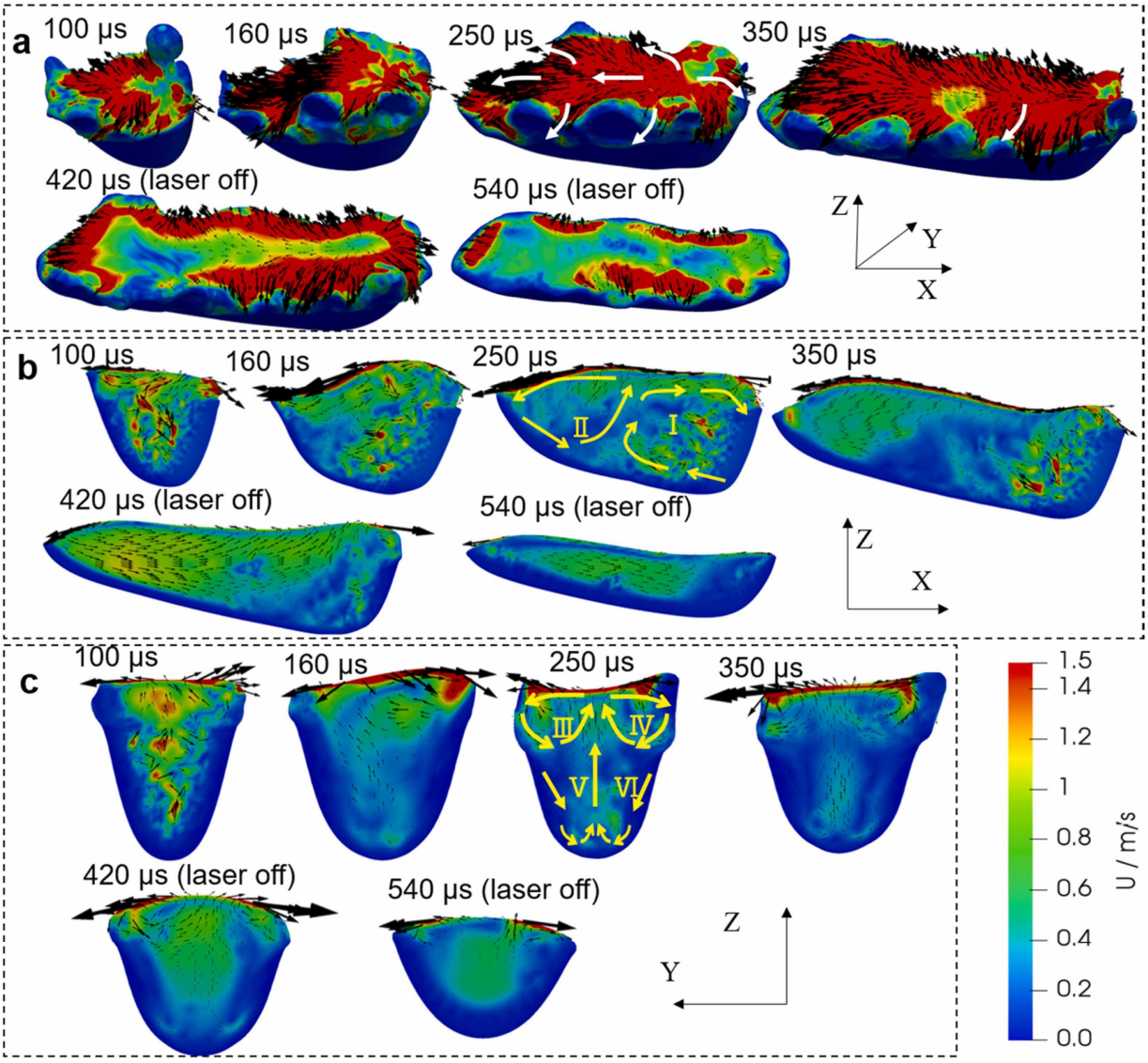



**Fig. 2.8. Melt pool flow dynamics. a, b and c present the global, transverse, and longitudinal views of melt pool flow. The black arrows indicate the velocity vector. The white (interface flow) and yellow (inside flow) arrows indicate the flow pattern [4].**

### iii. Evaporation

During the PBF-LB process, elemental evaporation is an unavoidable problem as the melt pool's maximum temperature is above the boiling point of metallic elements when there is

sufficient energy to boil the liquid [14]. Thus, the chemical composition of the PBF-LBed part differs from the raw material. The intense element vaporisation disturbs the molten pool's stability by applying recoil pressure to liquid metal [15]. The vapour depression is shallow, as the evaporation of the material is less. Most laser energy is reflected by the surface of the molten pool, which results in a lower molten pool depth/width ratio [16, 17]. When the evaporation is severe, the vapour depression is deep. Most laser energy is absorbed by the molten pool's surface, resulting in a molten pool with a high depth/width ratio [16, 18, 19]. These factors may affect the final product's properties, especially those sensitive to chemical composition, such as MCE, and shape memory property.

Juechter et al. reported [20] the number of evaporation losses (mainly aluminium) depending on the line energy for a scanning speed during the additive manufacturing process of Ti–6Al–4V. Chen et al. [21] studied the PBF-LB of NiTi alloy. They reported that higher laser power induces more evaporation than conditions with lower laser power when applied to the same energy density.

### 2.1.2 Process parameters in PBF-LB

Fig. 2.9 [22] shows a simple overview of the PBF-LB process. There are lots of parameters which affect the PBF-LB processes and results. Among all parameters in the PBF-LB process, adequate laser power, laser scan speed, laser scan spacing or hatch distance, and layer thickness are essential [23, 24]. Fig. 2.10 presents the PBF-LB terminology. The laser power (P), the laser scan speed (V), and the hatch distance (h) are chosen as three varied parameters for process optimisation. During the PBF-LB process, the volume energy density ($E_v$) and the linear energy density ($E_L$) define the laser energy applied per volume of powers and line, which is given by [25]:

$$E_v = \frac{P}{\mathrm{V} \cdot h \cdot d} \tag{2.2}$$

$$E_L = \frac{P}{\mathrm{V}} \tag{2.3}$$

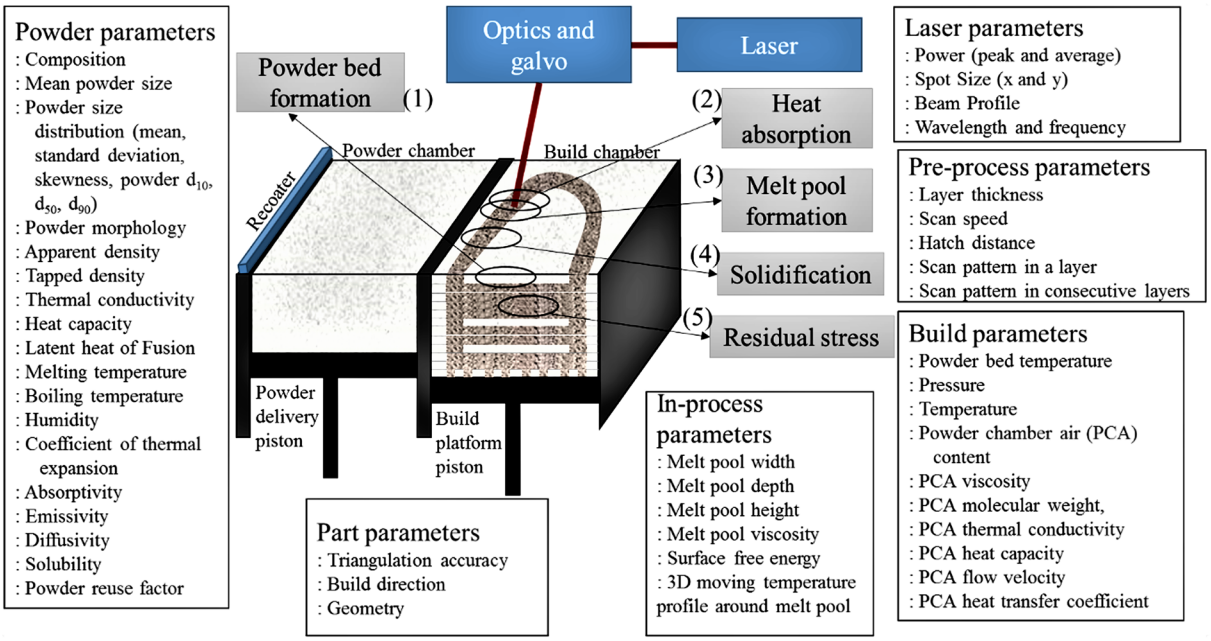



**Fig. 2.9. The PBF-LB process and process parameters [22].**

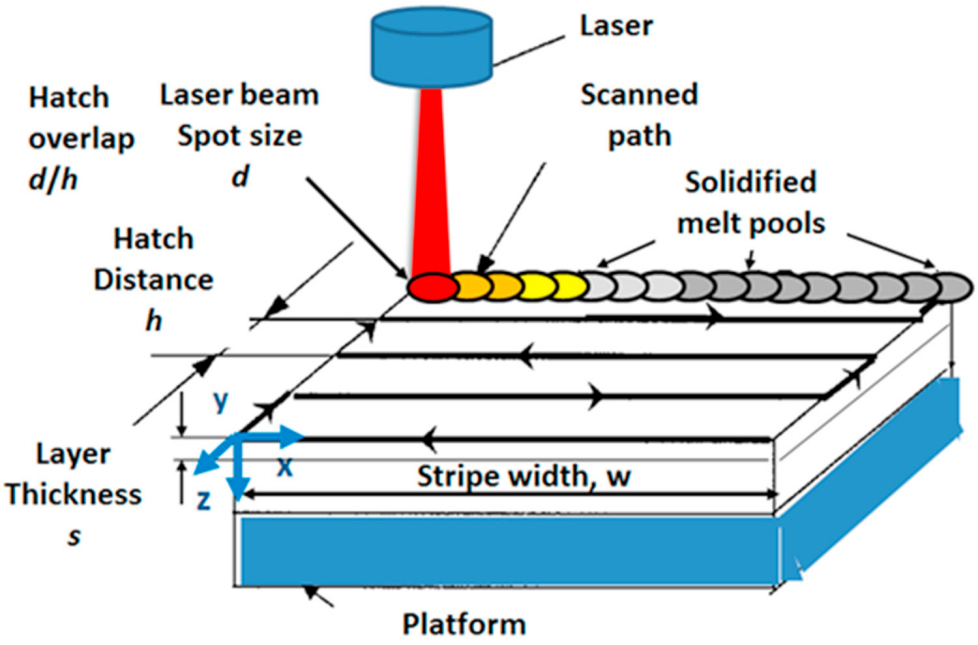



**Fig. 2.10. PBF-LB terminology [26, 27].**

In addition, the scanning strategy is the moving pattern of the laser beam, which is also essential [28]. Fig. 2.11 presents common scanning strategies. The different scanning strategies are identified according to the scanning direction, sequence, vector length, rotation angle, time, and hatch space.

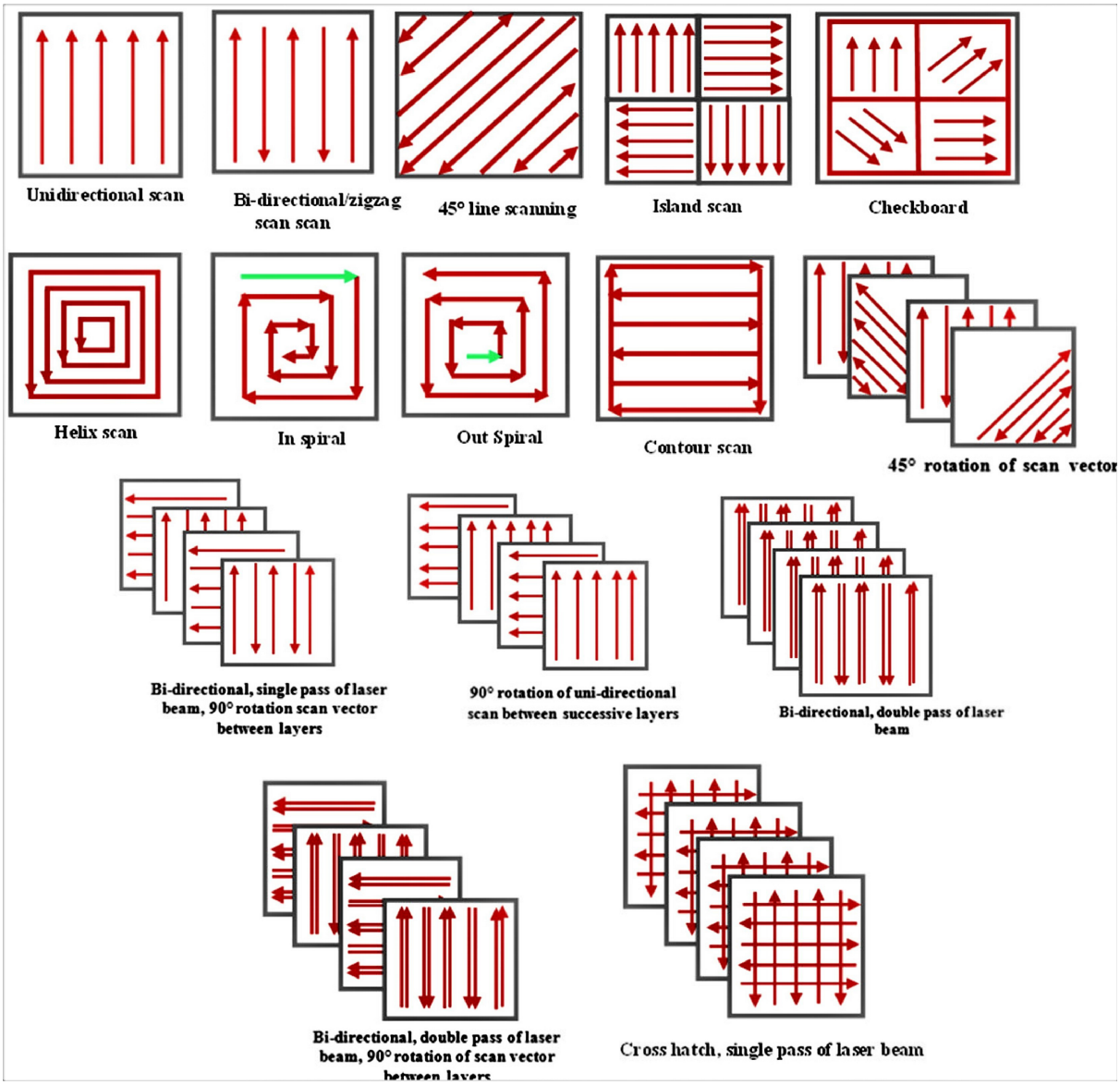



**Fig. 2.11. Schematic of different scanning strategies [28].**

### 2.1.3 The defects in PBF-LB

The defect is an inevitable problem during the PBF-LB process [24]. Understanding the defects' formation mechanism, including pores, lack of fusion, and cracks, is essential. The formation mechanism helps find the method to avoid them. J. Fu et al. [29] believed that defects in the PBF-LBed alloy could be classified into three categories: geometry-related, surface integrity-related, and microstructural defects, as shown in Fig. 2.12.

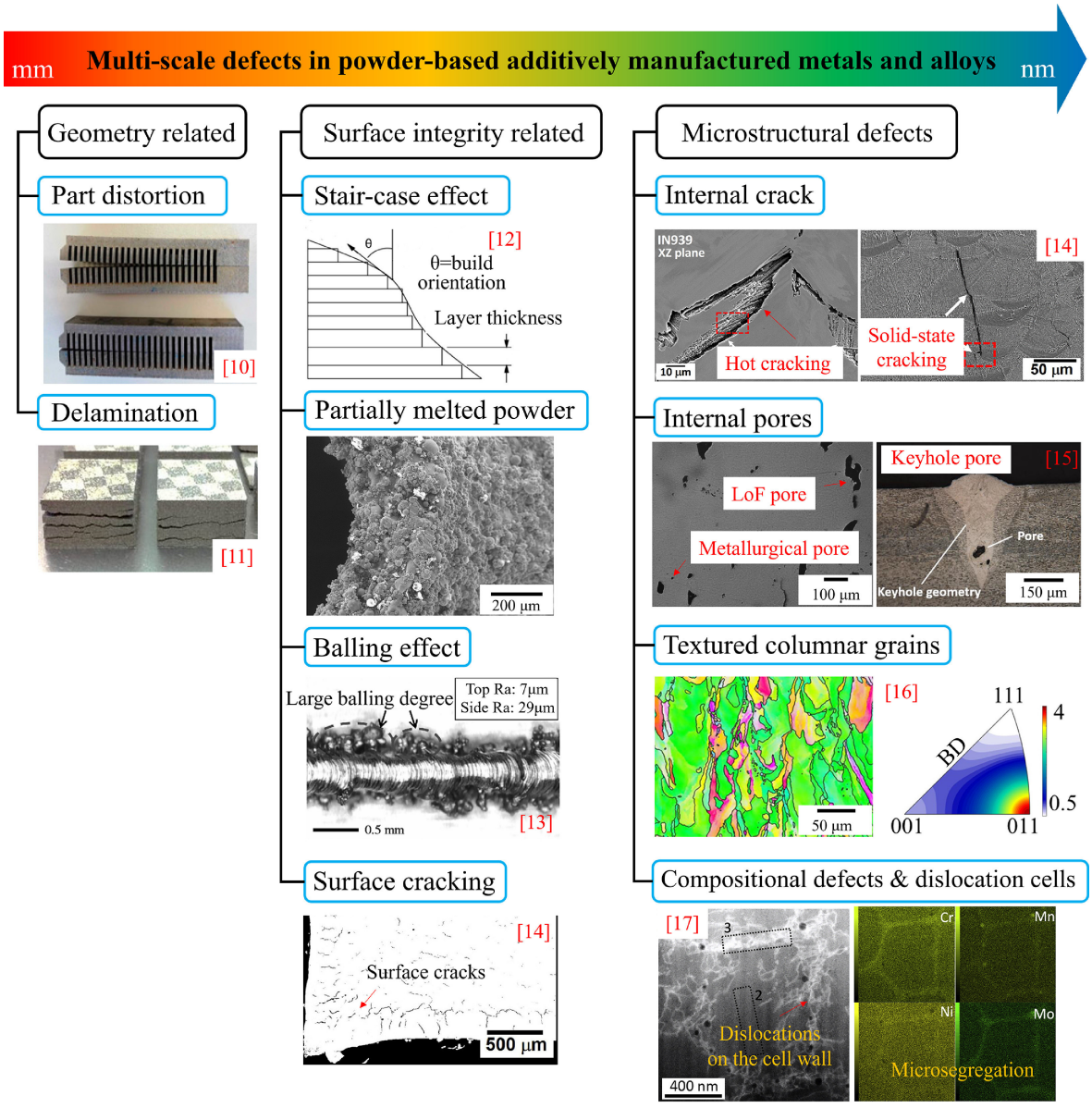



**Fig. 2.12. Classification of defects [29].**

a. Geometry-related defects

These defects are the dimensional and geometrical deviations between as-fabricated structures and the designed CAD models. They are mainly part distortion and delamination caused by macroscopic residual stress. During the PBF-LB process, the material experienced high-speed heating and cooling, resulting in uneven material expansion and contraction and macroscopic residual stress [29-31].

b. Surface integrity-related defects

These defects are uneven surface features, such as the staircase effect, the partially melted powders, balling effect, and the surface cracks, which deviate from the profile of the ideal model [29].

c. Microstructural defects

The microstructural defects were divided into internal cracks and pores, compositional defects, and dislocations [29]. A phenomenological classification of cracks was used to characterise cracking behaviour within the PBF-LBed sample [32-35]. The observed cracking is categorised into two types based on the cause of cracking: (i) hot cracking (including solidification cracking and liquation cracking) and (ii) solid-state cracking. Internal pores are classified into lack-of-fusions, keyhole, and shrink-age pores. The textured columnar grain structures, caused by the natural cooling of PBF-LB, lead to undesired anisotropic properties. Compositional defects mainly include microsegregation, loss of alloying elements, and oxidation [29].

## 2.2 Solidification theory

As solidification proceeds, microstructure influences both micro and macro scale segregation, inclusion distribution, pores, cracks, grain size, and grain morphology. These factors influence

the performance of solid metals. The final microstructure is determined by nucleation and growth. By contrast to casting, PBF-LB involves moving molten metal in the form of a molten pool that solidifies during cooling, similar to welding and a mini casting without nucleation [36]. Thus, this section focuses on solidifying structures and their growth. The melt pools' melting and solidification determine the material's grain structure and crystallographic texture. The process parameters and the heat conduction affect the melt pool's shape [37]. Additionally, high-energy laser in PBF-LB move rapidly, causing solid-liquid interfaces to expand rapidly. PBF-LB and laser surface treatment processing are considered to be quasi-steady state processes, so steady-state growth theory can be applied to a large extent based on their quasi-steady state properties.

### 2.2.1 Nucleation

The nucleation during PBF-LB is divided into two types regarding the chemical composition of adjacent melted layers. Firstly, the next layer always has the same chemical composition as the deposited metal. In this situation, the existing metal has the same crystal structure as the solidifying metal [35, 37]. When the temperature drops below the liquidus, the grain spontaneously grows with no activation energy barrier, as the nucleation for new phases is not required [38].

Another situation is the PBF-LB of dissimilar metals, such as PBF-LB of heterogeneous materials and laser surface cladding [39-41]. This situation may require nucleation at the melt pool boundary. When the heterogeneous materials grow on the existing materials, nucleation of new phases is necessary if there is a massive difference between the crystal structure of the two materials. When the substrate metal's crystal structure is like the depositing metal, nucleation is not required [42, 43].

### 2.2.2 Growth

The growth occurs at the solid/liquid interface by adding atoms from the liquid to the interface. The base metal dominates the structure near the melt pool boundary during the solidification [44, 45]. However, the microstructure in the melt pool's centre presents competitive growth [37, 46]. The temperature gradient (G), solidification rate (R), and undercooling (ΔT) determine the materials' solidification and growth rate [47]. Fig. 2.13 presents the temperature gradient and growth rate's effect on the solidification substructures and modes [37]. The G/R determines the solidification structure's morphology, with the G×R determining the solidification structure's size. The solidification structure's morphology gradually changed when the decreasing G/R (Planar → Cellular → Columnar dendritic → Equiaxed dendritic). During the PBF-LB process, the solidification microstructures always present columnar and equiaxed structures [38].

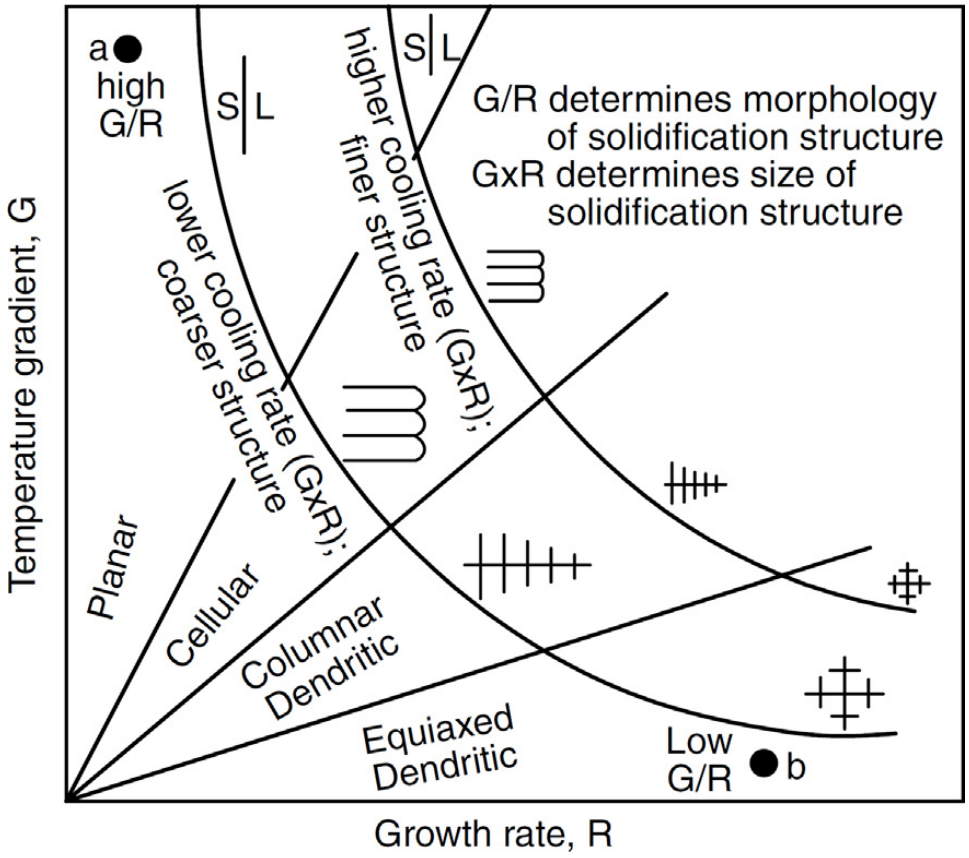



**Fig. 2.13. Temperature gradient G and growth rate R's effect on microstructure's morphology and size [37].**

## 2.2.3 Undercooling

Undercooling provides the driving force for dendrite growth. The total undercooling is divided into four parts [37, 48]:

$$\Delta T_{total} = \Delta T_C + \Delta T_T + \Delta T_K + \Delta T_R \tag{2.4}$$

where $\Delta T_C$ is the undercooling from solute diffusion, $\Delta T_T$ is the undercooling from thermal diffusion, $\Delta T_K$ is the undercooling from attachment kinetics, and $\Delta T_R$ is the undercooling from solid-liquid interface curvature. $\Delta T_C$ (also called constitutional supercooling) plays a significant role in solidifying most metallic alloys under normal solidification conditions. The different constitutional supercooling at the solidification interface changes solidification microstructures,

from planar to cells, columnar dendrites, or equiaxed dendrites, as shown in Fig. 2.14. Hunziker et al. [49] reported that undercooling increased with dendrite growth velocity.

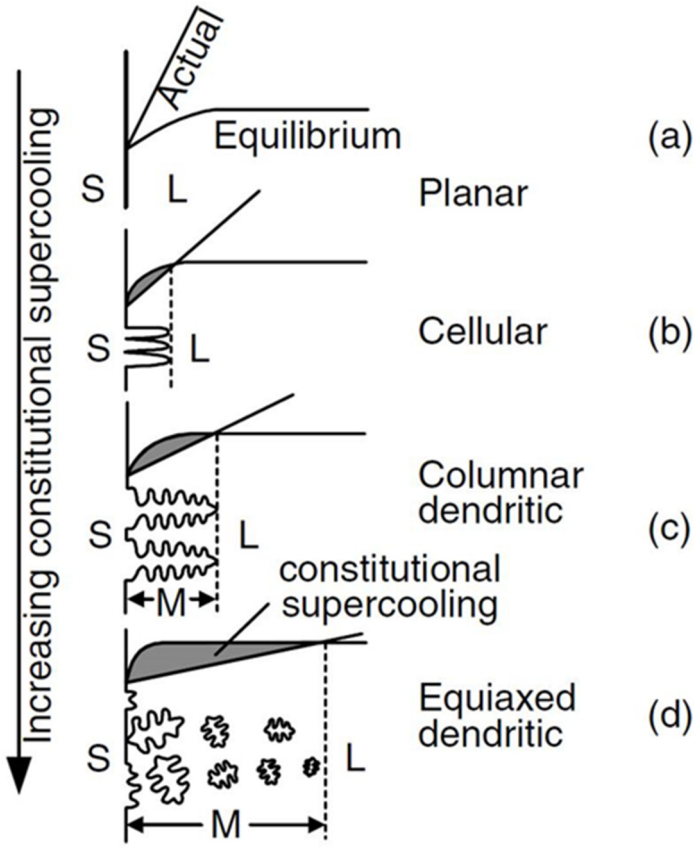



**Fig. 2.14. The influence of constitutional supercooling on different structural morphologies [37].**

## 2.3 Magnetocaloric materials

The magnetocaloric material exhibits a remarkable MCE [50, 51]. MCE is the reversible temperature change of a magnetic material upon a magnetic field's application or removal [50].

### 2.3.1 Magnetocaloric materials' history

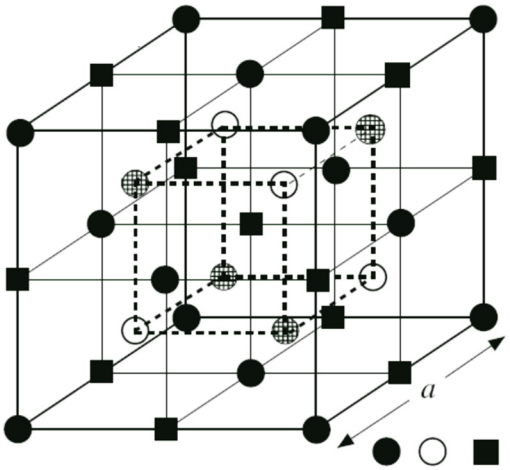
In 1918, Weiss and Piccard discovered a reversible temperature change near the Curie's vicinity temperature (354 °C) in nickel [52, 53]. They found a temperature change of 0.7 K upon magnetic field application (1.5 T), which marks the actual discovery of MCE [52]. In 1926,

Debye realised that MCE could be used for refrigeration at lower temperatures [54]. Brown found the curie point of gadolinium was 293 °C in 1976. They reported that Gd has a heat release of 4 kJ/kg under isothermal conditions when applying a 7 T magnetic field at the Curie point, which shows Gd is a suitable working material for magnetic refrigeration [55]. In 1977, Pecharsky and Gschneidner found a substantial magnetic entropy change in $Gd_5Si_2Ge_2$ at 273 K, which is caused by a first-order transition from ferromagnetic (I) to ferromagnetic (II) phases [56]. Since then, magnetocaloric materials have interested many scholars. Several families of magnetocaloric materials have been studied during the last decade. The primary information and classification of them are shown in Fig. 1.3.

In 1903, Heusler discovered an alloy ($Cu_2MnAl$), which behaves like a ferromagnet, although the composing elements are not magnetic [57]. Thus, this kind of alloy is named the Heusler alloy. According to the different space-occupying of three atoms, the Heusler alloys comprise four types. Felser and Hirohata show the structure of four main kinds of Heusler alloys ($L2_1$ structure, $C1_b$ structure, Quaternary Heuslers, and Inverse Heuslers) shown in Fig. 2.15 [58]. The generic formula of full-Heusler alloys is $X_2YZ$, and they crystallise in an $L2_1$ cubic structure (space group Fm-3m). X and Y are 3d elements, with Z the IIIA-VA group element. These alloys show magnetism because of the existence of X and Y elements. Austenitic to martensitic transformations may occur in alloys with a suitable composition range [50]. By now, more than 1000 Heusler alloys have been invented by scholars [57]. In 1996, Ullakko et al. discovered large magnetic field-induced strains in $Ni_2MnGa$ alloy [59]. After that, the Ni-Mn-based Heusler alloy attracted numerous scientists' interest. Many Heusler alloys have also been studied due to the magnetocaloric effect. The magnetocaloric effect's essential characteristics are the effect being maximised in the transition's vicinity temperature and being reversible. NiMn-based HA is magnetic material which shows the promising magnetocaloric effect and

controllable working temperature of magnetic refrigeration. NiMn-based HAs are cheap and more environmentally friendly candidates for magnetic refrigeration, compared with rare-earth-based materials [60].

The La and Fe elements cannot react and form any intermetallic compound, but minor addition of Si yields the $NaZn_{13}$-type structure's formation (space group Fm-3c), as shown in Fig. 2.16 [51, 61]. In the coordination polyhedra, La and Fe-I atoms occupy 8a and 8b sites, respectively, while Fe-II and Si atoms randomly occupy 96i sites [62]. In 2001, Hu et al. reported that $La(FeSi)_{13}$ alloys exhibit interesting magnetic behaviour and huge MCE due to the existence of $NaZn_{13}$-type structure intermetallic compound [63]. Numerous research studies have been conducted to improve the MCE of these LaFeSi-based alloys [62, 64-68].




| | A | B | C | D |
|---|---|---|---|---|
| Semi–Heuslers ($C1_b$) : XYZ | X | Y | | Z |
| Full–Heuslers ($L2_1$) : $X_2YZ$ | X | Y | X | Z |
| Quaternary Heuslers : (XX')YZ | X | Y | X' | Z |
| Inverse Heuslers (XA) : $X_2YZ$ | X | X | Y | Z |

**Fig. 2.15. The schematic representation of the structures of the semi and full-Heusler compounds [69].**

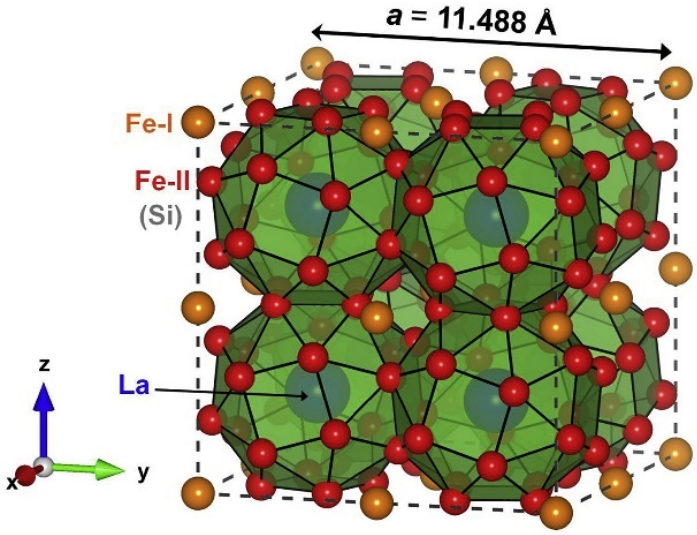



**Fig. 2.16. Schematic representation of the unit cell of $LaFe_{11.6}Si_{1.4}$ (space group Fm-3c) [62].**

## 2.3.2 The characterisation of magnetocaloric materials

The magnetocaloric material is separated into two groups according to the magnetic phase transition: the magnetic moments and the lattice [50]. Thus, there are two groups of magnetocaloric materials.

a. First-order phase transition (FOPT)

   FOPT is a phase transition with un-continuous first derivatives of free energy regarding a thermodynamic variable [50].

b. Second-order phase transition (SOPT)

   In SOPT, the first derivative of Gibbs free energy is continuous, and the second derivative of Gibbs free energy is un-continuous [50].

Fig. 2.17 presents the schematic representation of the magnetisation (M) for second-order (a) and first-order (b) materials regarding their temperatures [70].

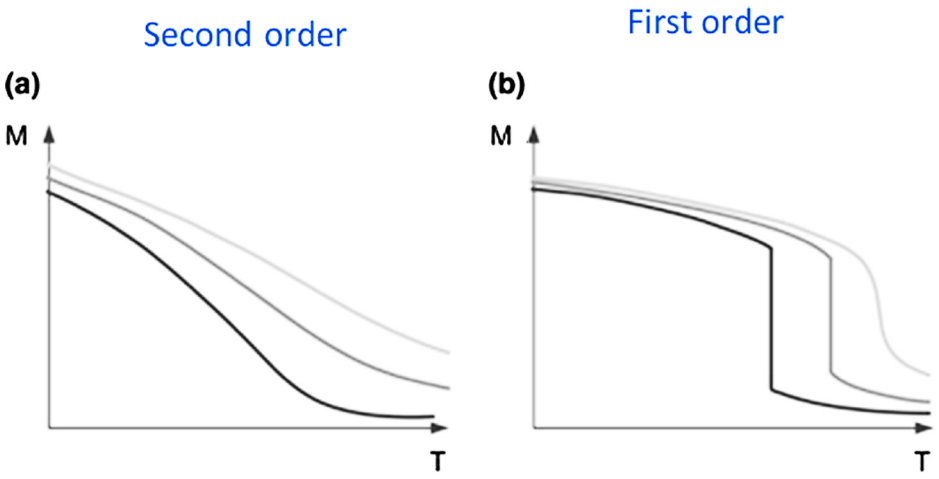



**Fig. 2.17. Schematic representation of magnetisation (M) concerning temperature [71].**

Electrons are usually found in pairs in atoms. Pairs of electrons spin oppositely. Electrons paired together produce opposite magnetic fields, so their magnetic fields cancel when they are paired together. As a result, there is no net magnetic field. If some electrons are unpaired in the material, there will be an external field that will react more strongly to the material. Most materials can be classified as paramagnetic, or ferromagnetic [72].

Paramagnetic materials are characterized by a slight attraction to magnetic fields. They lose their magnetic properties when the external field is removed. The paramagnetic behaviour of these materials is due to the presence of unpaired electrons that experience a realignment of their paths induced by the external magnetic field [72-74]. Ferromagnetic materials show a strong attraction to external magnetic fields and have a large and positive susceptibility. They are capable of retaining their magnetic properties after the external field has been removed. The net magnetic moment of their atoms results from the presence of unpaired electrons. The strong magnetic properties of ferromagnetic materials originate from the existence of magnetic domains, wherein a large number of atom moments are aligned parallel, generating a powerful magnetic force within the domain. In the unmagnetized state, domains in ferromagnetic materials are nearly randomly arranged, and the net magnetic field for the material as a whole

is zero. Upon application of a magnetizing force, the domains become aligned, leading to the production of a strong magnetic field within the material [72-74]. The ferromagnetic-paramagnetic phase transition near the Curie temperature is SOPT [75].

### 2.3.3 The magnetic refrigeration cycles

The magnetic refrigeration cycle of magnetocaloric material is explained regarding entropy change caused by magnetic moments, lattice vibrations, and electronic states. Among these entropies, magnetic entropy (related to its spin subsystem) is considered a function of temperature and magnetic field, with lattice (related to atomic vibrations) and electronic entropy regarded as functions of temperatures. Thus, the entropy of a magnetic solid (S) at constant pressure is a function of both temperature (T) and magnetic field (H), as shown in the following Eq. 2.5 [70].

$$S(T,H) = S_M(T,H) + S_{Lat}(T) + S_{el}(T) \tag{2.5}$$

The typical magnetic refrigeration cycle is described below [76]. The number of parallel magnetic moments aligned parallel to the field increases (the magnetic entropy decreases) when a magnetic field is applied adiabatically. Due to the adiabaticity's condition, the reduced magnetic part of entropy should be compensated by an increased entropy of the lattice vibrations (see Fig. 2.18 and Fig. 2.19). Hence, the system's temperature increased [70, 76]. At this stage, the heat transfer fluid, such as water, brings the heat from the system to a colder environment. During the adiabatic demagnetisation process, the increased magnetic entropy and decreased lattice vibrations result in reduced temperature [70]. Now, the temperature of magnetocaloric material is low and absorbs heat from the surrounding environment. Thus, a magnetic refrigeration cycle is constructed.

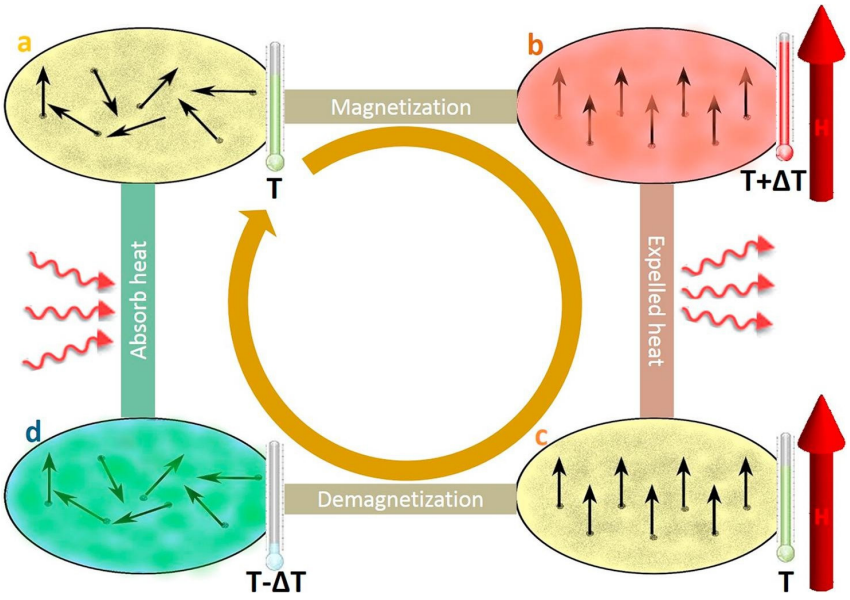



**Fig. 2.18. The magnetocaloric cycle [70].**

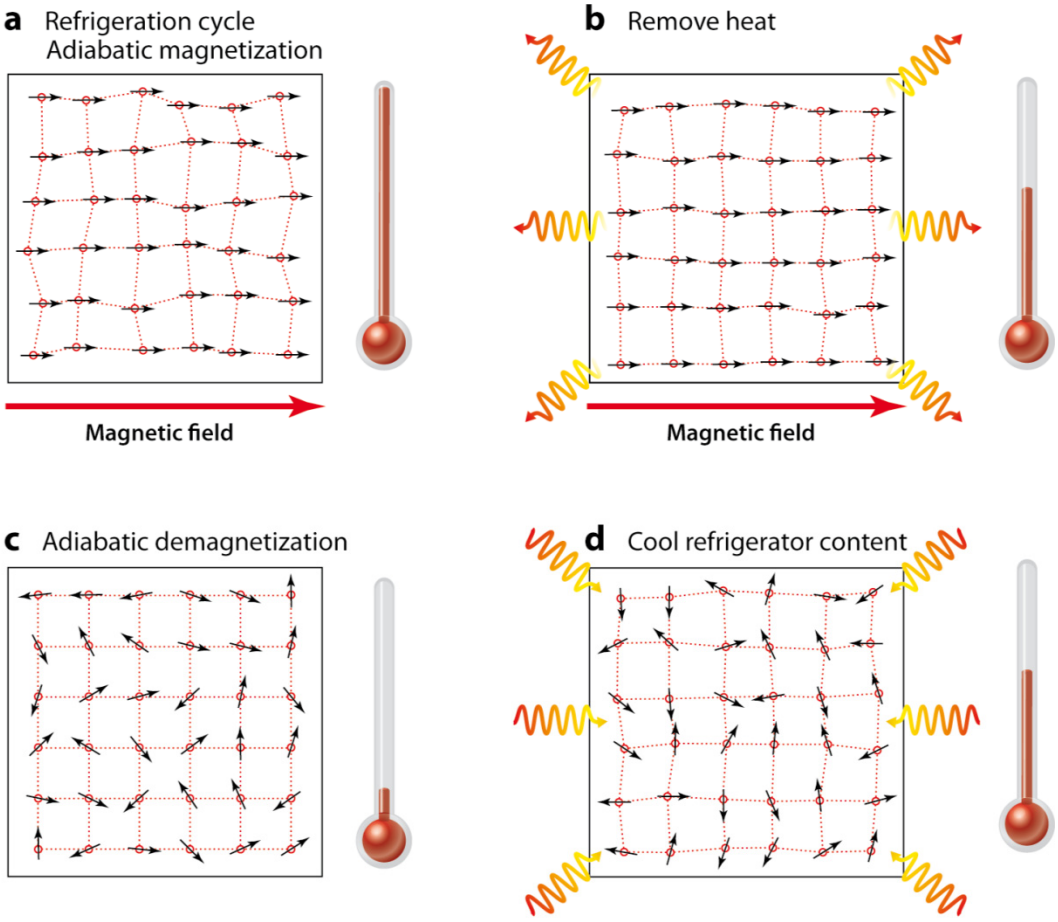



**Fig. 2.19. Four stages of a magnetic refrigeration cycle [50].**

### 2.3.4 Magnetic entropy change ($\Delta S$) and adiabatic temperature change ($\Delta T_{ad}$)

In an adiabatic process, $\Delta S$ and $\Delta T_{ad}$ are used to evaluate the magnetocaloric materials' MCE when the applied magnetic field changes. Fig. 2.20 shows the relationship between $\Delta T_{ad}$, $\Delta S_m$, and the applied magnetic field change. This diagram represents the isothermal and adiabatic processes. During the isothermal process, magnetic entropy decreases when the difference in an applied magnetic field is above 0. During the adiabatic process, the temperature of this system increased when the magnetic field increased from 0 to above 0.

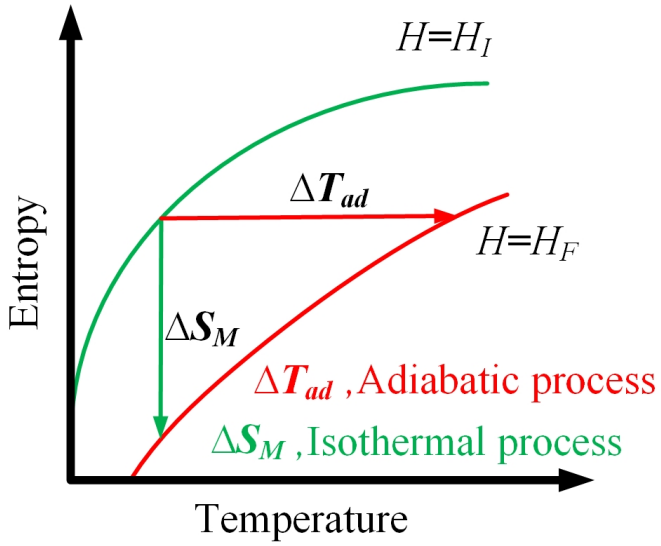



**Fig. 2.20. Schematic of the relationship between the entropy of magnetocaloric material and temperature.**

$\Delta S$ and $\Delta T_{ad}$ is defined as Eq. 2.6 and Eq. 2.7 [44] ($\Delta$H represents the change in the applied magnetic field):

$$\Delta T_{ad} = -\mu_0 \int_{H_I}^{H_F} \frac{T}{C_p} \left(\frac{\partial M}{\partial T}\right)_H dH \tag{2.6}$$

$$\Delta S = \mu_0 \int_{H_I}^{H_F} \left(\frac{\partial M}{\partial T}\right)_H dH \quad (2.7)$$

$\mu_0$ is the permeability of free space. $H_F$ and $H_I$ are the final and initial magnetic fields, respectively. The $C_p$ is the specific heat capacity [50]. However, it is easy to calculate $\Delta S$, although the magnetic entropy change is less straightforward. $\Delta S$ is also an important factor in estimating the quality of magnetic refrigerant materials as the change of magnetic moments causes temperature changes.

In addition, $C_p$ is approximated in the literature as field-independent. Eq. 2.6 is replaced by Eq. 2.8 [50]:

$$\Delta T_{ad} \approx -\frac{T\Delta S}{C_p} \quad (2.8)$$

## 2.4 Metallurgy of NiMnSn alloy

### 2.4.1 The crystal structure of NiMnSn alloy

For full NiMnSn Heusler alloys, the generic formula is $Ni_2MnSn$. Ni occupies the A and C positions, Mn occupies the B, and Sn occupies the D (See Fig. 2.15). However, Ni, Mn, and Sn are not exactly 2:1:1. Occasionally, excess atoms can be found in other places in space Fig. 2.21 presents the spatial structure of $Ni_{50}Mn_{36}Sn_{14}$. Thus, NiMnSn alloys with different compositions have different magnetic properties as different space-occupying ratios of three different atoms affect the curie temperatures, martensitic transformation temperatures, and different magnetism. Structural and magnetic transformation is also tuned by changing the Ni, Mn, and Sn ratio in the NiMnSn alloys.

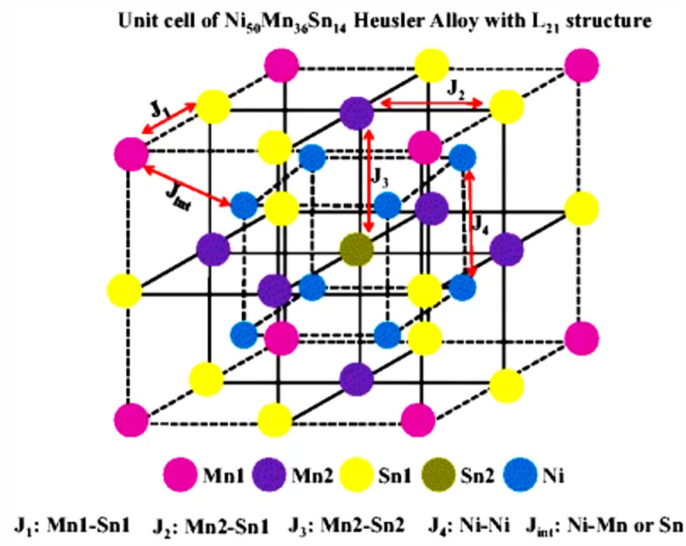



**Fig. 2.21. Schematic representation of the $L2_1$-NiMnSn HA and its components [77, 78].**

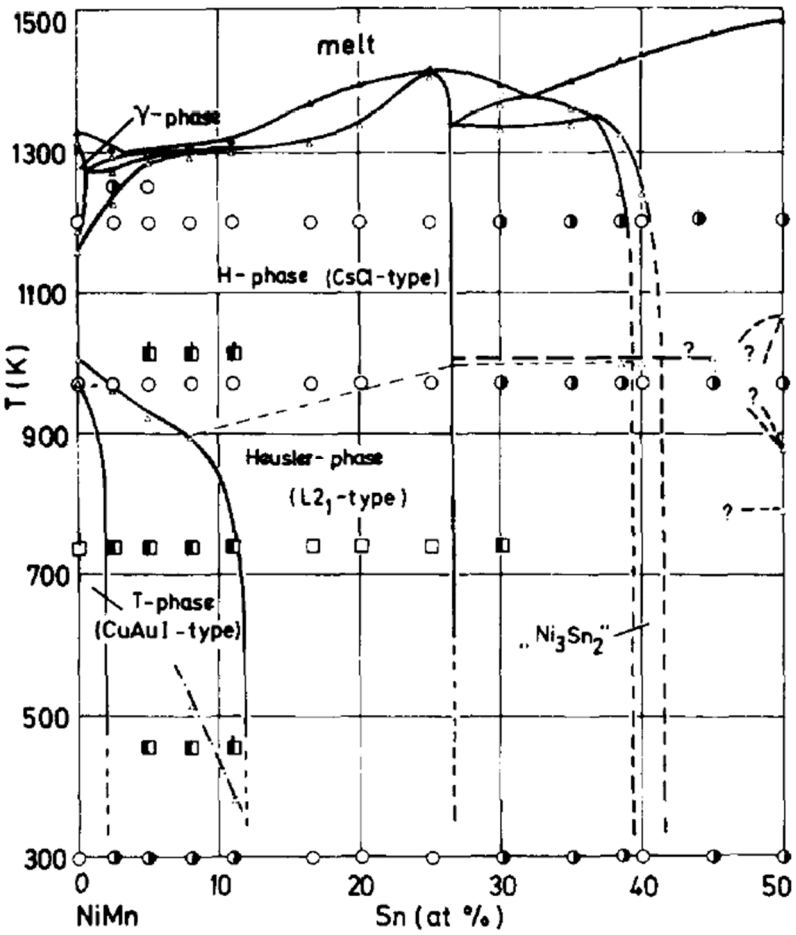



**Fig. 2.22. NiMnSn ternary phase diagrams with Ni content of 50 at.% [79].**

Fig. 2.22 presents the ternary phase diagrams with Ni content of 50 at.%. For the alloy with Sn=13%, the CsCl-type phases precipitate from the liquid metal during solidification (from 1500 to about 1000 K). Then, the $L2_1$-type phase formed during the subsequent cooling process. When the Sn at.% is above 30%, the transformation L → CsCl-type phases + $Ni_3Sn_2$ will happen.

Krenke et al. [80] presented a study on the alloy series $Ni_{50}Mn_{50-x}Sn_x$ with $5 \leq x \leq 25$ (annealed at 1273 K for two h, then quenched in ice water). No structural transformation has been observed for the alloys with $x \geq 18$. However, For alloys with $10 \leq x \leq 18$ ($8.0 \leq e/a \leq 8.2$) feature diverse structural and magnetic transitions. Dan et al.[81] also investigated the MCE of $Ni_{50}Mn_{50-x}Sn_x$ alloys (x=0–40) and reported that crystalline phases ($Ni_2MnSn$, NiMn, $Ni_3Sn_2$, $Mn_3Sn$, and $MnSn_2$) may occur in these alloys. Fig. 2.23 shows the XRD results at room temperature. They reported how the annealing process does not impact the alloys' SOPT but the FOPT. A martensitic-austenitic transition occurs only in alloys that undergo annealing with an Sn-concentration range of 13-15 at.%. However, all alloys with an as-melted state almost behave as the single ferromagnetic phase.

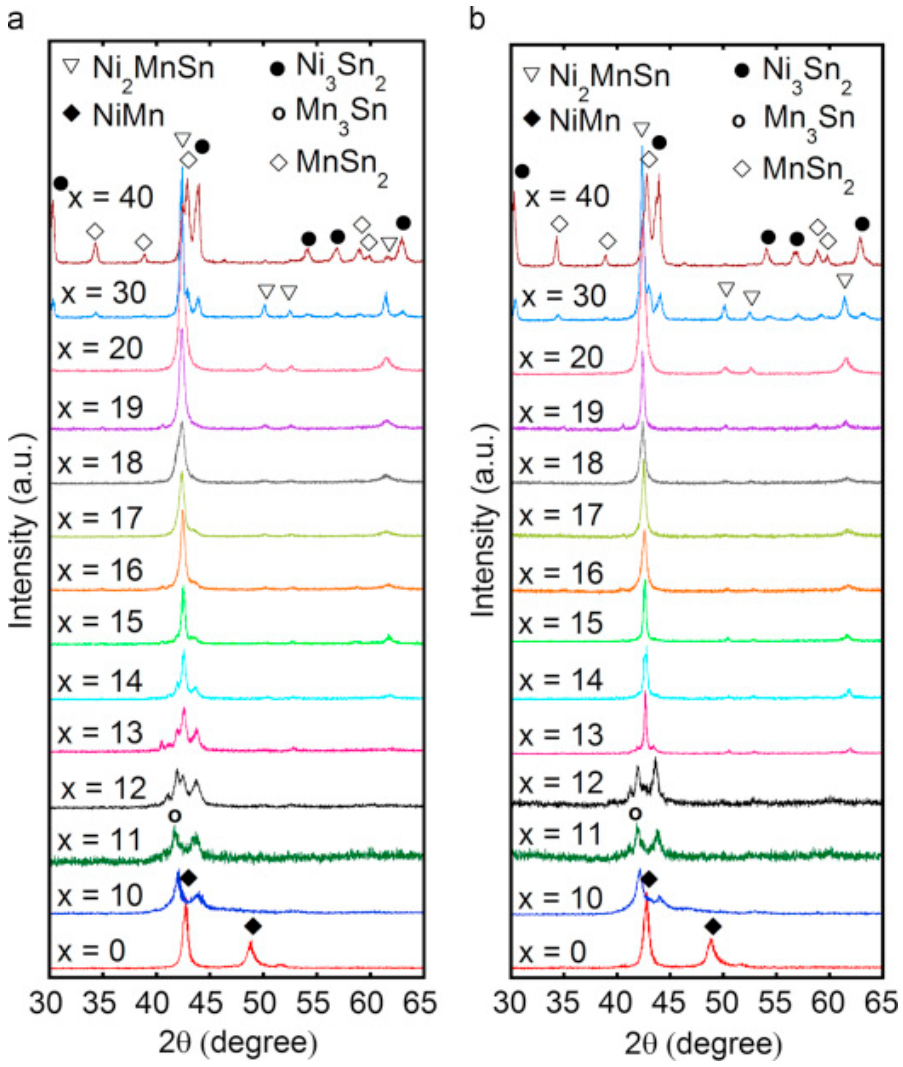



**Fig. 2.23. The $Ni_{50}Mn_{50-x}Sn_x$ alloys' XRD results: (a) as-melted samples, (b) annealed samples [81].**

## 2.4.2 The martensite phase structure of NiMn-based alloy

The $L2_1$-type phases transform to low-symmetry martensite (A-M transformation) when the temperature drops. Several martensite crystal forms (the modulated martensite with a monoclinic six-layered (6M), modulated martensite with a monoclinic five-layered (5M), modulated martensite with an orthorhombic four-layered (4O), modulated martensite with a monoclinic seven-layered (7M) structures, and on-modulated martensite ($L1_0$)) can be seen in NiMnSn alloys with varying Sn concentrations [82, 83]. Fig. 2.24 and Fig. 2.25 show the austenite's crystal structures and all kinds of martensite.

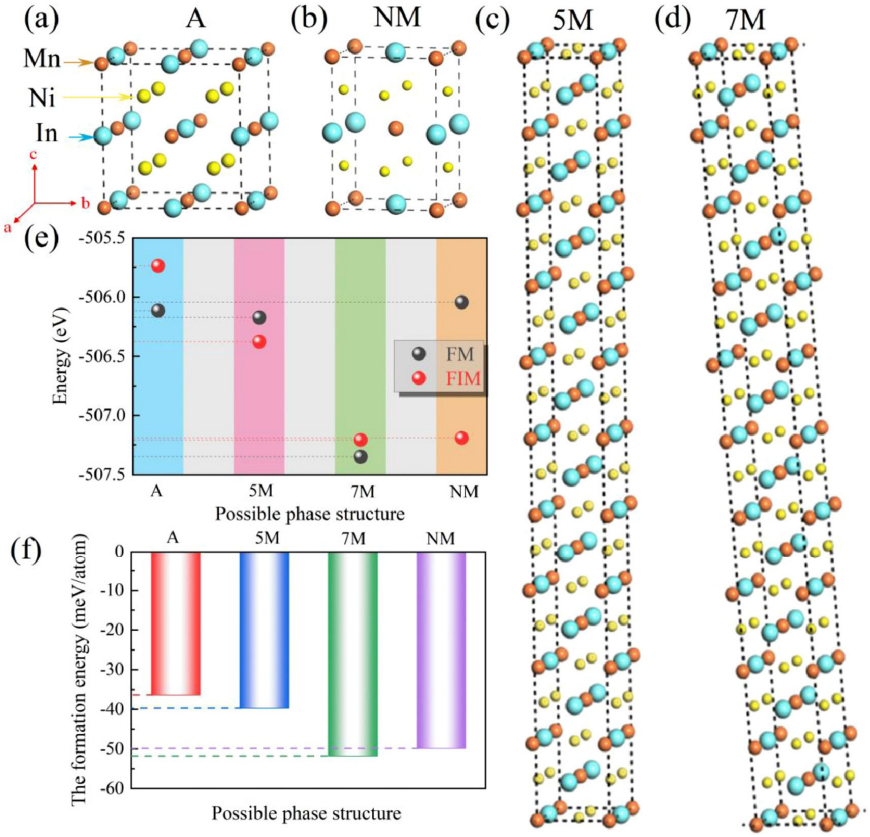



**Fig. 2.24. The crystal structures of austenite and different martensites in Ni-Mn-In alloys [84].**

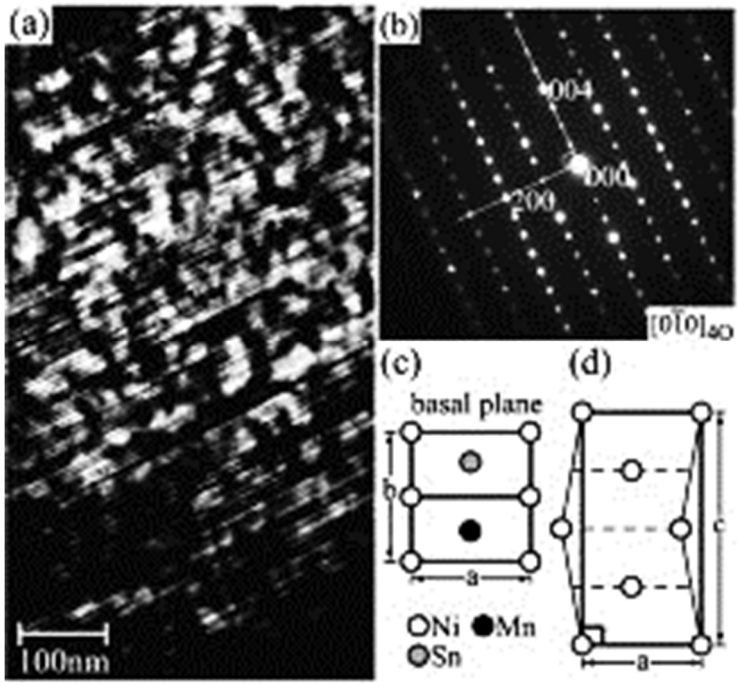



**Fig. 2.25. Crystal structures of 4O martensite [83].**

Çakır et al. [85] manufactured $Ni_{50}Mn_{50-x}Sn_x$ samples using arc melting and annealing them under an argon atmosphere at 1073 K for five days. They studied the compositional behaviour of martensitic transitions in $Ni_{50}Mn_xSn_{50-x}$ alloys ($7.8 \leq e/a \leq 8.2$). They reported that inter-martensitic changes happen with decreased temperatures after the austenite–martensite transition. The martensite states changed an $L1_0$, 7M, and 5M sequence with decreasing e/a (see Fig. 2.26 and Fig. 2.27).

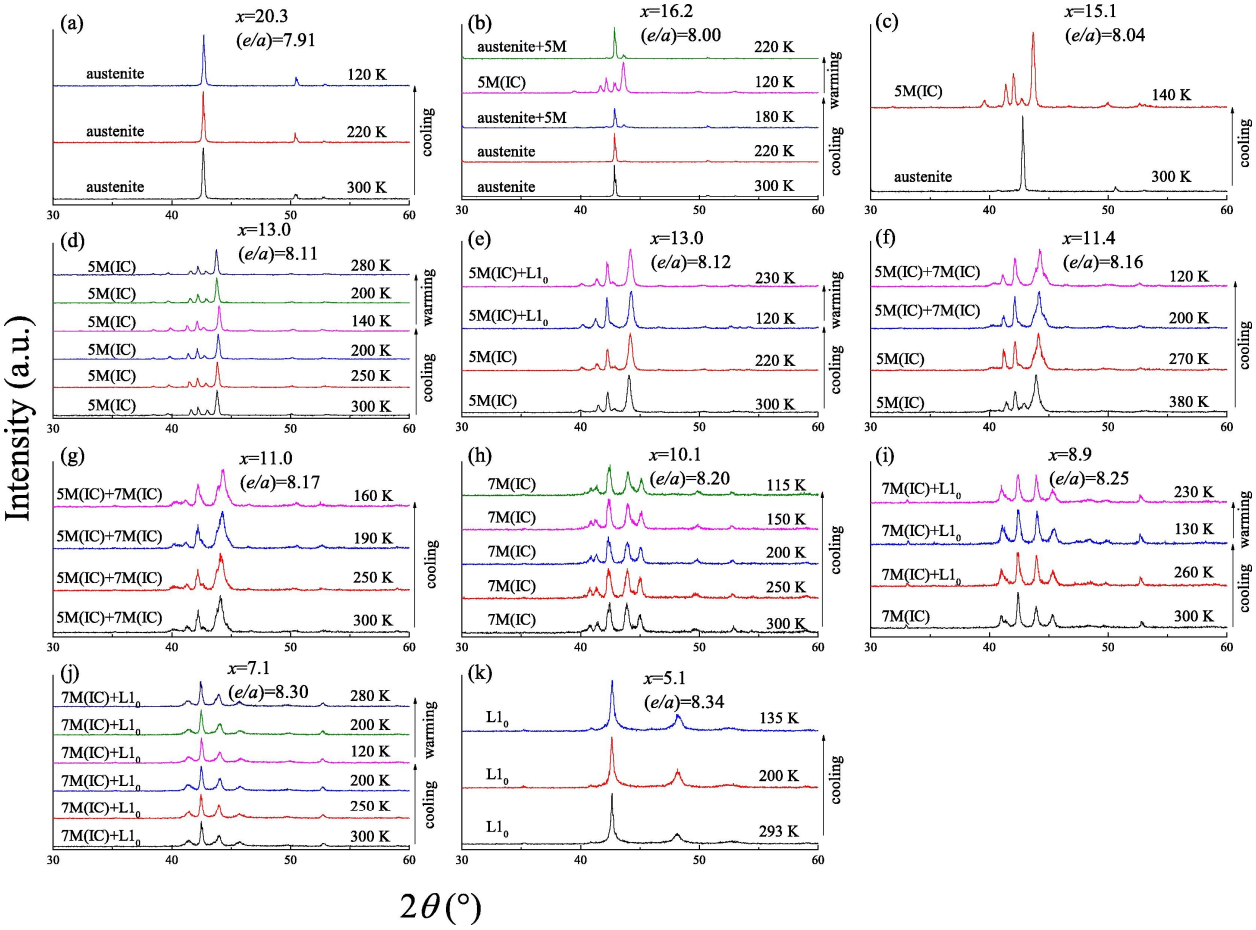



**Fig. 2.26. XRD results with varying temperatures for NiMnSn alloys with different e/a [85].**

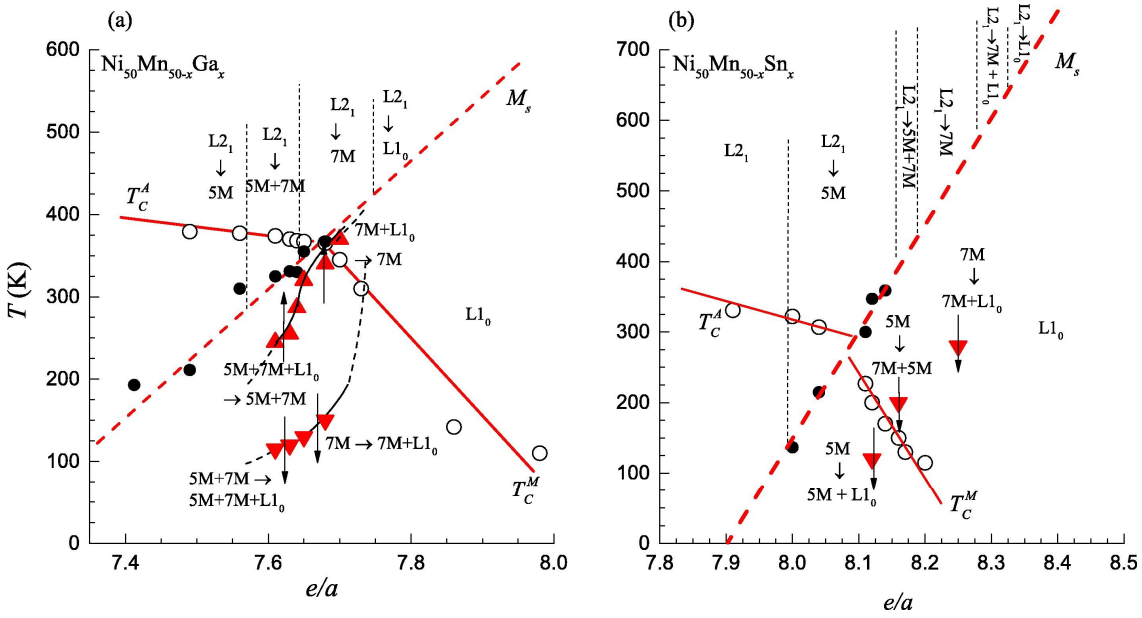



**Fig. 2.27. Phase diagrams for $Ni_{50}Mn_{50-x}Ga_x$ (a) and $Ni_{50}Mn_{50-x}Sn_x$ (b) Heusler alloys [85, 86].**

## 2.4.3 The magnetic transformation of NiMnSn alloy

Magnetism and its magnetic behaviours are summarized in Fig. 2.28. NiMnSn alloys also observe the magnetic transformation near the curie temperature. The transformation between different magnetic states (ferromagnetic austenite, paramagnetic austenite, ferromagnetic martensite and paramagnetic martensite) is the second-order phase transformation. This transformation is just a magnetic transformation rather than the structural one.

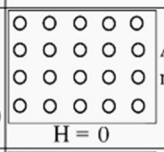
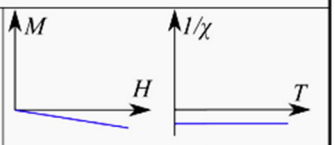
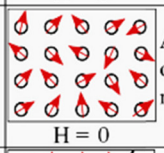
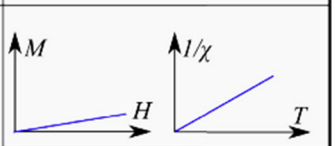
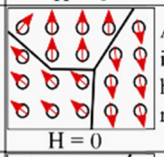
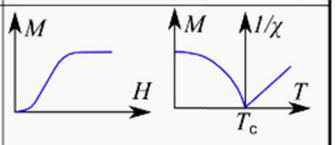
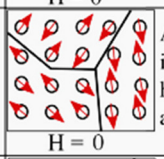
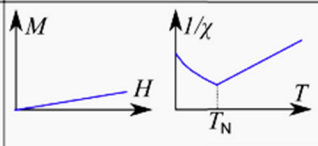
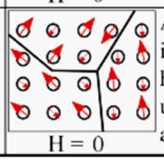
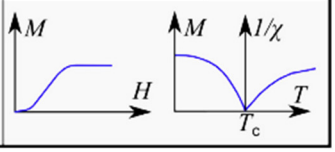
| Magnetism | Examples | Magnetic behaviour |
|---|---|---|
| Diamagnetism | Bi, Si, Cu, inert gases<br><br>Susceptibility small and negative ($-10^{-6}$ to $-10^{-5}$) |  Atoms have no magnetic moments.  |
| Paramagnetism | Al, $O_2$, MnBi<br><br>Susceptibilty small and positive ($10^{-5}$ to $10^{-3}$) |  Atoms have randomly oriented magnetic moments.  |
| Ferromagnetism | Fe, Ni, Co, Gd<br><br>Susceptibility large (generally > 100) |  Atoms are organized in domains which have parallel aligned magnetic moments.  |
| Antiferromagnetism | Cr, MnO, FeO<br><br>Susceptibilty small and positive ($10^{-5}$ to $10^{-3}$) |  Atoms are organized in domains which have antiparallel aligned moments.  |
| Ferrimagnetism | $Fe_3O_4$, $MnFe_2O_4$, $NiFe_2O_4$<br><br>Susceptibility large (generally > 100) |  Atoms are organized in domains which have a mixture of unequal antiparallel aligned moments.  |

**Fig. 2.28. Summary of the main relevant forms of magnetism and their features [73].**

These alloys show magnetism as the d-d interactions between Mn and its neighbour Ni [60, 87]. The Ni-Mn interaction makes the magnetic short-range order effects stronger. The Ni-Mn interactions are limited by first neighbours, while Mn-Mn interactions are long-ranged [88]. Although the d states on different Mn atoms did not interact with each other, the d states of different Mn atoms have indirect interaction through the conditions at the Sn atoms [60, 89]. Kubler et al. believed the Mn-Mn interaction is ferromagnetic when the Ni sublattice mediates the interaction lattice. The Sn sublattice mediates the interaction lattice. It has either sign, depending on the Fermi level's position in the Mn-F p-d hybrid states [89]. In addition, the principal role of the Ni atoms is to determine the lattice constant, and the Sn atoms provide the p orbitals mediating the covalent Mn-Mn interactions [89]. The Mn/Ni and Mn/Sn ratios significantly affect the magnetisation and the Curie temperature. The microscopic mechanisms responsible for forming and coupling magnetic moments in Heusler alloys were studied [60, 87,

89, 90]. The favourable exchange interaction of Mn with Ni atoms defined the ferromagnetic order. Thus, the curie temperature is insensitive to the Mn/Sn ratio (see Fig. 2.29) [60].

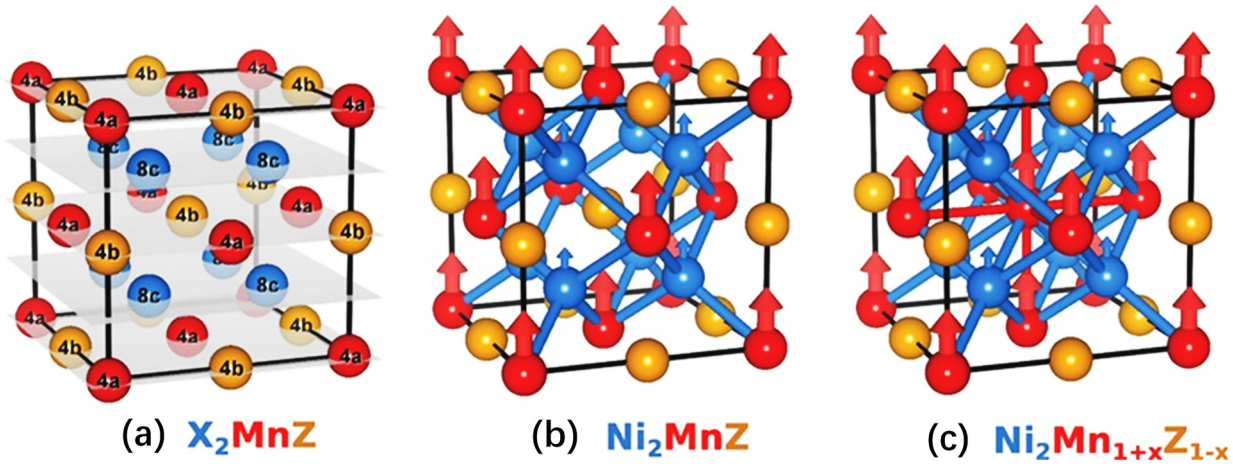



**Fig. 2.29. The effects of different chemical substitutions on the magnetic structure of the austenite phase. a) Unit cell of the $L2_1$ structure (Wyckoff sites 4a, 4b, and 8c are marked by red, yellow, and blue colors, respectively) corresponding to the $X_2MnZ$ (X—late transition element, Z—main group element) composition. The colour of a particular Wyckoff site matches that of the occupying element. d) In case of $Ni_2MnZ$, the parallel Mn–Ni coupling is much weak. e) In the case of $Ni_2Mn_{1+x}Z_{1-x}$, excess Mn randomly substitutes Z atoms in the 4b sites (indicated by mixed-coloured spheres). This leads to the emergence of antiparallel Mn(4a)–Mn(4b) exchange coupling (indicated by the red bonds) [60].**

## 2.4.4 FOPT and SOPT of NiMnSn alloy

From the viewpoint of phase transition thermodynamics, the martensitic-austenite transformation is FOPT. The Gibbs Free Energy (G) does not change before or after the phase transition. But the magnetisation, entropy, and volume do not stay the same during the transformation process. Magnetisation is the first-order partial derivative of G regarding the magnet field. The entropy is the first-order partial derivative of G regarding the temperature. The volume is the first-order partial derivative of G regarding the pressure (see Eqs. 2.9, 2.10, 2.11). Thus, the latent heat, volume, magnetism, and crystal structure change discontinuously

during the FOPT. FOPT leads to large anisotropy, entropy, and adiabatic temperature changes [76, 91-93]. However, significant hysteresis losses and lower efficiency for cooling applications are essential issues during FOPT. Using these materials is necessary to reduce thermal hysteresis [58] drastically.

$$S(T, \mu_0 H, p) = -(\frac{\partial G}{\partial T})_{p,\mu_0 H} \tag{2.9}$$

$$M(T, \mu_0 H, p) = -(\frac{\partial G}{\partial T})_{p,T} \tag{2.10}$$

$$V(T, \mu_0 H, p) = -(\frac{\partial G}{\partial T})_{T,\mu_0 H} \tag{2.11}$$

In addition, the SOPT happens at the curie temperature. Both G and the first-order partial derivative of G do not change. Thus, there is no thermal effect during the SOPT process. Magnetisation and entropy are continuous functions of temperature.

The NiMnSn alloy with different chemical compositions presents different magnetic transition characteristics. Fig. 2.30 presents the M(T) curves for the alloy series $Ni_{50}Mn_{50-x}Sn_x$ under the high magnetic field of 5 T and the low magnetic field of 5 mT. No structural transformation has been observed for the alloys with $x \geq 14$. However, For alloys with $13 \leq x \leq 16.2$ feature diverse structural and magnetic transitions [85].

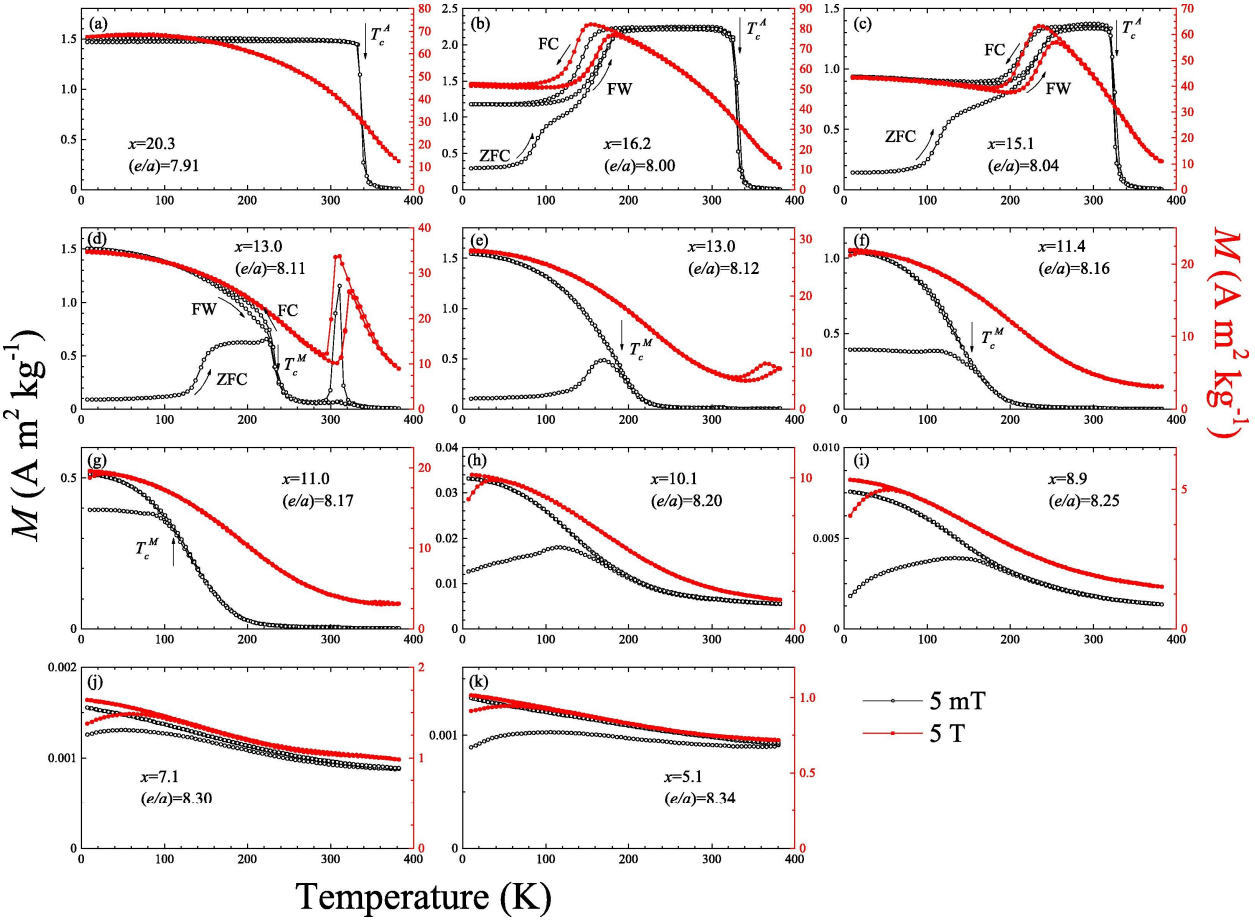



**Fig. 2.30. M (T) at H = 5 mT and 5 T. (a)–(j) show ZFC, FC, and FW runs for $Ni_{50}Mn_{50-x}Sn_x$ samples with x=20.3, 16.2, 15.1, 13.0 {(e/a) = 8.11}, 13.0 {(e/a) = 8.12}, 11.4, 11.0, 10.1, 8.9, 7.1, and 5.1, respectively [85].**

## 2.4.5 The heat treatment process

After short-term annealing times (hours), the microstructure of the as-cast $Ni_{50}Mn_{37}Sn_{13}$ sample quickly converts to a single crystallographic phase (see Fig. 2.31). Although the structural homogenization was rapid (hours), the chemical composition is not still uniform. For at least a few weeks, compositional homogenization appears to continue to evolve [94]. Therefore, magnetic behaviour varies according to homogenization degree.

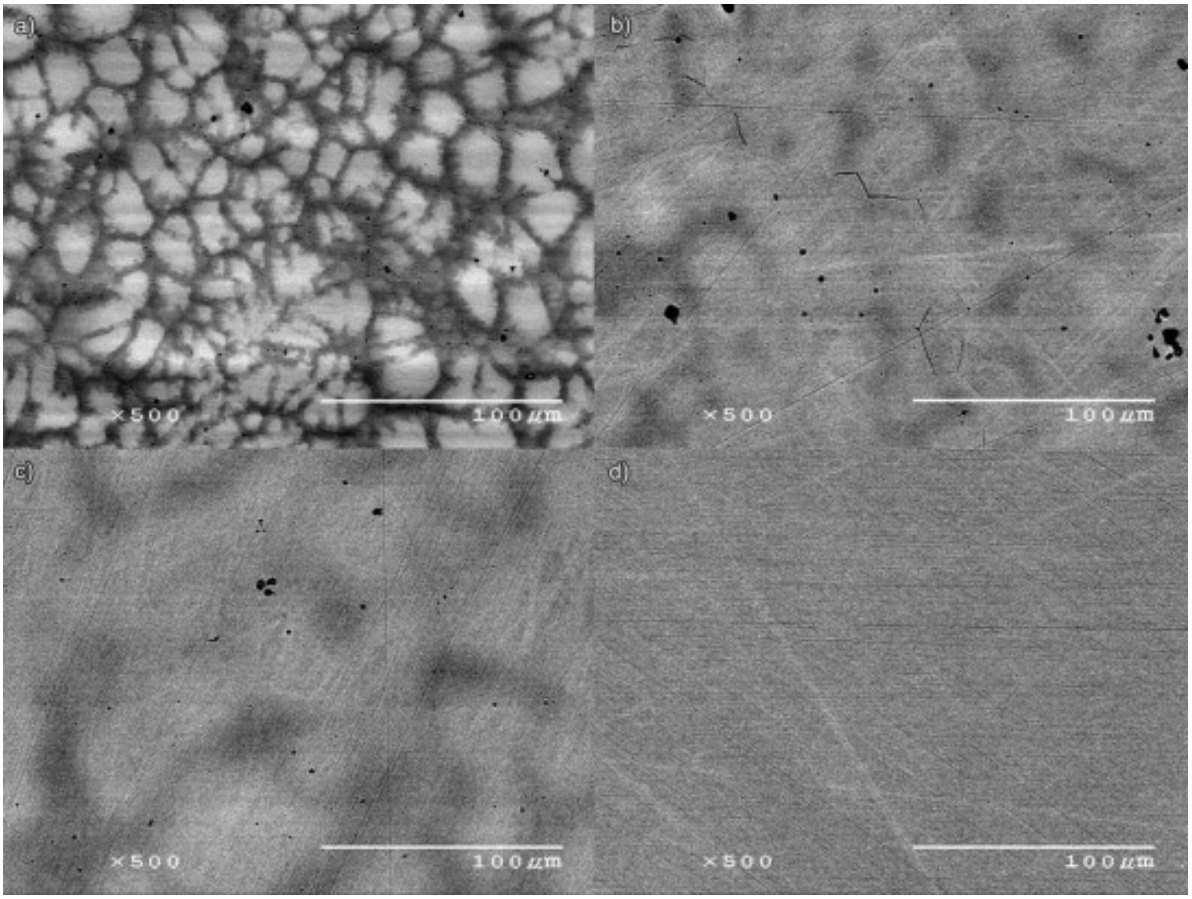



**Fig. 2.31. SEM micrographs of $Ni_{50}Mn_{37}Sn_{13}$ showing the effects of heat treatment at 950 °C followed by water quench: (a) as-cast; (b) 1 h; (c) 2 h; (d) 72 h [94].**

Ghosha and Mandal [95] manufactured a series of $Ni_{50}Mn_{36.5}Sn_{13.5}$ samples by processing different heat treatments (anneal 0, 6, 12, 18, and 24 h at 1173 K, then quenched in ice water) and studied their magnetocaloric properties. They observed magnetic hysteresis caused by a field in all samples, which increased with increasing annealing time. It is because the heat treatment process affects the magnetic properties of both structural phases to a significant extent—the increasing annealing time results in the rising atomic ordering and sharping martensitic transitions ($T_M$). The sample annealed for 24 h shows a large $\Delta S_m$ (~5.1 J/kgK at 15 kOe) near its $T_M$ (271 K). But, the refrigerant capacity of the sample annealed for 12 h ($RCP_{Net}$=~5.2 J/kg at 15 kOe, $T_M$=275 K) is larger than the former one. Dan et al. [81]

manufactured several $Ni_2Mn_{1+x}Sn_{1-x}$ alloys (x=0, 10, 11, 12, 13, 14, 15, 16, 17, 18, 19, 20, 30 and 40) by using arc-melting and annealing processes and they compared $Ni_2Mn_{1+x}Sn_{1-x}$ alloys after different manufacture processes. They found that the alloys with the as-melted state are almost a single ferromagnetic phase. The alloys' curie temperature ($T_c$) increased with Sn-concentrations (from about 240 K for x=0 to 360 K for x=40). However, the martensitic-austenitic transition only occurred in the annealed alloys with a narrow range of Sn-concentration (x=13-15), as the annealing process leads to the transition of the magnetic phases in the annealed alloys [81, 94] causing higher homogenisation, which affects the magnetic behaviours' appearance [94].

## 2.5 Metallurgy of LaFeSi-based alloy

### 2.5.1 The LaFeSi alloy

The MCE of LaFeSi alloys is attributed to the $NaZn_{13}$-type $La(Fe,Si)_{13}$ phases (1:13 phase) [96], as the $La(Fe,Si)_{13}$ phase is the functional phase with MCE. LaFeSi alloys present obvious MCEs when there is a large amount of $La(Fe,Si)_{13}$ phases within the alloy. However, the traditional solidification process cannot form the peritectic phase $La(Fe,Si)_{13}$ [97]. To increase the $La(Fe,Si)_{13}$ phase volume fraction, the as-casted LaFeSi alloy must examine a long heat-treatment process at higher temperatures and quenching [98].

### 2.5.2 The crystal structure and phase transformation

The crystal structure of $LaFe_{13-x}Si_x$ is closely related to the Si content [99]. The crystal structure of $LaFe_{13-x}Si_x$ presents the $NaZn_{13}$-type phases when $1.2 \leq x \leq 2.6$. When the Si increased ($3.2 \leq x \leq 5.0$), the crystal structure of $LaFe_{13-x}Si_x$ presented a square structure, as shown in Fig. 2.32 b. The space group is I4/mcm. La atom occupies the 4a position. The $Fe^I$ atom occupies

the 4d position, the $Fe^{II}$ atom occupies the 16k position, and the $Fe^{III}$ or Si atom occupies the 16l position.

In addition, the ferromagnetic phase transition of $LaFe_{13-x}Si_x$ gradually slows down with increasing Si at.% for $1.2 \leq x \leq 2.6$. The difference between the lattice parameters of the two phases also decreased. Thus, the type of phase transition transforms from FOPT to SOPT. For $La(Fe,Si)_{13}$ alloys with lower Si content, the massive difference in magnetisation, negative lattice expansion, and magnetic transition of touring electron result in grant MCE [100, 101].

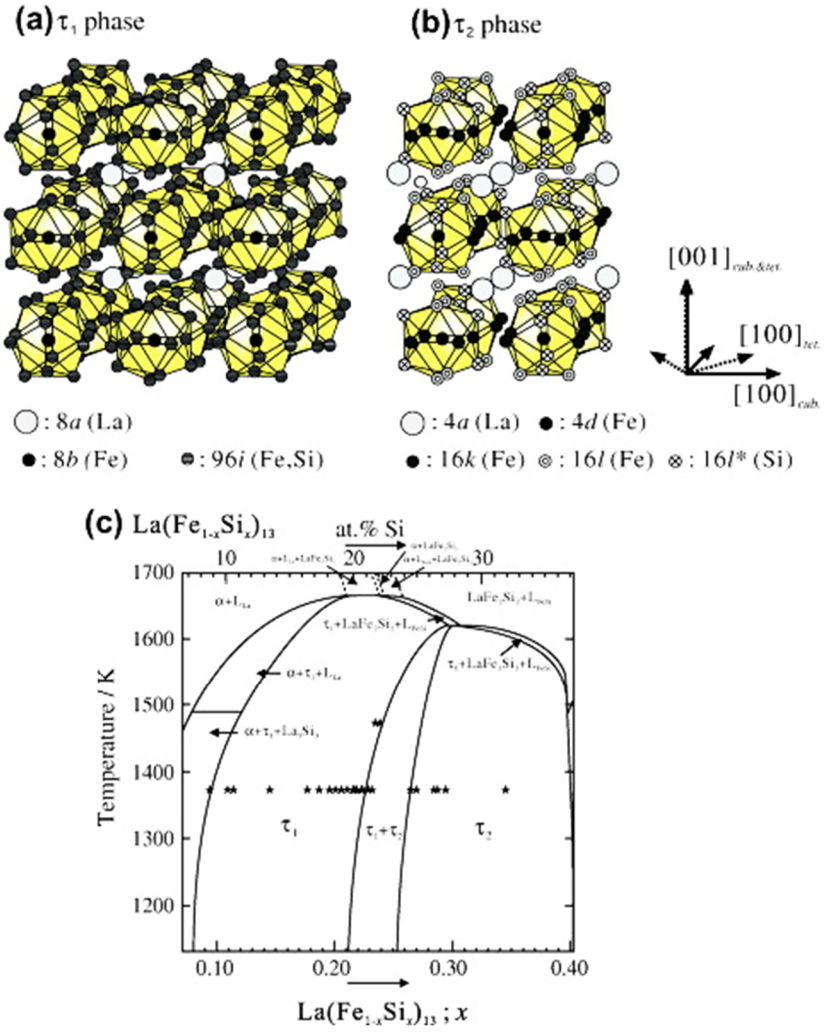



**Fig. 2.32. Schematic illustrations of the (a) cubic-type, (b) tetragonal-type $LaFe_{13-x}Si_x$ phases with their Wyckoff positions [102], and (c) Vertical section phase diagram in $La(Fe_{1-x}Si_x)_{13}$ ($0.07 \leq x \leq 0.40$) [103].**

### 2.5.3 The optimisation of MCE

There are two main methods for optimising the MCE. The first method is gap mixing N, H and B atoms [104-107]. The second method is element substitution. Small amounts of Co and Mn elements replace the Fe elements [108, 109]. Rare earth elements, such as Ce and Pr, replaced part of La elements [109, 110].

In 1993, Tang et al. [111] reported that the insertion of nitrogen atoms has a significant effect on the cubic phase, expanding lattice parameters (6.2 to 10.8%), increasing the curie temperature (52 to 80 K), and improving magnetisation (~10%). Balli et al. [107] reported the insertion of nitrogen atoms per $LaFe_{11.7}Si_{1.3}$ formula results in increased lattice parameters and curie temperatures. The absorption of nitrogen decreased the MCE. The $\Delta S_m$ decreased from 28 to 3.5 J/kgK when applying 5 T. Zhang et al. [106] studied the interstitial H and C atoms' effects on the magnetic and magnetocaloric properties of $La(Fe,Si)_{13}$ compounds. They reported the interstitial H and C atoms increased the curie temperature. The MCE is still high after hydrogen absorption. However, the partially hydrogenated compounds are not long-term stable. Thus, the Fe atoms are partially substituted by Mn atoms for adjusting the curie temperature. The type of magnetic transition shifts gradually from FOPT to SOPT with increasing Mn content [109]. Fujieda et al. [110] reported that partial substitution of Ce for La results in the decreased curie temperature, with the magnetisation change at curie temperature becoming larger with increasing Ce elements.

### 2.5.4 The heat treatment process

The as-cast LaFeSi alloy cannot get enough $La(Fe,Si)_{13}$ phases. The heat treatment process promotes the formation of $La(Fe,Si)_{13}$ phases. Thus, many researchers studied the heat treatment processes' effect on the microstructure and MCE of LaFeSi alloys. Fujieda et al. [112]

annealed the LaFeSi alloy at 1323 K for different times (0, 25, 50, 100, 200, and 300 h), quenched it, and then observed the microstructure. They reported the $La(Fe,Si)_{13}$ phase forms in the region between the α-Fe and LaFeSi phases. The amount of $La(Fe,Si)_{13}$ phases increases with the increasing HT time (see Fig. 2.33). The specimen annealed at 1323 K for 300 h saw a complete single phase of the $La(Fe,Si)_{13}$. Liu et al. [113] systematically studied the microstructure and MCE in LaFeSi-based alloys annealed at different temperatures and times. They reported that two different LaFeSi alloys ($LaFe_{11.8}Si_{1.2}$ and $LaFe_{11.6}Si_{1.4}$) own their best HT temperatures and times. Both 1373 K and 1323 K are suitable temperatures for $LaFe_{11.8}Si_{1.2}$ and $LaFe_{11.6}Si_{1.4}$, respectively. The difference in optimal temperature relates to the chemical composition of LaFeSi alloys. Löwe et al. [114] reported that $La(Fe,Si)_{13}$ phases are unstable and are broken down in temperature between 873 K and 1173 K. It also forms again when the temperature is above 1173 K. Liu et al. [115] reported that higher temperatures promote $La(Fe,Si)_{13}$ phases' formations. But the hysteresis also increased with the increasing HT temperatures.

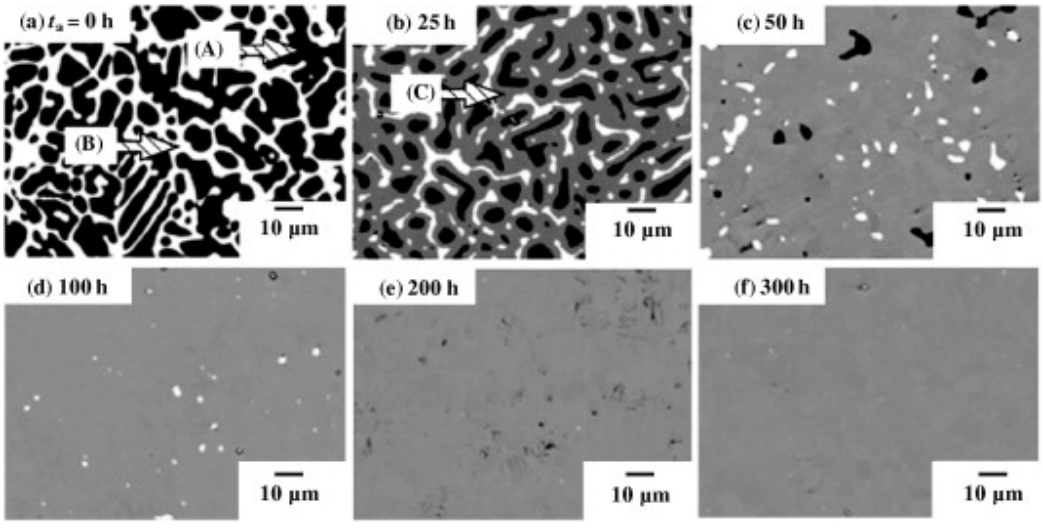



**Fig. 2.33. Backscattering images (BSIs) of the specimens annealed at 1323 K for different annealing times. (a) 0, (b) 25, (c) 50, (d) 100, (e) 200 and (f) 300 h [112]. (The α-Fe and LaFeSi phases are the (A) and (B) phases, respectively. The (C) phase, identified as the $NaZn_{13}$-type phase.)**

## 2.6 The manufacturing methods of magnetocaloric materials

Until now, several popular methods are used to produce magnetocaloric Ni-Mn-based Heusler alloys, such as conventional casting (arc or induction melting) [116], mechanical alloying (MA) [117], and rapid crystallization process (melt spinning technique) [118]. The form of magnetocaloric materials is mostly bulk, film, and ribbon. There are a few common manufacturing methods.

- Arc melting: A corresponding ratio of raw materials was mixed. To prepare the alloys, a mixture of the corresponding elements was vacuum arc melted. The arc-melted pellets were flipped and remelted several times to achieve a homogeneous distribution of elements. The alloy bulk is produced by conventional arc or induction melting and suitable heat treatment. Conventional melting and heat treatment can ensure good chemical homogeneity due to long-time annealing [116].

- Mechanical alloying: The mixed different materials' powder with the corresponding atomic ratio was enclosed in a stainless steel vial with ϕ6 mm and ϕ10 mm stainless balls. Argon was used to prevent oxidation during loading, milling, and sampling. The milling process was performed discontinuously [119].

- Melt spinning technique: The raw materials were first melted by induction heating and then moulded in copper. A copper roller with a high linear speed was then used to reject the cylinder ingots under low pressure (such as 0.02 MPa) [118]. Then, the ribbon sample can be obtained. The melt spinning technique offers several potential advantages for the fabrication of magnetocaloric materials. This technique can avoid or reduce the thermal annealing step to reach a homogeneous single-phase alloy and the synthesis of highly textured polycrystalline ribbons [118]. This technique can be a mass-production method of

melt-spun ribbons. In addition, ribbon shape can be also more appropriate for use in practical devices, such as sensors or actuators [118, 120]. Compared with the bulk sample, the magnetocaloric materials in the form of ribbons can improve the heat transfer between the heat source, working body and sink because of the larger surface area [121].

In addition, films, microwires and single crystals of Heusler alloy also attract scholars' attention. The thin films were deposited by co-sputtering of Heusler alloy targets onto Si (100) substrates at substrate temperature [122]. The films can also be prepared by pulsed laser deposition (PLD) [123]. The microwires were produced using the Taylor-Ulitovsky technique or a melt-extraction method [44][124]. Single crystals of Heusler alloy could be grown by applying Bridgman's method [125, 126].

## 2.7 Additive manufacturing of the magnetocaloric materials

### 2.7.1 Additive manufacturing of the magnetic materials

Additive manufacturing is a fast-evolving field of science that has demonstrated promise for producing magnetic materials. Due to their distinctive magnetic qualities, magnetic materials are highly sought-after in various industries, including healthcare, energy, and electronics. The ability to AM magnetic materials allows for constructing intricate geometries and unique shapes that are challenging or impossible to achieve using conventional manufacturing techniques.

Due to the careful management of the material's morphology and chemistry, AMed magnetic materials have a wide range of possible uses in multiple industries [127, 128]. Medical applications for AMed magnetic devices include medicine delivery and prosthetic device integration. Magnetic materials that can be AMed in the energy industry may be employed for magnetic refrigeration or constructing magnetic generators. Magnetic sensors, actuators, and

electronic data storage components may be made using AMed magnetic materials [129]. The ability to AM magnetic materials has enormous potential in many different industries.

### 2.7.2 PBF-LB of magnetocaloric materials

Some AM processes, such as PBF-LB, inkjet printing, and binder jet printing, have been utilised to create magnetic materials [127]. To precisely regulate the shape and chemistry of magnetic materials, PBF-LB has emerged as a potential approach. PBF-LB has been used previously in 3D printing of several functional magnetic materials such as $AlFe_2B_2$ alloy[130], CoFeNi [131-133], FeNi [134], functionally graded magnetic materials [18] and in particular MCMs (See Fig. 2.34) such as $LaCe(Fe,Mn,Si)_{13}$ [135], $La(Fe,Co,Si)_{13}$ [136] $(Mn,Fe)_2(P,Si)$ [137]. The importance of 3D printing of MCMs in increasing the effectiveness of magnetic refrigeration has been demonstrated in the research mentioned above. The improvement in heat transfer between the heat source, working body, and washbasin was made possible by the production of parts with high surface-area-to-volume ratios [121]. Controlling the heat transfer by increasing the surface area of MCMs by 3D printing has previously been described [135, 136, 138, 139]. They created blocks with straight microchannels, lattices, and interior micro-wavy channels [135, 136]. HA Ni-Mn-X(In, Sn, and Ga) show a considerable MCE associated with the martensitic transition [140]. In addition, these alloys show a conventional MCE at the austenite phase transition, which can be used as a double cooling capacity [141]. NiMnSn shows a near-room temperature magnetic transition in this category, making this alloy attractive [85, 140]. Only one work has been reported in the 3D printing of NiMnSn using the PBF-LB technique [142]. This work used a pre-alloyed powder to manufacture parts with hexagonal/square/circular macro channels (3 mm) inside, with reported magnetic properties of $\Delta S$ of 1.4 $Jkg^{-1}K^{-1}$ at 288 K and 1 T [142]. In addition, Mohamed Abd El-Moez et al. also successfully manufactured the $LaCe(Fe,Mn,Si)_{13}$ into bulks, strut lattice, and microchannel

blocks. They proved LaCe(Fe,Mn,Si)$_{13}$ magnetocaloric material's processability using PBF-LB [135].

Even though the PBF-LB of MCMs plays a significant role, several problems have been found. Elemental evaporation may alter the magnetic alloy's nominal chemical composition and cause an irregularity in the related magnetic characteristics [135]. Printed parts can exhibit residual stress and distortion that can affect the parts' magnetic properties and dimensional accuracy. The defects, such as cracks and lack of fusion defects (LOFs), are an unavoidable problem in the PBF-LB of the MCMs process. This difficulty can be solved by employing comparatively lower laser energy densities, optimising laser parameters, and correcting for evaporated elements. Thus, laser parameters optimisation is necessary [127, 135, 142].

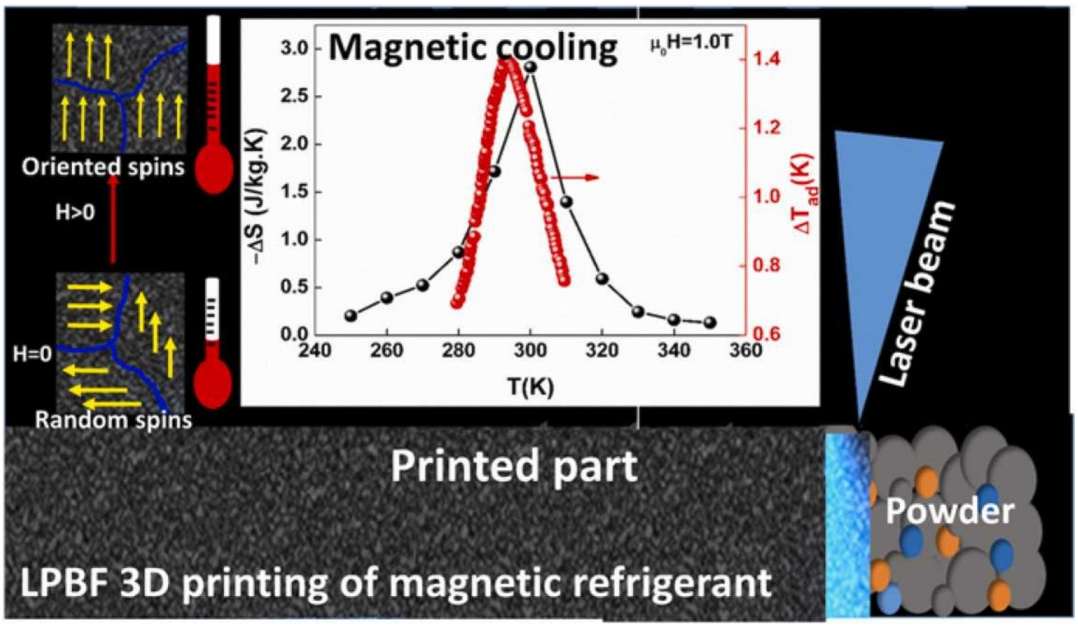



**Fig. 2.34. The 3D printing of magnetic refrigerant [135].**

## 2.8 Summary of the literature and areas for further investigation

Magnetic refrigeration is an environmentally friendly recent technique, which is based on the magnetocaloric effect (MCE). This literature review focussed on the PBF-LB technology and its physical aspects during processing. The metallurgy of NiMnSn and $La(Fe,Si)_{13}$-based alloys were introduced, such as the crystal structure, phase transformation, magnetic transformation, and the improvement of the MCE by adding different elements. The magnetocaloric materials are great of interest due to their high MCE, however, the materials also have limited uses due to poor mechanical properties. The laser powder bed fusion (PBF-LB) technology can overcome the disadvantages of difficult-to-machine alloys and directly produce parts with complex shapes, especially porous magnetocaloric materials with predefined external shapes and internal architecture. The samples with high surface-area-to-volume were built to decrease the temperature exchange time between the fluid and the magnetocaloric material in a magnetic refrigerator, thereby increasing the refrigeration efficiency.

The main concerns of PBF-LB magnetocaloric materials are holes, cracking and magnetocaloric properties. Although there are some reports about the PBF-LB of magnetocaloric material, numerous questions within the PBF-LB progress of the magnetocaloric material are still unclear. One work has been reported in the 3D printing of Ni-Mn-Sn using the PBF-LB technique [142]. Several works have been reported in the PBF-LB of the $La(Fe,Si)_{13}$ based alloy blocks and lattice structures [135, 136]. Although they optimised the PBF-LB process, they did not extend their study to explain the defects formation, such as cracks and lack of fusion defects (LOFs). A limitation of their study included the authors' manufacturing samples using high laser powers, which lead to the formation of defects in the build. This may have affected the optimisation results. The relationship between the

microstructure of alloy and the cracking susceptibility during the PBF-LB process has also not been rationalized convincingly so far. In addition, different heat treatments' effects on the metallurgy and MCE of the two alloys also require further improvement.

The gaps which have been identified and which will be addressed in this thesis are:

a. Studying the effect of PBF-LB processing parameters on defects (cracks and pores) of NiMnSn alloys and good structural integrity and microstructure uniformity using parametric studies.

b. Identifying the thermal post-processing treatment's effect on the microstructural development, mechanical property, and MCE of NiMnSn-based alloys. SEM and EBSD have been used to understand microstructural evolution.

c. Exploring the formation mechanism of defects within the PBF-LBed $LaCe(Fe,Mn,Si)_{13}$, especially the formation mechanism of cracks.

d. Exploring the effect of thermal post-processing treatment on the microstructural development and MCE of PBF-LBed $LaCe(Fe,Mn,Si)_{13}$.

## 2.9 References

[1] S.R. Narasimharaju, W. Zeng, T.L. See, Z. Zhu, P. Scott, X. Jiang, S. Lou, A comprehensive review on laser powder bed fusion of steels: Processing, microstructure, defects and control methods, mechanical properties, current challenges and future trends, Journal of Manufacturing Processes 75 (2022) 375-414.

[2] A. Queva, G. Guillemot, C. Moriconi, C. Metton, M. Bellet, Numerical study of the impact of vaporisation on melt pool dynamics in Laser Powder Bed Fusion - Application to IN718 and Ti–6Al–4V, Addit Manuf 35 (2020) 101249.

[3] S.A. Khairallah, A.T. Anderson, A. Rubenchik, W.E. King, Laser powder-bed fusion additive manufacturing: Physics of complex melt flow and formation mechanisms of pores, spatter, and denudation zones, Acta Mater 108 (2016) 36-45.

[4] E. Li, Z. Zhou, L. Wang, R. Zou, A. Yu, Numerical studies of melt pool and gas bubble dynamics in laser powder bed fusion process, Addit Manuf 56 (2022) 102913.

[5] I.A. Roberts, C.J. Wang, R. Esterlein, M. Stanford, D.J. Mynors, A three-dimensional finite element analysis of the temperature field during laser melting of metal powders in additive layer manufacturing, International Journal of Machine Tools and Manufacture 49(12) (2009) 916-923.

[6] S.A. Khairallah, A. Anderson, Mesoscopic simulation model of selective laser melting of stainless steel powder, Journal of Materials Processing Technology 214(11) (2014) 2627-2636.

[7] B. Liu, R. Wildman, C. Tuck, I. Ashcroft, R. Hague, Investigation the effect of particle size distribution on processing parameters optimisation in selective laser melting process, 2011 International Solid Freeform Fabrication Symposium, University of Texas at Austin, 2011.

[8] N.K. Tolochko, Y.V. Khlopkov, S.E. Mozzharov, M.B. Ignatiev, T. Laoui, V.I. Titov, Absorptance of powder materials suitable for laser sintering, Rapid Prototyping Journal 6(3) (2000) 155-161.

[9] J. Zhang, D. Gu, Y. Yang, H. Zhang, H. Chen, D. Dai, K. Lin, Influence of Particle Size on Laser Absorption and Scanning Track Formation Mechanisms of Pure Tungsten Powder During Selective Laser Melting, Engineering 5(4) (2019) 736-745.

[10] L.R. Scime, Methods for the expansion of additive manufacturing process space and the development of in-situ process monitoring methodologies, Carnegie Mellon University, 2018.

[11] M. Khorasani, A. Ghasemi, M. Leary, E. Sharabian, L. Cordova, I. Gibson, D. Downing, S. Bateman, M. Brandt, B. Rolfe, The effect of absorption ratio on meltpool features in laser-based powder bed fusion of IN718, Optics & Laser Technology 153 (2022) 108263.

[12] A. Ladewig, G. Schlick, M. Fisser, V. Schulze, U. Glatzel, Influence of the shielding gas flow on the removal of process by-products in the selective laser melting process, Addit Manuf 10 (2016) 1-9.

[13] C. Qiu, C. Panwisawas, M. Ward, H.C. Basoalto, J.W. Brooks, M.M. Attallah, On the role of melt flow into the surface structure and porosity development during selective laser melting, Acta Mater 96 (2015) 72-79.

[14] Y. Lu, Y. Wang, Physics based compressive sensing to monitor temperature and melt flow in laser powder bed fusion, Addit Manuf 47 (2021) 102304.

[15] K. Wei, Z. Wang, X. Zeng, Influence of element vaporization on formability, composition, microstructure, and mechanical performance of the selective laser melted Mg–Zn–Zr components, Mater Lett 156 (2015) 187-190.

[16] W. Wang, H. Garmestani, S.Y. Liang, Prediction of molten pool size and vapor depression depth in keyhole melting mode of laser powder bed fusion, The International Journal of Advanced Manufacturing Technology 119(9) (2022) 6215-6223.

[17] R. Cunningham, C. Zhao, N. Parab, C. Kantzos, J. Pauza, K. Fezzaa, T. Sun, A.D. Rollett, Keyhole threshold and morphology in laser melting revealed by ultrahigh-speed x-ray imaging, 363(6429) (2019) 849-852.

[18] S. Patel, M. Vlasea, Melting modes in laser powder bed fusion, Materialia 9 (2020) 100591.

[19] L. Johnson, M. Mahmoudi, B. Zhang, R. Seede, X. Huang, J.T. Maier, H.J. Maier, I. Karaman, A. Elwany, R. Arróyave, Assessing printability maps in additive manufacturing of metal alloys, Acta Mater 176 (2019) 199-210.

[20] V. Juechter, T. Scharowsky, R.F. Singer, C. Körner, Processing window and evaporation phenomena for Ti–6Al–4V produced by selective electron beam melting, Acta Mater 76 (2014) 252-258.

[21] W. Chen, Q. Yang, S. Huang, S. Huang, J.J. Kruzic, X. Li, Laser power modulated microstructure evolution, phase transformation and mechanical properties in NiTi fabricated by laser powder bed fusion, J Alloy Compd 861 (2021) 157959.

[22] T. Moges, G. Ameta, P. Witherell, A Review of Model Inaccuracy and Parameter Uncertainty in Laser Powder Bed Fusion Models and Simulations, Journal of Manufacturing Science and Engineering 141(4) (2019).

[23] F. Nilsén, I.F. Ituarte, M. Salmi, J. Partanen, S.-P. Hannula, Effect of process parameters on non-modulated Ni-Mn-Ga alloy manufactured using powder bed fusion, Addit Manuf 28 (2019) 464-474.

[24] Z. Gu, S. Sharma, D.A. Riley, M.V. Pantawane, S.S. Joshi, S. Fu, N.B. Dahotre, A universal predictor-based machine learning model for optimal process maps in laser powder bed fusion process, Journal of Intelligent Manufacturing (2022).

[25] K.G. Prashanth, S. Scudino, T. Maity, J. Das, J. Eckert, Is the energy density a reliable parameter for materials synthesis by selective laser melting, Materials Research Letters 5(6) (2017) 386-390.

[26] L.E. Criales, Y.M. Arısoy, B. Lane, S. Moylan, A. Donmez, T. Özel, Laser powder bed fusion of nickel alloy 625: Experimental investigations of effects of process parameters on melt pool size and shape with spatter analysis, International Journal of Machine Tools and Manufacture 121 (2017) 22-36.

[27] L.E. Criales, Y.M. Arısoy, T. Özel, Sensitivity analysis of material and process parameters in finite element modeling of selective laser melting of Inconel 625, The International Journal of Advanced Manufacturing Technology 86(9) (2016) 2653-2666.

[28] W. Abd-Elaziem, S. Elkatatny, A.-E. Abd-Elaziem, M. Khedr, M.A. Abd El-baky, M.A. Hassan, M. Abu-Okail, M. Mohammed, A. Järvenpää, T. Allam, A. Hamada, On the current research progress of metallic materials fabricated by laser powder bed fusion process: a review, Journal of Materials Research and Technology 20 (2022) 681-707.

[29] J. Fu, H. Li, X. Song, M.W. Fu, Multi-scale defects in powder-based additively manufactured metals and alloys, J Mater Sci Technol 122 (2022) 165-199.

[30] P. Mercelis, J.P. Kruth, Residual stresses in selective laser sintering and selective laser melting, Rapid Prototyping Journal 12(5) (2006) 254-265.

[31] H. Shipley, D. McDonnell, M. Culleton, R. Coull, R. Lupoi, G. O'Donnell, D. Trimble, Optimisation of process parameters to address fundamental challenges during selective laser melting of Ti-6Al-4V: A review, International Journal of Machine Tools and Manufacture 128 (2018) 1-20.

[32] Y.T. Tang, C. Panwisawas, J.N. Ghoussoub, Y. Gong, J.W.G. Clark, A.A.N. Németh, D.G. McCartney, R.C. Reed, Alloys-by-design: Application to new superalloys for additive manufacturing, Acta Mater 202 (2021) 417-436.

[33] Library, MRS Bulletin 28(9) (2003) 674-675.

[34] D. Dye, O. Hunziker, R.C. Reed, Numerical analysis of the weldability of superalloys, Acta Materialia 49(4) (2001) 683-697.

[35] J.C. Lippold, Welding metallurgy and weldability, John Wiley & Sons2014.

[36] S. David, S. Babu, J. Vitek, Welding: Solidification and microstructure, Jom 55(6) (2003) 14-20.

[37] S.J.N.J. Kou, USA, Welding metallurgy, 431(446) (2003) 223-225.

[38] T. DebRoy, H.L. Wei, J.S. Zuback, T. Mukherjee, J.W. Elmer, J.O. Milewski, A.M. Beese, A. Wilson-Heid, A. De, W. Zhang, Additive manufacturing of metallic components – Process, structure and properties, Prog Mater Sci 92 (2018) 112-224.

[39] R. Vilar, E.C. Santos, P.N. Ferreira, N. Franco, R.C. da Silva, Structure of NiCrAlY coatings deposited on single-crystal alloy turbine blade material by laser cladding, Acta Mater 57(18) (2009) 5292-5302.

[40] V. Ocelík, I. Furár, J.T.M. De Hosson, Microstructure and properties of laser clad coatings studied by orientation imaging microscopy, Acta Mater 58(20) (2010) 6763-6772.

[41] S. Sun, Y. Durandet, M. Brandt, Parametric investigation of pulsed Nd: YAG laser cladding of stellite 6 on stainless steel, Surface and Coatings Technology 194(2) (2005) 225-231.

[42] G.P. Dinda, A.K. Dasgupta, J. Mazumder, Laser aided direct metal deposition of Inconel 625 superalloy: Microstructural evolution and thermal stability, Materials Science and Engineering: A 509(1) (2009) 98-104.

[43] G.P. Dinda, A.K. Dasgupta, J. Mazumder, Texture control during laser deposition of nickel-based superalloy, Scripta Mater 67(5) (2012) 503-506.

[44] L. Thijs, F. Verhaeghe, T. Craeghs, J.V. Humbeeck, J.-P. Kruth, A study of the microstructural evolution during selective laser melting of Ti–6Al–4V, Acta Mater 58(9) (2010) 3303-3312.

[45] M. Rappaz, C.A. Gandin, Probabilistic modelling of microstructure formation in solidification processes, Acta Metallurgica et Materialia 41(2) (1993) 345-360.

[46] S.A. David, J.M. Vitek, Correlation between solidification parameters and weld microstructures, Int Mater Rev 34(1) (1989) 213-245.

[47] W. Kurz, B. Giovanola, R. Trivedi, Theory of microstructural development during rapid solidification, Acta Metallurgica 34(5) (1986) 823-830.

[48] T. DebRoy, S.A. David, Physical processes in fusion welding, Reviews of Modern Physics 67(1) (1995) 85-112.

[49] O. Hunziker, D. Dye, R.C. Reed, On the formation of a centreline grain boundary during fusion welding, Acta Mater 48(17) (2000) 4191-4201.

[50] V. Franco, J.S. Blazquez, B. Ingale, A. Conde, The Magnetocaloric Effect and Magnetic Refrigeration Near Room Temperature: Materials and Models, Annu Rev Mater Res 42 (2012) 305-342.

[51] V. Franco, J.S. Blazquez, J.J. Ipus, J.Y. Law, L.M. Moreno-Ramirez, A. Conde, Magnetocaloric effect: From materials research to refrigeration devices, Prog Mater Sci 93 (2018) 112-232.

[52] A. Smith, C.R.H. Bahl, R. Bjørk, K. Engelbrecht, K.K. Nielsen, N. Pryds, Materials Challenges for High Performance Magnetocaloric Refrigeration Devices, Adv Energy Mater 2(11) (2012) 1288-1318.

[53] P. Weiss, A. Piccard, Sur un nouveau phénomène magnétocalorique, Comptes Rendus 166 (1918) 352-354.

[54] P. Debye, Einige Bemerkungen zur Magnetisierung bei tiefer Temperatur, Annalen der Physik 386(25) (1926) 1154-1160.

[55] G.V. Brown, Magnetic heat pumping near room temperature, J Appl Phys 47(8) (1976) 3673-3680.

[56] V.K. Pecharsky, J.K.A. Gschneidner, Giant magnetocaloric effect in Gd 5 (Si 2 Ge 2), Physical Review Letters 78(23) (1997) 4494-4497.

[57] T. Graf, C. Felser, S.S.P. Parkin, Simple rules for the understanding of Heusler compounds, Prog Solid State Ch 39(1) (2011) 1-50.

[58] C. Felser, A. Hirohata, Heusler alloys, Springer2015.

[59] K. Ullakko, J.K. Huang, C. Kantner, R.C. O'Handley, V.V. Kokorin, Large magnetic-field-induced strains in Ni2MnGa single crystals, Appl Phys Lett 69(13) (1996) 1966-1968.

[60] S. Singh, L. Caron, S.W. D'Souza, T. Fichtner, G. Porcari, S. Fabbrici, C. Shekhar, S. Chadov, M. Solzi, C. Felser, Large Magnetization and Reversible Magnetocaloric Effect at the Second-Order Magnetic Transition in Heusler Materials, Adv Mater 28(17) (2016) 3321-3325.

[61] F. Wang, G.-j. Wang, F.-x. Hu, A. Kurbakov, B.-g. Shen, Z.-h. Cheng, Strong interplay between structure and magnetism in the giant magnetocaloric intermetallic compound LaFe11.4Si1.6: a neutron diffraction study, Journal of Physics: Condensed Matter 15(30) (2003) 5269-5278.

[62] L.M. Moreno-Ramírez, C. Romero-Muñiz, J.Y. Law, V. Franco, A. Conde, I.A. Radulov, F. Maccari, K.P. Skokov, O. Gutfleisch, Tunable first order transition in La(Fe,Cr,Si)13 compounds: Retaining magnetocaloric response despite a magnetic moment reduction, Acta Mater 175 (2019) 406-414.

[63] F.-x. Hu, B.-g. Shen, J.-r. Sun, Z.-h. Cheng, G.-h. Rao, X.-x. Zhang, Influence of negative lattice expansion and metamagnetic transition on magnetic entropy change in the compound LaFe11.4Si1.6, Appl Phys Lett 78(23) (2001) 3675-3677.

[64] Y. Ouyang, M. Zhang, A. Yan, W. Wang, F. Guillou, J. Liu, Plastically deformed La–Fe–Si: Microstructural evolution, magnetocaloric effect and anisotropic thermal conductivity, Acta Mater 187 (2020) 1-11.

[65] G.F. Wang, W. Ren, B.Y. Yang, Study on magnetocaloric effect and phase transition in La0.7(La–Ce)0.3FexAl11.5−xSi1.5 alloys, Intermetallics 136 (2021) 107269.

[66] X. Hou, P. Lampen-Kelley, Y. Xue, C. Liu, H. Xu, N. Han, C. Ma, H. Srikanth, M.-H. Phan, Formation mechanisms of NaZn13-type phase in giant magnetocaloric La–Fe–Si compounds during rapid solidification and annealing, J Alloy Compd 646 (2015) 503-511.

[67] L. Yang, Z. Zhou, S. Feng, J. Li, J. Liu, J. Li, Q. Hu, J. Li, Microstructure and magnetic property of LaFe11.6Si1.4 magnetocaloric alloys by a novel short time heat treatment, Intermetallics 105 (2019) 1-5.

[68] X. Chen, Y. Chen, Y. Tang, The influence of different cooling processes on phase, microstructure, and magnetocaloric properties of LaFe11.6Si1.4 compounds, Solid State Commun 186 (2014) 56-63.

[69] G.H. Yu, Y.L. Xu, Z.H. Liu, H.M. Qiu, Z.Y. Zhu, X.P. Huang, L.Q. Pan, Recent progress in Heusler-type magnetic shape memory alloys, Rare Metals 34(8) (2015) 527-539.

[70] V. Chaudhary, X. Chen, R.V. Ramanujan, Iron and manganese based magnetocaloric materials for near room temperature thermal management, Prog Mater Sci 100 (2019) 64-98.

[71] A. Kitanovski, J. Tušek, U. Tomc, U. Plaznik, M. Ožbolt, A. Poredoš, Magnetocaloric energy conversion, Springer2016.

[72] D. Jiles, Introduction to magnetism and magnetic materials, CRC press2015.

[73] S. Palagummi, F.G. Yuan, 8 - Magnetic levitation and its application for low frequency vibration energy harvesting, in: F.-G. Yuan (Ed.), Structural Health Monitoring (SHM) in Aerospace Structures, Woodhead Publishing2016, pp. 213-251.

[74] R.E. Hummel, Electronic properties of materials, Springer2011.

[75] J. Kiss, L. Szarka, E. Prácser, Second-order magnetic phase transition in the Earth, 32(24) (2005).

[76] V.D. Buchelnikov, V.V. Sokolovskiy, Magnetocaloric effect in Ni-Mn-X (X = Ga, In, Sn, Sb) Heusler alloys, Phys Met Metallogr 112(7) (2011) 633-665.

[77] A. Duran, Surface Superconductivity in Ni50Mn36Sn14 Heusler Alloy, J Supercond Nov Magn 31(12) (2018) 4053-4062.

[78] A. Duran, Lattice Location Effect of Ni50Mn36Sn14 Heusler Alloy, J Supercond Nov Magn 31(4) (2018) 1101-1109.

[79] E. Wachtel, F. Henninger, B. Predel, Constitution and magnetic properties of Ni-Mn-Sn alloys - solid and liquid state, J Magn Magn Mater 38(3) (1983) 305-315.

[80] T. Krenke, M. Acet, E.F. Wassermann, X. Moya, L. Mañosa, A. Planes, Martensitic transitions and the nature of ferromagnetism in the austenitic and martensitic states of Ni-Mn-Sn alloys, Phys Rev B 72(1) (2005) 014412.

[81] N.H. Dan, N.H. Duc, N.H. Yen, P.T. Thanh, L.V. Bau, N.M. An, D.T.K. Anh, N.A. Bang, N.T. Mai, P.K. Anh, T.D. Thanh, T.L. Phan, S.C. Yu, Magnetic properties and magnetocaloric effect in Ni-Mn-Sn alloys, J Magn Magn Mater 374 (2015) 372-375.

[82] T. Krenke, M. Acet, E.F. Wassermann, X. Moya, L. Mañosa, A. Planes, Martensitic transitions and the nature of ferromagnetism in the austenitic and martensitic states of NiMnSn alloys, Phys Rev B 72(1) (2005) 014412.

[83] Y. Sutou, Y. Imano, N. Koeda, T. Omori, R. Kainuma, K. Ishida, K. Oikawa, Magnetic and martensitic transformations of NiMnX(X=In,Sn,Sb) ferromagnetic shape memory alloys, 85(19) (2004) 4358-4360.

[84] X. Liang, X. Jiang, J. Gu, J. Bai, Z. Guan, Z. Li, H. Yan, Y. Zhang, C. Esling, X. Zhao, L. Zuo, 5M and 7M martensitic stability and associated physical properties in Ni50Mn35In15 alloy: first-principles calculations and experimental verification, Scripta Mater 204 (2021) 114140.

[85] A. Cakir, L. Righi, F. Albertini, M. Acet, M. Farle, Intermartensitic transitions and phase stability in Ni50Mn50-xSnx Heusler alloys, Acta Mater 99 (2015) 140-149.

[86] A. Çakır, L. Righi, F. Albertini, M. Acet, M. Farle, S. Aktürk, Extended investigation of intermartensitic transitions in Ni-Mn-Ga magnetic shape memory alloys: A detailed phase diagram determination, J Appl Phys 114(18) (2013) 183912.

[87] P.J. Webster, Magnetic phase transitions in the Pd2−xCuxMnIn system, J Appl Phys 52(3) (1981) 2040-2042.

[88] Y. Kurtulus, R. Dronskowski, G.D. Samolyuk, V.P. Antropov, Electronic structure and magnetic exchange coupling in ferromagnetic full Heusler alloys, Phys Rev B 71(1) (2005) 014425.

[89] J. Kübler, A.R. William, C.B. Sommers, Formation and coupling of magnetic moments in Heusler alloys, Phys Rev B 28(4) (1983) 1745-1755.

[90] E. Şaşıoğlu, L.M. Sandratskii, P. Bruno, First-principles calculation of the intersublattice exchange interactions and Curie temperatures of the full Heusler alloys Ni2MnX (X=Ga, In, Sn, Sb), Phys Rev B 70(2) (2004) 024427.

[91] R. Caballero-Flores, L. Gonzalez-Legarreta, W.O. Rosa, T. Sanchez, V.M. Prida, L. Escoda, J.J. Sunol, A.B. Batdalov, A.M. Aliev, V.V. Koledov, V.G. Shavrov, B. Hernando, Magnetocaloric effect, magnetostructural and magnetic phase transformations in Ni50.3Mn36.5Sn13.2 Heusler alloy ribbons, J Alloy Compd 629 (2015) 332-342.

[92] J.H. Chen, N.M. Bruno, Z.H. Ning, W.A. Shelton, I. Karaman, Y.J. Huang, J.G. Li, J.H. Ross, Relative cooling power enhancement by tuning magneto-structural stability in Ni-Mn-In Heusler alloys, J Alloy Compd 744 (2018) 785-790.

[93] P.J. Shamberger, F. Ohuchi, Hysteresis of the martensitic phase transition in magnetocaloric-effect Ni-Mn-Sn alloys, Phys Rev B 79(14) (2009) 144407.

[94] D.L. Schlagel, R.W. McCallum, T.A. Lograsso, Influence of solidification microstructure on the magnetic properties of Ni-Mn-Sn Heusler alloys, J Alloy Compd 463(1-2) (2008) 38-46.

[95] A. Ghosh, K. Mandal, Effect of structural disorder on the magnetocaloric properties of Ni-Mn-Sn alloy, Appl Phys Lett 104(3) (2014).

[96] G. Cao, Q. Wang, J. Liu, Y. Zhang, X. Wang, M. Huang, H. Shen, L. Zheng, Enhanced magnetic entropy change and refrigeration capacity of La(Fe,Ni)11.5Si1.5 alloys through vacuum annealing treatment, J Alloy Compd 800 (2019) 363-371.

[97] X.C. Zhong, X.T. Dong, D.R. Peng, S.M. Wu, C.L. Liu, J.H. Huang, H. Zhang, K.W. Long, D.L. Jiao, H. Zhang, W.Q. Qiu, H.Y. Yu, Z.W. Liu, R.V. Ramanujan, Microstructural evolution, magnetocaloric effect, mechanical and thermal properties of hot-pressed LaFe11.6Si1.4/Ce2Co7 composites prepared using strip-cast master alloy flakes, Journal of Magnetism and Magnetic Materials 525 (2021) 167652.

[98] X. Chen, Y. Chen, Y. Tang, The studies of high-temperature and short-time annealing, phase transition process, and magnetic property for LaFe11.7Si1.3 compound, Phase Transitions 85(1-2) (2012) 27-40.

[99] K. Niitsu, S. Fujieda, A. Fujita, R. Kainuma, Microstructure and magnetic properties of as-quenched cubic and tetragonal La(Fe1−xSix)13 compounds, J Alloy Compd 578 (2013) 220-227.

[100] K.A. Gschneidner, Y. Mudryk, V.K. Pecharsky, On the nature of the magnetocaloric effect of the first-order magnetostructural transition, Scripta Mater 67(6) (2012) 572-577.

[101] Q.Y. Dong, H.W. Zhang, J.R. Sun, B.G. Shen, Effect of Si doping on the magnetic properties and magnetic entropy changes in the LaFe11.4Al1.6intermetallic compound, Journal of Physics: Condensed Matter 20(13) (2008) 135205.

[102] W. Tang, J. Liang, G. Rao, X. Yan, Study of AC susceptibility on the LaFe13–xSix system, 141(1) (1994) 217-222.

[103] K. Niitsu, R. Kainuma, Effect of Microalloying Elements on Solidification Microstructure of the La(Fe0.89Si0.11)13 Alloy, Key Engineering Materials 508 (2012) 172-177.

[104] B.G. Shen, J.R. Sun, F.X. Hu, H.W. Zhang, Z.H. Cheng, Recent Progress in Exploring Magnetocaloric Materials, Adv Mater 21(45) (2009) 4545-4564.

[105] H. Zhang, Y. Long, Q. Cao, Y. Mudryk, M. Zou, K.A. Gschneidner, V.K. Pecharsky, Microstructure and magnetocaloric effect in cast LaFe11.5Si1.5Bx (x=0.5, 1.0), J Magn Magn Mater 322(13) (2010) 1710-1714.

[106] H. Zhang, F. Hu, J. Sun, B. Shen, Effects of interstitial H and/or C atoms on the magnetic and magnetocaloric properties of La(Fe, Si)13-based compounds, Science China Physics, Mechanics and Astronomy 56(12) (2013) 2302-2311.

[107] M. Balli, M. Rosca, D. Fruchart, D. Gignoux, Effect of interstitial nitrogen on magnetism and entropy change of LaFe11.7Si1.3 compound, J Magn Magn Mater 321(2) (2009) 123-125.

[108] X.B. Liu, Z. Altounian, Effect of Co content on magnetic entropy change and structure of La(Fe1−xCox)11.4Si1.6, J Magn Magn Mater 264(2) (2003) 209-213.

[109] M. Krautz, K. Skokov, T. Gottschall, C.S. Teixeira, A. Waske, J. Liu, L. Schultz, O. Gutfleisch, Systematic investigation of Mn substituted La(Fe,Si)13 alloys and their hydrides for room-temperature magnetocaloric application, J Alloy Compd 598 (2014) 27-32.

[110] S. Fujieda, A. Fujita, K. Fukamichi, N. Hirano, S. Nagaya, Large magnetocaloric effects enhanced by partial substitution of Ce for La in La(Fe0.88Si0.12)13 compound, J Alloy Compd 408-412 (2006) 1165-1168.

[111] Z. Tang, X. Deng, G.C. Hadjipanayis, V. Papaefthymiou, D.J. Sellmyer, Structural and magnetic properties of LaFe 13-x Si x nitrides, (1993).

[112] S. Fujieda, K. Fukamichi, S. Suzuki, Microstructure and isothermal magnetic entropy change of La(Fe0.89Si0.11)13 in a single-phase formation process by annealing, J Alloy Compd 566 (2013) 196-200.

[113] J. Liu, M. Krautz, K. Skokov, T.G. Woodcock, O. Gutfleisch, Systematic study of the microstructure, entropy change and adiabatic temperature change in optimized La–Fe–Si alloys, Acta Mater 59(9) (2011) 3602-3611.

[114] K. Löwe, J. Liu, K. Skokov, J.D. Moore, H. Sepehri-Amin, K. Hono, M. Katter, O. Gutfleisch, The effect of the thermal decomposition reaction on the mechanical and magnetocaloric properties of La(Fe,Si,Co)13, Acta Mater 60(10) (2012) 4268-4276.

[115] T. Liu, Y. Chen, Y. Tang, S. Xiao, E. Zhang, J. Wang, Structure and magnetic properties of shortly high temperature annealing LaFe11.6Si1.4 compound, J Alloy Compd 475(1) (2009) 672-675.

[116] Z. Zhang, S. Fu, F. Aversano, M. Bortolotti, H. Zhang, C. Hu, S. Grasso, Arc melting: a novel method to prepare homogeneous solid solutions of transition metal carbides (Zr, Ta, Hf), Ceram Int 45(7, Part A) (2019) 9316-9319.

[117] A. Ghotbi Varzaneh, P. Kameli, F. Karimzadeh, B. Aslibeiki, G. Varvaro, H. Salamati, Magnetocaloric effect in Ni47Mn40Sn13 alloy prepared by mechanical alloying, J Alloy Compd 598 (2014) 6-10.

[118] B. Hernando, J.L.S. Llamazares, J.D. Santos, L. Escoda, J.J. Suñol, R. Varga, D. Baldomir, D. Serantes, Thermal and magnetic field-induced martensite-austenite transition in Ni50.3Mn35.3Sn14.4 ribbons, Appl Phys Lett 92(4) (2008) 042504.

[119] X. Li, X. Wen, H. Zhao, Z. Ma, L. Yu, C. Li, C. Liu, Q. Guo, Y. Liu, The formation and evolution mechanism of amorphous layer surrounding Nb nano-grains in Nb-Al system during mechanical alloying process, J Alloy Compd 779 (2019) 175-182.

[120] B. Hernando, J.L.S. Llamazares, J.D. Santos, M.L. Sánchez, L. Escoda, J.J. Suñol, R. Varga, C. García, J. González, Grain oriented NiMnSn and NiMnIn Heusler alloys ribbons produced by melt spinning: Martensitic transformation and magnetic properties, J Magn Magn Mater 321(7) (2009) 763-768.

[121] Z. Li, N. Zou, C.F. Sánchez-Valdés, J.L. Sánchez Llamazares, B. Yang, Y. Hu, Y. Zhang, C. Esling, X. Zhao, L. Zuo, Thermal and magnetic field-induced martensitic transformation in Ni50Mn25−xGa25Cux($0 \leqslant x \leqslant 7$) melt-spun ribbons, Journal of Physics D: Applied Physics 49(2) (2015) 025002.

[122] H.S. Akkera, N. Choudhary, D. Kaur, Martensitic phase transformations and magnetocaloric effect in Al co-sputtered Ni-Mn-Sb alloy thin films, Mater Sci Eng B-Adv 198 (2015) 113-119.

[123] D. Qu, Y. Ling, J. Wang, R. Liu, Z. Han, Q. Li, J. Du, Q. Xu, The preparation of flexible Ni-Mn-In thin films on mica substrates by pulsed laser deposition, J Magn Magn Mater 488 (2019) 165244.

[124] P.J. Ibarra-Gaytan, L. Frolova, L. Galdun, T. Ryba, P. Diko, V. Kavecansky, J.L.S. Llamazares, Z. Vargova, R. Varga, Glass-coated Ni2MnGa microwires with narrow structural transition range and enhanced magnetocaloric effect at low fields, J Alloy Compd 786 (2019) 65-70.

[125] I. Radelytskyi, M. Pekala, R. Szymczak, D.J. Gawryluk, M. Berkowski, J. Fink-Finowicki, R. Diduszko, V. Dyakonov, H. Szymczak, Magnetocaloric effect in Ni2MnGa single crystal in the vicinity of the martensitic phase transition, J Magn Magn Mater 430 (2017) 16-21.

[126] D. Bourgault, J. Tillier, P. Courtois, D. Maillard, X. Chaud, Large inverse magnetocaloric effect in Ni45Co5Mn37.5In12.5 single crystal above 300 K, Appl Phys Lett 96(13) (2010).

[127] V. Chaudhary, S.A. Mantri, R.V. Ramanujan, R. Banerjee, Additive manufacturing of magnetic materials, Prog Mater Sci 114 (2020) 100688.

[128] E.A. Périgo, J. Jacimovic, F. García Ferré, L.M. Scherf, Additive manufacturing of magnetic materials, Addit Manuf 30 (2019) 100870.

[129] D. Goll, D. Schuller, G. Martinek, T. Kunert, J. Schurr, C. Sinz, T. Schubert, T. Bernthaler, H. Riegel, G. Schneider, Additive manufacturing of soft magnetic materials and components, Addit Manuf 27 (2019) 428-439.

[130] B.T. Lejeune, R. Barua, E. Simsek, R.W. McCallum, R.T. Ott, M.J. Kramer, L.H. Lewis, Towards additive manufacturing of magnetocaloric working materials, Materialia 16 (2021) 101071.

[131] M.S.K.K.Y. Nartu, A. Jagetia, V. Chaudhary, S.A. Mantri, E. Ivanov, N.B. Dahotre, R.V. Ramanujan, R. Banerjee, Magnetic and mechanical properties of an additively manufactured equiatomic CoFeNi complex concentrated alloy, Scripta Mater 187 (2020) 30-36.

[132] V. Chaudhary, M.S.K.K.Y. Nartu, S. Dasari, S.M. Varahabhatla, A. Sharma, M. Radhakrishnan, S.A. Mantri, S. Gorsse, N.B. Dahotre, R.V. Ramanujan, R. Banerjee, Magnetic and mechanical properties of additively manufactured Alx(CoFeNi) complex concentrated alloys, Scripta Mater 224 (2023) 115149.

[133] W.H. Teh, V. Chaudhary, S. Chen, S.H. Lim, F. Wei, J.Y. Lee, P. Wang, S.P. Padhy, C.C. Tan, R.V. Ramanujan, High throughput multi-property evaluation of additively manufactured Co-Fe-Ni materials libraries, Addit Manuf 58 (2022) 102983.

[134] C. Shen, K.-D. Liss, M. Reid, Z. Pan, X. Hua, F. Li, G. Mou, Y. Huang, Y. Zhu, H. Li, Fabrication of FeNi intermetallic using the wire-arc additive manufacturing process: A feasibility and neutron diffraction phase characterization study, Journal of Manufacturing Processes 57 (2020) 691-699.

[135] A.E.-M.A. Mohamed, M. Jeong, R.S. Sheridan, M.M. Attallah, Enabling high efficiency magnetic refrigeration using laser powder bed fusion of porous LaCe(Fe,Mn,Si)13 structures, Addit Manuf 51 (2022) 102620.

[136] J.D. Moore, D. Klemm, D. Lindackers, S. Grasemann, R. Träger, J. Eckert, L. Löber, S. Scudino, M. Katter, A. Barcza, K.P. Skokov, O. Gutfleisch, Selective laser melting of La(Fe,Co,Si)13 geometries for magnetic refrigeration, J Appl Phys 114(4) (2013) 043907.

[137] X. Miao, W. Wang, H. Liang, F. Qian, M. Cong, Y. Zhang, A. Muhammad, Z. Tian, F. Xu, Printing (Mn,Fe)2(P,Si) magnetocaloric alloys for magnetic refrigeration applications, J Mater Sci 55(15) (2020) 6660-6668.

[138] K. Navickaitė, J. Liang, C. Bahl, S. Wieland, T. Buchenau, K. Engelbrecht, Experimental characterization of active magnetic regenerators constructed using laser beam melting technique, Applied Thermal Engineering 174 (2020) 115297.

[139] J. Kagathara, S. Wieland, E. Gärtner, V. Uhlenwinkel, M. Steinbacher, Heat Treatment and Formation of Magnetocaloric 1:13 Phase in LaFe11.4Si1.2Co0.4 Processed by Laser Beam Melting, 13(3) (2020) 773.

[140] A. Deltell, A.E.-M.A. Mohamed, P. Álvarez-Alonso, M. Ipatov, J.P. Andrés, J.A. González, T. Sánchez, A. Zhukov, M.L. Escoda, J.J. Suñol, R. López Antón, Martensitic transformation, magnetic and magnetocaloric properties of Ni–Mn–Fe–Sn Heusler ribbons, Journal of Materials Research and Technology 12 (2021) 1091-1103.

[141] I. Titov, M. Acet, M. Farle, D. González-Alonso, L. Mañosa, A. Planes, T. Krenke, Hysteresis effects in the inverse magnetocaloric effect in martensitic Ni-Mn-In and Ni-Mn-Sn, 112(7) (2012) 073914.

[142] W. Sun, X. Lu, Z. Wei, Q. Li, Z. Li, Y. Zhang, J. Liu, Multicaloric effect in Ni–Mn–Sn metamagnetic shape memory alloys by laser powder bed fusion, Addit Manuf 59 (2022) 103125.

# CHAPTER 3: Experimental Methods

## 3.1 Introduction

This chapter details the test schemes, experimental methods, and techniques used within this thesis.

## 3.2 Materials

### 3.2.1 The details of powders

The $Ni_{50}Mn_{37}Sn_{13}$ alloy was prepared by in-situ alloying as seen in Fig. 3.1 of spherical gas atomised Ni powder (TLS Technik GmbH, Germany, Purity ≥ 99.5%), spherical Sn powder (Sigma-Aldrich, USA, Purity ≥ 99.8%) and irregular Mn powder (Aldrich, USA, Purity ≥ 99%),. Additional 2 at.% Mn and 1 at.% Sn powders were added to compensate for the elemental evaporation during the PBF-LB process, which was observed following initial trials. Ni, Mn, and Sn powders were blended for 48 hours. The size range of every kind of powder is below 45 µm. The mixed powders were blended for 48 h, using a tumbler mixer filled with argon to ensure uniform blending. The SEM graph of the mixed powder was shown in Fig. 3.1. The particle size distribution for all powder details is listed in Table 3.1.

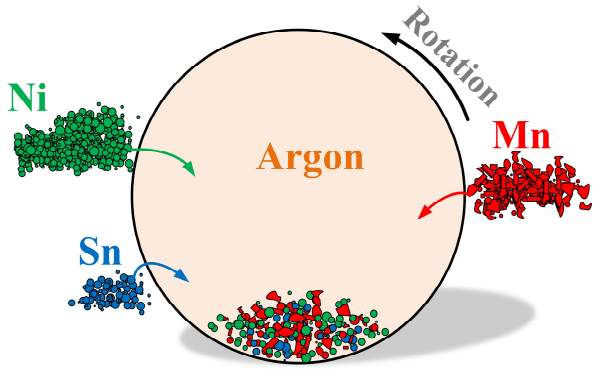



**Fig. 3.1. Schematic illustration of the powder blending process.**

**Table 3.1. Starting powders characteristics.**

| Elements | Ni | Mn | Sn |
|---|---|---|---|
| Particle size range (μm) | 20~45 | <44 | <45 |
| Shape of powder | Spherical | Cubic | Spherical |
| Melting point (℃) | 1455 | 1426 | 232 |
| Boiling point (℃) | 2913 | 2061 | 2602 |

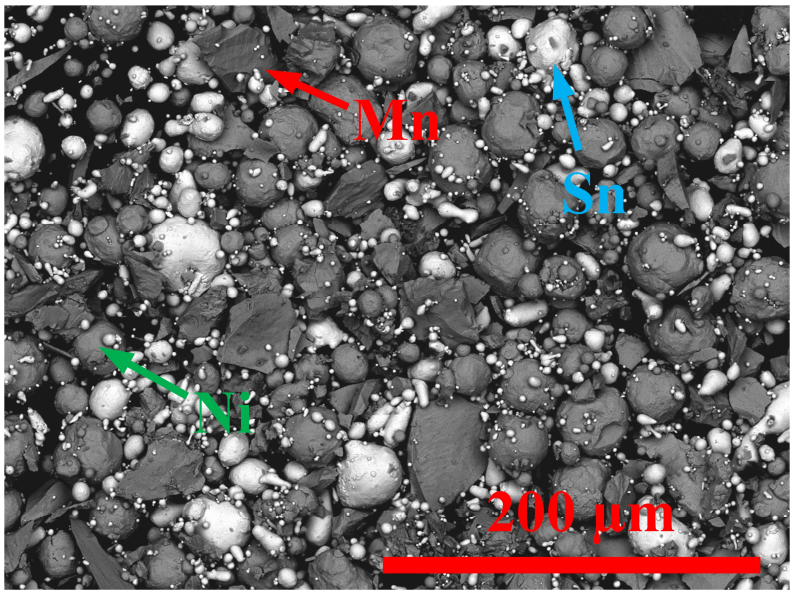



**Fig. 3.2. The mixed Ni, Mn, and Sn powders.**

The gas-atomised $LaCe(Fe,Mn,Si)_{13}$ pre-alloyed powders were provided by Erasteal. As shown in Fig. 3.3, the morphology of the pre-alloy powder was spherical and irregular-shaped particles with satellites. The powder was sieved to a 63 μm mesh.

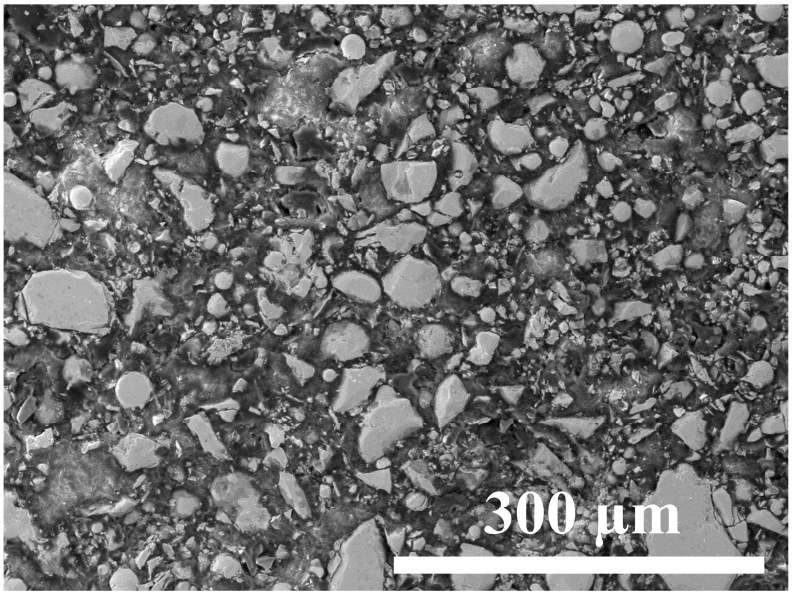



**Fig. 3.3. The microstructure of pre-alloy powder.**

### 3.2.2 As-received powder particle size distribution measurement

Particle size distribution measurements of the Ni, Mn, and Sn powders were conducted with a HELOS laser diffractometer (Sympatec Inc., Clausthal-Zellerfeld, Germany). The particle size distribution result can be found in Chapter 4. A small amount of powder was fed in a phial followed by mixing of a drop of dispersed chemical $Na_4P_2O_7$ and deionised water. Measurements were conducted with the laser diffractometer set to 50% maximum stirrer speed and 80% maximum pump speed (the details of laser diffraction are described in [1]).

### 3.2.3 Chemical composition analysis

The powder's chemical composition and PBF-LBed parts were analysed externally (AMG ANALYTICAL). X-ray fluoresce (XRF) determined the chemical composition of Ce and La, inductively coupled plasma (ICP) for Ni, Sn, Fe, Mn, Si, and Lab Equipment Corporation (LECO) for Oxygen and Hydrogen.

## 3.3 Laser powder bed fusion (PBF-LB)

### 3.3.1 Machine set-up

All specimens were fabricated using the Concept Laser M2 Laser Powder Bed machine that utilises a continuous wave mode Yb-fibre laser ($\lambda \approx 67$ µm, maximum Pavg=400 W) as the primary heat source for melting. A hopper metering mechanism was used to deposit mixed powder before a wiper blade that spread the powder on the substrate to form a thin, uniform layer. The NiMnSn HA and $LaCe(Fe,Mn,Si)_{13}$ specimens were built layer by layer on an stainless steel substrate. Fig. 3.4 shows the Concept Laser M2 powder bed machine, located at the University of Birmingham, which was used to produce PBF-LBed NiMn-based HA and $LaCe(Fe,Mn,Si)_{13}$ samples. The device was made up of three parts: the handling chamber (I), the processing chamber (II), and the user interface (III). During the handling and processing, protective gas (Argon) was filled into the handling chamber (I) and the processing chamber (II), and keep the oxygen content below 1000 ppm before the introduction of powder. Fig. 3.5 shows the simple experimental flow chart.




**Fig. 3.4. Photographs showing the main features of the 'Concept Laser M2 Laser Powder Bed'.**

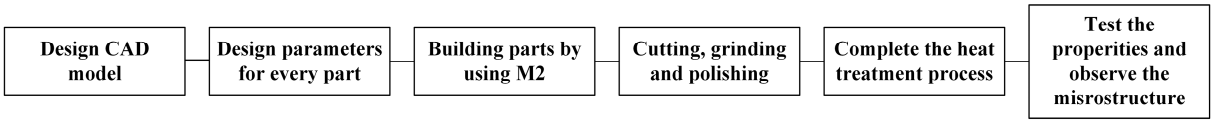



**Fig. 3.5. Experimental flow chart.**

The build platform is lowered after scanning the deposited power layer. The powder platform is raised after the scan is completed and fresh powder is spread across the build platform with the assistance of a recoater blade. A powder overflow reservoir is used to store excess powder. The detailed processing procedure is reviewed in Chapter 2.

Three designs were optimised for NiMnSn alloy, 5×5×10 mm blocks, body-centred cubic (BCC) strut-based lattice structure and cylinders with microchannels (MC cylinders) using a fixed layer thickness of 30 µm (see Fig. 3.6). Among the parameters in the PBF-LB process, adequate laser power (P), the laser scan speed (V), the laser scan spacing or hatch distance (h), and the layer thickness (d) are the most important in controlling the build integrity [2]. Different scanning strategies were used, as shown in Fig. 3.7. The island in the island and chess scan strategy was 3×3 mm.

The 10×10×10 mm $LaCe(Fe,Mn,Si)_{13}$ blocks were also fabricated. A chess scan strategy was used with a 30 µm layer thickness. The island in the chess scan strategy was 5×5 mm, which was scanned in a random order, with a rotation of 90° within each layer. There was a 1 mm by 1 mm shift between each successive layer in both the X and Y directions. During the PBF-LB process, the volumetric energy density ($E_V$) and linear energy density ($E_L$) using the critical process parameters, as given by Eq. 3.1 and Eq. 3.2 [3]:

$$E_v = \frac{P}{V \cdot h \cdot d} \tag{3.1}$$

$$E_L = \frac{P}{V} \tag{3.2}$$

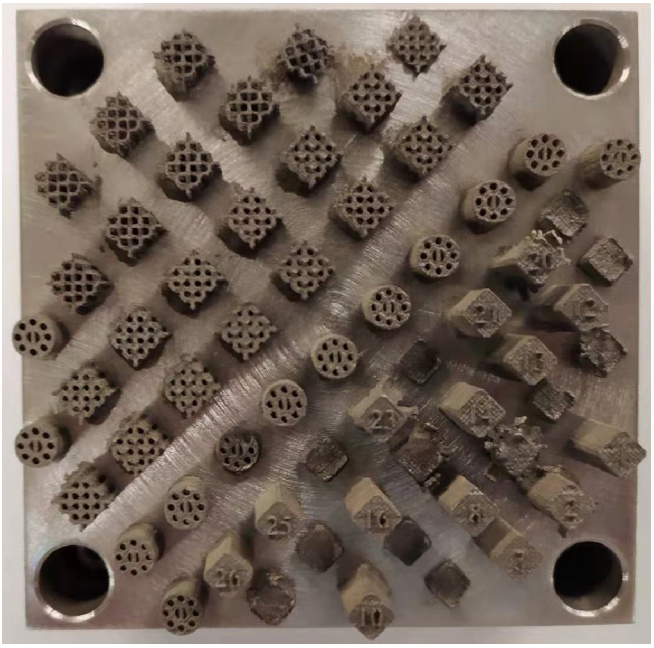


**Fig. 3.6. PBF-LBed NiMnSn blocks, lattices, and microchannel cylinders.**

## 3.3.2 PBF-LB Parameters and scanning strategy

The applied PBF-LB parameters were shown in Chapters 4-7. The different scan strategies are shown in Fig. 3.7, such as the 90° raster scan strategy, Island, and Chess scan. The layer thickness is 30 µm. Each powder layer is 30 µm, and each layer was melted randomly.

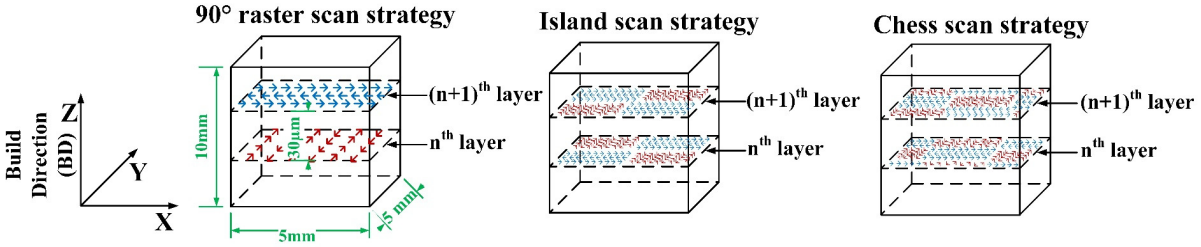



**Fig. 3.7. A schematic illustration shows the three scanning strategies for building block samples in this study.**

## 3.4 The post-processing treatment

Thermal processes were used to enhance the property of PBF-LBed parts. It is primarily heat treatment processes to form the desired microstructures, relieve residual stresses, and improve MCE properties [4].

The PBF-LBed NiMnSn samples were encapsulated in argon-filled quartz ampules and heat-treated (HT) in a LJD 1500 °C furnace (see Fig. 3.8 a) at 1123 K for different times (168 h, 336 h, and 504 h) before water quenching. The PBF-LBed $LaCe(Fe,Mn,Si)_{13}$ specimens were encapsulated in Argon-filled quartz ampules and heat-treated held at 1323 K for 168 hours before water quenching. To remove the specimens' Oxygen content, all heat-treated specimens went through another heat-treatment process in a hydrogen atmosphere. All specimens were heated at 673 K for 5.5 hours in a tube furnace (both heating and cooling rate is 10 K/min, see Fig. 3.8 b), which was filled with hydrogen gas with one-bar pressure (1 MPa).

The HIPing is useless for closing the cracks in the PBF-LB NiMnSn alloys and $LaCe(Fe,Mn,Si)_{13}$ because cracks in the sample are in contact with the surroundings.




**Fig. 3.8. (a) The LJD 1500 °C furnace, and (b) the tube furnace is filled with hydrogen gas.**

## 3.5 Microstructural characterisation

### 3.5.1 Metallurgical samples preparation

**Electrical discharge machining cutting:**

Electrical discharge machining (EDM) was used to section metallurgical samples, as shown in Fig. 3.9. Firstly, samples and the substrate were divided by using EDM. Then, the samples were sectioned in the middle of the Y direction longitudinally to the build direction. The purple-shaded plane represents the cutting surface. The cutting process is shown in Fig. 3.10. The cutting voltage is 70~90 V; the cutting current is 2~3 A; the cutting speed is 1mm/min.




**Fig. 3.9. The electrical discharge machining (EDM).**

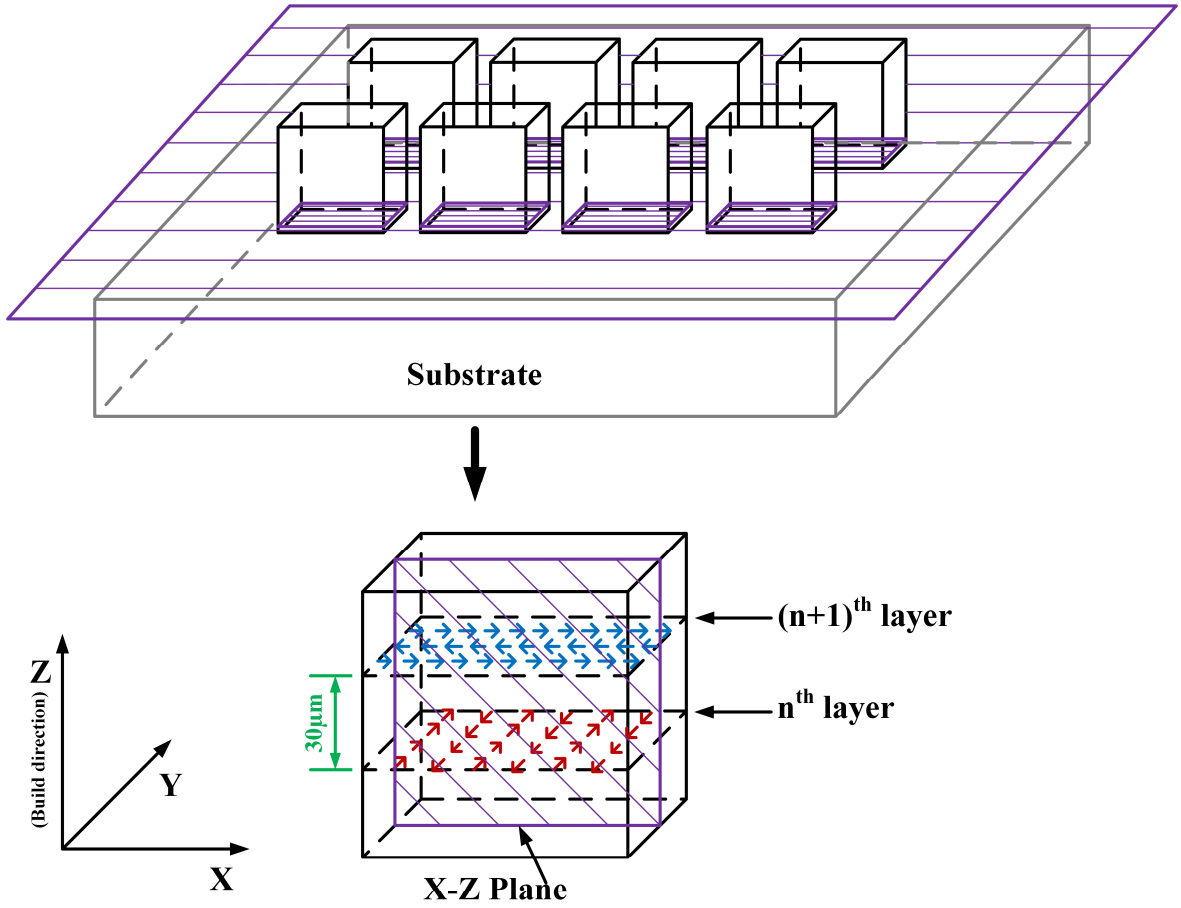



**Fig. 3.10. The whole cutting process.**

**Density measurement:**

The density of PBF-LB specimens was evaluated using the Archimedes method (Density of Object = Mass of Object / Volume of Fluid Displaced) [5]. Through the derivation and transformation of the formula for calculating buoyancy and density to form an equation, the weight of the sample to be tested in air (W1) and the weight in Alcohol (W2) are first calculated separately using a high-precision solids analysis balance, and the value of W1-W2 is calculated. The density of Alcohol is $\rho_{Alcohol}$, and by establishing the equation through the volume of sample = the volume of drainage, the density value of the sample can be calculated:

$$\rho=W1 \cdot \rho_{Alcohol} /(W1-W2) \quad (3.3)$$

The density testing equipment is shown in Fig. 3.11.

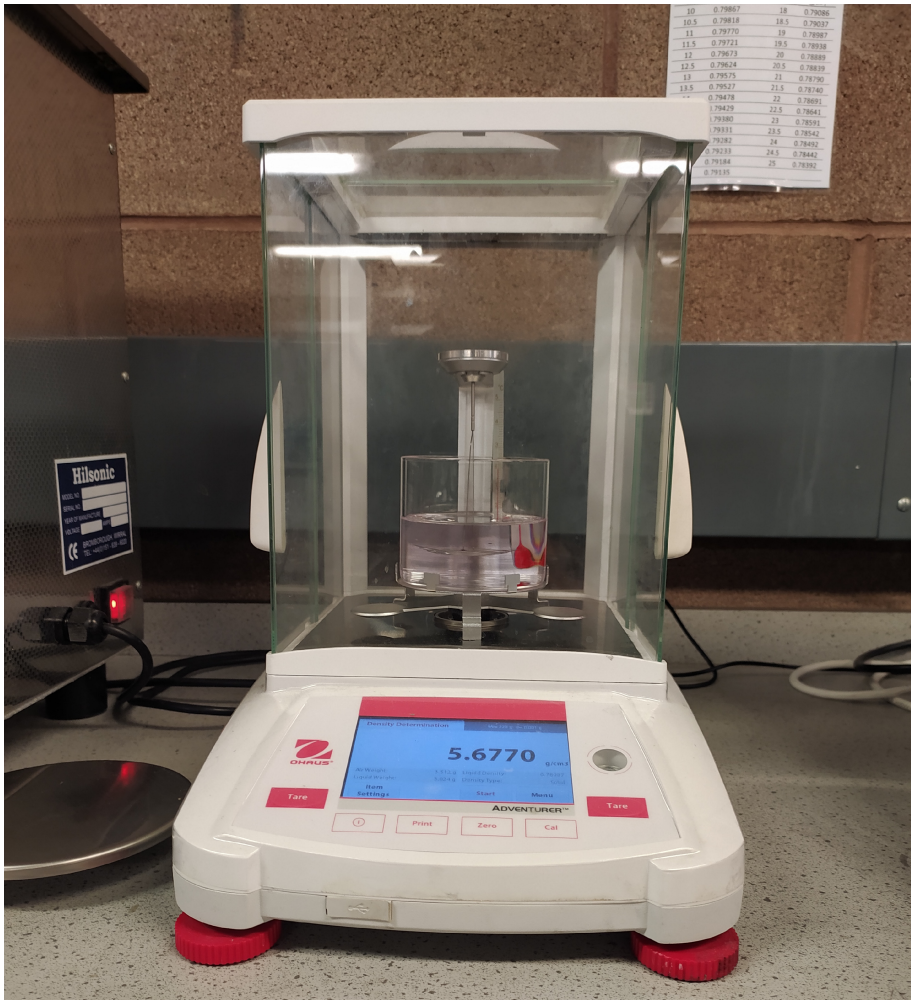



**Fig. 3.11. Density testing equipment.**

**Metallographic preparation:**

The as-fabricated NiMnSn specimens were sectioned for microstructural characterisation. For scanning electron microscopy (SEM) and optical microscopy (OM) observations, the specimens were sequentially grounded with 220 (3 min), 1200 (5 min) and 4000 (5 min) MD-Piano and polished by MD-Chem with OPS solution supplied by Struers, Denmark (30 min) by using the Struers-Tegramin grinding and polishing machines (see Fig. 3.12). The force for grinding and polishing is 5 N.

The as-fabricated $LaCe(Fe,Mn,Si)_{13}$ specimens were sequentially grounded with 220 (3 min), 1200 (5 min) and 4000 (5 min) MD-Piano and polished by MD-Chem with OPS solution supplied by Struers, Denmark (30 min). The Struers-Tegramin grinding and polishing machines (see Fig. 3.12) were used to grind and polish specimens. The force for grinding and polishing is 5 N. Once finish the grinding or polishing, the specimens should be immersed in the Acetone solution to prevent oxidation.

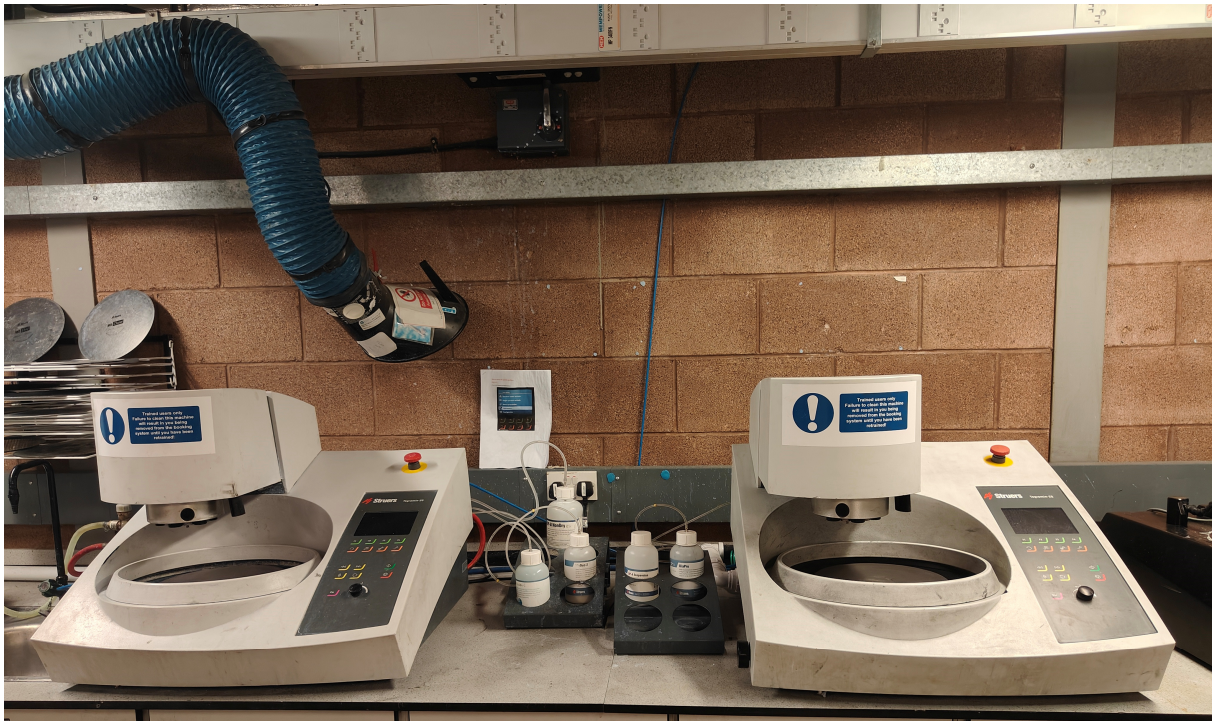


**Fig. 3.12. Struers-Tegramin grinding and polishing machines.**

## 3.5.2 Scanning electron microscopy (SEM)

Fig. 3.13 shows the schematic diagrams for SEM. SEMs use electron beams to form images, but secondary electrons are collected by a detector after they are released from a specimen's surface. Specimens with raised areas release more electrons, while those with sunken areas collect fewer electrons. A 3D image of the specimen's external features is generated by scanning an electron beam over its surface [6]. The basic operation of obtaining an electron backscatter

diffraction pattern in a scanning electron microscope is simple. The sample is tilted at a high angle concerning the incident electron beam so that the backscattered (i.e. diffracted) signal Electron Backscattered Diffraction (EBSD) is sufficiently intensified to be picked up by a fluorescent screen (in the microscope sample chamber), which is connected to a CCD camera and the EBSD can be observed on the fluorescent screen either directly or by magnifying and storing the image. With minimal input, the software programme calibrates the pattern to obtain crystallographic information [7].

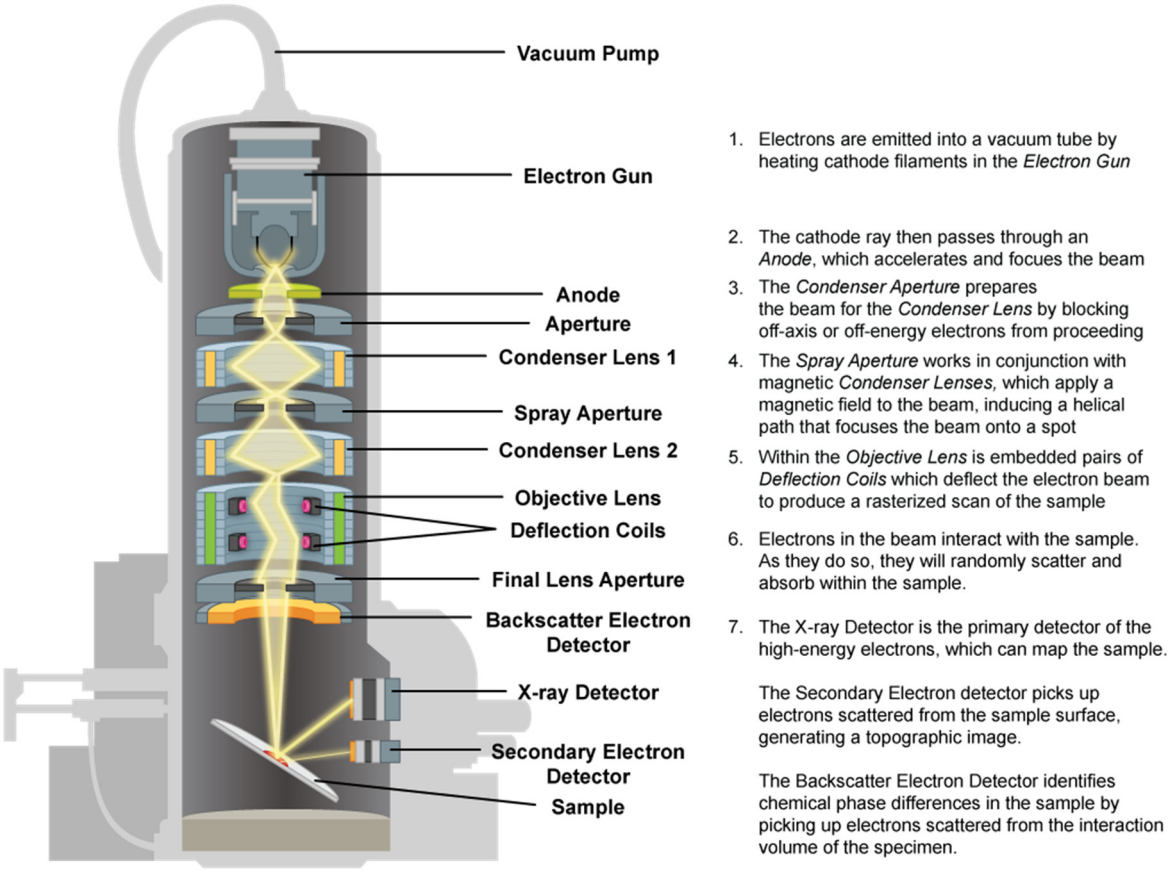



**Fig. 3.13. Schematic diagrams for SEM [6].**

SEM with Energy Dispersive X-Ray Spectroscopy (EDX), Backscattered Electrons (BSE) and Electron Backscattered Diffraction (EBSD) was used to study the powder, the characterisation

of defects, microstructure, grain structure, and chemical composition. All SEMs used in this thesis are shown in Fig. 3.14, Fig. 3.15, and Fig. 3.16.

i. The powder observation

The Hitachi TM3000 SEM with EDX assessed the powder morphology and chemical composition.

ii. Characterisation of defects

The samples were polished before using SEM. The Hitachi TM3000 SEM, and Jeol 7000 SEM fitted with backscattered electrons (BSE) were used to characterise the defects (pores and cracks) in polished samples. Image analysis was used to quantify various features, such as crack density, porosity, and defect fraction, by observing SEM micrographs. Image analysis using Image J software was used to quantify the defects fraction (defects area/area, %) and cracking density (sum of cracks length/total image area, 1/mm) [8]. The Micro-Computed Tomography (micro-CT) is an X-ray transmission image technique, which is very helpful to observe the defects in the PBF-LBed samples. But this machine is temporarily unaviable for us to use.

iii. Microstructure, grain structure, and Chemical composition

A SEM (Quanta 3D FEG) with electron backscatter diffraction (EBSD, the step size is 1.5 μm) and Energy-dispersive X-ray Spectroscopy system analysed the microstructural structure and the chemical composition of NiMnSn alloys. The SEM (Jeol 7000F) with electron backscatter diffraction (EBSD, the step size is 1.5 μm) and energy-dispersive X-ray spectroscopy system analysed the microstructural structure and the chemical composition of $LaCe(Fe,Mn,Si)_{13}$. The EBSD results shows the SEM image quality maps, inverse pole figure (IPF) map, and kernel-averaged misorientation (KAM) map.

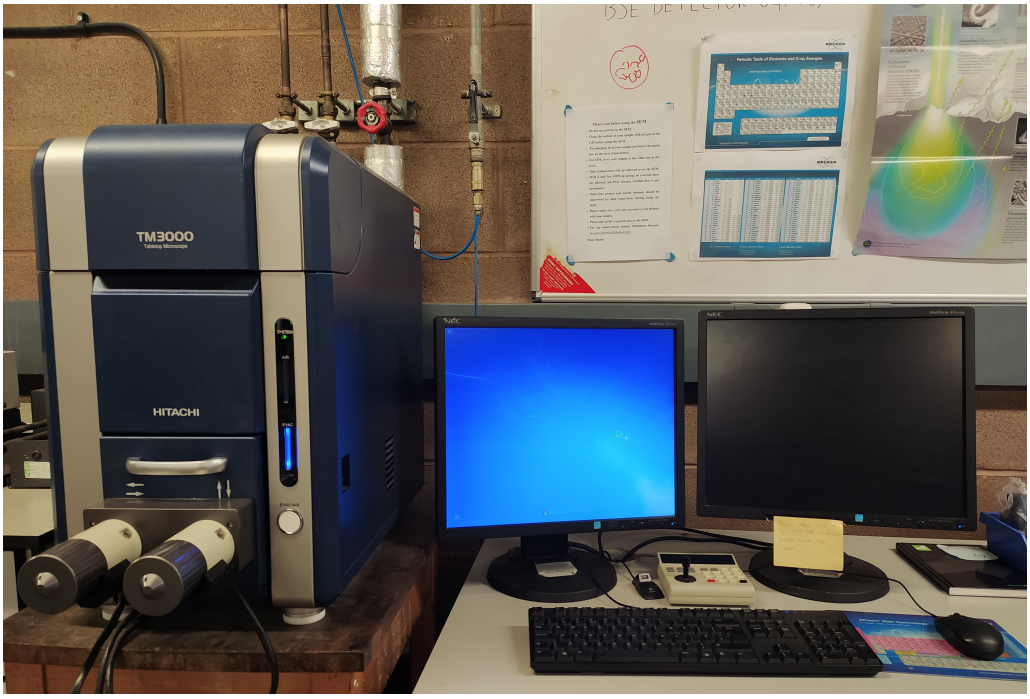



**Fig. 3.14. The Hitachi TM3000 SEM.**

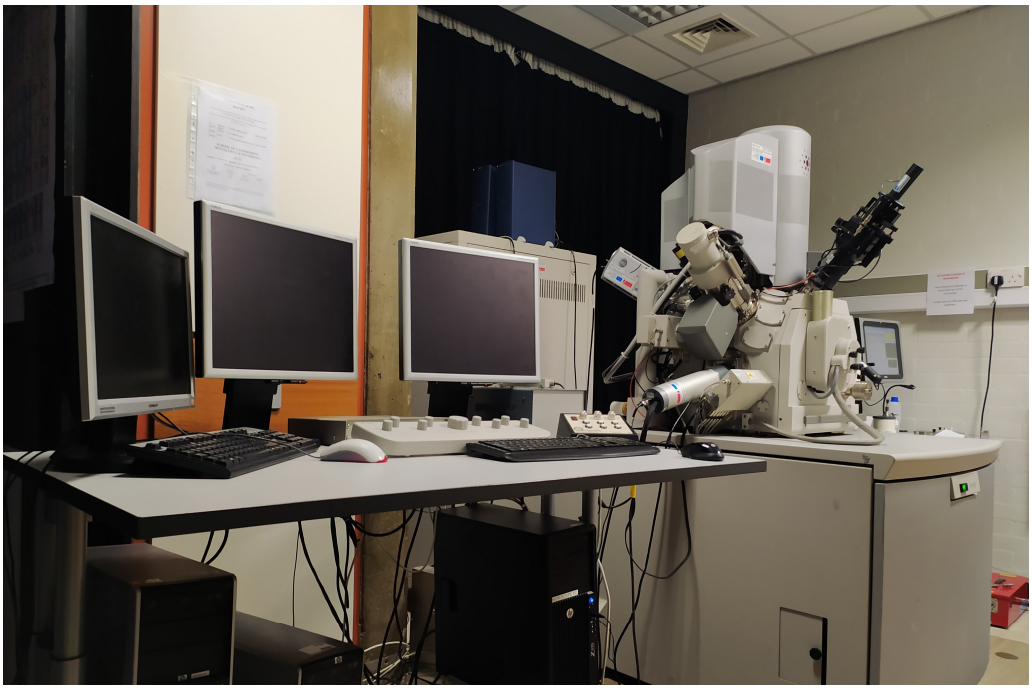


**Fig. 3.15. The FEI FIB Quanta 3D SEM.**

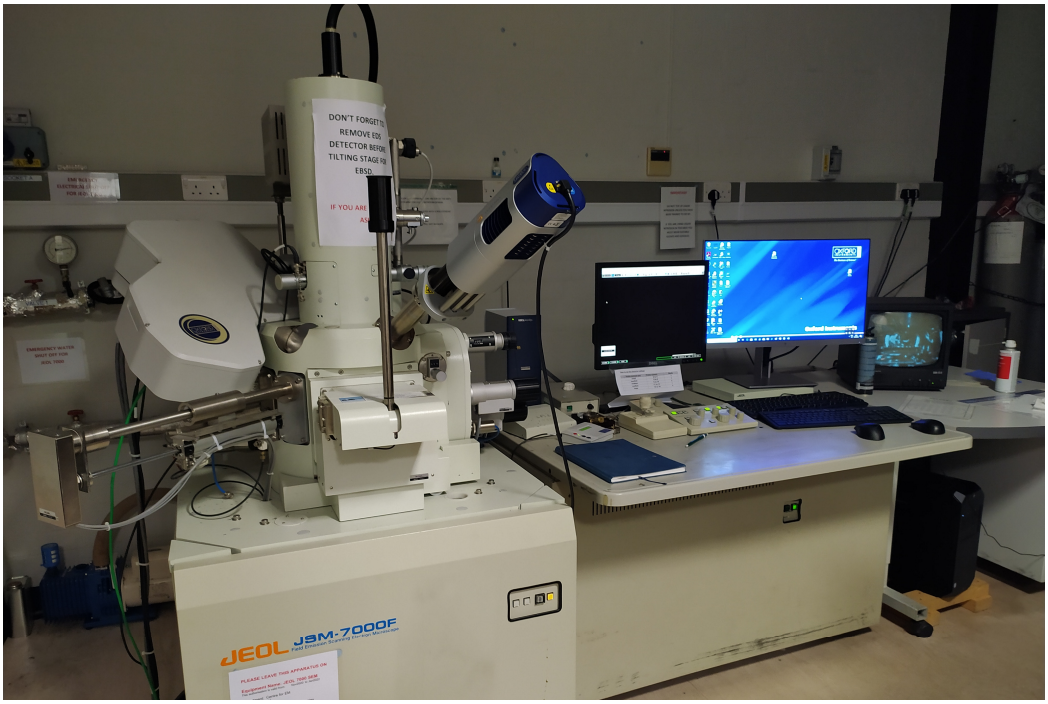



**Fig. 3.16. The Jeol 7000 SEM.**

## 3.5.3 X-Ray Diffraction (XRD)

Fig. 3.17 presents the schematic representation for the XRD measurement. When X-rays interact with matter, they are generally divided into three parts: one part is scattered, one part is absorbed and one part continues to travel in the original direction through the matter. Diffraction occurs when the scattered X-rays are of the same wavelength as the incident X-rays, i.e. when the difference in the optical range produced by the crystal plane spacing is equal to an integer multiple of the wavelength. By comparing the diffraction pattern specific to each crystalline substance with a standard diffraction pattern and using the principle of three strong peaks, the phases present in the sample can be identified [9].

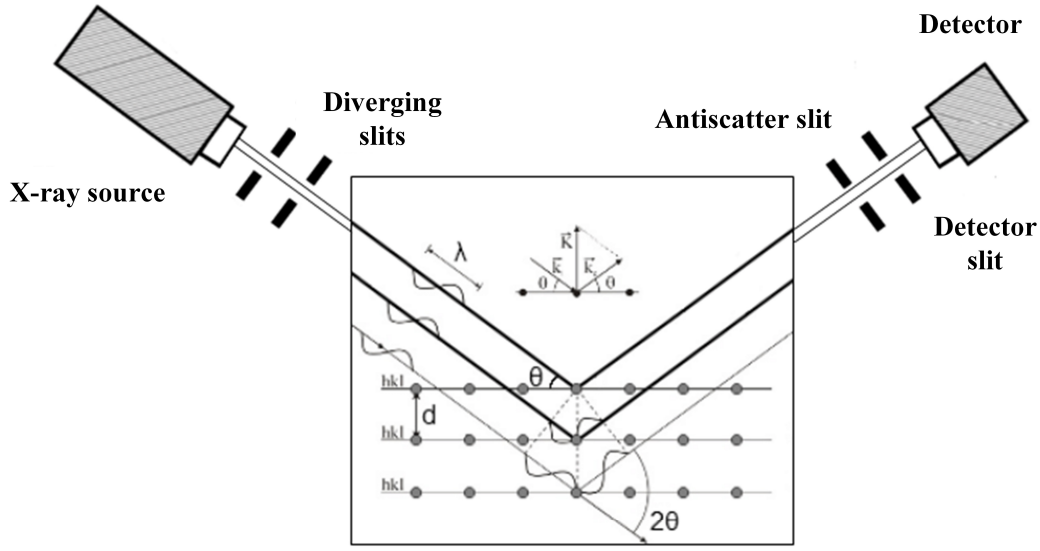



**Fig. 3.17. The schematic representation for the XRD measurement [9].**

The XRD measurements were performed on the X-Z cross-sections for microstructural specimens. A Proto AXRD with Cu Kα radiation (λ = 1.5406 Å) (see Fig. 3.18) was used for tests at room temperature. The XRD test angle are from 30° to 90°and from 20° to 100° for NiMnSn alloys and $LaCe(Fe,Mn,Si)_{13}$ alloys respectively. A Panalytical Empyrean instrument with Mo Kα radiation (λ = 0.7093 Å) for tests at low temperature (100 K, 200 K, and 295 K). The XRD test angle at low temperature is from 30° to 60° for NiMnSn alloys. For comparison, all XRD results with Mo Kα radiation were converted to Cu Kα radiation using Bragg's Law.

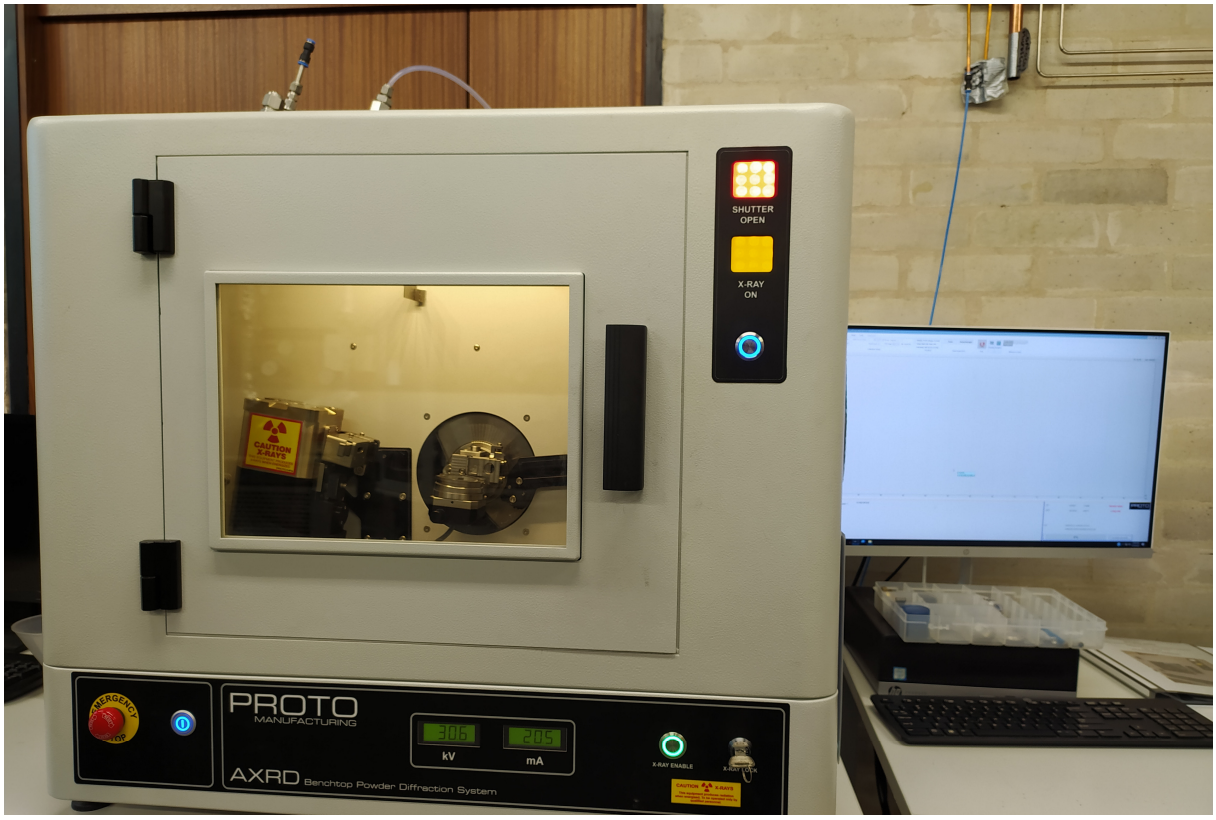



**Fig. 3.18. The Proto AXRD.**

## 3.5.4 Transmission electron microscopy (TEM)

Fig. 3.19 presents the schematic diagrams for TEM. The transmission electron microscope utilizes an electron beam directed at the specimen with the use of electromagnets. An electron beam of a certain energy interacts with the sample and produces a variety of information reflecting the thickness of the sample microregion, the average atomic number, the crystal structure or differences in orientation. The intensity of the electron beam passing through the sample (depending on the above information) is focused and magnified by the objective lens to form a transmission electron image in its image plane reflecting this information, which is further magnified by the intermediate and projection mirrors to give a three-stage magnified final electron image on the fluorescent screen [6].

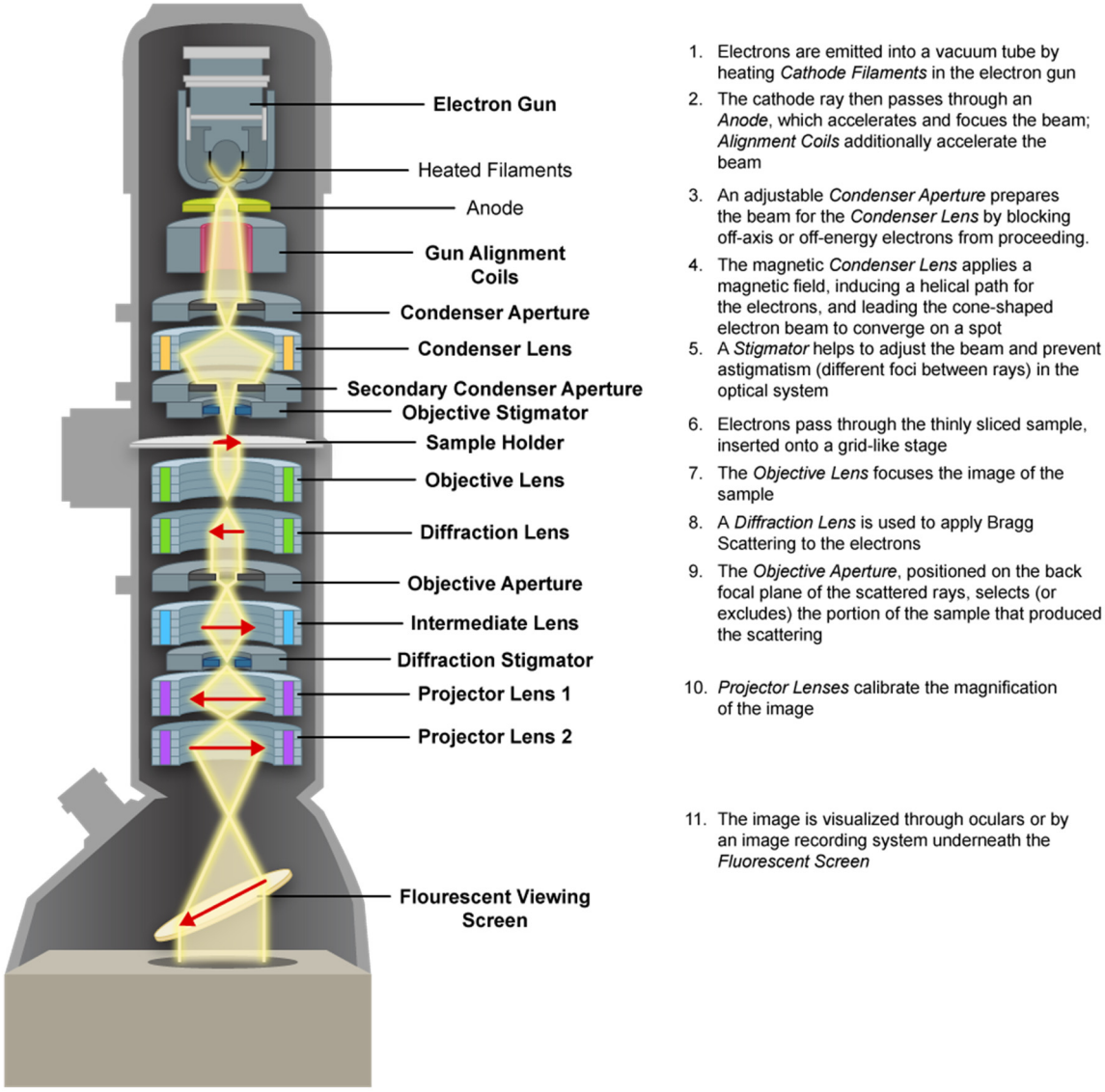



**Fig. 3.19. Schematic diagrams for TEM [6].**

The microstructure was investigated using a transmission electron microscope (TEM; Tecnai F20) operated at 300 kV. The high-angle annular dark-field scanning TEM imaging and EDX mapping were also performed. The Tecnai F20 TEM is shown in Fig. 3.20. The TEM samples were prepared using focus ion beam (FEI FIB Quanta 3D SEM) milling.

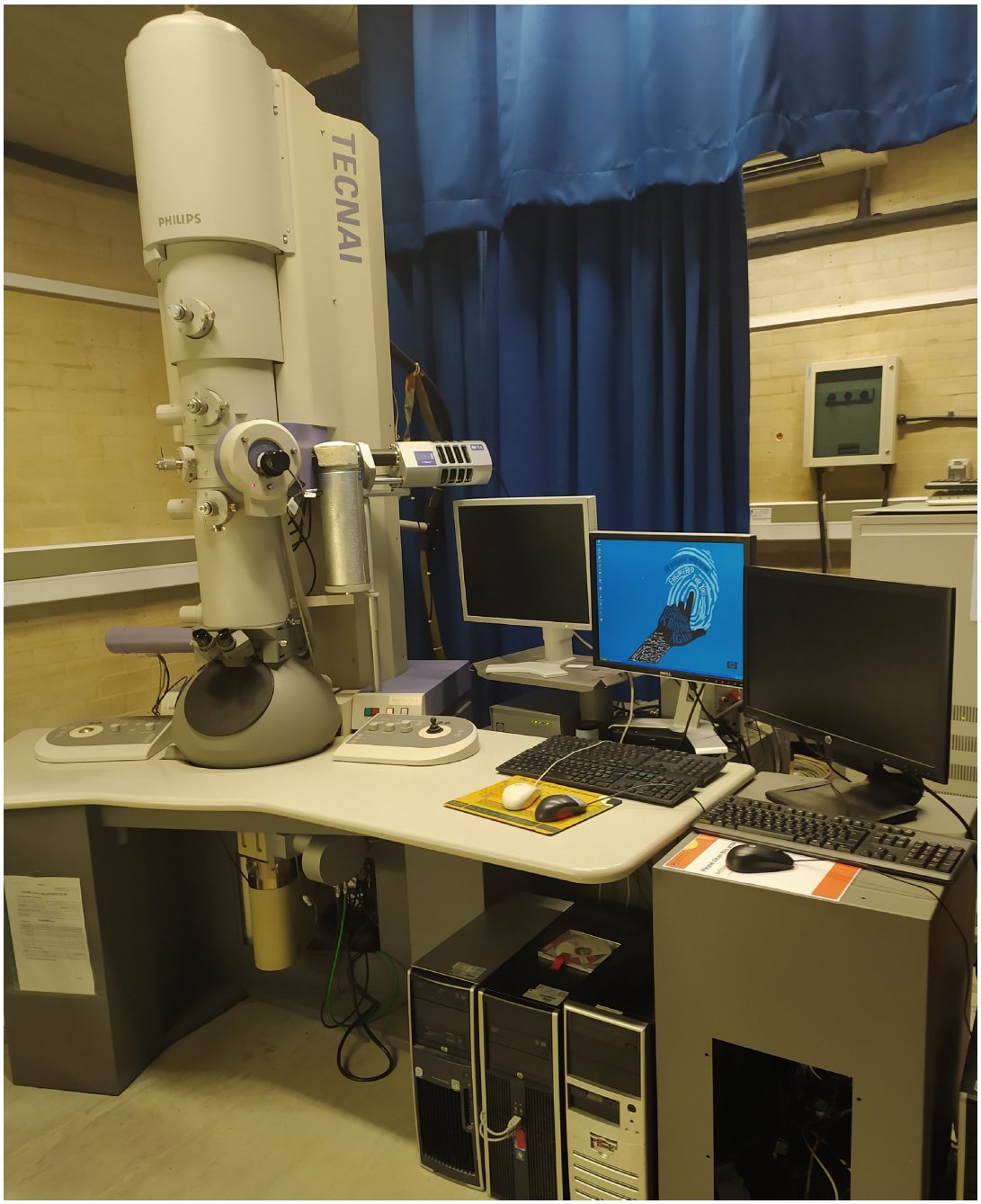



**Fig. 3.20. Tecnai F20 TEM.**

## 3.6 Superconducting quantum interference device (SQUID) Magnetic property measurement system (MPMS)

Magnetic measurements were performed using a Quantum Design Magnetic Property Measurement System (MPMS, see Fig. 3.21). All test samples were extracted from the centre of the blocks.

The measurement of thermo-magnetisation curves gives a characteristic temperature for the transformation of a material because the magnetic change or structural transformation of a material is usually accompanied by a change in magnetic or magneto-thermal properties. By measuring the thermo-magnetisation curves of a material in the presence of an applied magnetic field, a characteristic signal associated with the magnetic change or structural transformation can be observed [10, 11]. The lower applied magnetic field can obtain more accurate results. In thermo-magnetisation curve measurements, the magneto-thermal behaviour of a material at different temperatures is typically recorded with temperature as the horizontal coordinate and magneto-thermal effects (e.g. changes in magnetisation intensity or magnetisation) as the vertical coordinate. When a material undergoes a magnetic change or structural transition, the magnetisation usually changes abruptly or significantly, creating a distinct peak or jump, called the magneto-thermal peak [12, 13]. The appearance of this magneto-thermal peak is associated with changes in the magnetic state or microstructure within the material [12, 13]. When a material undergoes a magnetic change or structural transition at a specific temperature, its magneto-thermal properties change dramatically, leading to the appearance of a magneto-thermal peak. This specific temperature is the transition characteristic temperature of the material. Measuring thermo-magnetisation curves can help to determine the characteristic

transition temperature of a material and thus to study and understand the phase transition behaviour, magnetic transformation and MCE of the material.

Measuring isothermal magnetisation curves does not provide direct information on the magnitude of the adiabatic magnetic entropy change. The relationship between the isothermal magnetisation curve and the adiabatic magnetic entropy change is established by using the basic principles of magneto thermodynamics and some additional assumptions. In magneto thermodynamics, the calculation of the magnetic entropy change is usually based on the integration of an isothermal magnetisation curve [14], see Eq. 3.2 [15]. However, such calculations usually need to satisfy many assumptions, such as that the magnetisation process is reversible and adiabatic.

For NiMnSn alloys, the zero-field cooled heating thermo-magnetisation data were collected under 0.01 T within the temperature range of 2 K to 380 K. The isothermal magnetisation curves were measured every 5 K (field up from 0 to 1 T, then back to 0 T). To observe the phase transformation of $LaCe(Fe,Mn,Si)_{13}$, the magnetisation vs. temperature curves under an applied field of 0.01 Tesla (T) was measured within a temperature range between 100 and 350 K. The isothermal magnetisation curves were tested from 280 to 319 K under the external magnetic field of 0-1 T. The temperature step is 3 K. The magnetic entropy change ($\Delta S$) was calculated from the isothermal magnetisation curves M(H) using Maxwell's relation (Eq. 3.4) [15]. The change in the applied magnetic field is represented by $\Delta H$ ($\Delta H = H_F - H_I$, $H_F$: the final magnetic field; $H_I$: the initial magnetic field). Matlab and Origin software was used to do the statistical treatments.

$$\Delta S = \int_{H_I}^{H_F} \left(\frac{\partial M}{\partial T}\right)_H dH \tag{3.4}$$

When it comes to second-order magnetic phase transitions, you can obtain valuable information from the Arrott plot, which consists in plotting H/M against $M^2$, with H the applied magnetic field and M the magnetization. First-order magnetic transitions are generally characterized by a negative slope in the Arrott plot. This is known as the Banerjee criterion [16]. To determine the nature of each magnetic transition, the induced Arrott plots were employed. Where the positive and negative slope of Arrott plots around the transition temperature indicates SOPT and FOPT, respectively [17].

A method for quantifying thermomagnetic phase transition order by using the magnetocaloric effect in a field-dependent manner was reported [10]. In Eq. 3.5, **a** is a constant and the magnetic state of the sample determines **n** power [18]. The ΔS dependence on the magnetic field (see Eq. 3.6) confirmed the nature of the magnetic transition [19].

$$\Delta S = \mathbf{a}(\mu_0 H)^{\mathbf{n}} \tag{3.5}$$

For samples with FOPT, $\Delta S_m$ depends on the field with exponent $\mathbf{n} > 2$. The value of the **n** constant is below 2, which is the case of SOPT around the transition temperature [10, 20].

$$\Delta S \alpha H^{\mathbf{n}} \tag{3.6}$$

Matlab, Origin and Excel software were used to do the calculation about the magnetic properties.




**Fig. 3.21. Quantum Design magnetic properties measurements system (MPMS).**

## 3.7 References

[1] F. Thümmler, R. Oberacker, An introduction to powder metallurgy, Institute of Materials London1993.

[2] F. Nilsén, I.F. Ituarte, M. Salmi, J. Partanen, S.-P. Hannula, Effect of process parameters on non-modulated Ni-Mn-Ga alloy manufactured using powder bed fusion, Addit Manuf 28 (2019) 464-474.

[3] K.G. Prashanth, S. Scudino, T. Maity, J. Das, J. Eckert, Is the energy density a reliable parameter for materials synthesis by selective laser melting?, Materials Research Letters 5(6) (2017) 386-390.

[4] I. Gibson, D.W. Rosen, B. Stucker, Post-Processing, in: I. Gibson, D.W. Rosen, B. Stucker (Eds.), Additive Manufacturing Technologies: Rapid Prototyping to Direct Digital Manufacturing, Springer US, Boston, MA, 2010, pp. 415-435.

[5] Standard Test Methods for Density of Compacted or Sintered Powder Metallurgy(PM) Products Using Archimedes, Principle, ASTM B962 e 17.

[6] L. Bruslind, General microbiology, Oregon State University2020.

[7] R.A. Schwarzer, J. Hjelen, Backscattered Electron Imaging with an EBSD Detector, Microscopy Today 23(1) (2015) 12-17.

[8] C.A. Schneider, W.S. Rasband, K.W. Eliceiri, NIH Image to ImageJ: 25 years of image analysis, Nature Methods 9(7) (2012) 671-675.

[9] C. Charpentier, Investigation of deposition conditions and annealing treatments on sputtered ZnO:Al thin films: Material properties and application to microcristalline silicon solar cells, Ecole Polytechnique X, 2012.

[10] J.Y. Law, V. Franco, L.M. Moreno-Ramírez, A. Conde, D.Y. Karpenkov, I. Radulov, K.P. Skokov, O. Gutfleisch, A quantitative criterion for determining the order of magnetic phase transitions using the magnetocaloric effect, Nature Communications 9(1) (2018) 2680.

[11] R.Z. Levitin, V.V. Snegirev, A.V. Kopylov, A.S. Lagutin, A. Gerber, Magnetic method of magnetocaloric effect determination in high pulsed magnetic fields, J Magn Magn Mater 170(1) (1997) 223-227.

[12] N.P. Grazhdankina, MAGNETIC FIRST ORDER PHASE TRANSITIONS, Soviet Physics Uspekhi 11(5) (1969) 727.

[13] O. Tegus, E. Brück, L. Zhang, Dagula, K.H.J. Buschow, F.R. de Boer, Magnetic-phase transitions and magnetocaloric effects, Physica B: Condensed Matter 319(1) (2002) 174-192.

[14] A.M. Tishin, Magnetocaloric effect in strong magnetic fields, Cryogenics 30(2) (1990) 127-136.

[15] V. Chaudhary, X. Chen, R.V. Ramanujan, Iron and manganese based magnetocaloric materials for near room temperature thermal management, Prog Mater Sci 100 (2019) 64-98.

[16] S. Bustingorry, F. Pomiro, G. Aurelio, J. Curiale, Second-order magnetic critical points at finite magnetic fields: Revisiting Arrott plots, Phys Rev B 93(22) (2016) 224429.

[17] B.J.P.l. Banerjee, On a generalised approach to first and second order magnetic transitions, 12(1) (1964) 16-17.

[18] A.E.-M.A. Mohamed, V. Vega, M. Ipatov, A.M. Ahmed, B. Hernando, Annealing temperature effect on magnetic and magnetocaloric properties of manganites, J Alloy Compd 665 (2016) 394-403.

[19] T.D. Shen, R.B. Schwarz, J.Y. Coulter, J.D. Thompson, Magnetocaloric effect in bulk amorphous Pd40Ni22.5Fe17.5P20 alloy, J Appl Phys 91(8) (2002) 5240-5245.

[20] C.F.J.I.d.I.y.T. Sánchez Valdés, Large magnetic entropy change and refrigeration capacity around room temperature in quinary Ni41Co9-xFexMn40Sn10 alloys (x= 2.0 and 2.5), (2020).

# CHAPTER 4: Laser Powder Bed Fusion of the NiMnSn Heusler Alloy for Magnetic Refrigeration Applications

## 4.1 Abstract

This study aims to develop a manufacturing route for a low-cost dense magnetocaloric NiMnSn Heusler alloy (HA) using laser powder bed fusion (PBF-LB) additive manufacturing technique by in-situ alloying from its elemental constituents. PBF-LB enables the production of high surface-area-to-volume 3D-printed components to increase heat transfer efficiency in magnetic refrigerators. A laser parametric study was performed on blocks, lattices and micro-channelled cylinders for maximum densification. The highest density was observed in the samples with laser energy density ($E_V$) of 18.52 J/mm$^3$, 53.33 J/mm$^3$ and 89.89 J/mm$^3$, where they achieved a density of 6.8 g/cm$^3$, 8.2 g/cm$^3$ and 8.3 g/cm$^3$, respectively. After heat treatment, the three samples show the $L2_1$ phase with a minor 4O orthorhombic phase and double magnetic transitions, martensite-austenite transition ($T_M$) and magnetic transition around curie temperature ($T_C^A$). The maximum magnetic entropy change ($\Delta S_m$) values of the three samples around $T_M$ are 0.53 Jkg$^{-1}$K$^{-1}$ at 160 K, 0.5 Jkg$^{-1}$K$^{-1}$ at 130 K, and 0.3 Jkg$^{-1}$K$^{-1}$ at 170 K, respectively. And $\Delta S_m$ of almost 1.0 Jkg$^{-1}$K$^{-1}$ at $T_C^A$ (~320 K) for these samples with a field change of 1 T.

*Keywords:* Laser powder bed fusion; Magnetocaloric material; Microstructure; Magnetic

properties; Heat treatment.

## 4.2 Introduction

Magnetic refrigeration is a promising environmentally friendly technology that may help address global warming and energy challenges worldwide. Compared with conventional cooling systems, magnetic refrigeration devices emit less mechanical noise and vibrations [1, 2] and theoretically achieve higher energy efficiency (60% of the Carnot cycle) [2]. Magnetic refrigeration is based on the magnetocaloric effect (MCE), which is a change in the magnetic entropy ($\Delta S$) upon applying/removing an external magnetic field, resulting in a temperature change ($\Delta T$) [1, 3], where $\Delta S$ and $\Delta T$ are being maximum around the magnetic transition temperature. The MCE has been observed in several magnetic materials. However, Gd has been reported with the highest room temperature MCE [4], but the high cost of that metal hinders its wide usage in applications. So it was essential to look for alternatives such as rare-earth-based composites and Heusler alloys, outstanding magnetocaloric with environmentally friendly effects, lower cost and adjustable magnetic transition temperature [4,5]. These magnetocaloric materials (MCMs) have been prepared via different synthesis methods, such as arc melting [5, 6] and powder metallurgy [7], …etc. The main problem of resultant samples from these traditional methods is the lack of shaping to suit a specific application, which is a challenge of being machined after fabrication due to the weak mechanical strength of these materials [8]. Additive manufacturing (AM) technology such as PBF-LB has overcome the challenge of machining by direct part production with the ability to do complex designs, where

components are designed using computer-aided design software and then built from a raw powder a layer-by-layer fusion [9]. However, the microstructure defects such as cracking and porosity cannot be avoided during the PBF-LB process, so laser parameters optimisation is needed [10-12]. PBF-LB has been used previously in 3D printing of several functional magnetic materials such as, $AlFe_2B_2$ alloy[13], CoFeNi [14-16], FeNi [17], functionally graded magnetic materials [18] and in particular MCMs such as $LaCe(Fe,Mn,Si)_{13}$ [11], $La(Fe,Co,Si)_{13}$ [8] $(Mn,Fe)_2(P,Si)$ [18]. These reported works have shown the vital role of 3D printing of MCMs in improving magnetic refrigeration efficiency. This occurred by producing parts with high surface-area-to-volume, which enhances the heat transfer between the heat source, working body and sink [19]. Controlling the heat transfer by increasing the surface area of MCMs by 3D printing was reported previously in PBF-LB, and laser beam melted LaFeSi-based alloy [8, 11, 20, 21]. They produced blocks with internal micro-wavy channels [8] and straight microchannels and lattices [11]. Despite the outstanding role of PBF-LB of MCMs, some challenges have been reported, such as the elemental evaporation that may interrupt the nominal chemical composition of the magnetic alloy, leading to a disturbance in the associated magnetic properties [11]. This challenge can be overcome by optimising laser parameters, using relatively lower laser energy densities and compensating the evaporated elements. Despite the interesting magnetic properties of LaFeSi, HAs have been reported with the same $\Delta S$ at a much lower cost, which make this category a kind of interest for applications, especially at room temperature [6,7]. HAs NiMn-X (In, Sn, …etc) show a huge MCE associated with the martensitic transition

[22]. In addition, these alloys show a conventional MCE at the austenite phase transition, which can be used as a double cooling capacity [23]. Among this category, NiMnSn shows a near-room temperature magnetic transition, which makes this alloy a kind of interest [22, 24]. Only one work has been reported in the 3D printing of NiMnSn using the PBF-LB technique [10]. This work used a pre-alloyed powder to manufacture parts with hexagonal/square/circular macro channels (3mm) that were built using PBF-LB pre-alloy NiMnSn powders, with reported magnetic properties of $\Delta S$ of 1.4 $Jkg^{-1}K^{-1}$ at 288 K and 1 T [10].

This study aims to manufacture high-performance MCE prototypes of $Ni_{50}Mn_{37}Sn_{13}$ HAs using PBF-LB in situ alloying as a low-cost approach and an alternative to the pre-alloyed powder. A series of experiments were designed to study the influence of the process parameters on the microstructure development of the in-situ alloyed NiMnSn block samples. Microchanelled cylinders and lattice strut samples were also manufactured to increase the surface-area-to-volume of the components, which can maximise heat transfer efficiency.

## 4.3 Material and methods

### 4.3.1 Powder preparation

The $Ni_{50}Mn_{37}Sn_{13}$ alloy was prepared by in-situ alloying as seen in Fig. 4.1 a of spherical gas atomised Ni powder (TLS Technik GmbH, Germany, Purity ≥ 99.5%), spherical Sn powder (Sigma-Aldrich, USA, Purity ≥ 99.8%) and irregular Mn powder (Aldrich, USA, Purity ≥ 99%), see Fig. 4.1 b. Additional 2 at.% Mn and 1 at.% Sn powders were added to compensate for the

elemental evaporation during the PBF-LB process, which was observed following initial trials. Ni, Mn, and Sn powders were blended for 48 hours. The particle size distribution for all powder is presented in Fig. 4.1 c, and details are listed in Table 4.1.

**Table 4.1. Starting raw powder characteristics.**

| Elements | Particle size range (μm) | d50 (μm) | Shape of powder | Melting point (°C) | Boiling point (°C) | Density ($g/cm^3$) |
|---|---|---|---|---|---|---|
| Ni | 20~45 | 0.38 | Spherical | 1455 | 2913 | 8.9 |
| Mn | <44 | 2.01 | Cubic | 1426 | 2061 | 7.44 |
| Sn | <45 | 0.74 | Spherical | 232 | 2602 | 6.54 |

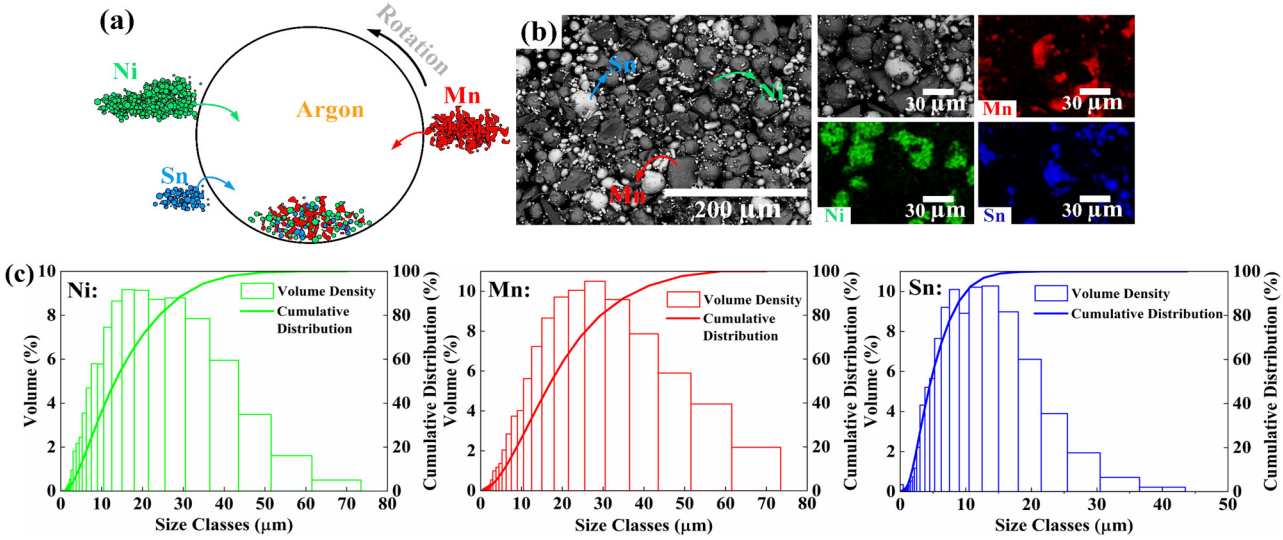



**Fig. 4.1. (a) Schematic illustration of the powder blending process, (b) Backscattered electron image and corresponding EDX elemental map of the $Ni_{50}Mn_{37}Sn_{13}$ blended powder, (c) Particle size distribution of the three powders.**

### 4.3.2 Sample fabrication and design of experiment

The as-fabricated (AF) samples were manufactured by PBF-LB technique on top of steel substrate using Concept Laser M2 machine attached with a continuous wave mode Yb-fibre laser (spot size is ≈ 67 µm, maximum power = 400 W) as the primary heat source for melting in an argon atmosphere with the oxygen content kept below 1000 ppm.

Three designs were optimised, 5×5×10 mm blocks, body-centred cubic (BCC) strut-based lattice structure and cylinders with microchannels (MC cylinders) (see Fig. 4.2 a-b) using a fixed layer thickness of 30 µm. The details of the three designs are shown in Fig. 4.2 c-d. Among the parameters in the PBF-LB process, adequate laser power (P), the laser scan speed (V), the laser scan spacing or hatch distance (h), and the layer thickness (d) are the most important in controlling the build integrity [25]. Different scanning strategies were used, as shown in Fig. 4.3. During the PBF-LB process, the volumetric energy density ($E_V$) and linear energy density ($E_L$) using the critical process parameters, as given by Eq. 4.1 and Eq. 4.2 [26]:

$$E_v = \frac{P}{V \cdot h \cdot d} \tag{4.1}$$

$$E_L = \frac{P}{V} \tag{4.2}$$

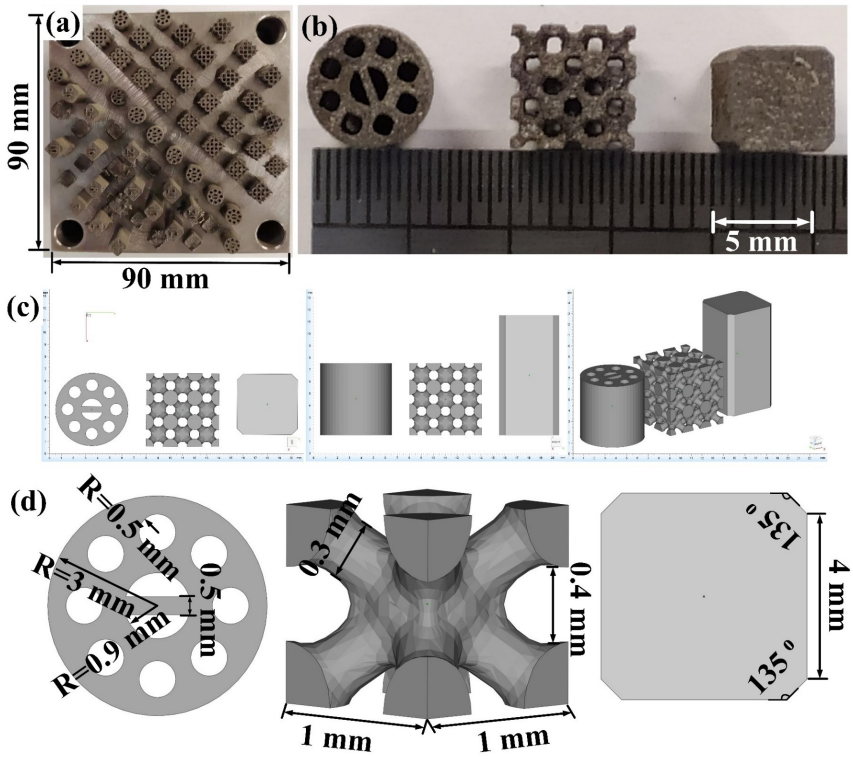



**Fig. 4.2. (a) and (b) PBF-LBed parts, (c) Geometry of blocks, lattices, and microchannel cylinders, (d) Details of three different designs.**

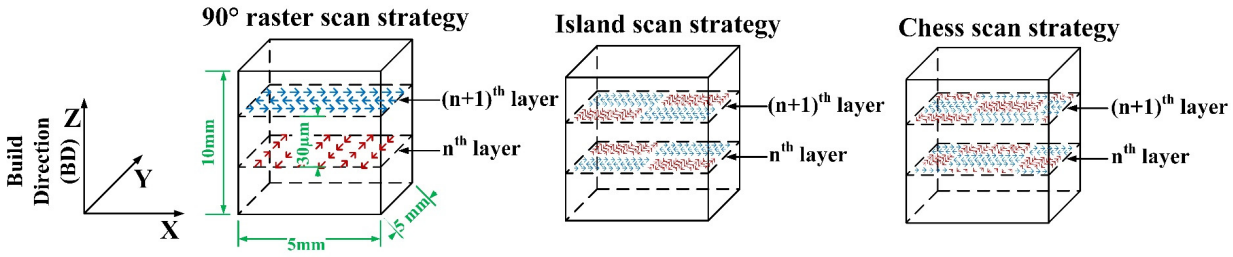



**Fig. 4.3. Three different scan strategies; 90° raster, island scan and chess scan strategies.**

The optimisation process for maximum densification was performed on blocks using the parametric combinations detailed in Table 4.2. The results of the microstructure of blocks assessed with continued scanning strategies, parameters (shown in Table 4.3) were observed to build satisfactory blocks with island and chess scanning strategies (with an island size of 3×3

mm), MC cylinders and lattices.

**Table 4.2. The investigated PBF-LB processing parameters for blocks with the 90° raster scan strategy.**

| Laser Power (W) | Scan Speed (mm/s) | Hatch Distance (mm) | Energy Density ($J/mm^3$) |
|---|---|---|---|
| 60-150 | 600-1500 | 0.03-0.09 | 18-133 |

The PBF-LB made (PBF-LBed) samples were encapsulated in argon-filled quartz ampules and heat-treated (HT) in a calibrated furnace at 1123 K for 504 hours before water quenching.

### 4.3.3 Sample preparation and analysis

The NiMnSn samples were cut from the steel substrate using Electrical discharge machine (EDM). The samples were then sectioned longitudinally to the build direction (to view the X-Z plane). The density of samples was measured using the Archimedes method in terms of ASTM B962-17 [27]. The samples were ground incrementally using SiC papers and then polished using 3 and 1 μm diamond suspensions, finishing with a 0.04 μm silica suspension. Then, Hitachi TM3030 and FEI Quanta 3D FEG Dual Beam SEM fitted with an Energy Dispersive X-ray microanalysis system (EDX) microscopes were used to analysing the microstructure of the polished samples. Image analysis using Image J software was used to quantify the defects fraction (defects area/area, %) and cracking density (sum of cracks length/total image area, 1/mm) [28]. 8 SEM images in the X-Z plane were considered for every sample at the mid-thickness of the Y-Z section. The crystal structure was examined using a Proto AXRD diffractometer X-ray diffraction (XRD) with Cu-Kα radiation (λ = 1.5406 Å) at room

temperature and using a Panalytical Empyrean XRD diffractometer with Mo-Kα radiation (λ = 0.7093 Å) for the tests at low temperature (100 K, 200 K and 295 K). For comparison, all XRD results with Mo-Kα radiation were converted to Cu Kα radiation using Bragg's Law. The chemical compositions of ten small uniform areas within the microstructure, without element segregation, of every sample, were confirmed using the FEI Quanta 3D FEG Dual Beam SEM-EDX. The average composition was then used to represent the chemical composition of all uniform areas. The chemical composition of the whole sample was determined using x-ray fluoresce (XRF) for Ni, Mn, and Sn, and combustion and non-dispersive single wavelength IR analysis for Oxygen analysis.

Magnetic measurements were performed using a Quantum Design Magnetic Property Measurement System (MPMS). All test samples were extracted from the centre of the blocks. The zero-field cooled heating (ZFCH) thermo-magnetisation data were collected under 0.01 T within the 2 K to 380 K temperature range. The isothermal magnetisation curves were measured every 5 K (field up from 0 to 1 T, then back to 0 T). The magnetic entropy change ($\Delta S$) was calculated from the isothermal magnetisation curves M(H) using Maxwell's relation (Eq. 4.3). The change in the applied magnetic field is represented by $\Delta H$ ($\Delta H = H_F - H_I$, $H_F$: the final magnetic field; $H_I$: the initial magnetic field).

$$\Delta S = \int_{H_I}^{H_F} \left(\frac{\partial M}{\partial T}\right)_H dH \tag{4.3}$$

The RCP of MCMs can be evaluated from the plots of ΔS vs T, as shown in Eq. 4.4. $\delta T_{FWHM}$ is the full width at half maximum of $\Delta S$ (T) curve [2].

$$RCP(S) = \Delta S_m \times \delta T_{FWHM} \quad (4.4)$$

**Table 4.3. The PBF-LB processing parameters for blocks with island and chess scan strategies, MC cylinders, and lattices. (√: Succeed; ×: Failed).**

| Laser Power (W) | Scan Speed (mm/s) | Hatch Distance (mm) | $E_V$ (J/mm³) | $E_L$ (J/mm) | Chess | Island | 90° Raster Scan Strategy | |
|---|---|---|---|---|---|---|---|---|
| | | | | | Blocks | | MC Cylinder | Lattice |
| 60 | 600 | 0.05 | 66.67 | 0.1 | √ | √ | √ | √ |
| 60 | 600 | 0.07 | 47.61 | 0.1 | √ | √ | √ | √ |
| 60 | 800 | 0.07 | 35.71 | 0.075 | √ | √ | √ | √ |
| 60 | 1000 | 0.05 | 40 | 0.06 | √ | √ | √ | √ |
| 70 | 1000 | 0.05 | 46.67 | 0.07 | √ | √ | √ | √ |
| 80 | 1000 | 0.05 | 53.33 | 0.08 | √ | √ | √ | √ |
| 80 | 600 | 0.07 | 63.49 | 0.13 | × | × | × | √ |
| 115 | 1750 | 0.05 | 43.8 | 0.065 | × | × | √ | √ |
| 115 | 2000 | 0.05 | 38.33 | 0.057 | × | × | √ | √ |
| 125 | 1500 | 0.06 | 46.29 | 0.083 | × | × | √ | √ |

| | | | | | | | | |
|---|---|---|---|---|---|---|---|---|
| 125 | 1750 | 0.05 | 47.62 | 0.071 | × | × | √ | √ |
| 125 | 2000 | 0.04 | 52.08 | 0.063 | × | × | √ | √ |
| 125 | 2500 | 0.045 | 37.04 | 0.05 | × | × | √ | √ |

## 4.4 Results and discussion

### 4.4.1 Microstructure of the as-fabricated samples

Contour plots were constructed to identify the processing windows that achieved the least pores and cracks. As shown in Fig. 4.4 a-b, the volumetric defects fraction (%) and crack density (crack length/area, 1/mm) were plotted against the $E_L$. The blocks with low $E_L$ and high hatch saw a high quantity of defects and a low number of cracks due to a large number of interconnected pores within the blocks possibly releasing the residual stress during PBF-LB processing, decreasing the cracking level illustrated in Fig. 4.4 c.

The quantity and size of the pores decreased with the increasing $E_L$ and decreasing hatch, as shown in Fig. 4.4 d. The results presented in Fig. 4.4 e-f display a denser microstructure yet with some cracks. Fig. 4.4 g-h revealed huge macrocracks because high $E_L$ and low hatch result in high $E_V$. The increasing residual stress caused by the rising energy density increases the cracking density. Although it was difficult to entirely eliminate the defects, especially cracking, a narrow processing window resulted in a lower density of defects and cracks, as shown in the red cycle within Fig. 4.4 b. It was established that the condition of $E_V$=53.33 J/mm$^3$ (80 W,

1000 mm/s and 0.05 mm, Fig. 4.4 e) showed the lowest defects and cracks fraction and the suitable densification. Thus, this condition is recommended as the optimum condition for block samples.

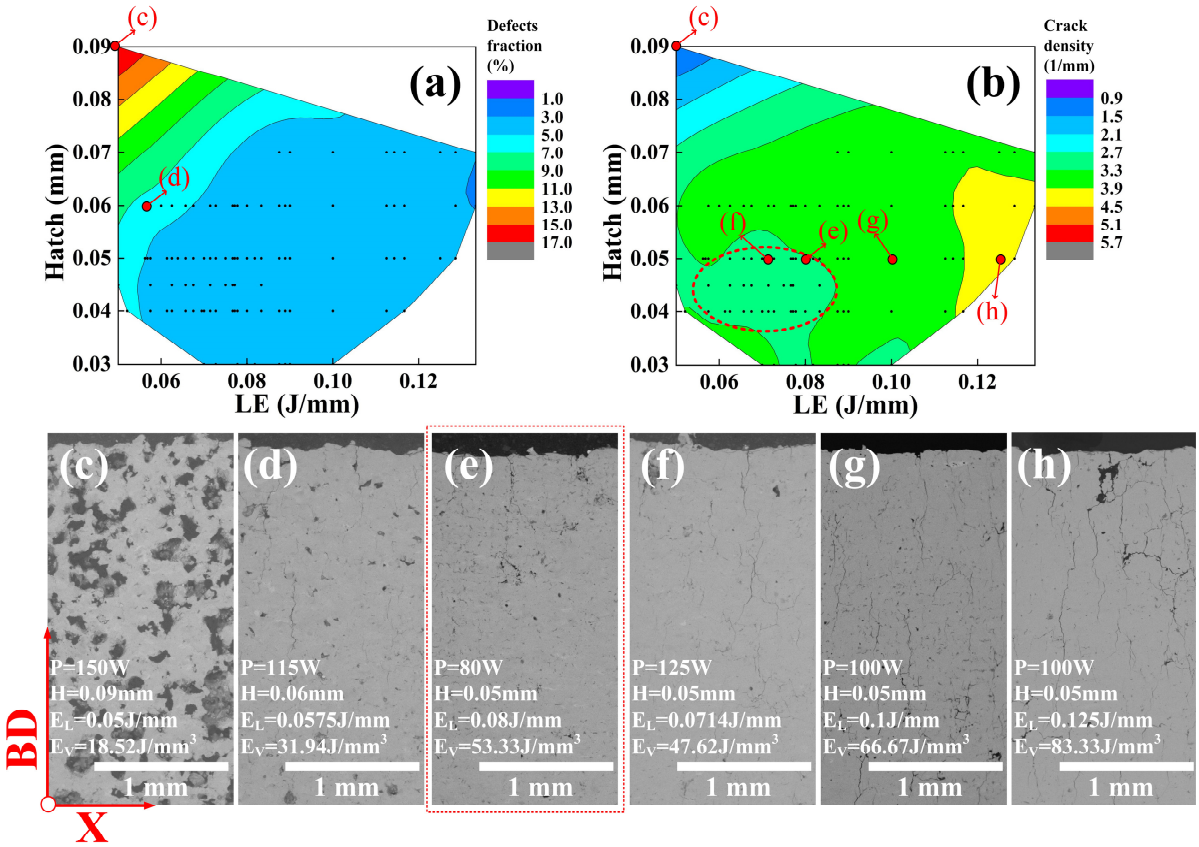



**Fig. 4.4. The correlation of $E_L$ and Hatch with the (a) Defects fraction, and (b) Crack density of all AF blocks with 90° raster scan strategy.**

## 4.4.2 Microstructure evolution and defects mechanism

Fig. 4.5, Fig. 4.6 and Fig. 4.7 show the SEM-BSE micrographs of selected block samples, which document the microstructural evolution with increasing $E_V$. Three segregations were observed in the microstructure of the samples. Ni segregation is grey, Mn segregation is dark grey, and Sn segregation is white in the SEM-BSE picture (proved in Fig. 4.9). As shown in Fig. 4.5 a-c,

the high defects, especially some of the irregularly formed pores, at low Ev of 18.52, 28.57 and 31.94 J/mm$^3$ was due to the insufficient overlap between the laser tracks caused by the large hatch spacing (90 µm), insufficient melting caused by lower laser power, and unsuitable scanning speed. The lack of fusion defects (LOFs) and un-melted powders are very common within the microstructure of blocks with low Ev, as shown in Fig. 4.5 d and e, resulting in low density and relative density (see Fig. 4.8 and Fig. 4.9). With increasing Ev, the un-melted powder caused by the LOFs almost disappears. The macrocracks were observed in the microstructure of the sample (Ev = 31.94 J/mm$^3$).

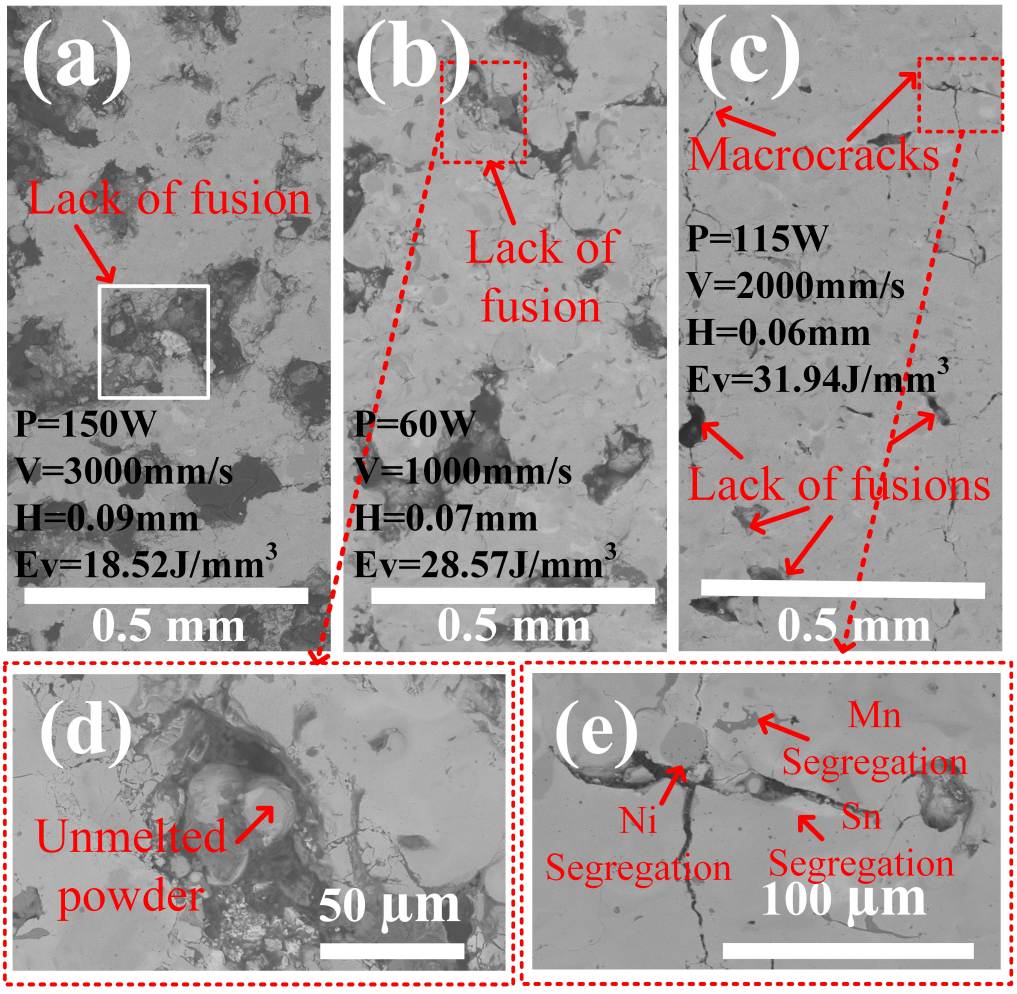



**Fig. 4.5. SEM-BSE micrographs showing the defects in the sample with low energy density.**

Fig. 4.6 presented the defects of the best sample (No.2-AF). Still, many cracks could also be observed, where the cracks have grown in a zig-zag movement. Some cracks occurred within the Sn segregation; see Fig. 4.6 c. The small LOFs were also observed (Fig. 4.6 d). It is caused by the liquid metal solidifying rapidly during the PBF-LB process. Furthermore, some cracks grow mainly through the fusion boundary (Fig. 4.6 e).

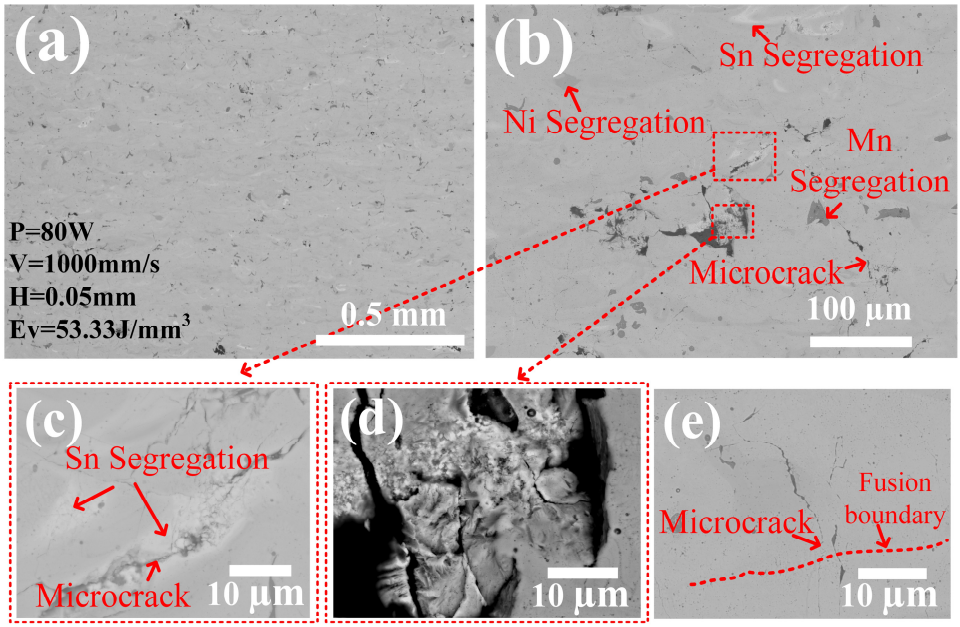



**Fig. 4.6. SEM-BSE micrographs showing the defects in the best sample (No.2-AF).**

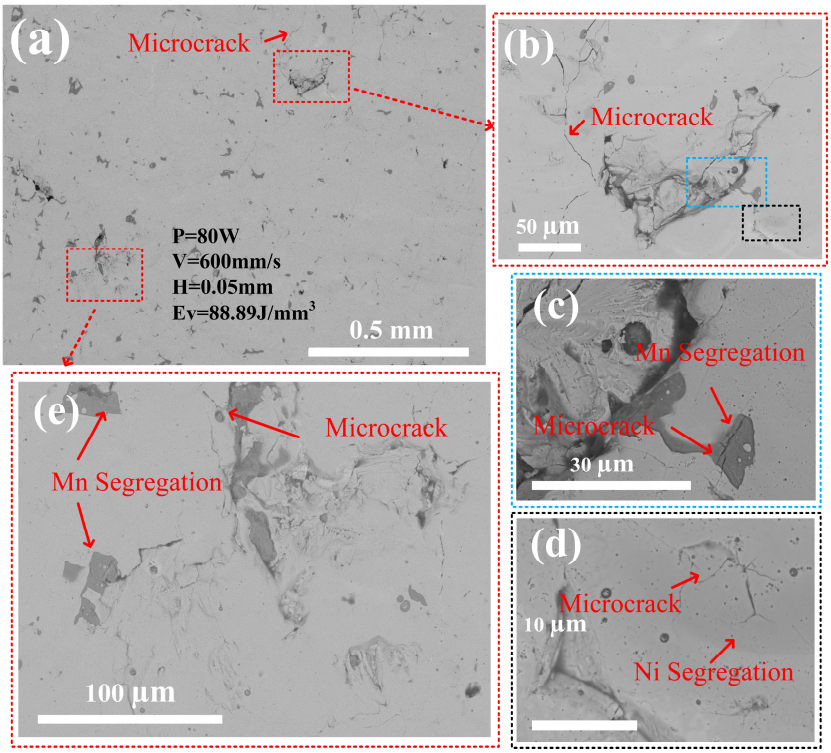



**Fig. 4.7. SEM-BSE micrographs showing the defects in the sample with high energy density.**

Fig. 4.7 presented the defects within the sample's microstructure with high energy density. The microcracks are obvious (Fig. 4.7 a and b). Some microcracks occurred within the Mn segregation region (Fig. 4.7 c) and the Ni segregation region (Fig. 4.7 d).

### 4.4.3 Influence of thermal quenching post-process on the microstructure

Fig. 4.8 shows SEM-BSE micrographs of the AF (a, c, d and g) and HT samples (b, e, f and h). Details of the PBF-LB and heat treatment processing parameters for picked blocks (No.1, No.2, and No.3) are shown in Table 4.4. The corresponding AF samples are No.1-AF, No.2-AF, and No.3-AF. The micrographs show some segregations: Sn (bright), Mn (dark grey) and Ni (light grey). Heat treatments promote microstructural homogeneity by decreasing segregation,

especially Sn segregation, due to its lower melting point (231.9 ºC) than the HT temperature. There is some remnant segregation of Ni and Mn.

**Table 4.4. The PBF-LB and heat treatment processing parameters for picked blocks.**

| No. | Laser Power (W) | Scan Speed (mm/s) | Hatch Distance (mm) | $E_V$ (J/mm$^3$) | Scan Strategy | Heat Treatment Process |
|---|---|---|---|---|---|---|
| No.1 | 150 | 3000 | 0.09 | 18.52 | | |
| No.2 | 80 | 1000 | 0.05 | 53.33 | 90° raster scan strategy | 950℃-504 hours-Quench |
| No.3 | 80 | 600 | 0.05 | 88.89 | | |

**Table 4.5. Average chemical composition analysis in at.% of the HT block samples using SEM-EDX.**

| | Ni | Mn | Sn | e/a |
|---|---|---|---|---|
| Initial Mixed Powder | 48.54 | 37.86 | 13.59 | |
| No.1 (18.52 J/mm$^3$) | 49.14 | 34.7 | 16.16 | 7.99 |
| No.2 (53.33 J/mm$^3$) | 48.80 | 33.91 | 17.29 | 7.95 |
| No.3 (88.89 J/mm$^3$) | 49.25 | 34.22 | 16.53 | 7.98 |

**Table 4.6. Chemical composition analysis (including oxygen analysis using LECO) in at. % for the HT block samples.**

| | Ni | Mn | Sn | O |
|---|---|---|---|---|
| No.1 (18.52 J/mm$^3$) | 46.95 | 33.50 | 13.50 | 6.00 |
| No.3 (88.89 J/mm$^3$) | 49.20 | 32.90 | 14.6 | 3.00 |

Different LPFB parameters caused different evaporation rates, which lead to the samples having different chemical compositions. Table. 4.5 shows the average chemical composition (including the electro-to-atom ratio; e/a) of the uniform area, without any segregation, in the three samples following the HT process. The HT processes and three different PBF-LB parameters did not significantly differ the average composition. Table. 4.6 shows the average chemical composition (including Oxygen) of the whole No.1 and No.3 samples.

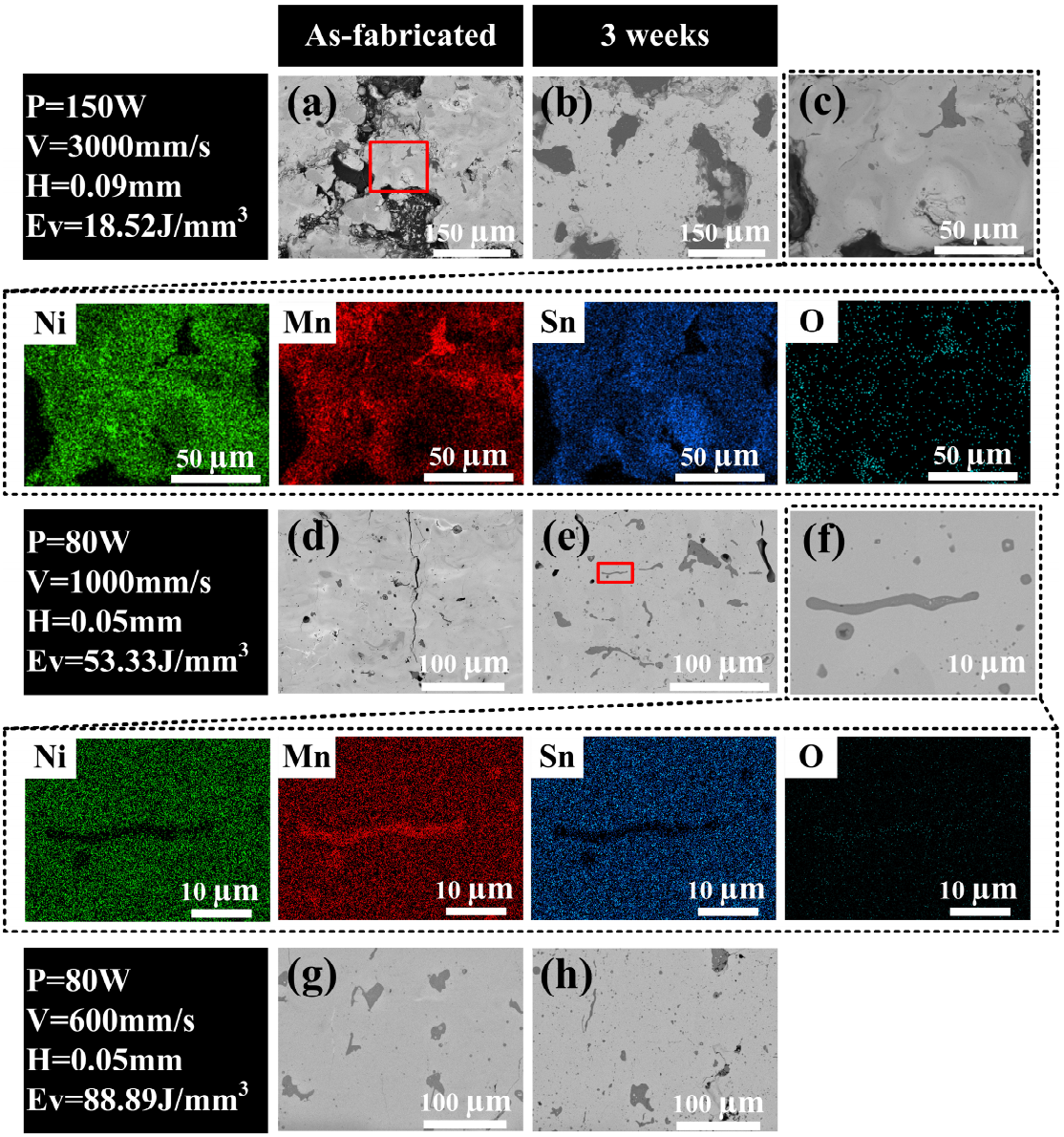



**Fig. 4.8. SEM-BSE micrographs showing the microstructure of PBF-LBed samples (a, c, d, and g) and HT PBF-LBed samples (b, e, f, and h), and EDX map for Ni, Mn and Sn element segregations in PBF-LBed and HT PBF-LBed samples.**

### 4.4.4 Density

Regarding the chemical composition, the theoretical density of the investigated NiMnSn alloy should be 8.326 g/cm$^3$ (the red-dotted line shown in Fig. 4.9), which was used as a reference

for all specimens. Fig. 4.9 shows the influence of $E_V$ on the Archimedes density of the AF specimens. When $E_V$ is less than 30 J/mm$^3$, the density is very low due to the large fraction of LOFs in the block, as shown in Fig. 4.4 c. When $E_V$ is very high (>100 J/mm$^3$), selective elemental vaporisation of Mn increases the blocks' density because Mn's density is lower than that of Ni and Sn. As observed in Table 4.3, high P or $E_L$ will result in failed blocks with chess and island scan strategies. Since $E_L$ density at the edge of a short raster scan within the chess and island scanned blocks was so high, the melted powder in that area was thicker, and other points in the same layer had less time to cool down. In addition, the residual stress and heat input also accumulated with the increasing number of printing layers. Fig. 4.9 b shows that the three different scan strategies did not result in a considerable variation in density (<0.25 g/cm$^3$). As shown in Fig. 4.10, the relative density of some PBF-LBed blocks, with high $E_V$ and $E_L$ was above 100%, indicating that the density is higher than the theoretical density. This has occurred because high P and $E_L$ will result in elemental evaporation, which will change the chemical composition and increase the density of the blocks.

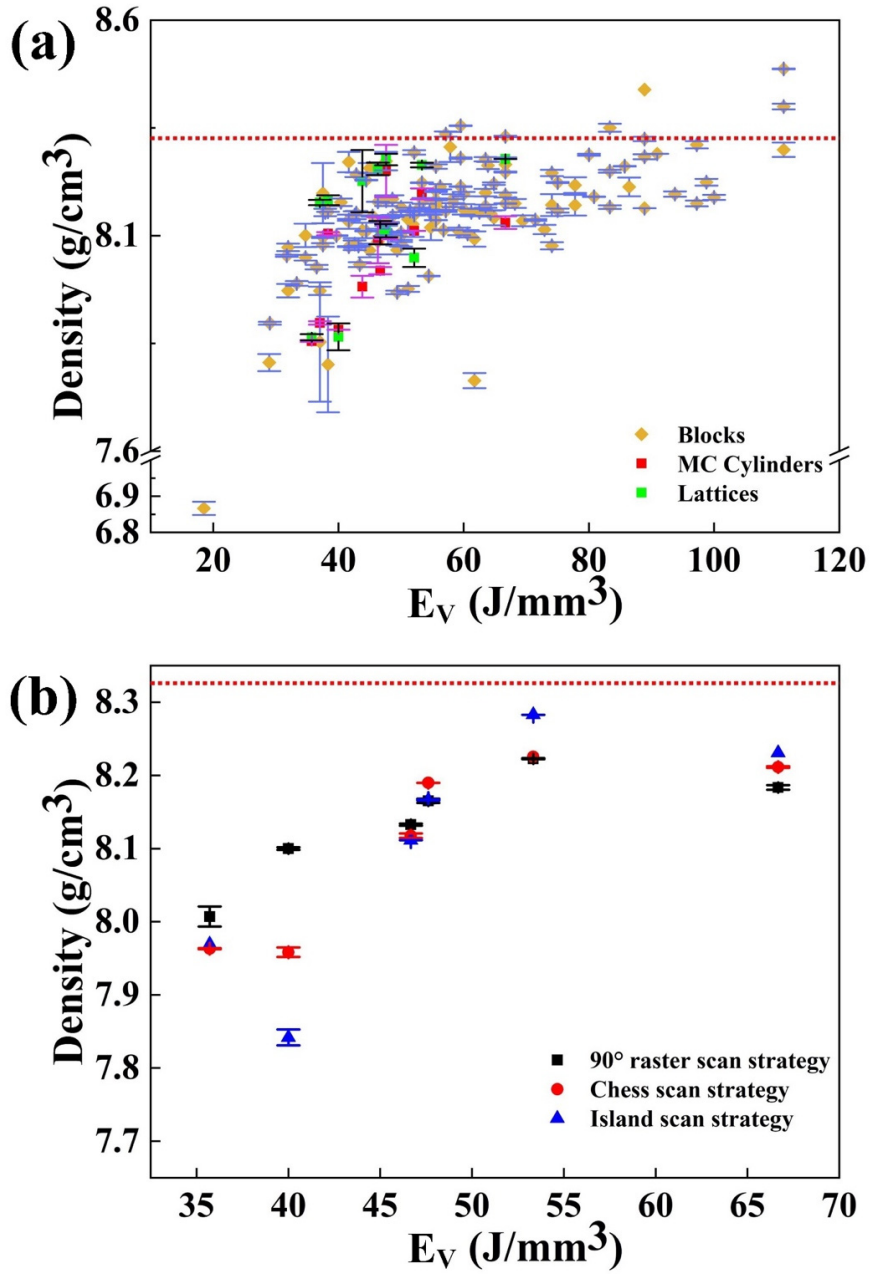



**Fig. 4.9. (a) Influence of $E_V$ on density, (b) Influence of laser scan strategy on the AF block density.**

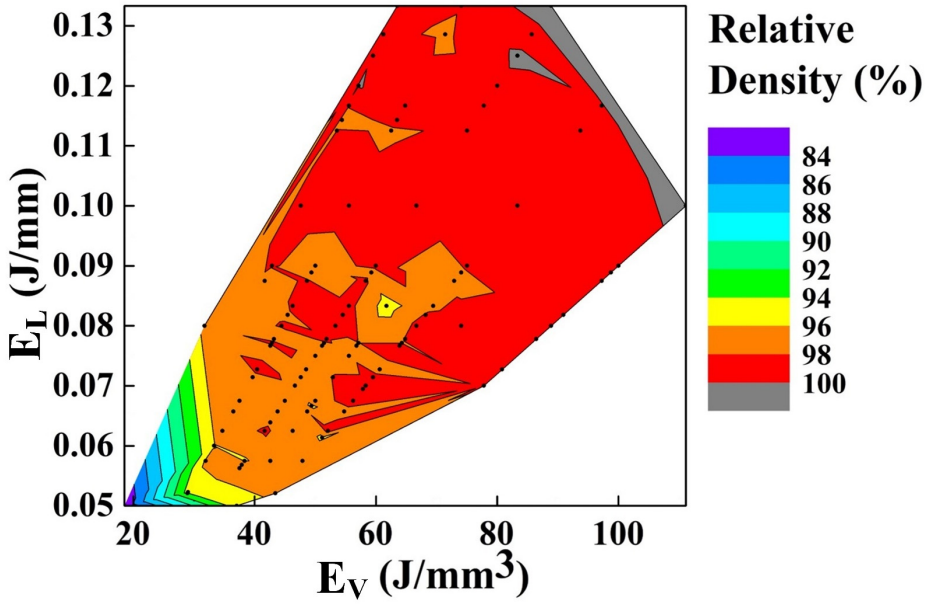



**Fig. 4.10. The relationship of $E_V$, $E_L$, and the relative density of all AF blocks with 90° raster scan strategy.**

The surface morphologies of the MC cylinders (X-Y, normal direction) and lattices and the cross-sectional (X-Y) microstructure of both parts, produced using six different PBF-LB process parameters, are shown in Fig. 4.11. The surface of MC cylinders and lattices contains some partially melted residual powder particles as a result of the PBF-LB process [29]. The Ev did not significantly change (37 J/mm$^3$ to 53 J/mm$^3$), but the laser power changed considerably (60 W to 125 W). Although MC cylinders and lattices are small, cracks can be seen in all the specimens. More LOFs and pores were observed in the microstructure of MC cylinders and lattices produced by using high laser power (>115 W) because of increased splashing and a high cooling speed. The Image J software was used to determine the effective diameters. The diameter of the holes in MC cylinders (1.0 mm) and X-Y plane of lattice structures (0.4 mm)

was built relatively accurately. However, the holes in the lattice structures' Y-Z plane were inaccurate. The diameter of the holes is small (~0.24 mm) when using high-laser power. The high laser power tended to block the pores (especially the surface morphology Y-Z, build direction) due to the broader melt pool and deeper melt depth resulting in more powder sticking to the channels. The MC cylinders and lattices produced by using lower laser powder saw more recognisable, uniform pore morphology and fewer pores within the microstructure. Therefore, it can be concluded that low laser power (60, 70 and 80 W) is more suitable for manufacturing MC cylinders and lattices when using the 90° raster scan strategy.

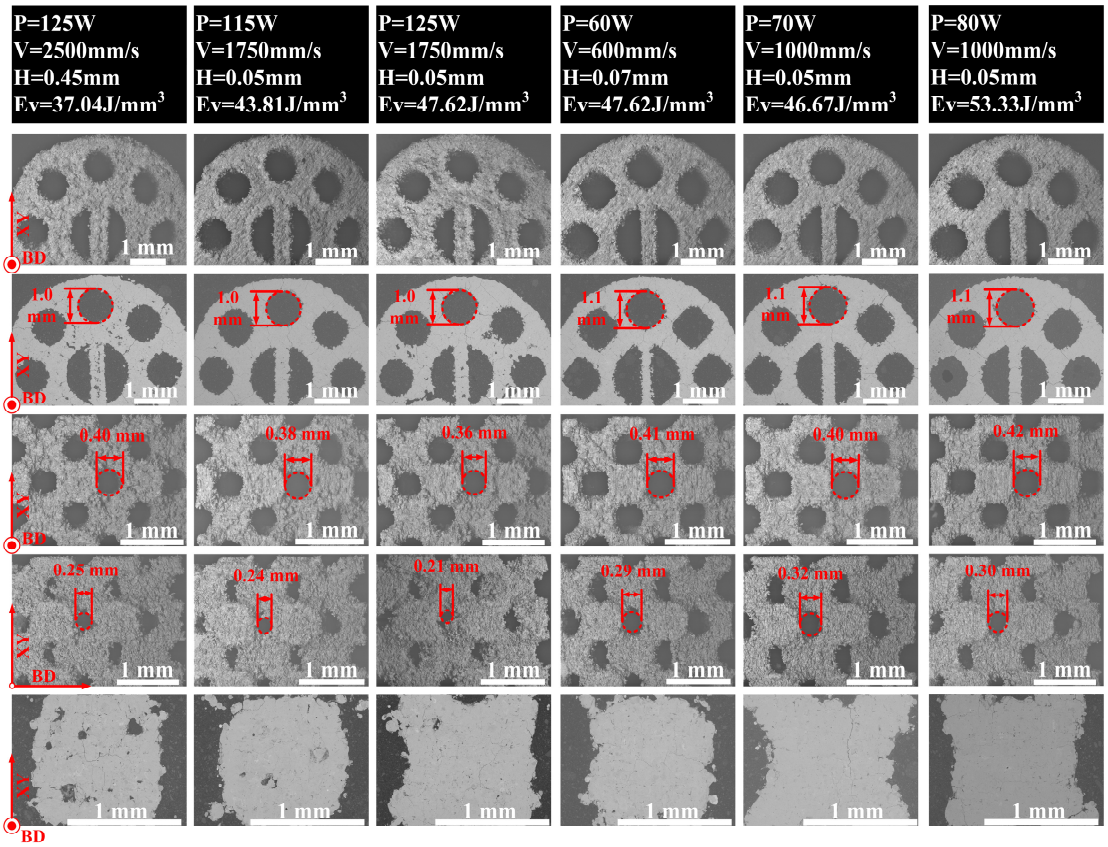



**Fig. 4.11. SEM-BSE micrographs showing surface morphologies (X-Y) and microstructure of cylinders with the microchannels (red circles); SEM-BSE micrographs showing surface morphologies (X-Y/Y-Z) and microstructure lattice strut samples.**

### 4.4.5 Influence of thermal quenching post-process on the phase formation

Fig. 4.12 shows the XRD patterns of the HT PBF-LBed NiMnSn samples at room temperature (RT). The images reveal the dominance of the $L2_1$ austenite phase in all samples at RT. In contrast, a 4-layered orthorhombic (221) peak was visible near the austenite (220) peak, revealing the coexistence of the 4O-type martensite phase at low temperatures (100 K) [30, 31], which decreases with increasing the temperature (see Fig. 4.13). Chemical composition plays an important role in the martensite phase volume and transition, where it has been reported that HAs with a chemical composition of $Ni_{50}Mn_{50-x}Sn_x$ (x = 13-15) show strong 4O and martensite phase peaks [32, 33]. The samples analysed had a low-intensity 4O martensite peak as a result of deviation of the chemical composition (See Table 4.5) from the optimum starting values due to evaporation and the microstructural inhomogeneity.

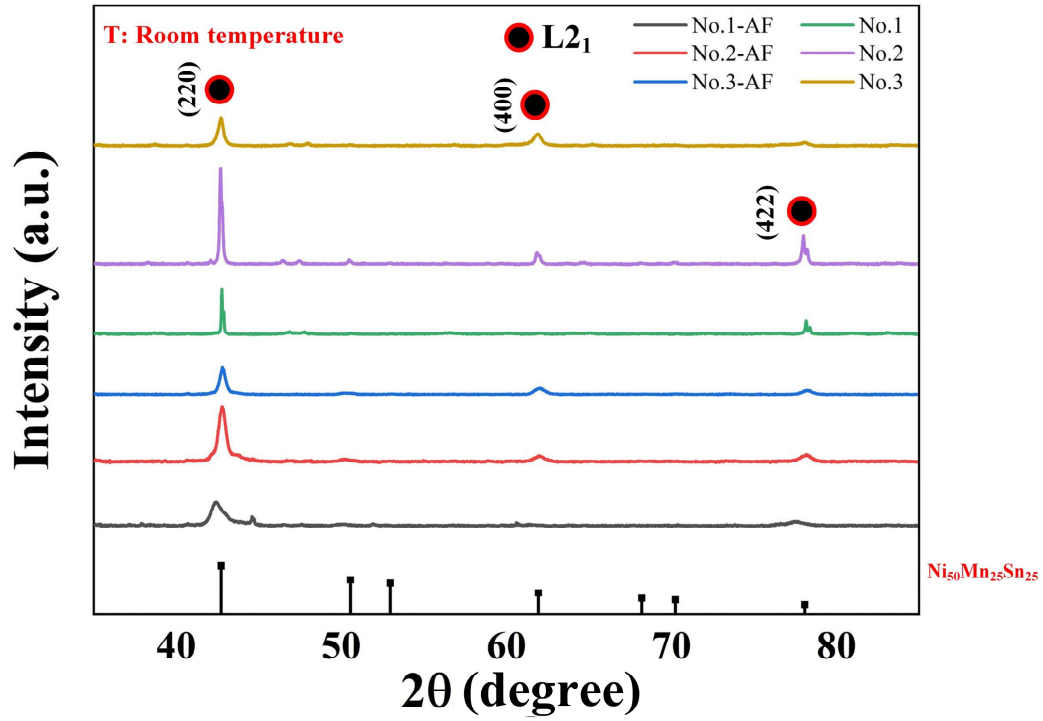



**Fig. 4.12. XRD patterns of the PBF-LBed and HT PBF-LBed NiMnSn alloys.**

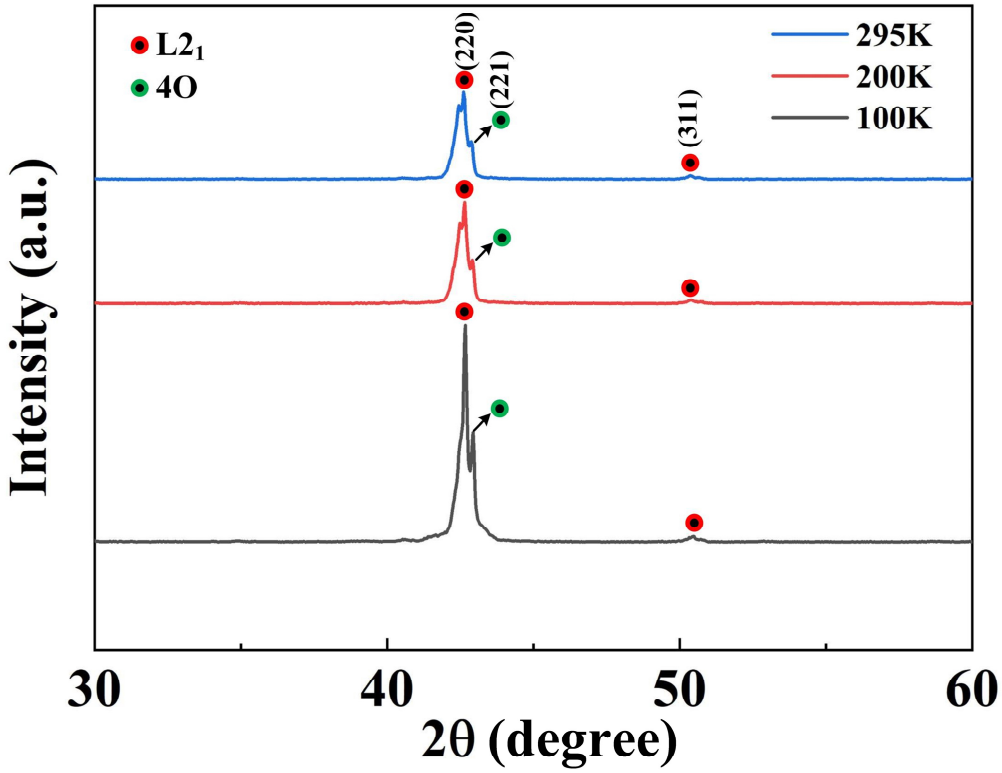



**Fig. 4.13. XRD patterns of the HT PBF-LBed NiMnSn (No.2) at different temperatures (100 K, 200 K, 295 K).**

## 4.4.6 Magnetic properties

### 4.4.6.1 Temperature dependence of magnetisation

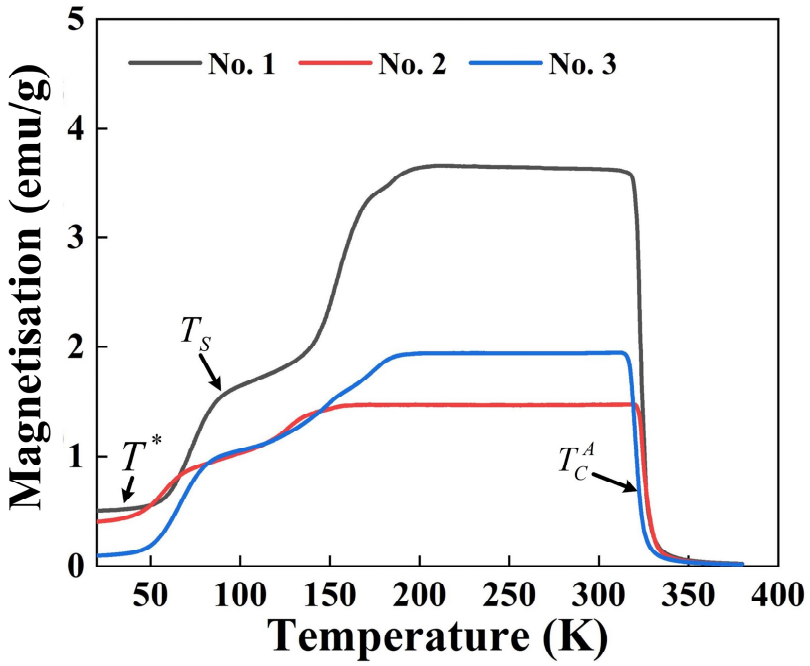



**Fig. 4.14. Thermo-magnetisation curves of HT PBF-LBed samples in an applied field of 0.01 T.**

Fig. 4.14 shows the thermal variation of magnetisation for the three blocks. The M(T) behaviour agrees with the previous studies of arc-melted NiMnSn alloys [30]. At high temperatures (340-400 K), the magnetisation value is close to zero due to the paramagnetic state in the austenite phase. By decreasing the temperature below 340 K, the three samples exhibit a sudden increase in the magnetisation in correspondence with the paramagnetic (PM)–ferromagnetic (FM) transition at $T_C^A$ (~320 K). The ($T_C^A$) value agrees with the previously reported values in the arc-melted NiMnSn alloys [33]. A further decrease in temperature leads to a reduction in magnetisation (antiferromagnetic behaviour) due to the start of the Martensitic transition, in

agreement with [30]. Magnetisation continued to decrease with temperature showing a step-like anomaly around Ts before remaining constant below T* (~50 K). The observed difference in the magnetisation behaviour in the austenite and martensite phases refers to the change in Mn-Mn distance [34] where, the Mn-Mn distance decreases after the martensitic transformation due to the twining of the martensitic phase [35] inducing an antiferromagnetic (AFM) coupling component [6, 36]. The presence of the AFM component has been reported previously in NiMnSn alloys and is attributed to the existence of ferromagnetic particles/grains, which are in a non-magnetic order [37] with inhomogeneous magnetic states [38]. The presence of the AFM component increases with a decrease in temperature. It leads to FM-AFM competition, locking spins from the contribution in magnetisation, which explains the constant value of M below $T^*$ [30, 39]. It is worth noting that the three samples show different magnetisation values, which may occur due to the change in chemical composition resulting from the different processing parameters (see Table 4.5 and Table 4.6). The lower Ni and Sn contents lead to some of the Mn ions occupying Ni and Sn sites, which are coupled antiferromagnetically to those on the regular Mn sites, and lead to the AFM interaction [34, 40]. Accordingly, the lower Ni and Sn content in sample No. 1 led to the highest magnetisation. It is worth to mention that NiMnSn alloys have shown small thermal magnetic hystersis 5 K in previous works of arc melted [41] and 5 K in HT PBF-LBed samples [10].

#### 4.4.6.2 Isothermal magnetisation

The initial M-H curves in Fig. 4.15 a-c, and Fig. 4.15 d-f show the magnetisation dynamics near

the martensite transition temperature ($T_M$) and $T_C^A$, respectively for the three samples, where the isothermal magnetisation process was taken at two steps every 5 K (from 0 to 1 T, then back to 0 T). Around $T_M$, a small magnetic hysteresis is observed within the temperature range 135-195 K for the No.1 sample, 115-160 K for the No.2 sample, and 125-195 K for the No.3 sample, which is a nature of the FOPT as a result of the structural transformation that occurs within these temperature ranges, in agreement with Raji [42]. The M-H curves in Fig. 4.15 d-f exhibit FM-paramagnetic (PM) transition of austenite around $T_C^A$, where below $T_C^A$, the magnetisation increases linearly with the applied magnetic field and then saturates at ~ 0.1 T, a characteristic of ferromagnetism. Meanwhile above $T_C^A$, the magnetisation increases linearly with the applied magnetic field in correspondence with the paramagnetism [42]. To determine the nature of each magnetic transition, the induced Arrott plots were employed as in Fig. 4.16. Where the positive and negative slope of Arrott plots around the transition temperature indicates SOPT and FOPT, respectively [43]. Accordingly, this reveals the SOPT nature around $T_C^A$ (Fig. 4.16 d-f), meanwhile, it is not the case around $T_M$ that shows also positive Arrott plots but with FOPT. The FOPT around $T_M$ is probably weak but can be confirmed by the existing magnetic hysteresis in M-H and Arrott plots, which is a character of the FOPT (Fig. 4.16 a-c), in agreement with [34]. The suppression/weakness of the FOPT arises from the existing inhomogeneity MnO segregation, see Fig. 4.11 and the presence of the orthorhombic 4O-type martensite phase (See Fig. 4.13). It can be seen in Fig. 4.14 and Fig. 4.16, the $T_C^A$ of the No.1 sample and No.3 sample was approximately 320 K, while the $T_C^A$ of the No.2 sample increased

marginally to 323 K. Because the No.1 and No.3 samples saw higher Ni content (see Table 4.5). The $T_C^A$ decreased with increasing Ni atoms because Ni has a lower magnetic moment than Mn the substitution of Ni atoms for Mn resulted in the dilution of the magnetic subsystem in the austenite phase [30]. The nature of magnetic transition can also be confirmed by the $\Delta S$ dependence on the magnetic field in Eq. 4.5 [44], where Fig. 4.17 shows that the value of the **n** constant is below 2, which is the case of SOPT around both $T_C^A$ and $T_M$ [45, 46].

$$\Delta S \alpha H^n \tag{4.5}$$

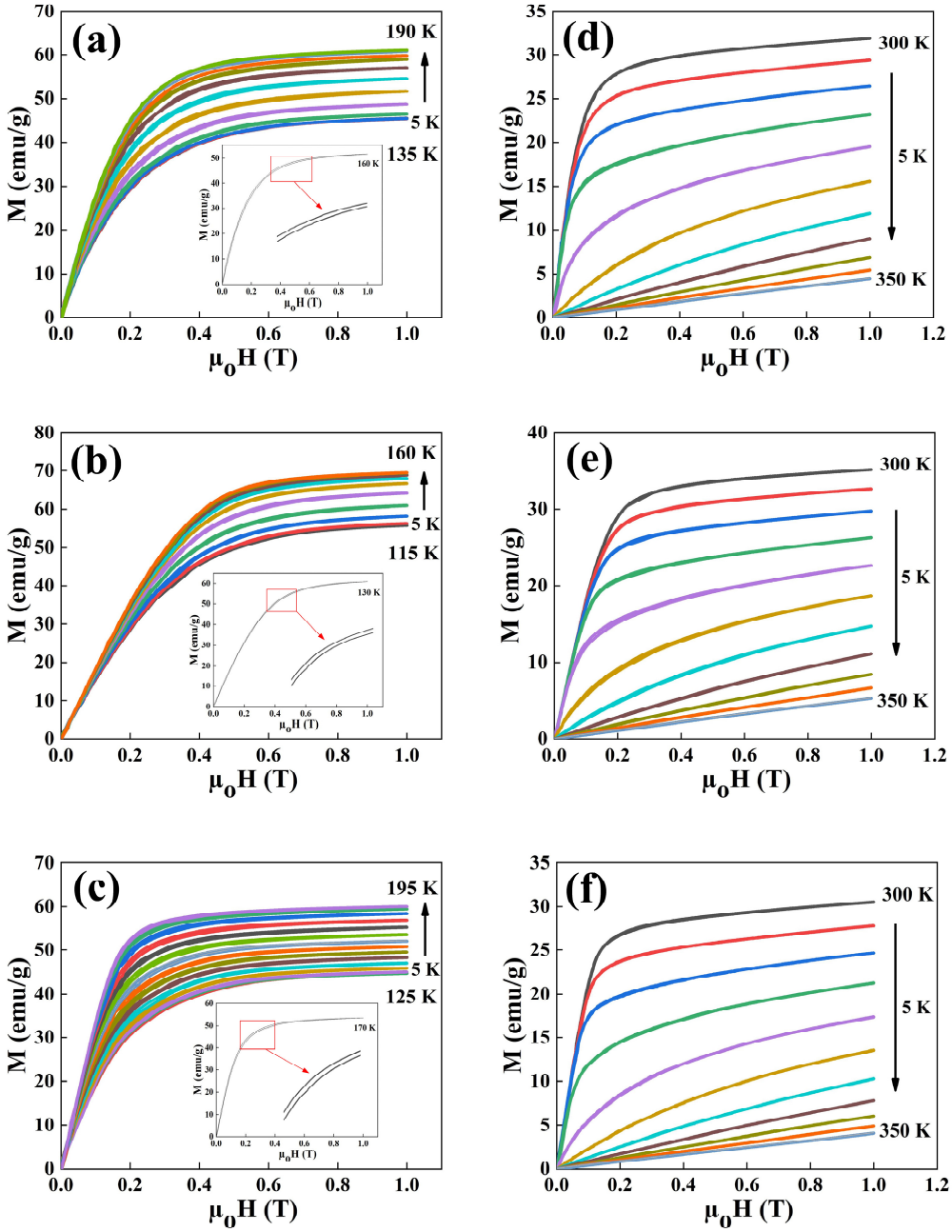



**Fig. 4.15. (a, b, c) Isothermal magnetisation curves of HT PBF-LBed block samples with E = 18.52 J/mm$^3$, 53.33 J/mm$^3$ and 88.89 J/mm$^3$ near the martensitic transition temperature, (d,e,f) Isothermal magnetisation curves of HT PBF-LBed block samples with E=18.52 J/mm$^3$, 53.33 J/mm$^3$, and E=88.89 J/mm$^3$ near the $T_C^A$.**

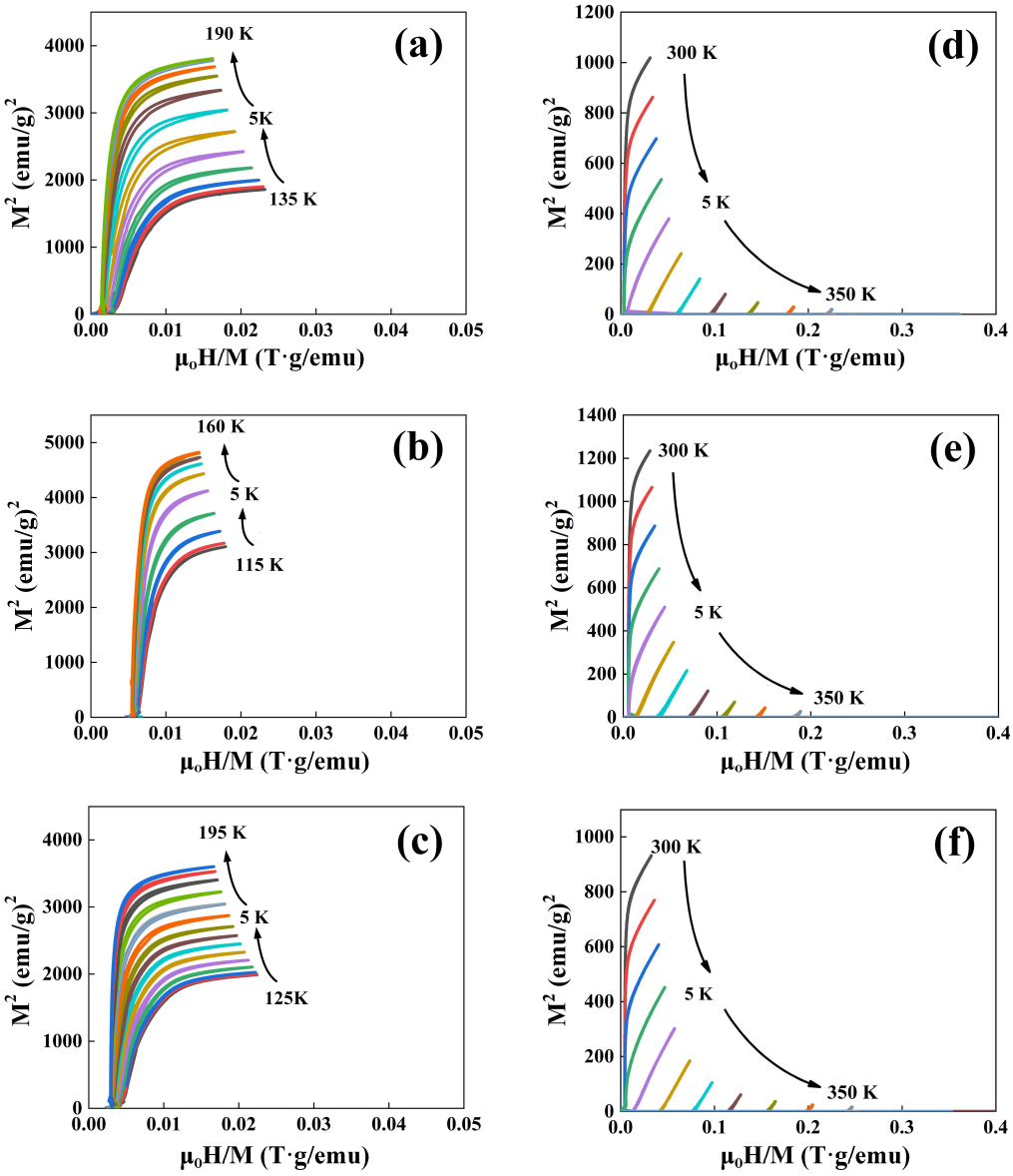



**Fig. 4.16. Arrott plots of HT PBF-LBed block samples with E=18.52 J/mm³, 53.33 J/mm³, and E=88.89 J/mm³ near (a,b,c) the martensitic transition temperature and (d, e, f) near the $T_C^A$.**

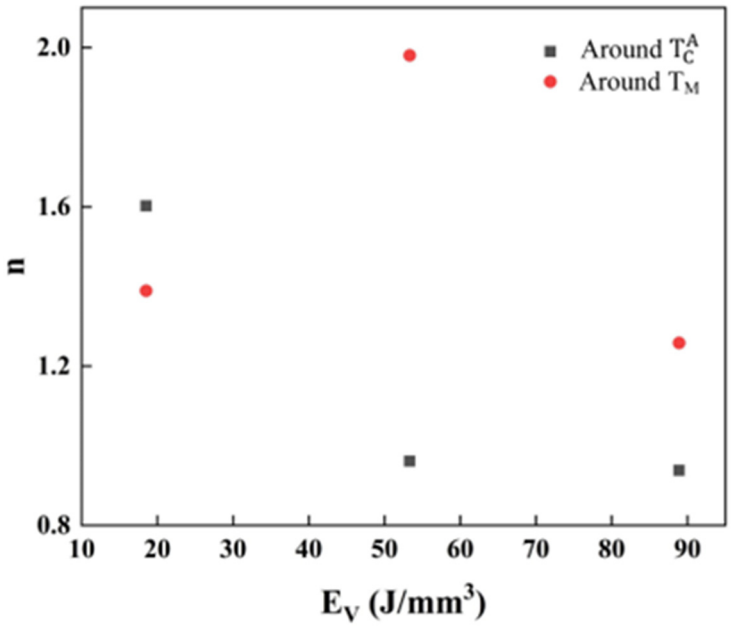



**Fig. 4.17. The value of n around the $T_C^A$ and $T_M$.**

### 4.4.6.3 Magnetocaloric effect (MCE)

The experimental results show that the start temperature of martensite (Ms) is susceptible to chemical composition [47]. The three samples showed different Ms, due to the different valence electron concentrations per atom (e/a; determined as the concentration-weighted sum of s, d, and p valence electrons [24, 48]), caused by different chemical compositions, as presented in Table 4.5. The No.2 sample had the lowest Ms because of the lower density of the valance electron number [24]. When the valance electron number increase, the energy of the system increase because the energy conduction electrons exceed the Fermi level and move to the corners of the Brillouin zone [49, 50]. The system tends to minimize the free energy by creating distortions and generating the new crystal structure, which is the martensite transition [49, 50]. In addition, Ms also decreased as the lattice parameter increased [24, 51, 52]. When the Sn

content of the No.2 sample was increased to 17.29%, the lattice parameter increased, leading to a decrease in Ms [24].

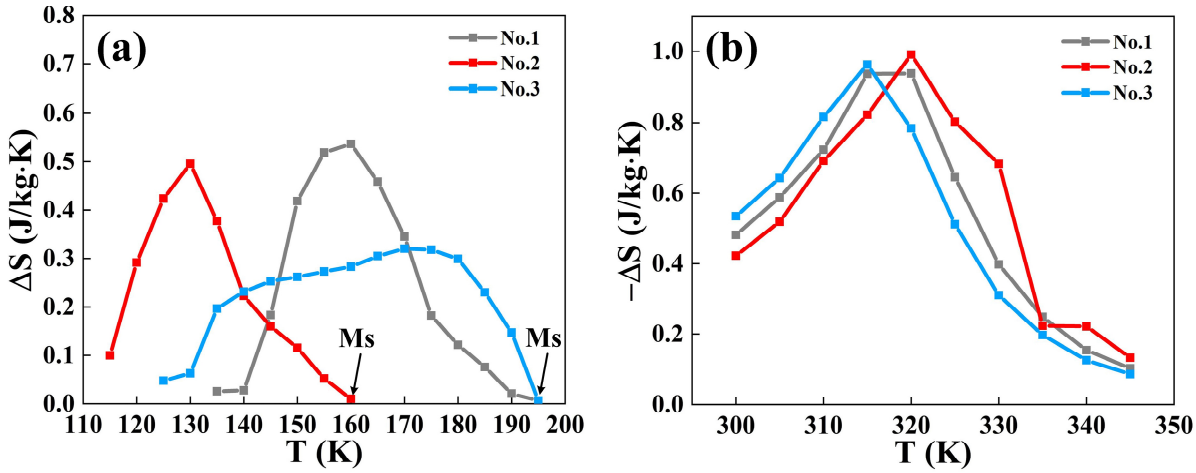



**Fig. 4.18. (a) Thermal variation of ΔS around FOPT of HT block samples at 1 T, and (b) Thermal variation of ΔS around SOPT of HT block samples at 1 T.**

The MCE is an intrinsic property of NiMn-based HAs [53]. To evaluate this characteristic in the vicinity of FOPT and SOPT, the reversible change of magnetic entropy ($\Delta S$) can be quantified from the magnetisation versus magnetic field (M–H) curves at various temperatures using Maxwell's relation (Eq. 4.3). Fig. 4.18 shows $\Delta S$ as a function of temperature when applied 1 Tesla (T) fields around the martensitic transition region and the $T_C^A$ range for the three samples with different parameters. The maximum magnetic entropy change ($\Delta S_m$) values of FOPT are 0.53 $Jkg^{-1}K^{-1}$ at 160 K, 0.5 $Jkg^{-1}K^{-1}$ at 130 K, and 0.3 $Jkg^{-1}K^{-1}$ at 170 K for the No.1, No.2, and No.3 samples, respectively. And $\Delta S_m$ of almost 1.0 $Jkg^{-1}K^{-1}$ at $T_C^A$ (~320 K) for the three HT PBF-LBed samples (see Fig. 4.18 b).

It is worth mentioning that the obtained results are lower than the recently published results of PBF-LB $Ni_{45}Mn_{44}Sn_{11}$ [10]. This is due to using a pre-alloyed powder that results in more homogeneity and strong FOPT. The study reported that the homogenised PBF-LBed $Ni_{45}Mn_{44}Sn_{11}$ alloys exhibited a FOPT, and the maximal value of $\Delta S$ is ≈1.3 $Jkg^{-1}K^{-1}$ at 1 T magnetic field [10]. Table. 4.7 compares the results of this work and previous works of NiMnSn HAs. It is evident that the $\Delta S_m$ in this work is lower than other reports. The difference in the $\Delta S_m$ was caused by the large amount of segregation within the HT PBF-LB samples. The PBF-LB process of in situ powder inevitably results in elemental segregations, as shown in Fig. 4.5-7 and Fig. 4.11. The segregations (Ni and Mn) cannot be reversed with future HT procedures and has a detrimental effect on the magnetic properties of the alloy. In addition, the different chemical compositions in the annealed PBF-LB samples can affect structural transition. In Fig. 4.13, the XRD result of the No.2 sample at low temperatures showed a little Martensite phase. It is evident that the $\Delta S_m$ of SOPT in this work is better than some reports, as shown in Table 4.7. The $T_C^A$ of the samples only changed marginally. The above results conclude that the different PBF-LB process parameters didn't significantly affect the $\Delta S$ value around $T_C^A$. Because the $T_C^A$ is insensitive to the changes in the Mn/Z ratio and remains close to RT in $Ni_2Mn_{1+x}Z_{1-x}$ (Z=In, Sn, Sb) series [54]. The FM order is almost entirely defined by the positive exchange interactions between the Mn and Ni atoms, which constantly constitute the same number of nearest neighbours [54]. Another factor in measuring the MCE efficiency is the RCP, as calculated and shown in Table 4.7. The RCP at $T_C^A$ of the three samples is similar (about

27.5 $Jkg^{-1}$). However, the RCP at $T_M$ of the three samples saw a difference. Although $\Delta S_m$ of No.3 is the lowest, the RCP of No.3 shows higher value (17.86 $Jkg^{-1}$) because of the broad working temperature. The high RCP implies excellent cooling efficiency.

**Table 4.7. Comparison of the magnetic entropy of the NiMnSn Heusler alloys with those reported in the literature.**

| Alloy | Applied Field (T) | $-\Delta S_m$ of SOPT ($Jkg^{-1}K^{-1}$) | $\Delta S_m$ of FOPT ($Jkg^{-1}K^{-1}$) | RCP at $T_C^A$ ($Jkg^{-1}$) | RCP at $T_M$ ($J/kg^{-1}$) | Manufactured method | Reference |
|---|---|---|---|---|---|---|---|
| $Ni_{49.14}Mn_{34.7}Sn_{16.16}$ | 1 | 0.94 | 0.5 | 27.27 | 13.73 | | This work |
| $Ni_{48.8}Mn_{33.91}Sn_{17.29}$ | 1 | 0.99 | 0.53 | 27.94 | 9.74 | Additive manufacturing in-situ powder & 950°C for 504 h & Quench | This work |
| $Ni_{49.25}Mn_{34.22}Sn_{16.53}$ | 1 | 0.96 | 0.3 | 27.56 | 17.86 | | This work |
| $Ni_{45}Mn_{44}Sn_{11}$ | 1.5 | / | 2.1 | / | / | Additive manufacturing pre-alloy powder & 1173 K for 24 h & Quench | [10] |
| $Ni_{45}Mn_{44}Sn_{11}$ | 5 | 4 | 15 | 34 | 71 | Arc melting & 1273 K for 24 h & quenched in ice water | [55] |
| $Ni_{50}Mn_{35}Sn_{15}$ | 5 | 2.105 | / | 132.5 | / | Arc melting & Melt-spun ribbons 40 m/s | [56] |

| | | | | | | | |
|---|---|---|---|---|---|---|---|
| $Ni_{2.12}Mn_{1.28}Sn_{0.6}$ | 5 | ~2 | 10.2 | / | 80 | Arc melting & 1173K for 24 h & slowly cooled down | [30] |
| $Ni_{2.18}Mn_{1.22}Sn_{0.6}$ | 5 | 5.9 | 2.16 | / | 89 | Arc melting & 1173K for 24 h & slowly cooled down | [30] |
| $Ni_{47}Mn_{40}Sn_{13}$ | 5 | / | 7.5 | 207 | 62 | Mechanical alloying & 1223K for 16 h & quenched in ice-water | [57] |
| $Ni_{48}Mn_{39.5}Sn_{12.5}$ | 2 | 1.8 | 7.8 | 92.1 | 55.5 | Melt-spun ribbons (25m/s) | [58] |
| $Ni_{50}Mn_{37}Sn_{13}$ | 1.2 | 1.1 | 1.9 | / | / | As melted & 1123K for 4 h & quenched by Ar-flow | [33] |
| $Ni_{50}Mn_{36}Sn_{14}$ | 1.2 | ~1.4 | / | / | / | As melted & 1123K for 4 h & quenched by Ar-flow | [33] |
| $Ni_{50}Mn_{35}Sn_{15}$ | 1.2 | ~1.2 | / | / | / | As melted & 1123K for 4 h & quenched by Ar-flow | [33] |

| | | | | | | | |
|---|---|---|---|---|---|---|---|
| $Ni_{50}Mn_{30}Sn_{20}$ | 1.2 | ~1.3 | / | / | / | As melted & 1123K for 4 h & quenched by Ar-flow | [33] |
| $Ni_{50}Mn_{20}Sn_{30}$ | 1.2 | ~1.12 | / | / | / | As melted & 1123K for 4 h & quenched by Ar-flow | [33] |
| $Ni_{50}Mn_{35}Sn_{15}$ | 5 | / | 15 | / | / | Arc melting & 1273 K for 2 h & quenched in ice water | [32] |
| $Ni_{50}Mn_{37}Sn_{13}$ | 5 | ~1.8 | 18 | / | / | Arc melting & 1273 K for 2 h & quenched in ice water | [32] |
| $Ni_{50}Mn_{25}Sn_{25}$ | 2 | 1.4 | / | / | / | Hybrid microwave heating method | [59] |
| $Ni_{43}Mn_{46}Sn_{11}$ | 5 | / | 43.2 | / | / | Arc melting & melt spun ribbons & 1173 K for 10 minutes | [60] |

## 4.5 Conclusion

This study investigated the PBF-LB of NiMnSn-based Heusler alloys with different shapes, blocks, MC cylinders and lattices.

1. The density increases with increasing $E_V$ reaching an average value of ~8.3 g/cm$^3$. The PBF-LB processing parameters were optimised where the block optimuim condition was defined as $E_V$ = 53.33 J/mm$^3$ (P=80W, V=1000 m/s and h=0.05 mm). The low laser powers (60, 70 and 80 W) with low energy density are more suitable for manufacturing MC cylinders and lattices when using the 90° raster scan strategy.

2. The AF parts were homogenised by heat treatment for 504 hours and then quenched in water. The XRD has shown the $L2_1$ phase for all samples with a minor 4O orthorhombic phase. The samples also showed double magnetic transitions, martensite-austenite transition, and curie temperature.

3. The maximum magnetic entropy change values of the three samples around $T_M$ are 0.53 Jkg$^{-1}$K$^{-1}$ at 160 K, 0.5 Jkg$^{-1}$K$^{-1}$ at 130 K, and 0.3 Jkg$^{-1}$K$^{-1}$ at 170 K, respectively. The different PBF-LB process parameters didn't significantly affect the $\Delta S$ value around $T_C^A$. Because it was insensitive to changes in the Mn/Sn ratio. The $\Delta S_m$ for the three PBF-LB samples around $T_C^A$ (~320 K) is approximately 1.0 Jkg$^{-1}$K$^{-1}$ when applied to the 1 T field. The results demonstrated that it is possible to successfully produce 3D printed NiMnSn Heusler alloy magnetic refrigerant with acceptable MCE efficiency. Although the MCE efficiency of the PBF-LB block samples

was lower than that of the alloy manufactured using arc melting, it is predicted that the MCE of PBF-LB samples can be increased using the pre-alloy powder.

Furthermore, The cracking problem of PBF-LBed NiMnSn HAs needs to be solved. Heat exchangers with a larger surface area should be manufactured to increase heat exchange efficiency. The structures in this work will also be used in a mini heat exchanger prototype to improve the cooling performance. The heat treatment processes will be studied to improve the magnetic refrigeration of PBF-LBed NiMnSn alloys.

## 4.6 References

[1] V. Franco, J.S. Blazquez, B. Ingale, A. Conde, The Magnetocaloric Effect and Magnetic Refrigeration Near Room Temperature: Materials and Models, Annu Rev Mater Res 42 (2012) 305-342.

[2] V. Chaudhary, X. Chen, R.V. Ramanujan, Iron and manganese based magnetocaloric materials for near room temperature thermal management, Prog Mater Sci 100 (2019) 64-98.

[3] V. Franco, J.S. Blazquez, J.J. Ipus, J.Y. Law, L.M. Moreno-Ramirez, A. Conde, Magnetocaloric effect: From materials research to refrigeration devices, Prog Mater Sci 93 (2018) 112-232.

[4] S.Y. Dan'kov, A.M. Tishin, V.K. Pecharsky, K.A. Gschneidner, Magnetic phase transitions and the magnetothermal properties of gadolinium, Phys Rev B 57(6) (1998) 3478-3490.

[5] P. Shamba, N.A. Morley, O. Cespedes, I.M. Reaney, W.M. Rainforth, Optimization of magnetocaloric properties of arc-melted and spark plasma-sintered LaFe11.6Si1.4, Applied Physics A 122(8) (2016) 732.

[6] Z. Zhong, S. Ma, D. Wang, Y. Du, A Review on the Regulation of Magnetic Transitions and the Related Magnetocaloric Properties in NiMn-Co-Sn Alloys, J Mater Sci Technol 28(3) (2012) 193-199.

[7] A.E.-M.A. Mohamed, B. Hernando, Self-assembled impurity and its effect on magnetic and magnetocaloric properties of manganites, Ceram Int 44(14) (2018) 17044-17049.

[8] J.D. Moore, D. Klemm, D. Lindackers, S. Grasemann, R. Träger, J. Eckert, L. Löber, S. Scudino, M. Katter, A. Barcza, K.P. Skokov, O. Gutfleisch, Selective laser melting of

La(Fe,Co,Si)13 geometries for magnetic refrigeration, J Appl Phys 114(4) (2013) 043907.

[9] T. DebRoy, H.L. Wei, J.S. Zuback, T. Mukherjee, J.W. Elmer, J.O. Milewski, A.M. Beese, A. Wilson-Heid, A. De, W. Zhang, Additive manufacturing of metallic components – Process, structure and properties, Prog Mater Sci 92 (2018) 112-224.

[10] W. Sun, X. Lu, Z. Wei, Q. Li, Z. Li, Y. Zhang, J. Liu, Multicaloric effect in Ni–Mn–Sn metamagnetic shape memory alloys by laser powder bed fusion, Addit Manuf 59 (2022) 103125.

[11] A.E.-M.A. Mohamed, M. Jeong, R.S. Sheridan, M.M. Attallah, Enabling high efficiency magnetic refrigeration using laser powder bed fusion of porous LaCe(Fe,Mn,Si)13 structures, Addit Manuf 51 (2022) 102620.

[12] V. Chaudhary, S.A. Mantri, R.V. Ramanujan, R. Banerjee, Additive manufacturing of magnetic materials, Prog Mater Sci 114 (2020) 100688.

[13] B.T. Lejeune, R. Barua, E. Simsek, R.W. McCallum, R.T. Ott, M.J. Kramer, L.H. Lewis, Towards additive manufacturing of magnetocaloric working materials, Materialia 16 (2021) 101071.

[14] M.S.K.K.Y. Nartu, A. Jagetia, V. Chaudhary, S.A. Mantri, E. Ivanov, N.B. Dahotre, R.V. Ramanujan, R. Banerjee, Magnetic and mechanical properties of an additively manufactured equiatomic CoFeNi complex concentrated alloy, Scripta Mater 187 (2020) 30-36.

[15] V. Chaudhary, M.S.K.K.Y. Nartu, S. Dasari, S.M. Varahabhatla, A. Sharma, M. Radhakrishnan, S.A. Mantri, S. Gorsse, N.B. Dahotre, R.V. Ramanujan, R. Banerjee, Magnetic and mechanical properties of additively manufactured Alx(CoFeNi) complex concentrated alloys, Scripta Mater 224 (2023) 115149.

[16] W.H. Teh, V. Chaudhary, S. Chen, S.H. Lim, F. Wei, J.Y. Lee, P. Wang, S.P. Padhy, C.C. Tan, R.V. Ramanujan, High throughput multi-property evaluation of additively manufactured Co-Fe-Ni materials libraries, Addit Manuf 58 (2022) 102983.

[17] C. Shen, K.-D. Liss, M. Reid, Z. Pan, X. Hua, F. Li, G. Mou, Y. Huang, Y. Zhu, H. Li, Fabrication of FeNi intermetallic using the wire-arc additive manufacturing process: A feasibility and neutron diffraction phase characterization study, Journal of Manufacturing Processes 57 (2020) 691-699.

[18] X. Miao, W. Wang, H. Liang, F. Qian, M. Cong, Y. Zhang, A. Muhammad, Z. Tian, F. Xu, Printing (Mn,Fe)2(P,Si) magnetocaloric alloys for magnetic refrigeration applications, J Mater Sci 55(15) (2020) 6660-6668.

[19] Z. Li, N. Zou, C.F. Sánchez-Valdés, J.L. Sánchez Llamazares, B. Yang, Y. Hu, Y. Zhang, C. Esling, X. Zhao, L. Zuo, Thermal and magnetic field-induced martensitic transformation in Ni50Mn25−xGa25Cux(0 ⩽ x ⩽ 7) melt-spun ribbons, Journal of Physics D: Applied Physics 49(2) (2015) 025002.

[20] K. Navickaitė, J. Liang, C. Bahl, S. Wieland, T. Buchenau, K. Engelbrecht, Experimental characterization of active magnetic regenerators constructed using laser beam melting technique, Applied Thermal Engineering 174 (2020) 115297.

[21] J. Kagathara, S. Wieland, E. Gärtner, V. Uhlenwinkel, M. Steinbacher, Heat Treatment and Formation of Magnetocaloric 1:13 Phase in LaFe11.4Si1.2Co0.4 Processed by Laser Beam Melting, 13(3) (2020) 773.

[22] A. Deltell, A.E.-M.A. Mohamed, P. Álvarez-Alonso, M. Ipatov, J.P. Andrés, J.A. González, T. Sánchez, A. Zhukov, M.L. Escoda, J.J. Suñol, R. López Antón, Martensitic transformation, magnetic and magnetocaloric properties of Ni–Mn–Fe–Sn Heusler ribbons, Journal of Materials Research and Technology 12 (2021) 1091-1103.

[23] I. Titov, M. Acet, M. Farle, D. González-Alonso, L. Mañosa, A. Planes, T. Krenke, Hysteresis effects in the inverse magnetocaloric effect in martensitic NiMn-In and NiMnSn, 112(7) (2012) 073914.

[24] A. Cakir, L. Righi, F. Albertini, M. Acet, M. Farle, Intermartensitic transitions and phase stability in Ni50Mn50-xSnx Heusler alloys, Acta Mater 99 (2015) 140-149.

[25] F. Nilsén, I.F. Ituarte, M. Salmi, J. Partanen, S.-P. Hannula, Effect of process parameters on non-modulated NiMn-Ga alloy manufactured using powder bed fusion, Addit Manuf 28 (2019) 464-474.

[26] K.G. Prashanth, S. Scudino, T. Maity, J. Das, J. Eckert, Is the energy density a reliable parameter for materials synthesis by selective laser melting?, Materials Research Letters 5(6) (2017) 386-390.

[27] Standard Test Methods for Density of Compacted or Sintered Powder Metallurgy(PM) Products Using Archimedes, Principle, ASTM B962 e 17.

[28] C.A. Schneider, W.S. Rasband, K.W. Eliceiri, NIH Image to ImageJ: 25 years of image analysis, Nature Methods 9(7) (2012) 671-675.

[29] C. Tan, S. Li, K. Essa, P. Jamshidi, K. Zhou, W. Ma, M.M. Attallah, Laser Powder Bed Fusion of Ti-rich TiNi lattice structures: Process optimisation, geometrical integrity, and phase transformations, International Journal of Machine Tools and Manufacture 141 (2019) 19-29.

[30] M.K. Ray, K. Bagani, S. Banerjee, Effect of excess Ni on martensitic transition, exchange bias and inverse magnetocaloric effect in Ni2+xMn1.4-xSn0.6 alloy, J Alloy Compd 600 (2014) 55-59.

[31] K. Fukushima, K. Sano, T. Kanomata, H. Nishihara, Y. Furutani, T. Shishido, W. Ito, R.Y. Umetsu, R. Kainuma, K. Oikawa, K. Ishida, Phase diagram of Fe-substituted Ni–Mn–Sn shape memory alloys, Scripta Mater 61(8) (2009) 813-816.

[32] T. Krenke, E. Duman, M. Acet, E.F. Wassermann, X. Moya, L. Mañosa, A. Planes, Inverse

magnetocaloric effect in ferromagnetic Ni–Mn–Sn alloys, Nat Mater 4(6) (2005) 450-454.

[33] N.H. Dan, N.H. Duc, N.H. Yen, P.T. Thanh, L.V. Bau, N.M. An, D.T.K. Anh, N.A. Bang, N.T. Mai, P.K. Anh, T.D. Thanh, T.L. Phan, S.C. Yu, Magnetic properties and magnetocaloric effect in NiMnSn alloys, J Magn Magn Mater 374 (2015) 372-375.

[34] H.C. Xuan, Q.Q. Cao, C.L. Zhang, S.C. Ma, S.Y. Chen, D.H. Wang, Y.W. Du, Large exchange bias field in the Ni–Mn–Sn Heusler alloys with high content of Mn, Appl Phys Lett 96(20) (2010) 202502.

[35] T. Krenke, M. Acet, E.F. Wassermann, X. Moya, L. Mañosa, A. Planes, Martensitic transitions and the nature of ferromagnetism in the austenitic and martensitic states of NiMnSn alloys, Phys Rev B 72(1) (2005) 014412.

[36] G. Kirat, O. Kizalaslan, M.A. Aksan, Magnetocaloric Properties of Ni-Rich Ni50-xCoxMn38Sn12B3 Shape Memory Ribbons, J Supercond Nov Magn 34(2) (2021) 581-588.

[37] C. Garcia, V. Zhukova, S. Shevyrtalov, M. Ipatov, P. Corte-Leon, A. Zhukov, Tuning of magnetic properties in NiMn-Ga Heusler-type glass-coated microwires by annealing, J Alloy Compd 838 (2020) 155481.

[38] J.D. Santos, T. Sanchez, P. Alvarez, M.L. Sanchez, J.L. Sánchez Llamazares, B. Hernando, L. Escoda, J.J. Suñol, R. Varga, Microstructure and magnetic properties of Ni50Mn37Sn13 Heusler alloy ribbons, J Appl Phys 103(7) (2008) 07B326.

[39] J. Mohanty, A. Persson, D. Arvanitis, K. Temst, C. Van Haesendonck, Direct observation of frozen moments in the NiFe/FeMn exchange bias system, New Journal of Physics 15(3) (2013) 033016.

[40] P.J. Brown, A.P. Gandy, K. Ishida, R. Kainuma, T. Kanomata, K.U. Neumann, K. Oikawa, B. Ouladdiaf, K.R.A. Ziebeck, The magnetic and structural properties of the magnetic shape memory compound Ni2Mn1.44Sn0.56, Journal of Physics: Condensed Matter 18(7) (2006) 2249-2259.

[41] X. Zhang, H. Zhang, M. Qian, L. Geng, Enhanced magnetocaloric effect in NiMnSn-Co alloys with two successive magnetostructural transformations, Sci Rep-Uk 8(1) (2018) 8235.

[42] G.R. Raji, A.P. Paulose, R.B. Job, S. Thomas, K.G. Suresh, M.R. Varma, Phase transformations, inverse magnetocaloric effect and critical behavior of Ni50Mn36Sn14-xSix Heusler alloys, Intermetallics 82 (2017) 59-67.

[43] B.J.P.l. Banerjee, On a generalised approach to first and second order magnetic transitions, 12(1) (1964) 16-17.

[44] T.D. Shen, R.B. Schwarz, J.Y. Coulter, J.D. Thompson, Magnetocaloric effect in bulk amorphous Pd40Ni22.5Fe17.5P20 alloy, J Appl Phys 91(8) (2002) 5240-5245.

[45] J.Y. Law, V. Franco, L.M. Moreno-Ramírez, A. Conde, D.Y. Karpenkov, I. Radulov, K.P. Skokov, O. Gutfleisch, A quantitative criterion for determining the order of magnetic phase transitions using the magnetocaloric effect, Nature Communications 9(1) (2018) 2680.

[46] C.F.J.I.d.I.y.T. Sánchez Valdés, Large magnetic entropy change and refrigeration capacity around room temperature in quinary Ni41Co9-xFexMn40Sn10 alloys (x= 2.0 and 2.5), (2020).

[47] V. Chernenko, E. Cesari, V. Kokorin, I. Vitenko, The development of new ferromagnetic shape memory alloys in NiMn-Ga system, Scripta metallurgica et materialia 33(8) (1995) 1239-1244.

[48] T. Krenke, Untersuchung der martensitischen Umwandlung und der magnetischen Eigenschaften Mangan-reicher NiMn-In-und NiMnSn-Heusler-Legierungen.

[49] X.Q. Chen, F.J. Yang, X. Lu, Z.X. Qin, The way composition affects martensitic transformation temperatures of Ni–Mn–Ga Heusler alloys, 244(3) (2007) 1047-1053.

[50] V.A. Chernenko, Compositional instability of β-phase in NiMn-Ga alloys, Scripta Mater 40(5) (1999) 523-527.

[51] X. Jin, M. Marioni, D. Bono, S.M. Allen, R.C. O'Handley, T.Y. Hsu, Empirical mapping of Ni–Mn–Ga properties with composition and valence electron concentration, J Appl Phys 91(10) (2002) 8222-8224.

[52] C. Jiang, G. Feng, S. Gong, H. Xu, Effect of Ni excess on phase transformation temperatures of NiMnGa alloys, Materials Science and Engineering: A 342(1) (2003) 231-235.

[53] J.R. Gomez, R.F. Garcia, A.D. Catoira, M.R. Gomez, Magnetocaloric effect: A review of the thermodynamic cycles in magnetic refrigeration, Renew Sust Energ Rev 17 (2013) 74-82.

[54] S. Singh, L. Caron, S.W. D'Souza, T. Fichtner, G. Porcari, S. Fabbrici, C. Shekhar, S. Chadov, M. Solzi, C. Felser, Large Magnetisation and Reversible Magnetocaloric Effect at the Second-Order Magnetic Transition in Heusler Materials, Adv Mater 28(17) (2016) 3321-3325.

[55] T. Chabri, A. Venimadhav, T.K. Nath, Interplay of austenite and martensite phase inside martensite transition regime and its role on magnetocaloric effect and magnetoresistance in NiMnSn based Heusler alloy, Intermetallics 102 (2018) 65-71.

[56] K. Dadda, S. Alleg, S. Souilah, J.J. Sunol, E. Dhahri, L. Bessais, E.K. Hlil, Critical behavior, magnetic and magnetocaloric properties of melt-spun Ni50Mn35Sn15 ribbons, J Alloy Compd 735 (2018) 1662-1672.

[57] A.G. Varzaneh, P. Kameli, T. Amiri, K.K. Ramachandran, A. Mar, I.A. Sarsari, J.L. Luo, T.H. Etsell, H. Salamati, Effect of Cu substitution on magnetocaloric and critical behavior in Ni47Mn40Sn13−xCux alloys, J Alloy Compd 708 (2017) 34-42.

[58] P. Czaja, W. Maziarz, J. Przewoznik, C. Kapusta, L. Hawelek, A. Chrobak, P. Drzymala,

M. Fitta, A. Kolano-Burian, Magnetocaloric properties and exchange bias effect in Al for Sn substituted Ni48Mn39.5Sn12.5 Heusler alloy ribbons, J Magn Magn Mater 358 (2014) 142-148.

[59] L. Trombi, F. Cugini, R. Rosa, N.S. Amadè, S. Chicco, M. Solzi, P. Veronesi, Rapid microwave synthesis of magnetocaloric Ni–Mn–Sn Heusler compounds, Scripta Mater 176 (2020) 63-66.

[60] Y. Zhang, L. Zhang, Q. Zheng, X. Zheng, M. Li, J. Du, A. Yan, Enhanced magnetic refrigeration properties in Mn-rich NiMnSn ribbons by optimal annealing, Sci Rep-Uk 5(1) (2015) 11010.

# CHAPTER 5: The effect of Thermal Post-processing Treatment on Laser Powder Bed Fusion Processed NiMnSn-based Alloy for Magnetic Refrigeration

## 5.1 Abstract

Using laser powder bed fusion (PBF-LB), this study aims to investigate the effects of heat treatment (HT) time (one, two, and three weeks) on the microstructure and magnetocaloric effect (MCE) of Ni-Mn-Sn alloys. The as-fabricated and heat-treated samples show typical columnar grains. With increased annealing time, chemical homogeneity improves, and highly ordered cubic $L2_1$ austenite is observed in the microstructure at room temperature. The local misorientation imparted by the PBF-LB process significantly decreased after the two and three weeks' HT process. When increasing the annealing time from one week to three, the maximum magnetic entropy change ($\Delta S_m$) values around the martensitic transition temperature ($T_M$) increased from about 0.2 J $kg^{-1}$ $K^{-1}$ to 0.45 J $kg^{-1}$ $K^{-1}$ when applying a 1 T field. However, the $\Delta S_m$ of the sample went through one week HT around the curie temperature ($T_c$) (0.90 $Jkg^{-1}K^{-1}$ at 315 K) is a little bit lower than the sample went through three week HT (0.94 $Jkg^{-1}K^{-1}$ at 320 K) and the sample went through two week HT (0.99 $Jkg^{-1}K^{-1}$ at 320 K).

*Keywords:* Laser powder bed fusion, Magnetocaloric material, Heat treatment, XRD, TEM, and SEM-EBSD.

## 5.2 Introduction

Compared with traditional cooling technologies, magnetic refrigeration has advantages such as producing lower noise, higher efficiency and being environmentally friendly [1]. Several magnetocaloric materials have been investigated for magnetic refrigeration, especially rare-earth-based alloys [2]. Heusler alloys (HAs) are the most suitable candidate due to their lower cost, non-toxic properties, and excellent magnetocaloric effect (MCE) [3, 4]. The Ni-Mn-Sn alloy is an intermetallic compound and is very brittle [5], and therefore traditional machining methods are unsuitable for manufacturing heat exchangers with complex shapes. Laser powder bed fusion (PBF-LB) is an effective method for manufacturing heat exchangers with high surface-to-volume ratios without the need for machining, therefore reducing material loss.

The higher cooling rates induced in PBF-LB result in an inhomogeneous microstructure when building parts using in-situ alloyed powder [6], this leads to local variations in chemical composition, which significantly influences the magnetocaloric performance. There are many studies on the effect of heat treatments (HT) on the microstructure and magnetic properties of arc-melted Ni-Mn-Sn-based alloys [7, 8]. The nanocrystalline state and annealing process is essential in determining martensite structure and transition temperature [9, 10]. Annealing affects the exchange interaction and properties by modifying short-range interactions [11]. Dan et al.[12] studied $Ni_{50}Mn_{50-x}Sn_x$ alloys with a wide range of Sn-concentration (x=0–40),

fabricated by arc-melting and subsequent annealing. Improving the composition uniformity is essential for PBF-LB fabricated NiMnSn parts, to ensure a consistent working temperature in the magnetic refrigeration field. Ghosha and Mandal [13] prepared a series of $Ni_{50}Mn_{36.5}Sn_{13.5}$ samples with various HTs (annealing 0, 6, 12, 18, and 24 h at 1173 K, followed by ice water quenching) and studied their magnetocaloric properties. Magnetic hysteresis and (the magnetic entropy change) ΔS increased with increasing annealing times, from 0 to 24 h. There have been reports of additional phases observed ($Ni_3Sn_2$ and $Mn_{1.77}Sn$) in melt-spun ribbons where cooling rate is in the order of ~$10^6$ K/s [14]. The Heusler structure ($L2_1$) is energetically the most favourable for formation [15]; however, it is challenging to obtain a homogeneous phase distribution, with up to 5% of $Ni_3Sn_2$ detectable within the microstructure [15, 16].

This study aims to optimise the HT process and manufacture $Ni_{50}Mn_{37}Sn_{13}$ HAs with higher MCE using PBF-LB in-situ alloying as a low-cost approach and alternative to the pre-alloyed powder. The microstructural changes, including segregation, the chemical composition and MCE were studied for PBF-LB samples treated with different HT processes.

## 5.3 Experimental

### 5.3.1 In-situ Powder

To fabricate in-situ Ni-Mn-Sn bulk HAs, Ni, Mn, and Sn elements were blended in stochiometric amounts. The properties of these raw materials are detailed in Table 5.1. The in-situ powders were mixed for two days in an argon atmosphere. Fig. 5.1 presents the schematic

of blending processing and the blend powders' morphology. Additional 2 at.% Mn and 1 at.% Sn powders were added to compensate for the evaporation of Mn and Sn elements during the PBF-LB process.

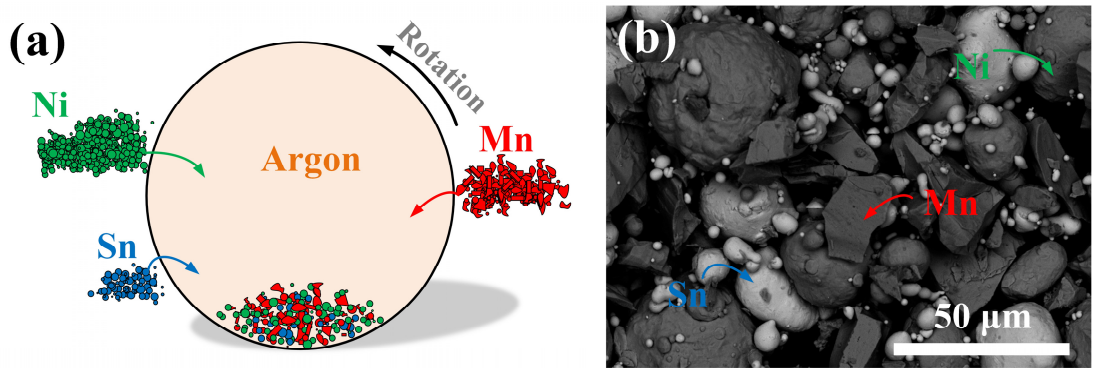



**Fig. 5.1. (a) The backscattered electron image and the corresponding EDX elemental map of NiMnSn blended powder. (b) The schematic of the powders blending processing.**

**Table 5.1. The information about powders.**

| Elements | Ni | Mn | Sn |
|---|---|---|---|
| The size range (μm) | 20~45 | <44 | <45 |
| The shape of the powder | Spherical | cubic | Spherical |
| Melting point (℃) | 1455 | 1426 | 231.9 |
| Boiling point (℃) | 2913 | 2061 | 2602 |

## 5.3.2 PBF-LB processing and heat treatment

Ni-Mn-Sn bulk HAs (5×5×10 mm) were fabricated via the PBF-LB technique. These bulk samples were manufactured on top of a steel substrate in a controlled argon environment ($O_2$<1000 ppm) using a Concept Laser M2 machine with a continuous wave mode Yb-fibre

laser (λ=67 nm, maximum laser power=400 W) as a primary heat source for melting. A 90˚ raster scan strategy was used to PBF-LB Ni-Mn-Sn bulk samples, as shown in Fig. 5.2. Table 5.2 shows the PBF-LB processing parameters and HT processes used for each of the samples in this study. Samples were encapsulated in separate quartz tubes in argon, and individually heat treated at 940 ℃ for different times before quenching into water (see Table 5.2).

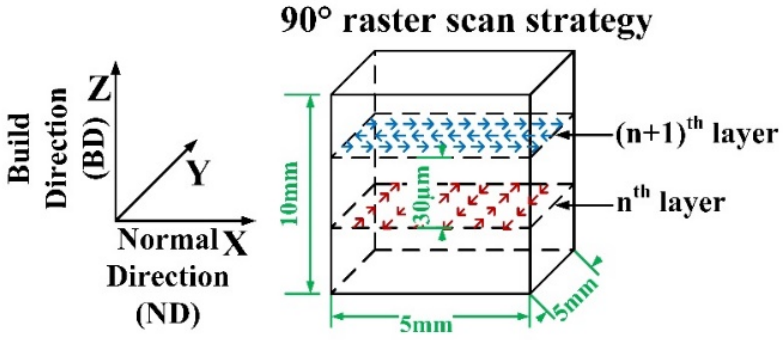



**Fig. 5.2. The scan strategy.**

**Table 5.2. The investigated PBF-LB processing parameters.**

| No. | Laser Power (W) | Scan Speed (mm/s) | Thickness (mm) | Scan spacing (mm) | The volume Energy density (J/mm$^3$) | The heat treatment process |
|---|---|---|---|---|---|---|
| As-Fabricated | 125 | 1750 | 0.03 | 0.05 | 47.62 | / |
| No.1 | | | | | | 940 ℃-1 week-Quench |
| No.2 | | | | | | 940 ℃-2 weeks-Quench |
| No.3 | | | | | | 940 ℃-3 weeks-Quench |

## 5.3.3 Microstructural characterisation and magnetic measurements

Microstructure at room temperature was examined using a backscattering Hitachi TM3030 scanning electron microscope (SEM). The SEM (Quanta 3D FEG) with EBSD analysed the

misorientation (the step size is 1.5 μm). Channel 5 software analysed the EBSD data. X-ray diffraction (XRD) with Cu-Kα radiation (λ = 1.5406 Å) analysed phases within the PBF-LBed samples at room temperature. The magnetic measurements were performed using a superconducting quantum interference device (SQUID) magnetometer magnetic properties measurements system. The temperature-dependent magnetisation curves (M-T curves) was obtained in zero-field cooled warming (ZFCW), field-cooled cooling (FCC), and field-cooled warming (FCW) modes at 0.01 T and 1 T, all to investigate the magnetic phase transitions and hysteresis. The isothermal magnetisation curves near the magnetic transition temperature were measured every 5 K under applied magnetic fields up to 1 T. The change in magnetic entropy ($\Delta S$) is calculated using Maxwell's relation [1] (Eq. 5.1), where $H_F$: the final magnetic field strength; $H_I$: the initial magnetic field strength).

$$\Delta S = \int_{H_I}^{H_F} \left(\frac{\partial M}{\partial T}\right)_H dH \tag{5.1}$$

# 5.4 Result and discussion

## 5.4.1 Microstructure

### 5.4.1.1 Influence of HT process on the microstructure and phase formation

SEM micrographs for the as-fabricated (AF) and heat-treated (HT) samples are shown in Fig. 5.3. After HT, the Sn segregations cannot be observed as the high HT temperature (940 °C) makes the Sn segregations disappear. The Ni element is a based alloying element. Mn segregations are observed even after the three weeks' HT process. Fig. 5.3 f and the

corresponding EDX map show a Mn segregation which contains oxygen elements, which is also proved by the EDX result in Fig. 5.5.

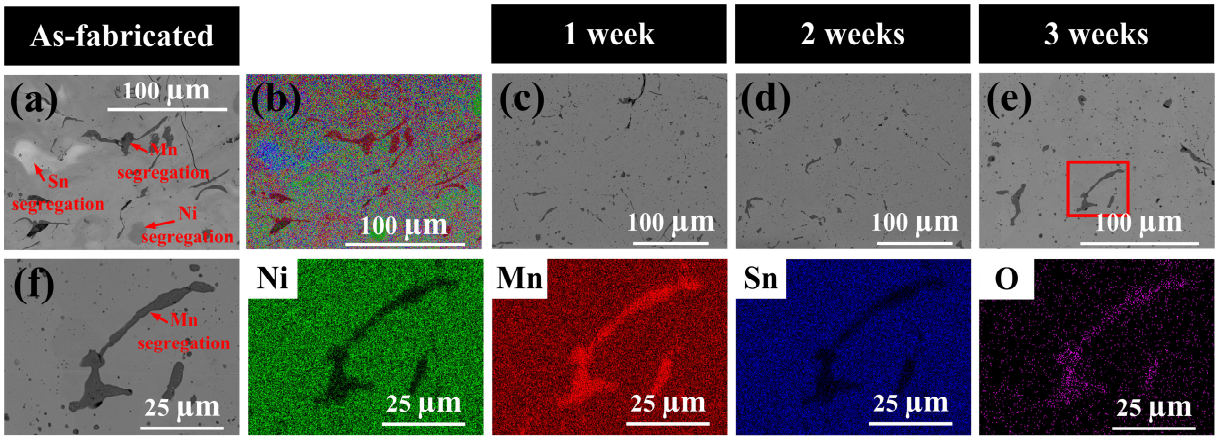



**Fig. 5.3. SEM-BSE micrographs of the microstructure of (a) the as-fabricated sample; (b) the Mixed EDX map for the as-fabricated sample; (c, d, e) the HT samples; (e) and (f) the Mn segregation (red box in (e)).**

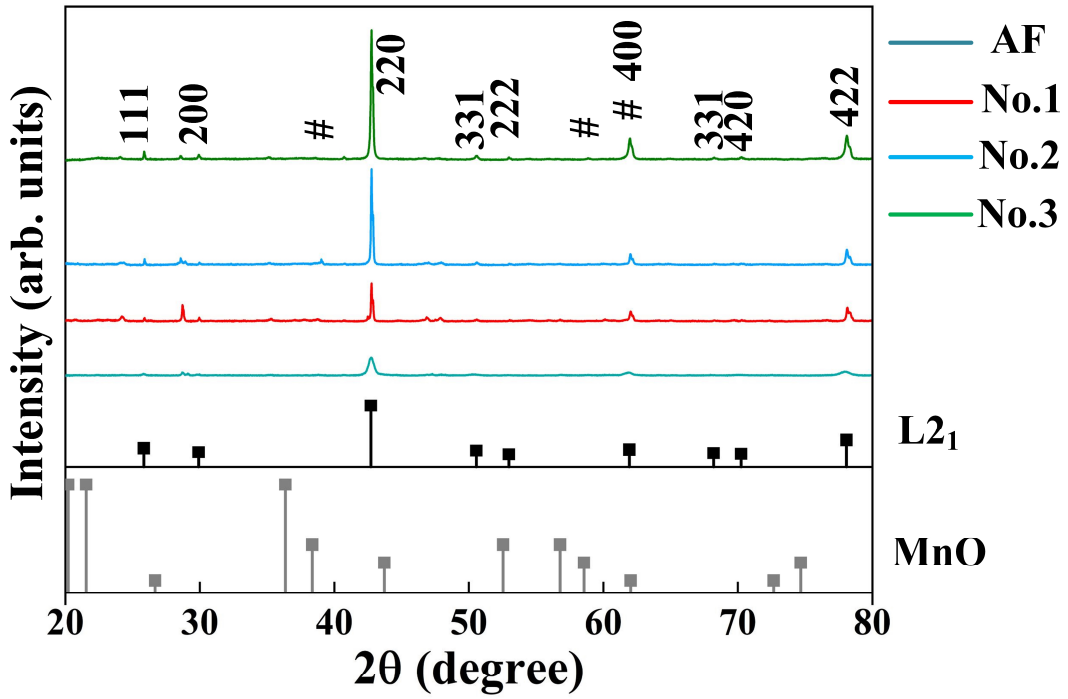



**Fig. 5.4. XRD patterns of AF and annealed PBF-LB processed NiMnSn alloys. The # peaks fit the MnO phase. Other peaks correspond to the $L2_1$ Heusler phase.**

Fig. 5.4 shows the XRD results with different HT times at room temperature. The AF sample shows the $L2_1$ austenite phase at room temperature. After HT all three samples displayed highly ordered cubic $L2_1$ austenite phase at room temperature, with minor peaks relevant to MnO. Mn is highly sensitive to oxygen, therefore MnO was observed within the structure due to oxygen infiltration during the PBF-LB process [17].

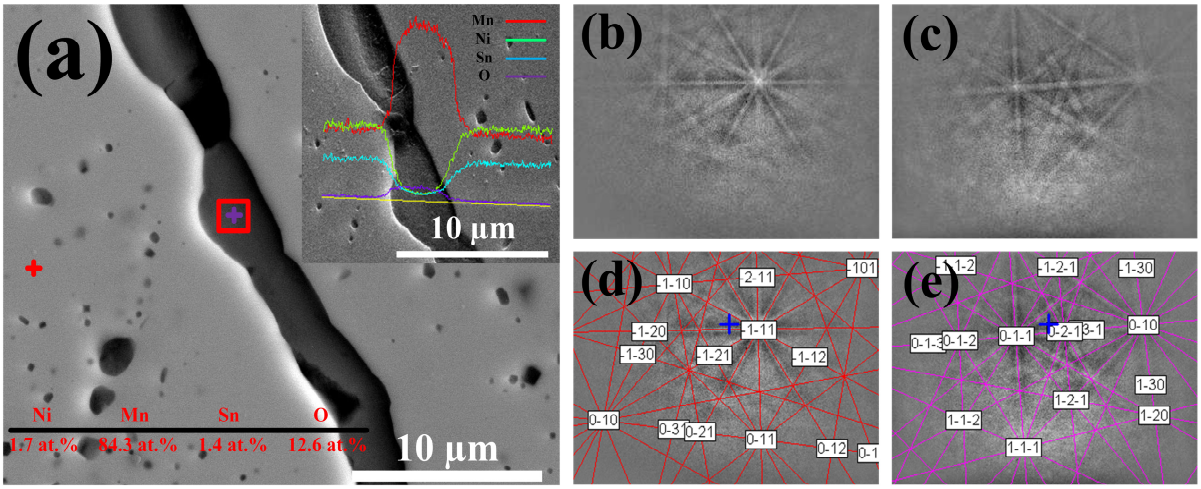



**Fig. 5.5. (a) The SEM picture of the No.3 sample (the inset picture is the EDX line analysis); (b and d) the EBSD Kikuchi pattern from $L2_1$ $Ni_2MnSn$ structure in the No.3 sample; (c and e) the EBSD Kikuchi pattern from MnO structure in the No.3 sample.**

To confirm the structure of segregated Mn, the diffraction pattern (Kikuchi pattern) was obtained using EBSD, as shown in Fig. 5.5. The red cross shows the Kikuchi pattern (Figs. 5.5 b) and d)) from the $L2_1$ $Ni_2MnSn$ structure, which is the primary phase. The Kikuchi pattern also confirmed the MnO cubic phase within the regions of Mn segregation. The EDX line analysis result was obtained through the Mn segregation, as shown in the inset picture in Fig. 5.5 a). The O and Mn elements increased significantly, especially the Mn, whereas the Ni and

Sn concentrations have significantly decreased in this region. The EDX compositional analysis shows that the small area of Mn segregation contains 1.7 at.% Ni, 84.3 at.% Mn, 1.4 at.% Sn, and 12.6 at.% O elements, as shown in the inset table in Fig. 5.5 a).

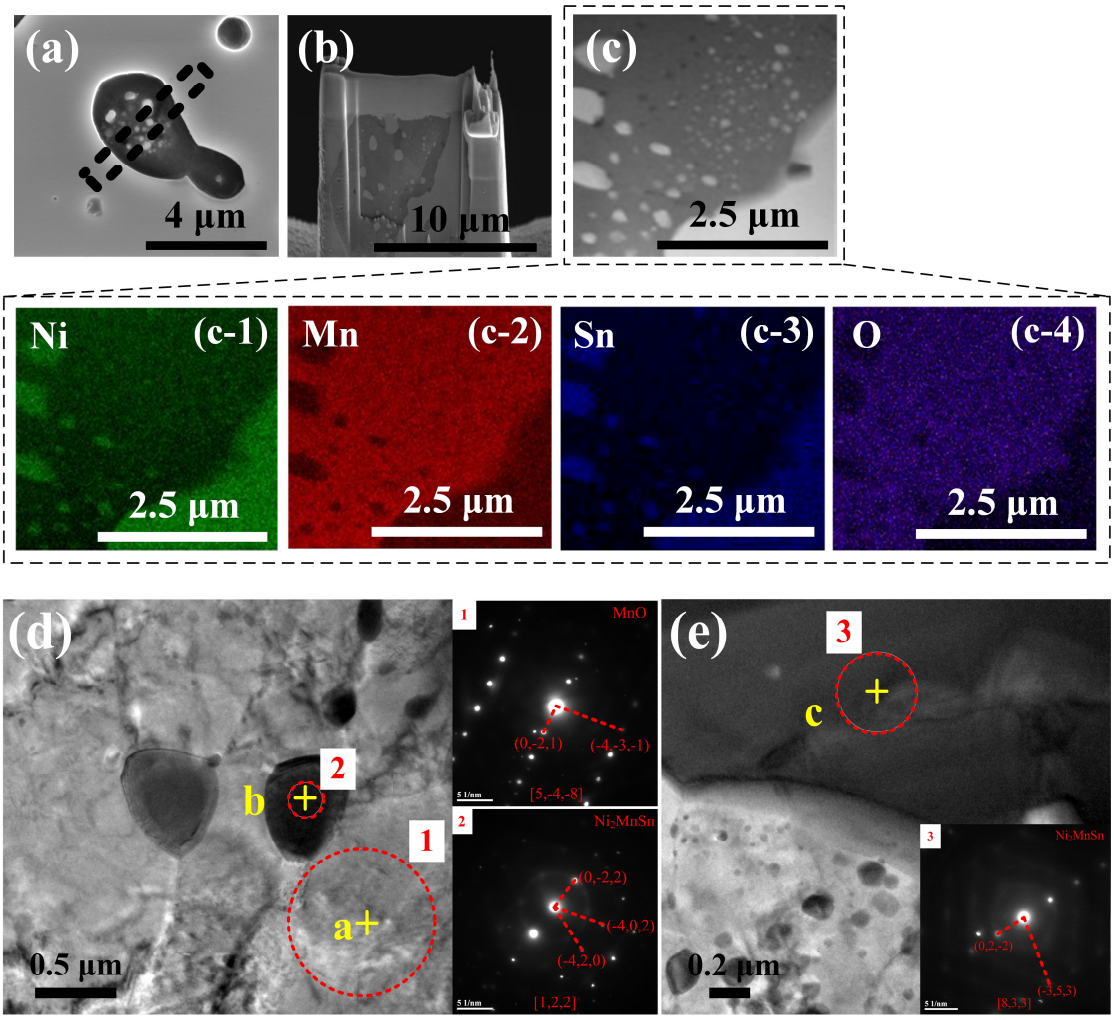



**Fig. 5.6. (a) The SEM picture of the No.3 sample (the inset picture is the EDX line analysis); (b and d) the EBSD Kikuchi pattern from $L2_1$ $Ni_2MnSn$ structure in the No.3 sample; (c and e) the EBSD Kikuchi pattern from MnO structure in the No.3 sample.**

Table 5.3 and Fig. 5.6 illustrate the chemical composition, morphology, and distribution of secondary phases within the No. 3 sample using TEM. The Mn-rich phases (dark grey phase in

Figs. 5.6 a)-c)) can be seen clearly. The selected area electron diffraction (SAED) in the 1st red dotted circle and the EDX at point **a** further show the Mn-rich phase contains MnO. The NiSn-rich phases (white phases) in the Mn-rich region (see Fig. 5.6 a)) are $L2_1$-type $Ni_2MnSn$ phases, as proven by the SAED in the 2nd red dotted circle and the EDX at point **b**. The crystal structure of the base metal is also the $L2_1$-type phase (see the SAED in the 3rd red dotted circle **c**, as shown in Fig. 5.6 e)). However, the chemical composition of the base metal differs from the white phases, as shown in Table 5.3. The EDX at point **d** with high Mn at.% proved the appearance of Mn segregation. MnO is a face-centred cubic antiferromagnetic phase [18] which has been shown to have deleterious effects on the MCE of these alloys [19].

**Table 5.3. Average chemical composition analysis in at.% of the No.3 sample at different points using SEM-EDX.**

| Point | Ni (at.%) | Mn (at.%) | Sn (at.%) | O (at.%) |
|---|---|---|---|---|
| a | 0.3 | 49.2 | 0.2 | 50.4 |
| b | 45.3 | 23.5 | 29.1 | 2.2 |
| c | 51.7 | 28.9 | 18.3 | 1.2 |
| d | 0.8 | 94.0 | 0.4 | 4.8 |

As shown in the SEM pictures in Fig. 5.7, the Mn segregation was observed within all samples, proving that the HT process cannot make the Mn segregations disappear. All grains within PBF-LB samples are equiaxed. Fig. 5.7 also shows the inverse pole figure (IPF) images of the AF and HT samples. The different colours within IPF images represent the different orientations of

the unit cells across the grains. As shown in Figs. 5.7 c, g, k, and o, all samples exhibited various colours, demonstrating how the samples did not possess strong preferential orientations.

A kernel-averaged misorientation (KAM) map estimates the plastic strain in individual grains, revealing local variations in lattice orientations and suggesting the change of dislocation density in the material [20, 21]. Figs. 5.7 d, h, l, and p present KAM maps of the PBF-LB Ni-Mn-Sn alloys in AF and HT conditions. Higher local misorientation was observed in the AF sample (Fig. 5.7 d), with an average KAM value of 0.34. Due to the complex thermal cycling, the rapid heating and solidification cycles in the PBF-LB process, plastic strain and residual stresses are created in the AF samples, which induced a higher dislocation density [22, 23]. In contrast, the KAM map of the No.1 sample presents a slight decrease in misorientation. The average KAM value decreased to 0.31. When the annealing time increased to two and three weeks, the average local misorientation within samples was further reduced to 0.21 and 0.23 respectively, indicating the internal plastic strain is mostly relieved [21]. The local misorientation within the PBF-LB samples decreased with the increasing annealing time as the rate of atomic diffusion increased and atoms preferred to move from high- to low-stress regions at high temperatures (940 °C) [23]. The KAM is often used as a qualitative measure of localised plastic deformation [24, 25]. Strain can indirectly represent residual stresses [26]. The HT processes (two weeks and three weeks) remove almost all local misorientation (see Fig. 5.7) and therefore, can release stored strain and residual stresses imparted by the PBF-LB process.

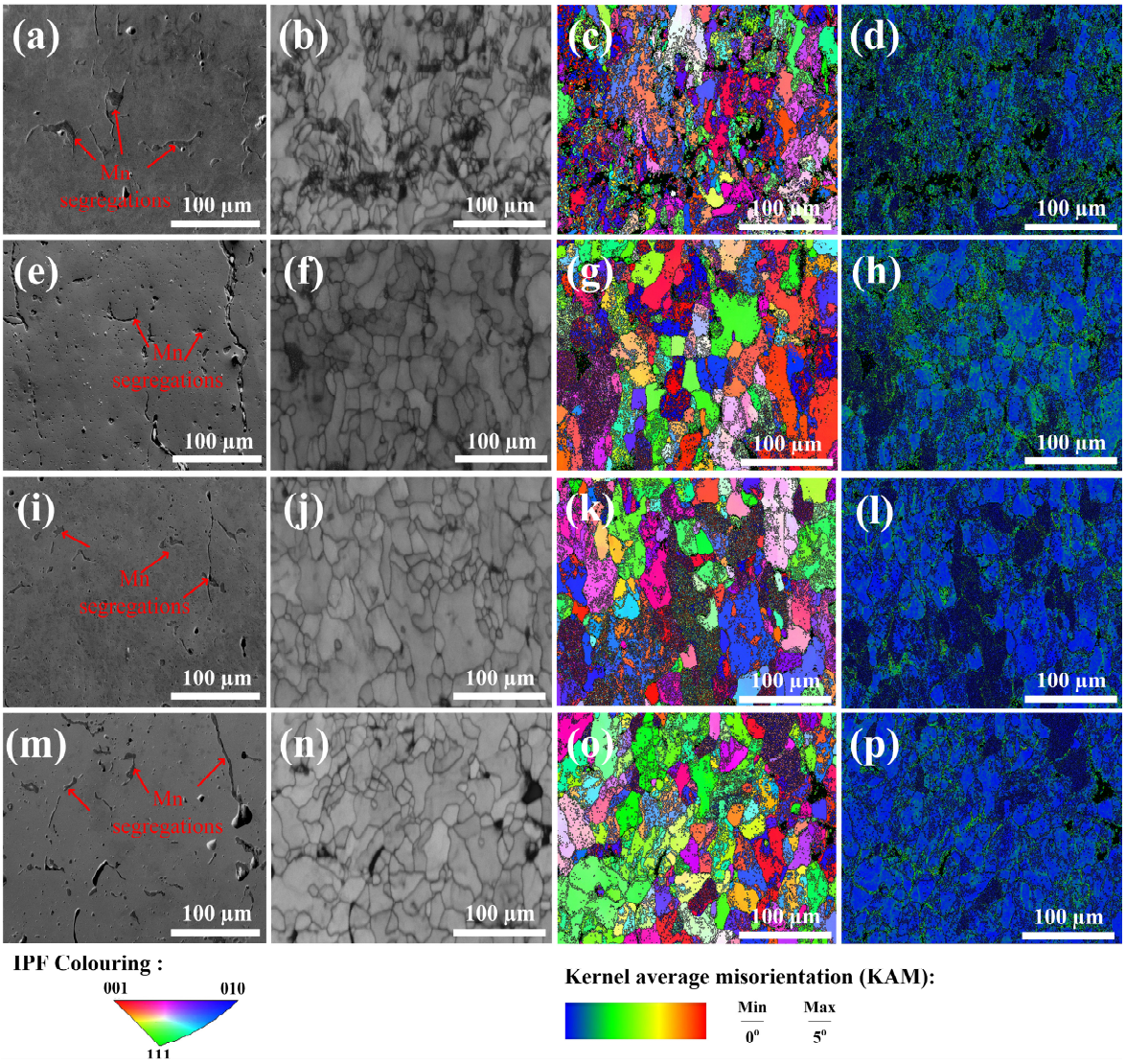



**Fig. 5.7. EBSD analyses of the PBF-LBed NiMnSn alloy (X-Z section) annealed at 940 °C (the SEM picture, corresponding image quality maps, IPF map, and KAM map): (a-d) as-fabricated sample, (e-h) annealed for one week, (i-l) annealed for two weeks, (m-p) annealed for three weeks.**

### 5.4.1.2 Composition evolution

The composition evolution also plays a vital role in the NiMnSn alloys' magnetic properties as the three elements' radio affect the characteristic transformation temperatures and the MCE [12, 27, 28]. To investigate the chemical composition evolution upon annealing time of PBF-LBed

NiMnSn alloys, the SEM-EDX shows the small areas' chemical composition within each sample. The five random tiny areas without massive Mn segregation within three different random areas of each sample (the total is 15 tiny areas) were selected for the SEM-EDX test. The composition of the 15 tiny regions for each sample is defined as $Ni_{Ci}$, $Mn_{Ci}$, and $Sn_{Ci}$ ($i$ is from 1 to 15). $Ni_{C0}$, $Mn_{C0}$, and $Sn_{C0}$ are the average chemical composition. The composition deviation of Ni, Mn, and Sn elements ($\zeta_{Ni}$ , $\zeta_{Mn}$ , and $\zeta_{Sn}$) and the composition deviation ($\zeta$) for all components are introduced and calculated regarding the Eqs. 5.2-5.5 [29]. The composition deviation of Oxygen should not be calculated as Oxygen always combines with the Mn segregation.

$$\zeta_{Ni} = [(Ni_{C1} - Ni_{C0})^2 + (Ni_{C2} - Ni_{C0})^2 + \cdots + (Ni_{C15} - Ni_{C0})^2]/15 \quad (5.2)$$

$$\zeta_{Mn} = [(Mn_{C1} - Mn_{C0})^2 + (Mn_{C2} - Mn_{C0})^2 + \cdots + (Mn_{C15} - Mn_{C0})^2]/15 \quad (5.3)$$

$$\zeta_{Sn} = [(Sn_{C1} - Sn_{C10})^2 + (Sn_{C2} - Sn_{C0})^2 + \cdots + (Sn_{C15} - Sn_{C0})^2]/15 \quad (5.4)$$

$$\zeta = \zeta_{Ni} + \zeta_{Mn} + \zeta_{Sn} \quad (5.5)$$

As shown in Table 5.4, although different HT processes did not affect the average chemical composition much, they reduced the composition deviation. The composition deviation ($\zeta$) decreased from 0.413 to 0.339 with the increasing HT time, which means the chemical composition is more uniform when increasing the HT time. The $\zeta_{Mn}$ and $\zeta_{Sn}$ decreased from 0.175 and 0.161 to 0.062 and 0.023, respectively, when the HT time increased from one week to three weeks. As the long annealing time improves the Mn and Sn elements' diffusion within

the PBF-LBed samples. The O and corresponding Mn elements were deleted to obtain the matrix's accurate chemical composition and the valence electron concentration (e/a). The O always combines with the Mn element to produce MnO, as shown in Fig. 5.3, 5.5, and 5.6. As shown in Table 5.4, the e/a of the No.1 sample was the biggest (8.038), then it decreased to 8.027 and 8.029 for No.2 and No.3, respectively. Although the three samples' e/a caused by the chemical composition shows slight differences, it also affects the characteristic temperature of structural transition (as shown in Fig. 5.9-5.10 and Table 5.5) as FOPT is sensitive to chemical composition changes [27, 30].

**Table 5.4. The average chemical composition and the composition deviation for PBF-LBed samples with different HT processes.**

| Sample | Average Composition | Average Composition without MnO | $\zeta$ | $\zeta_{Ni}$ | $\zeta_{Mn}$ | $\zeta_{Sn}$ | e/a |
|---|---|---|---|---|---|---|---|
| No.1 | $Ni_{48.0}Mn_{32.9}Sn_{15.7}O_{3.4}$ | $Ni_{51.5}Mn_{31.6}Sn_{16.9}$ | 0.413 | 0.078 | 0.175 | 0.161 | 8.038 |
| No.2 | $Ni_{48.1}Mn_{32.5}Sn_{16.1}O_{3.2}$ | $Ni_{51.5}Mn_{31.3}Sn_{17.2}$ | 0.343 | 0.178 | 0.130 | 0.035 | 8.027 |
| No.3 | $Ni_{47.8}Mn_{33.5}Sn_{15.6}O_{3.0}$ | $Ni_{50.9}Mn_{32.5}Sn_{16.6}$ | 0.339 | 0.254 | 0.062 | 0.023 | 8.029 |

## 5.4.2 Magnetic properties

### 5.4.2.1 Thermo-magnetisation curves

Fig. 5.8 a shows the thermo-magnetisation curve in an applied field of 0.01 T, with Fig. 5.8 b showing dM/dT vs Temperature for HT Ni-Mn-Sn alloys. The AF sample's magnetisation does not show the structural transformation. In contrast, the HT samples show different behaviours,

where the magnetisation remains constant with the increase in temperature up to 30K ($T^*$), as the spin moments are locked/frozen [21, 24]. The further temperature increases above T* increased the thermal energy of these spin moments, leading to unlocking and observing abrupt increases in magnetisation [21]. The HT samples show two transitions in an applied field of 0.01 T. At 150 K, the martensite-austenite structural transition occurred. The magnetic transition (from ferromagnetic to paramagnetic) occurred at the Curie temperature ($T_c$~320K, see Table 5.5). The AF sample did not observe any transition. The chemical composition is more uniform after long HT processes, as shown in Table 5.5. Therefore, a uniform chemical composition and homogeneity are more important factors affecting the magnetic properties of PBF-LB Ni-Mn-Sn alloys. The long HT process releases stress in the structure, re-ordering the Mn-Mn distance and enhancing the magnetisation [9, 31, 32]. Thus, the sample with the longest HT processing time (No .3) has more uniform chemical composition and homogeneity, and reduced stress, leading to more significant magnetisation. The $T_c$ of the samples are evident from the dM/dT vs Temperature curve in Fig. 8 b which shows that the variation in chemical composition and homogeneity had minimal effect on the $T_c$. In addition, there is no evidence of the Néel temperature for MnO, as there was only trace MnO present in these samples. This antiferromagnetic transition of MnO occurs around 120 K and shows only a slight kink in pure MnO, which is not apparent from these magnetisation measurements [33].

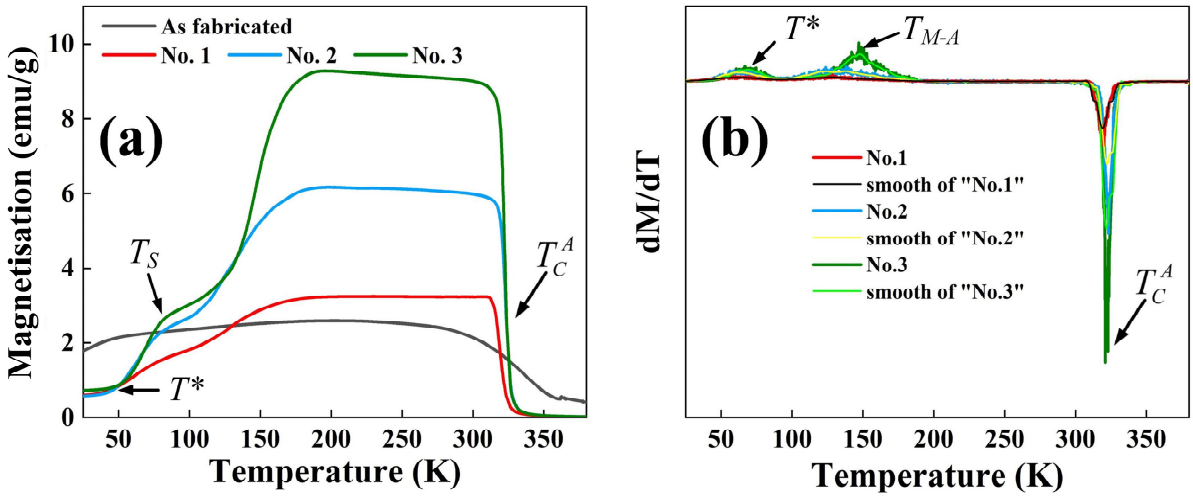



**Fig. 5.8. Thermo-magnetisation curves in an applied field of 0.01 T for the annealed PBF-LB processed NiMnSn alloys; the inset displays the dM/dT vs temperature for NiMnSn alloys.**

### 5.4.2.2 Temperature dependence of magnetisation at 1 T magnetic field

As shown in Fig. 5.9, the field cooling (FC) and field warming (FW) curves measured at 1 T were used to study the characteristics of the magnetic phase transformations. The FC and FH curves provided further evidence of the structural transformation in the annealed samples [34-36]. Thus, the transition around $T_M$ might be the weak first-order structural transformation (FOPT) [37]. The characteristic transformation temperatures for the structural transformation (austenitic start temperature ($A_s$), austenitic finish temperature ($A_f$), martensite start temperature ($M_s$), and martensite finish temperature ($M_f$)), as well as the thermal hysteresis ($\Delta T_{hys}$), are essential. These temperatures were calculated by extrapolating from both sides of bends in curves through intersections between straight lines [34, 35]. The martensitic transformation temperature ($T_M$) is determined as $((A_s+A_f+M_s+M_f)/4)$. The thermal hysteresis between the FC and FW curves was defined as the difference between $A_s$ and $M_f$ ($\Delta T_{hys}= A_s-$

$M_f$) [34, 35], confirming the nature of the martensite transition [31]. Table 5.5 shows the structural characteristic transformation temperatures at 1 T and $T_c$ at 0.01 T. With decreasing temperature (FC) from the $M_s$, the martensite phase increased, and the austenite phase decreased. The magnetisation decreased down to $M_f$, where all austenite phases transform into the martensite phase as the austenite phase possesses higher magnetisation than martensite [30]. When increasing the temperature (FW) from the $A_s$, the martensite phase transforms into austenite, and the magnetisation gradually increases until it reaches $A_f$. Here, all the martensite phase transforms into the austenite phase.

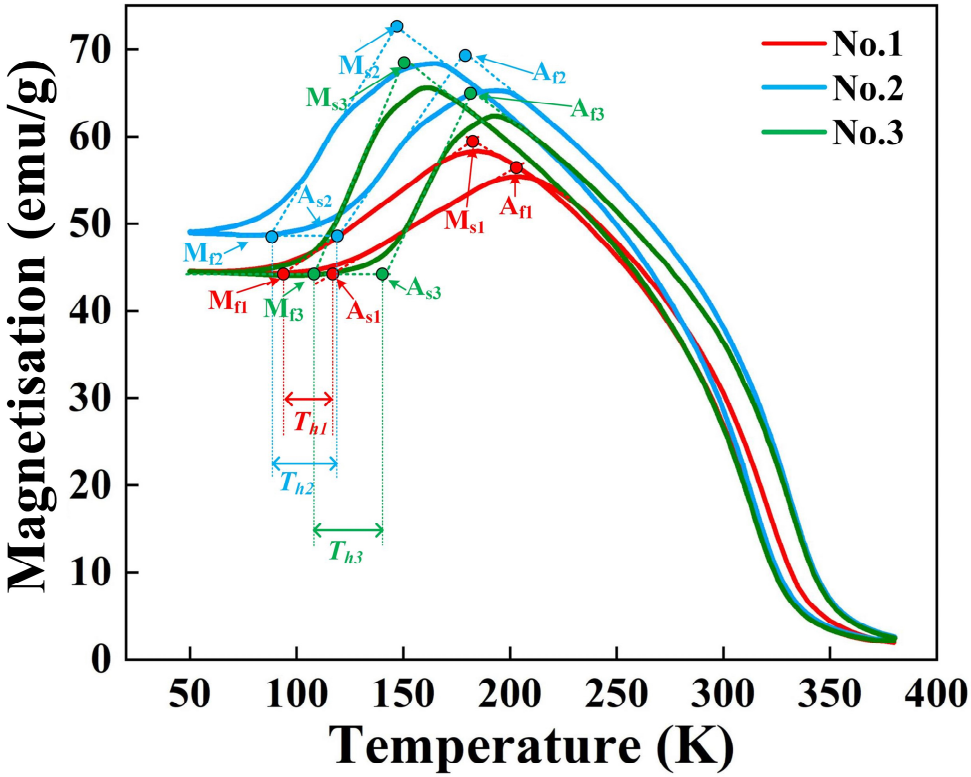



**Fig. 5.9. Thermo-magnetisation curves in an applied field of 1 T for the annealed PBF-LB processed NiMnSn alloys.**

**Table 5.5. The characteristic temperature of the magnetic phase transformation.**

| Sample | $M_s$ (K) | $M_f$ (K) | $A_s$ (K) | $A_f$ (K) | $T_c$(K) | $\Delta T_{hys}$ (K) | $T_M$(K) | $\Delta T_{int}$ (K) |
|---|---|---|---|---|---|---|---|---|
| No. 1 | 183 | 90 | 105 | 205 | 319.2 | 15 | 145.75 | 96.5 |
| No. 2 | 160 | 81 | 113 | 193 | 322.1 | 32 | 136.75 | 79.5 |
| No. 3 | 163 | 109 | 139 | 192 | 322.6 | 30 | 150.75 | 53.5 |

The $M_s$ (182 K) of No.1 is higher than the No.2 (146 K) and No.3 (150 K), as shown in Table 5.5. The $M_s$ value has been shown to be sensitive to the chemical composition and the Mn-excess [38, 39]. The Mn-excess atoms increase the e/a, as observed in No. 1, as such the energy of the system increases as the energy of the conduction electrons exceeded the Fermi level and move to the Brillouin zone's corners [3]. The lattice distortion (martensite transition) in these systems accommodates these corner states within a new zone pattern to achieve minimum free energy [40]. Thus, the increase in e/a leads to a higher $M_s$ [3]. The e/a decrease from sample No.1 to No.2 and increases again in case of the No.3, thus, the $M_s$ of No.1 and No.3 is higher than No.2. As shown in Table 5.5, the $T_c$ increased from 319.2 K to 322.6 K (under the field of 0.01 T) when the annealing time increased from one week to three. As shown in Table 5.4, the Ni content decreased with the increasing annealing time. The Ni atom has a lower moment than the Mn atom, and substituting the Ni atom for Mn results in the magnetic subsystem's dilution in the austenite phase [27]. Thus, the $T_c$ increased with the decreasing Ni atoms. In addition, residual stress is released and structurally relaxed with longer annealing time, which results in an improved $T_c$ [31].

### 5.4.2.3 Isothermal magnetisation

The isothermal magnetisation (M-H) curves were measured around the structural and magnetic transformation temperatures ($T_M$ and $T_c$) under a decreasing field (1 to 0 T). Fig. 5.10 shows the isothermal magnetisation M-H curves at different test temperatures (every 5 K) around $T_M$ (a, c, and e) and $T_c$ (b, d, and f) of three samples. The field scanning was performed from 1 to 0 T. From Figs. 5.10 a, c, and e, the magnetisation increased with increasing temperatures as the weak magnetic martensite gradually transformed into the strong magnetic austenite. Fig. 5.10 b, d, and f show that the austenite converted from ferromagnetic (FM) to paramagnetic (PM) states at higher temperatures, which led to a decrease in magnetisation.

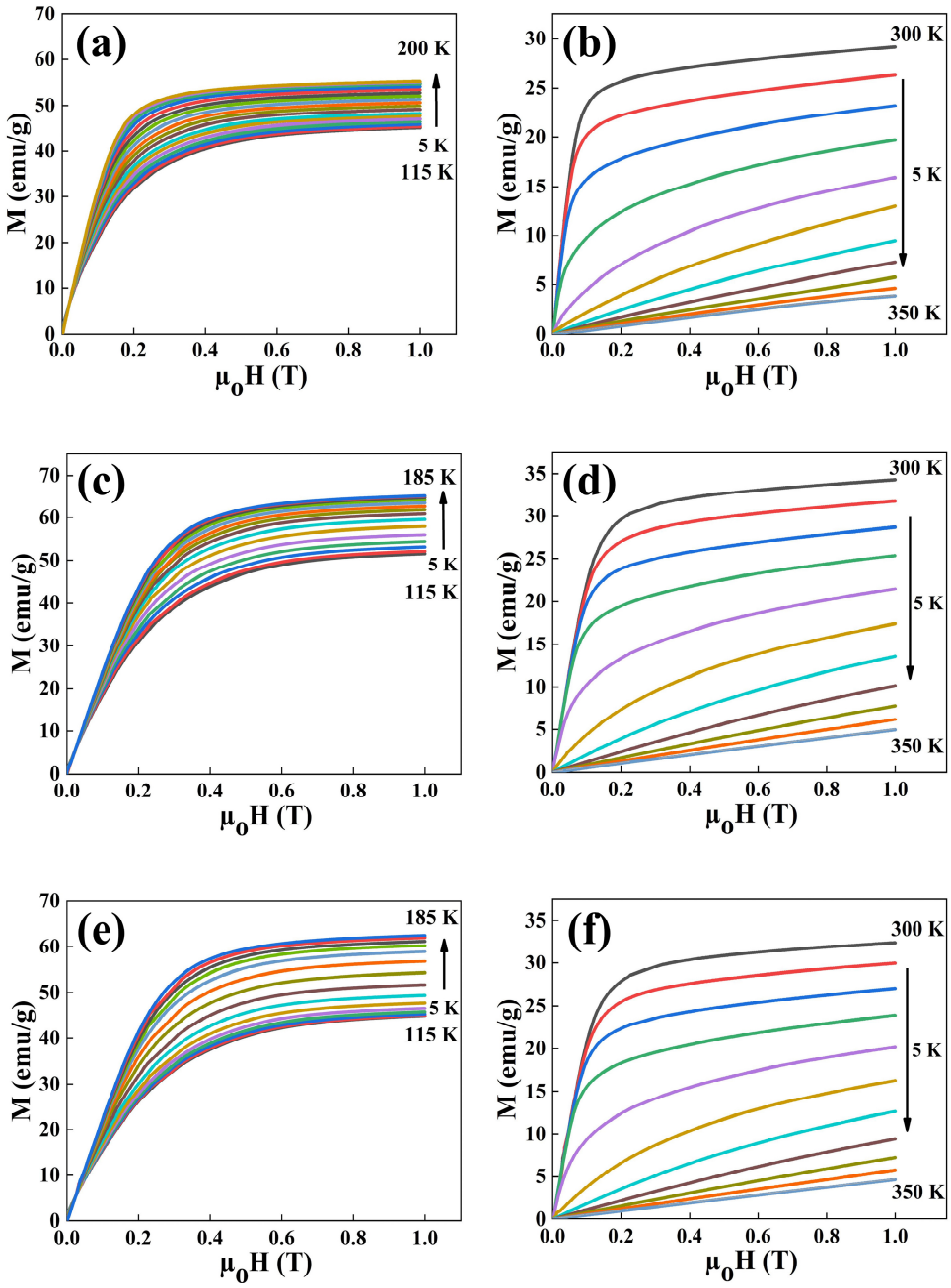



**Fig. 5.10. (a,c,e) Isothermal magnetisation curves of PBF-LBed NiMnSn samples with annealing time of one week, two weeks, and three weeks near the martensitic transition temperature; (b,d,f) Isothermal magnetisation curves of PBF-LBed NiMnSn samples with annealing time of one week, two weeks, and three weeks near the curie temperature of the austenite phase.**

The Arrott plots were employed to determine the nature of each magnetic transition, as shown in Fig. 5.11. The negative slope of Arrott plots around $T_M$ and $T_c$ indicates SOPT [41]. However, the existing magnetic hysteresis in the M-T curve (Fig. 5.9) confirmed the transition around the $T_M$ is FOPT [42]. Figs. 5.11 a, c, and e reveal the SOPT nature around the $T_M$ due to the weak FOPT around $T_M$. The suppression/weakness of the FOPT arises from the existing Mn segregation (see Figs. 5.5 and 5.6), the NiSn-rich phases within the $L2_1$ phase (see Fig. 5.6), and the inhomogeneous chemical composition. For Ni-Mn-Sn alloys with higher Sn content, FOPT is not observed [3, 27]. As the SOPT is observed on the Arrott plots, the magnetic field dependence of ΔS should vary according to Eq. 5.6 [43, 44]. In Eq. 5.6, **a** is a constant and the magnetic state of the sample determines **n** power [43]. The ΔS dependence on the magnetic field (see Eq. 5.7) confirmed the nature of the magnetic transition [45].

$$\Delta S = \mathbf{a}(\mu_0 H)^{\mathbf{n}} \tag{5.6}$$

Fig. 5.12 shows the value of the **n** constant is below 2, which is the case of SOPT around both $T_c$ and $T_M$ [46, 47].

$$\Delta S \alpha H^{\mathbf{n}} \tag{5.7}$$

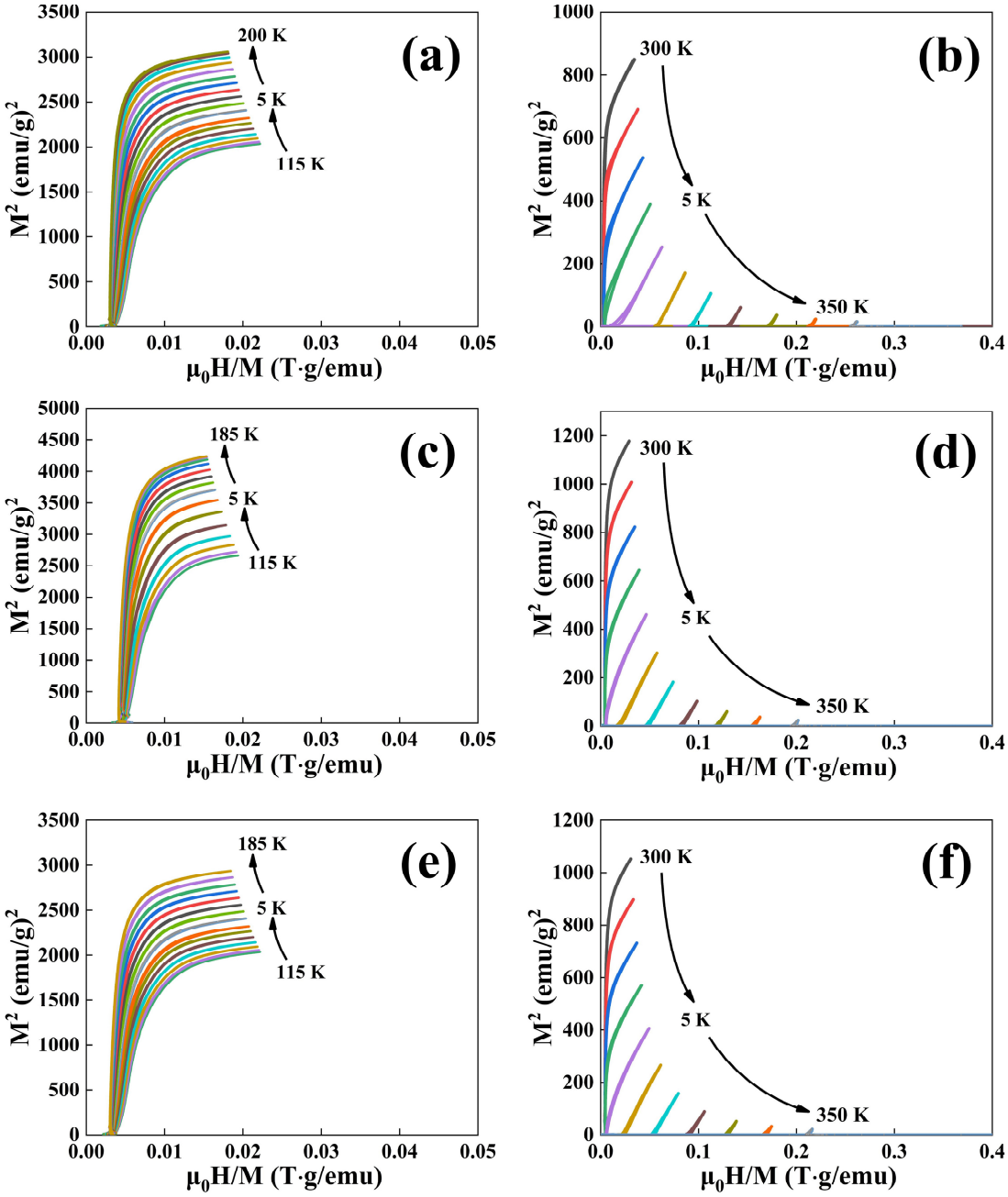



**Fig. 5.11. Arrott plots of annealed PBF-LBed block samples with annealing time of 1 week, 2 weeks, and 3 weeks near (a,c,e) the martensitic transition temperature and (b,d,f) near the curie temperature.**

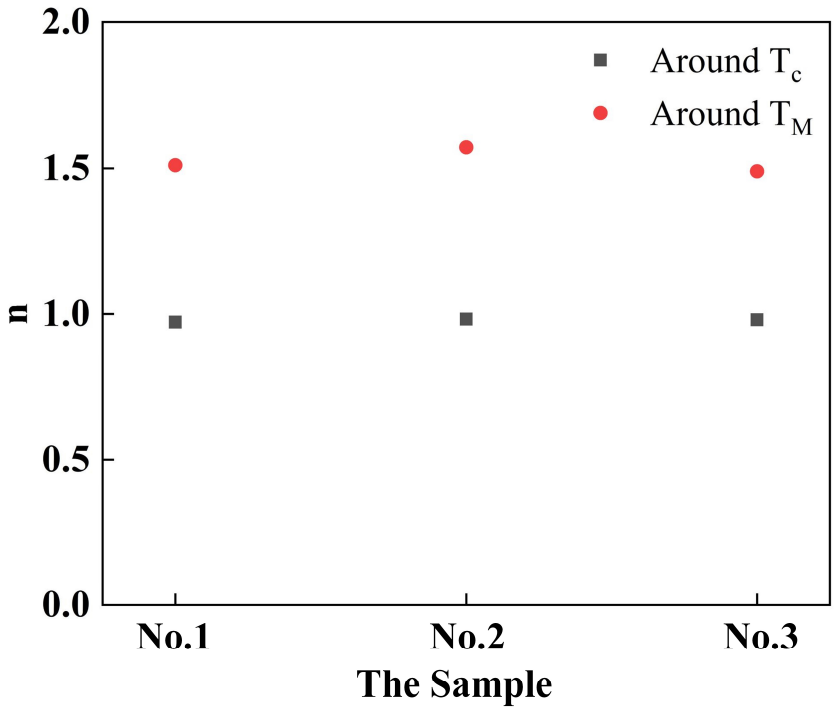



**Fig. 5.12. The value of n around the $T_c$ and $T_M$.**

### 5.4.2.4 Magnetocaloric effect (MCE)

Maxwell's relation (Eq. 5.1) is applied to calculate the magnetic entropy change under 1 T field near $T_c$ and $T_M$. As shown in Fig. 5.13 a, the maximum magnetic entropy change ($\Delta S_m$) values around the martensitic transition region increased from about 0.2 J $kg^{-1}$ $K^{-1}$ to 0.45J $kg^{-1}$ $K^{-1}$ when the HT time increased from one week to three. The No.2 and No.3 samples show better MCE than No.1, as the chemical composition is more homogeneous. As shown in Fig. 5.13 b, the $\Delta S_m$ of No.1 sample around $T_c$ (0.90 $Jkg^{-1}K^{-1}$ at 315 K) is slightly lower than No.3 (0.94 $Jkg^{-1}K^{-1}$ at 320 K) and No.2 (0.99 $Jkg^{-1}K^{-1}$ at 320 K).

Thus, the different annealing times did not significantly affect the MCE of the PBF-LB sample. This is to be expected as the FM order is almost entirely defined by the positive exchange interactions between the Mn and Ni atoms [48], thus, as the chemical composition (Table 5.4)

has minimal change with HT, this will also remain unchanged. Dan et al. also reported this phenomenon [12]. However, the temperature of $\Delta S_m$ of No.1 is lower than No.2 and No.3 samples due to different $T_c$.

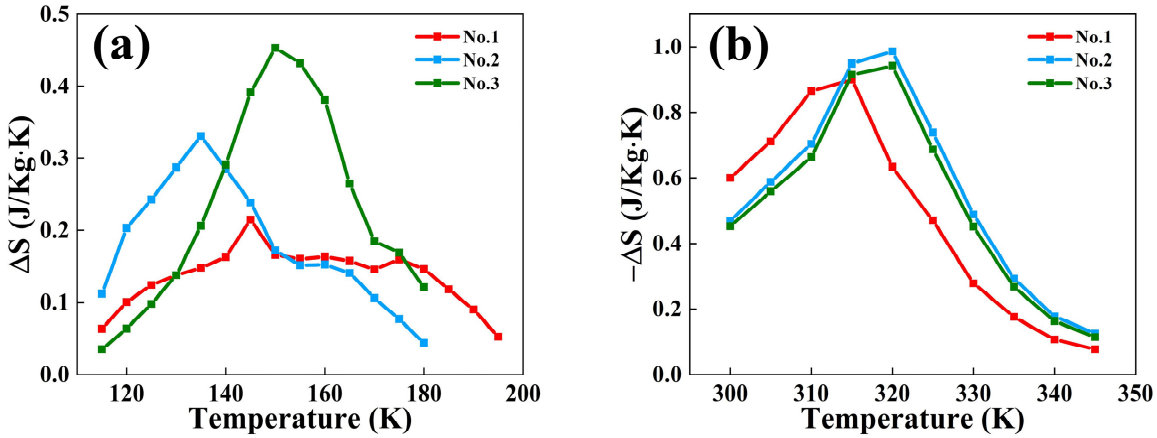



**Fig. 5.13. (a) the thermal variation of ΔS around the FOPT of the HTed block samples; (b) the thermal variation of ΔS around the SOPT of the HTed block samples.**

## 5.5 Conclusion

This study presents a distinct influence of the heat treatment (HT) process on applying Laser Powder Bed Fusion (PBF-LB) Ni-Mn-Sn Heusler Alloys for magnetic refrigeration applications. The following conclusions are drawn from this work:

1. All samples exhibited highly ordered cubic $L2_1$ austenite at room temperature. The Mn segregation was ubiquitous even after a three weeks' HT process. The Mn segregation contained oxygen elements and was confirmed by XRD, EBSD and TEM results to be MnO.

2. All grains within PBF-LB samples were equiaxed, and all samples did not possess strong

preferential orientations. The HT process relieved almost all stored strain and residual stresses imparted by the PBF-LB processes.

3. The chemical composition was more uniform when increasing the HT time, where composition deviation (ζ) decreased from 0.413 to 0.339 with the increasing HT time. Different chemical compositions resulted in different transition temperatures. The martensite start temperature (182 K) of samples HT for one week was higher than samples HT for two weeks (146 K) and three weeks (150 K), while the Curie temperature ($T_c$) increased from 319.2 K to 322.6 K with increased HT duration.

4. The maximum magnetic entropy change ($\Delta S_m$) values around $T_M$ increased from about 0.2 J $kg^{-1}$ $K^{-1}$ to 0.45 J $kg^{-1}$ $K^{-1}$ when the HT time increased from one week to three. Around $T_c$ the $\Delta S_m$ of the one week HT (0.90 $Jkg^{-1}K^{-1}$ at 315 K) was slightly lower than three week HT (0.94 $Jkg^{-1}K^{-1}$ at 320 K) and two week HT (0.99 $Jkg^{-1}K^{-1}$ at 320 K).

## 5.6 Reference

[1] V. Franco, J.S. Blazquez, B. Ingale, A. Conde, The Magnetocaloric Effect and Magnetic Refrigeration Near Room Temperature: Materials and Models, Annu Rev Mater Res 42 (2012) 305-342.

[2] A.E.-M.A. Mohamed, M. Jeong, R.S. Sheridan, M.M. Attallah, Enabling high efficiency magnetic refrigeration using laser powder bed fusion of porous LaCe(Fe,Mn,Si)13 structures, Addit Manuf 51 (2022) 102620.

[3] A. Cakir, L. Righi, F. Albertini, M. Acet, M. Farle, Intermartensitic transitions and phase stability in Ni50Mn50-xSnx Heusler alloys, Acta Mater 99 (2015) 140-149.

[4] L. Hou, Y. Dai, Y. Fautrelle, Z. Li, Z. Ren, X. Li, Control of microstructure using magnetic fields and study of the mechanical behavior of Ni-rich Ni-Mn-Ga alloys, Acta Mater 199 (2020) 383-396.

[5] W. Sun, X. Lu, Z. Wei, Q. Li, Z. Li, Y. Zhang, J. Liu, Multicaloric effect in Ni–Mn–Sn metamagnetic shape memory alloys by laser powder bed fusion, Addit Manuf 59 (2022) 103125.

[6] R. Duan, S. Li, B. Cai, W. Zhu, F. Ren, M.M. Attallah, A high strength and low modulus metastable β Ti-12Mo-6Zr-2Fe alloy fabricated by laser powder bed fusion in-situ alloying, Addit Manuf (2020) 101708.

[7] N.M. Bruno, C. Yegin, I. Karaman, J.H. Chen, J.H. Ross, J. Liu, J.G. Li, The effect of heat treatments on Ni43Mn42Co4Sn11 meta-magnetic shape memory alloys for magnetic refrigeration, Acta Mater 74 (2014) 66-84.

[8] A.S. Kalbfleisch, G. Matthews, P.J. Jacques, On the influence of the cooling rate on the martensitic transformation of Ni-Mn-Sn Heusler alloys, Scripta Mater 114 (2016) 121-124.

[9] H.C. Xuan, K.X. Xie, D.H. Wang, Z.D. Han, C.L. Zhang, B.X. Gu, Y.W. Du, Effect of annealing on the martensitic transformation and magnetocaloric effect in Ni44.1Mn44.2Sn11.7 ribbons, Appl Phys Lett 92(24) (2008) 242506.

[10] M. Nazmunnahar, T. Ryba, J.J. del Val, M. Ipatov, J. González, V. Hašková, P. Szabó, P. Samuely, J. Kravcak, Z. Vargova, R. Varga, Half-metallic Ni2MnSn Heusler alloy prepared by rapid quenching, J Magn Magn Mater 386 (2015) 98-101.

[11] Martensitic transformation and related magnetic effects in Ni—Mn-based ferromagnetic shape memory alloys, Chinese Phys B 22(7) (2013) 077506.

[12] N.H. Dan, N.H. Duc, N.H. Yen, P.T. Thanh, L.V. Bau, N.M. An, D.T.K. Anh, N.A. Bang, N.T. Mai, P.K. Anh, T.D. Thanh, T.L. Phan, S.C. Yu, Magnetic properties and magnetocaloric effect in Ni-Mn-Sn alloys, J Magn Magn Mater 374 (2015) 372-375.

[13] A. Ghosh, K. Mandal, Effect of structural disorder on the magnetocaloric properties of Ni-Mn-Sn alloy, Appl Phys Lett 104(3) (2014).

[14] H.D. Nguyen, T.H. Do, H.Y. Nguyen, T.T. Pham, H.D. Nguyen, T.N.N. Nguyen, D.T. Tran, T.L. Phan, S.C. Yu, Influence of fabrication conditions on giant magnetocaloric effect of Ni–Mn–Sn ribbons, Advances in Natural Sciences: Nanoscience and Nanotechnology 4(2) (2013) 025011.

[15] M. Yin, P. Nash, W. Chen, S. Chen, Standard enthalpies of formation of selected Ni2YZ Heusler compounds, J Alloy Compd 660 (2016) 258-265.

[16] H. Zhang, X. Zhang, Y. Xiao, M. Yang, Z. Xu, Z. Yao, M. Qian, L. Zhang, L. Yin, D. Jia, Peculiarity of magnetocaloric and magnetoresistance effects in Ni–Mn–Sn–Fe alloy with successive metamagnetic structural transitions, Intermetallics 149 (2022) 107651.

[17] M. Hasegawa, Chapter 3.3 - Ellingham Diagram, in: S. Seetharaman (Ed.), Treatise on Process Metallurgy, Elsevier, Boston, 2014, pp. 507-516.

[18] M.E. Lines, E.D. Jones, Antiferromagnetism in the Face-Centered Cubic Lattice. II. Magnetic Properties of MnO, Physical Review 139(4A) (1965) A1313-A1327.

[19] G.H. Lee, S.H. Huh, J.W. Jeong, B.J. Choi, S.H. Kim, H.-C. Ri, Anomalous Magnetic Properties of MnO Nanoclusters, Journal of the American Chemical Society 124(41) (2002) 12094-12095.

[20] S.-S. Rui, L.-S. Niu, H.-J. Shi, S. Wei, C.C. Tasan, Diffraction-based misorientation mapping: A continuum mechanics description, Journal of the Mechanics and Physics of Solids 133 (2019) 103709.

[21] E.M. Fayed, M. Saadati, D. Shahriari, V. Brailovski, M. Jahazi, M. Medraj, Effect of homogenization and solution treatments time on the elevated-temperature mechanical behavior of Inconel 718 fabricated by laser powder bed fusion, Sci Rep-Uk 11(1) (2021) 2020.

[22] D. Kong, C. Dong, X. Ni, L. Zhang, J. Yao, C. Man, X. Cheng, K. Xiao, X. Li, Mechanical properties and corrosion behavior of selective laser melted 316L stainless steel after different heat treatment processes, J Mater Sci Technol 35(7) (2019) 1499-1507.

[23] A. Tajyar, N. Brooks, N. Holtham, R. Rowe, D.J. Newell, A.N. Palazotto, K. Davami, Effects of a modified heat-treatment on microstructure and mechanical properties of additively manufactured Inconel 718, Materials Science and Engineering: A 838 (2022) 142770.

[24] P. Lehto, Adaptive domain misorientation approach for the EBSD measurement of deformation induced dislocation sub-structures, Ultramicroscopy 222 (2021) 113203.

[25] R. Unnikrishnan, S.M. Northover, H. Jazaeri, P.J. Bouchard, Investigating plastic deformation around a reheat-crack in a 316H austenitic stainless steel weldment by misorientation mapping, Procedia Structural Integrity 2 (2016) 3501-3507.

[26] T.-S. Jun, A.M. Korsunsky, Evaluation of residual stresses and strains using the Eigenstrain Reconstruction Method, International Journal of Solids and Structures 47(13) (2010) 1678-1686.

[27] M.K. Ray, K. Bagani, S. Banerjee, Effect of excess Ni on martensitic transition, exchange bias and inverse magnetocaloric effect in Ni2+xMn1.4-xSn0.6 alloy, J Alloy Compd 600 (2014) 55-59.

[28] P. Czaja, A. Wierzbicka-Miernik, Ł. Rogal, Segregation and microstructure evolution in chill cast and directionally solidified Ni-Mn-Sn metamagnetic shape memory alloys, Journal of Crystal Growth 492 (2018) 50-59.

[29] Y. Zhang, L.L. Zhang, Q. Zheng, X.Q. Zheng, M. Li, J. Du, A. Yan, Enhanced magnetic refrigeration properties in Mn-rich Ni-Mn-Sn ribbons by optimal annealing, Sci Rep-Uk 5 (2015).

[30] T. Chabri, A. Venimadhav, T.K. Nath, Interplay of austenite and martensite phase inside

martensite transition regime and its role on magnetocaloric effect and magnetoresistance in Ni-Mn-Sn based Heusler alloy, Intermetallics 102 (2018) 65-71.

[31] H. Zhang, X. Zhang, M. Qian, L. Zhang, L. Zhang, S. Chai, L. Yin, Martensite transformation behavior and magnetocaloric effect in annealed Ni-Co-Mn-Sn microwires, Materials Science and Engineering: B 274 (2021) 115477.

[32] Z. Li, S. Dong, Z. Li, B. Yang, F. Liu, C.F. Sánchez-Valdés, J.L. Sánchez Llamazares, Y. Zhang, C. Esling, X. Zhao, L. Zuo, Giant low-field magnetocaloric effect in Si alloyed Ni-Co-Mn-In alloys, Scripta Mater 159 (2019) 113-118.

[33] X. Sun, E. Feng, Y. Su, K. Nemkovski, O. Petracic, T. Brückel, Magnetic properties and spin structure of MnO single crystal and powder, Journal of Physics: Conference Series 862(1) (2017) 012027.

[34] A.S.B. Madiligama, P. Ari-Gur, Y. Ren, V.V. Koledov, E.T. Dilmieva, A.P. Kamantsev, A.V. Mashirov, V.G. Shavrov, L. Gonzalez-Legarreta, B.H. Grande, Thermal and magnetic hysteresis associated with martensitic and magnetic phase transformations in Ni52Mn25In16Co7 Heusler alloy, J Magn Magn Mater 442 (2017) 25-35.

[35] B. Hernando, J.L.S. Llamazares, J.D. Santos, M.L. Sánchez, L. Escoda, J.J. Suñol, R. Varga, C. García, J. González, Grain oriented NiMnSn and NiMnIn Heusler alloys ribbons produced by melt spinning: Martensitic transformation and magnetic properties, J Magn Magn Mater 321(7) (2009) 763-768.

[36] J. Kamarád, J. Kaštil, M. Friák, M. Mazalová, O. Schneeweiss, M. Míšek, O. Kaman, Z. Arnold, Pressure study of magnetism in off-stoichiometric Ni2MnSn-based alloys, J Magn Magn Mater 539 (2021) 168345.

[37] K. Sun, A.E.-M.A. Mohamed, S. Li, M. Jeong, J. Head, M.M. Attallah, Laser powder bed fusion of the Ni-Mn-Sn Heusler alloy for magnetic refrigeration applications, Addit Manuf 69 (2023) 103536.

[38] V. Chernenko, E. Cesari, V. Kokorin, I. Vitenko, The development of new ferromagnetic shape memory alloys in Ni-Mn-Ga system, Scripta metallurgica et materialia 33(8) (1995) 1239-1244.

[39] P. Entel, M. Siewert, M.E. Gruner, H.C. Herper, D. Comtesse, R. Arróyave, N. Singh, A. Talapatra, V.V. Sokolovskiy, V.D. Buchelnikov, F. Albertini, L. Righi, V.A. Chernenko, Complex magnetic ordering as a driving mechanism of multifunctional properties of Heusler alloys from first principles, The European Physical Journal B 86(2) (2013) 65.

[40] V.A. Chernenko, Compositional instability of β-phase in Ni-Mn-Ga alloys, Scripta Mater 40(5) (1999) 523-527.

[41] B.J.P.l. Banerjee, On a generalised approach to first and second order magnetic transitions,

12(1) (1964) 16-17.

[42] K. Liu, S. Ma, C. Ma, X. Han, K. Yu, S. Yang, Z. Zhang, Y. Song, X. Luo, C. Chen, S.U. Rehman, Z. Zhong, Martensitic transformation and giant magneto-functional properties in all-d-metal Ni-Co-Mn-Ti alloy ribbons, J Alloy Compd 790 (2019) 78-92.

[43] A.E.-M.A. Mohamed, V. Vega, M. Ipatov, A.M. Ahmed, B. Hernando, Annealing temperature effect on magnetic and magnetocaloric properties of manganites, J Alloy Compd 665 (2016) 394-403.

[44] V.K. Pecharsky, K.A. Gschneidner Jr, Magnetocaloric effect from indirect measurements: Magnetisation and heat capacity, J Appl Phys 86(1) (1999) 565-575.

[45] T.D. Shen, R.B. Schwarz, J.Y. Coulter, J.D. Thompson, Magnetocaloric effect in bulk amorphous Pd40Ni22.5Fe17.5P20 alloy, J Appl Phys 91(8) (2002) 5240-5245.

[46] J.Y. Law, V. Franco, L.M. Moreno-Ramírez, A. Conde, D.Y. Karpenkov, I. Radulov, K.P. Skokov, O. Gutfleisch, A quantitative criterion for determining the order of magnetic phase transitions using the magnetocaloric effect, Nature Communications 9(1) (2018) 2680.

[47] C.F.J.I.d.I.y.T. Sánchez Valdés, Large magnetic entropy change and refrigeration capacity around room temperature in quinary Ni41Co9-xFexMn40Sn10 alloys (x= 2.0 and 2.5), (2020).

[48] S. Singh, L. Caron, S.W. D'Souza, T. Fichtner, G. Porcari, S. Fabbrici, C. Shekhar, S. Chadov, M. Solzi, C. Felser, Large Magnetisation and Reversible Magnetocaloric Effect at the Second-Order Magnetic Transition in Heusler Materials, Adv Mater 28(17) (2016) 3321-3325.

# CHAPTER 6: On the Origin of Cracking in Laser Powder Bed Fusion Processed $LaCe(Fe,Mn,Si)_{13}$, and The Impact of Post-Processing

## 6.1 Abstract

The $LaCe(Fe,Mn,Si)_{13}$ magnetocaloric material printed by laser powder bed fusion (PBF-LB) has huge potential for magnetic refrigeration. However, the high crack and defect susceptibility during the PBF-LB processing remain limitations for its application. This study optimised the PBF-LB process parameters for optimally-dense blocks. The condition of $E_V$ = 250 J/mm$^3$ shows the lowest crack density and porosity fraction. The behaviour and mechanism of different cracks and defects were revealed. The lower energy density, caused by the higher scanning speed and hatch space, can cause a lack of fusion defects. The solidification cracking is attributable to the stress concentration and a stable liquid film. The solid-state cracks are normal in the microstructure of the as-fabricated (AF) sample due to the poor toughness of the La/Ce/Si-rich phases. Thermal heat treatment and quenching increased the magnetocaloric effect (MCE) of the AF sample. The maximum magnetic entropy change ($\Delta S_m$) of the heat-treated sample was -3.68 Jkg$^{-1}$K$^{-1}$ at 294 K when applied to the 1 T field. The Curie temperature

($T_c$) (298 K when applied 0.01 T field) and good MCE make the material ideal for realising room-temperature magnetic refrigeration.

*Keywords:* Laser powder bed fusion; Cracks and defects; Heat-treatment; Magnetic properties; Magnetocaloric effect.

## 6.2 Introduction

Reliable cooling technologies, such as household ammonia refrigerators, room air-conditioners, and cryogenic storage, play an essential role in our society. Traditional gas compression cooling technology releases global warming gas emissions as it is freon in nature and has poor Carnot cycle efficiency (~10%) [1]. To solve the environmental pollution caused by traditional gas compression cooling technology, novel magnetic refrigeration technology has attracted interest within the industry due to its higher theoretical efficiency, making it an environmentally-friendly alternative [2].

$La(Fe,Si)_{13}$-based alloys have been targeted as potential magnetic refrigerants due to their lower costs and hysteresis loss, non-toxic effects, and a more significant magnetocaloric effect (MCE) [3-5]. The MCE of $La(Fe, Si)_{13}$-based alloys is attributed to the $NaZn_{13}$-type $La(Fe,Si)_{13}$ phases (1:13 phase) [5]. However, the as-cast $La(Fe,Si)_{13}$-based alloys comprise a more significant amount of the α-Fe and LaFeSi phases and a few other phases, where conventional melt processes cannot produce the required peritectic reaction ($\alpha\text{-Fe}+\text{LaFeSi}\rightarrow La(Fe,Si)_{13}$) [6]. To increase the volume fraction of the 1:13 phase, the as-casted $La(Fe,Si)_{13}$-based alloys require long heat-treatment processes at high temperatures and quenching [7]. The disadvantage of $La(Fe,Si)_{13}$-based alloys is their poor mechanical properties. Manufacturing alloys into

complex shapes with a huge surface-area-to-volume is also difficult. Thus, it is impossible to manufacture this alloy directly into a heat exchanger with complex shape geometry using traditional subtractive machining methods.

However, additive manufacturing processes, such as laser powder bed fusion (PBF-LB), are a suitable technology for manufacturing the $La(Fe,Si)_{13}$-based alloys into net-shape complex parts, such as heat exchangers [8]. This is because the complex parts can be manufactured by melting the powder directly layer-by-layer subsequently [9, 10]. The higher cooling speed of PBF-LB aid in the formation of $NaZn_{13}$-type $La(Fe,Si)_{13}$ phases [11]. Moore et al. manufactured blocks with wavy-channel inside and fin-shaped rods of the $La(Fe,Co,Si)_{13}$ alloy through the PBF-LB process [12]. Mohamed Abd El-Moez et al. successfully manufactured the $LaCe(Fe,Mn,Si)_{13}$ into bulks, strut lattice, and microchannel blocks. They proved $LaCe(Fe,Mn,Si)_{13}$ magnetocaloric material's processability using PBF-LB [8]. Although they optimised the PBF-LB process, they did not extend their study to explain the defects formation, such as cracks and lack of fusion defects (LOFs). A limitation of their research included the authors' manufacturing samples using high laser powers, which lead to the formation of defects in the build. This has affected the optimisation results. The relationship between the microstructure of $LaCe(Fe,Mn,Si)_{13}$ alloy and the high cracking susceptibility during the PBF-LB process has also not been rationalized convincingly so far.

In this study, the PBF-LB process of the $LaCe(Fe,Mn,Si)_{13}$ alloy was optimised to minimise the defects, especially the cracks, with the mechanism of the defect, especially the cracking mechanism, discussed. Following thermal heat treatment and quenching, the MCE of the as-fabricated (AF) sample increased. The heat treatment process' effect on microstructure and MCE was also studied.

## 6.3 Experimental

### 6.3.1 Laser powder bed fusion

An M2 machine fabricated 10×10×10 mm blocks. All processing was done under argon gas (<1000 ppm $O_2$). A chess scan strategy was used with a 30 µm layer thickness, as shown in Fig. 6.1. The island in the chess scan strategy was 5×5 mm, which was scanned in a random order, with a rotation of 90° within each layer. There was a 1 mm by 1 mm shift between each successive layer in both the X and Y directions. This study chose the laser power (P), the laser scan speed (V), the hatch distance (h), and layer thickness (d) for the process parameter optimisation. During the PBF-LB process, the volume energy density ($E_V$) and the line energy density ($E_L$) defined the effective laser energy applied per volume and per line of powers, which were calculated using Eq. 6.1 and 6.2 [13]:

$$E_v = \frac{P}{V \cdot h \cdot d} \tag{6.1}$$

$$E_L = \frac{P}{V} \tag{6.2}$$

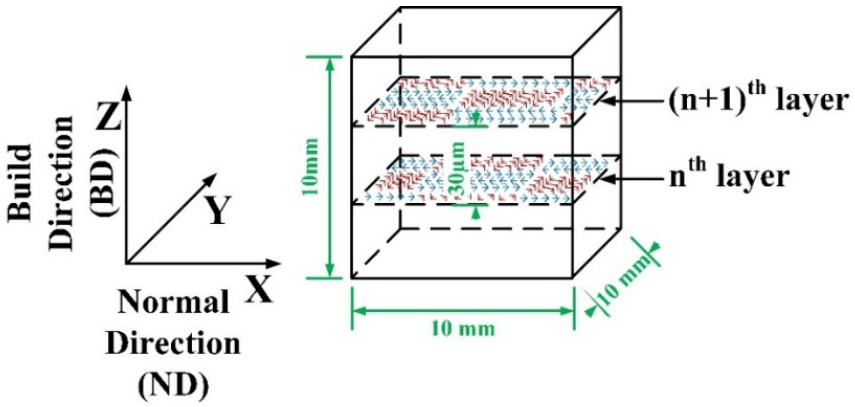



**Fig. 6.1. The chess scan strategy.**

Table 6.1 presents all process parameters used for PBF-LB of $LaCe(Fe,Mn,Si)_{13}$ blocks. The microstructure is taken from the XZ plane.

**Table 6.1. The investigated PBF-LB process parameters for blocks with the chess scan strategy.**

| Laser Power (W) | Scan Speed (mm/s) | Hatch Distance (mm) | Volumetric Energy Density (J/mm$^3$) |
|---|---|---|---|
| 90-125 | 450-1000 | 0.02-0.06 | 62.5-333.3 |

## 6.3.2 Powder characterisation

The gas-atomised LaCe(Fe,Mn,Si)$_{13}$ pre-alloyed powders provided by Erasteal (Fig. 6.2). The powder was sieved to a 63 μm mesh. As shown in Fig. 6.2 a and b, the morphology of the pre-alloy powder was spherical and irregular-shaped particles with satellites [3].

## 6.3.3 Heat-treatment

The AF PBF-LB specimen (#90-4) was encapsulated in Argon-filled quartz ampules and heat-treated, held at 1323 K for 168 hours before water quenching. To remove the specimens' Oxygen content, all heat-treated specimens underwent another heat-treatment process in a hydrogen atmosphere. All specimens were heated at 673 K for 5.5 hours in a tube furnace (heating and cooling rate is 10 K/min), and filled with hydrogen gas with one-bar pressure (1 MPa). The AF PBF-LB specimen was heat-treated at 1323 K for 168 hours before water quenching+heat-treatment in a hydrogen atmosphere, defined as HTH.

**Table 6.2. The heat-treatment (HT) processing.**

| No. | HT 1 | HT 2 |
|---|---|---|
| #90-4 | / | / |
| HTH | 1323 K for 168 hours + Quench | 673K for 5.5 hours at $H_2$ with 1 MPa |

### 6.3.4 Microstructural characterisation and Magnetic measurements

The AF samples were sectioned along the build direction (BD), then ground and polished. Optical microscopy (OM) characterised the defects in every sample. A Hitachi TM3000 tabletop scanning electron microscope (SEM) with backscattered electrons (BSE) characterised the microstructure, especially the segregations. X-ray diffraction (XRD, Proto A-XRD) using Cu–Kα radiation identified the samples' phases. The SEM (Jeol 7000F) with electron backscatter diffraction (EBSD) and energy-dispersive X-ray spectroscopy (EDX) system analysed the microstructural structure and the chemical composition. X-ray fluoresce (XRF) determined the chemical composition of Ce and La, inductively coupled plasma (ICP) for Fe, Mn, Si, and non-dispersive single wavelength IR analysis for Oxygen and Hydrogen. The magnetisation was performed using a magnetic property measurement system: a Quantum Design Magnetic Properties Measurements System (MPMS). The magnetisation vs. temperature curves under an applied field of 0.01 Tesla (T) was measured within a temperature range between 100 and 350 K to observe the phase transformation. The magnetic entropy change ($\Delta S$) was evaluated from isothermal magnetisation curves (M–H curves) under a magnetic field of 0–1 T around the Martensite's vicinity transition temperature ($T_M$) or the Curie temperature ($T_c$) using the Maxwell relation (Eq 6.3), where $H_F$ and $H_I$ are the final magnetic field and the initial magnetic field. The adiabatic temperature change ($\Delta T_{ad}$) was measured directly according to DIN SPEC 91373-2.

$$\Delta S = \int_{H_I}^{H_F} \left(\frac{\partial M}{\partial T}\right)_H dH \tag{6.3}$$

## 6.4 Results and Discussion

### 6.4.1 Characteristics of the pre-alloy powder

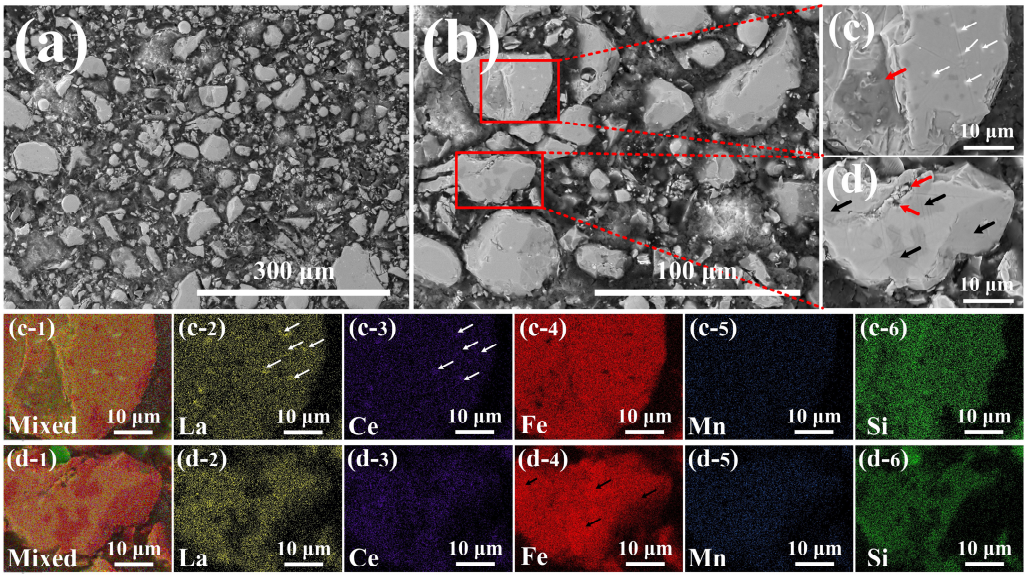



**Fig. 6.2. (a-c) The microstructure of pre-alloy powder. (c-1, …, c-6) The SEM-EDX map of the pre-alloy powder in (c). (d-1, …, d-6) The SEM-EDX map of the pre-alloy powder in (d).**

Fig. 6.2 a-d presents the microstructure of the $LaCe(Fe,Mn,Si)_{13}$ pre-alloy powder. As shown in Fig. 6.2 c and d, the two different segregations were observed in the pre-alloy powders. The white areas are rich in La and Ce elements (La/Ce segregation), as shown in the white arrows in Fig. 6.2 c-1…, and c-6. The SEM-EDX maps identified the dark grey areas rich in Fe elements (Fe segregation), as shown in the black arrows in Fig. 6.2 d-1…, and d-6. In addition, as shown in the red arrows in Fig. 6.2 c, and d, the microstructure of pre-alloy powders showed defects, such as cracks, pores, and step defects.

**Table 6.3. Chemical composition analysis in wt.% of the pre-alloy powder and as-fabricated #90-4 sample and HTH sample with $E_V$=250 J/mm$^3$.**

| | La | Ce | Fe | Mn | Si | O (ppm) | H | <0.02 |
|---|---|---|---|---|---|---|---|---|
| Powder | 14.3 | 6.3 | Bal | 1.17 | 4.44 | 3987 | / | Traces |
| #90-4 | 12.65 | 6.13 | Bal | 0.79 | 5.17 | 1829 | / | Traces |
| HTH | 11.71 | 5.80 | Bal | 0.86 | 4.77 | 7212 | 1556 | Traces |

## 6.4.2 PBF-LB parameters and flaw characterisation

### 6.4.2.1 The defects within the microstructure

The $LaCe(Fe,Mn,Si)_{13}$ alloys are quite brittle [14], and it is prone to cracking during the PBF-LB process, especially using high laser powers [8]. Low laser powers, including 90 W, 100 W, and 125 W, were used in this study to obtain an effective microstructure. Fig. 6.3 shows the microstructure of the 27 (from #90-1 to #125-9) AF $LaCe(Fe,Mn,Si)_{13}$ blocks.

The laser power, scanning speed, and hatch spacing have essential effects on the defect of AF specimens, including crack and porosity. Fig. 6.3 shows the row with 800 mm/s, the column with 0.04 mm, and the high scanning speed and hatch space can cause numerous LOFs. During the PBF-LB process of $LaCe(Fe,Mn,Si)_{13}$, lower energy density, driven by higher speeds and hatch space, could not sufficiently melt the powder with 30 μm thickness. The redeposits (unmelted powder and spatter) remain on the surface of the last melted layer in the middle of the scanning island. These powders gather and increase in volume after going through subsequent scanning layers, such as Fig. 6.4's black arrow. These unmelted powders result in coherent deep LOFs, as shown in #100-7~#100-9, and #125-8~#125-9. The higher scanning speeds also push redeposits to the island's edge during the chess scanning strategy, as shown in

Fig. 6.4's blue box. The redeposits gathered at the edge of the scanning island, and the middle of the scanning island increased the difficulty of fully melting during the next layer, as shown in Fig. 6.5 a and b red arrow.

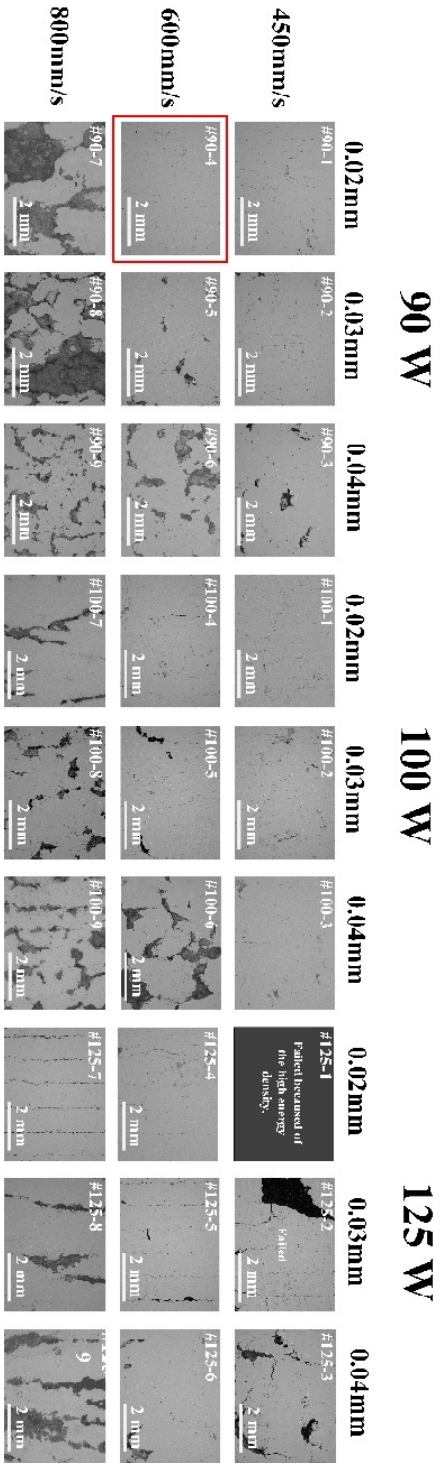



**Fig. 6.3. Defects distribution in SEM images evolution with PBF-LB laser power for 90 W, 100 W, and 125 W.**

The higher energy density caused by, the lower scanning speed and hatch space resulted in the formation of cracks. The amount and size of cracks increased with the increasing laser power when using the low speed 450 mm/s and low hatch 0.02 mm, as shown in Fig. 6.3 (the rows with 0.02 mm). The high energy density causes higher heat input and lower cooling speeds, which increases the possibility of cracks due to higher residual stress and stable liquid forms [15, 16]. Excessively, higher energy density failed some parts, such as #125-1 and #125-2. Cracking can also be observed within the microstructure of bulk material, even if the parameters are suitable, as shown in #90-4, as the $LaCe(Fe,Mn,Si)_{13}$ is sensitive to cracks. Although the lower speeds also push the redeposits to the edge of the island, no large LOFs were found in this bulk material as there were fewer redeposits caused by the low scanning speed. The subsequent higher energy density can sufficiently melt these powders.

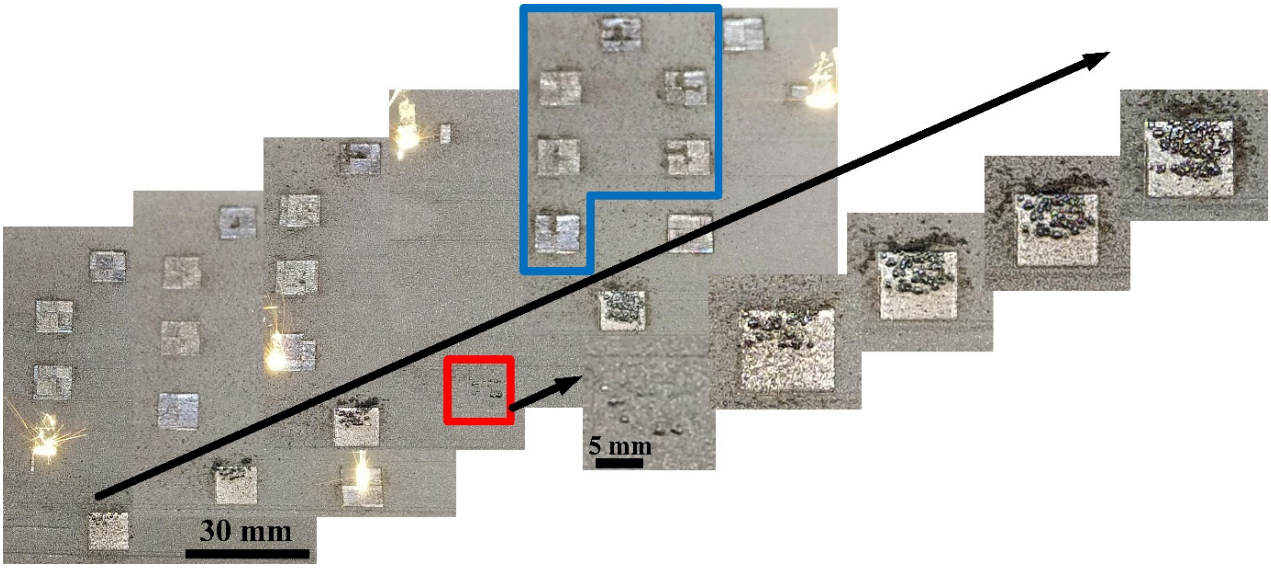



**Fig. 6.4. The redeposits during the PBF-LB process.**

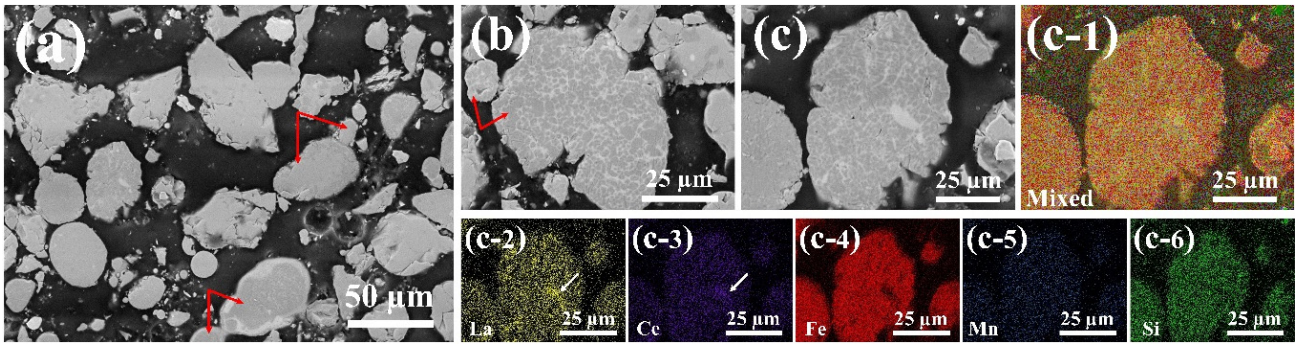



**Fig. 6.5. The microstructure of the redeposits.**

### 6.4.2.2 The relationship between the linear energy density and the hatch

The contour plots were constructed to study the relationship between the line energy density ($E_L$), hatch, crack, and porosity. The most suitable line energy density and the corresponding hatch are obtainable clearly from the contour plots, as shown in Fig. 6.6 a and b. The blocks with lower $E_L$ saw higher porosity and lower cracks, as shown in Fig. 6.6 c and d. This was because the LOFs and holes within the blocks released the residual stress, which decreased the likelihood of cracking. The amount and size of the LOFs decreased when the $E_L$ was increased, as shown in Fig. 6.6 d and e. Fig. 6.6 e saw some LOFs as the hatch (0.03 mm) was too high for the $E_L$ (0.15 J/mm). Fig. 6.6 f saw the best microstructure, with few cracks and LOFs due to the suitable $E_L$ (0.15 J/mm) and hatch (0.02 mm). Fig. 6.6 g saw plenty of huge cracks with large widths that went through several layers. The higher $E_L$ in these samples resulted in significant residual stress [17]. Although it was difficult to eliminate the LOFs and cracks, some parameters showed lower porosity fraction and crack density. The condition of $E_L$=0.15 J/mm and hatch=0.02 mm ($E_V$ is 250 J/mm$^3$, the laser power is 90 W, and the scanning speed is 600 mm/s, see Fig. 6.6 f) shows the lowest porosity fraction and crack density. These parameters have been recommended as the optimum condition for blocks.

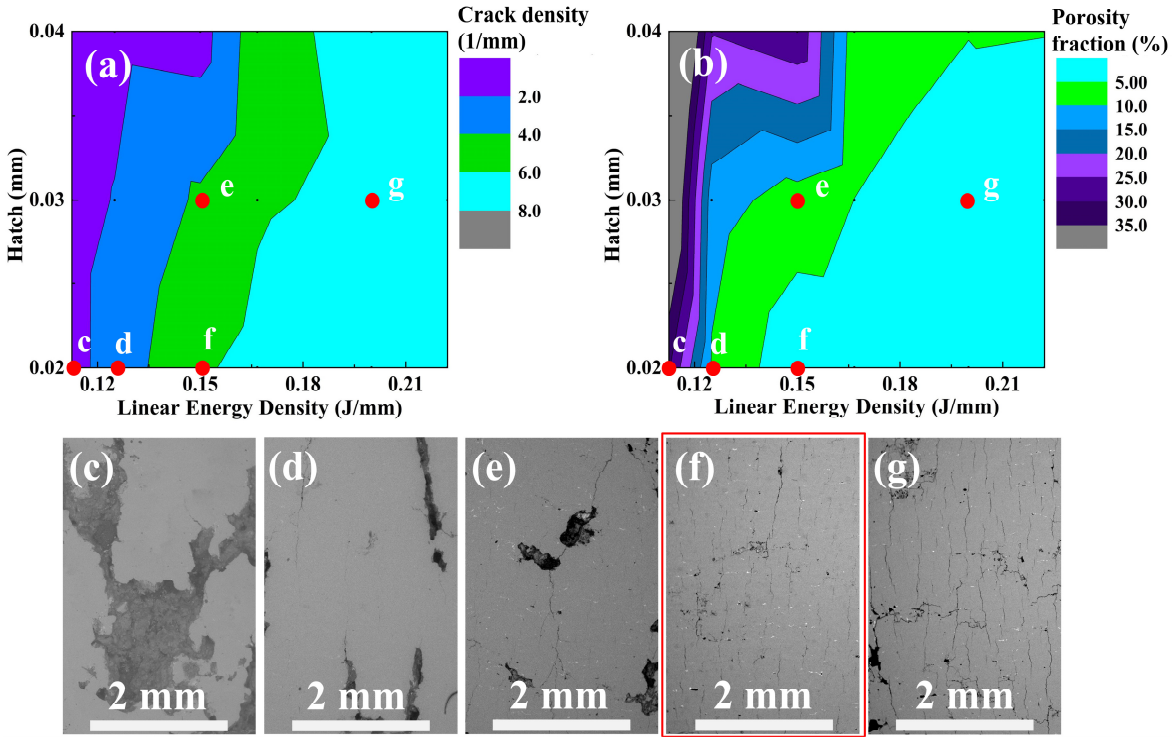



**Fig. 6.6. Influence of the line energy density and hatch on the crack density and porosity fraction.**

## 6.4.3 Microstructure and crystallographic texture

### 6.4.3.1 The Microstructure of the as-fabricated sample

Fig. 6.7 shows the microstructure of the AF sample with the optimum condition (#90-4). The microstructure of #90-4 exhibited a well-developed dendritic morphology, comprising α-(Fe,Mn) and La/Ce/Si-rich dendrites, as shown in Fig. 6.7 a, b, g, and h. During the PBF-LB processing of $LaCe(Fe,Mn,Si)_{13}$, the α-(Fe,Mn) formed first and was the primary phase. A La/Ce/Si-rich phase forms by solidifying the residual liquid phase. Fig. 6.7 h shows a BSE image of the melt pools section. Different colours indicated variations in chemical composition. In the BSE image of the #90-4, the white phases were identified as La/Ce/Si-rich phases, and the black phases as α-(Fe,Mn).

The microstructure and the melt-pool boundaries were also characterised by EBSD mapping. The inverse polar figure (IPF) maps of the #90-4 at the XZ plane are presented in Fig. 6.7 c and d. The grain microstructure varied significantly from the boundaries of the solidified melt pools to the top/centre. Ultra-fine equiaxed grains (2-5 μm) were observed at the melt pool's edges. The grains at the melt pool bottom were elongated due to the thermal gradients in PBF-LB, with several equiaxed grains observed at the melt pool top/centre due to lower gradients and higher solidification velocity [18]. The elongated columnar grains have a length between 10 and 30 μm and a width between 2 and 10 μm. These grains grew radially from the boundary to the centre of the melt pool and coincided with the thermal gradient. This is driven by the steep variation of both the solidification rate and thermal gradient across the melt pool [18].

Fig. 6.8 is the SEM (Fig. 6.8 a), SEM-BSE (Fig. 6.8 b), and EDX mapping with higher magnification. Table 6.4 presents the chemical compositions of the dark and white phases in the BSE map. The dark phases in the SEM-BSE image are α-(Fe,Mn) phases, which show prominent dendritic in the SEM image. The white phases in the SEM-BSE image are La/Ce/Si rich, concave phases between dendrites. The oxygen was found in #90-4 (Fig. 6.8 O) due to the powder containing oxygen (Table 6.3) and partial oxygen gas in the PBF-LB process.

**Table 6.4. Composition at points shown in Fig. 6.8 b was obtained via EDX.**

| Points | Compositions (at%) | | | | | |
|---|---|---|---|---|---|---|
| | La | Ce | Fe | Mn | Si | O |
| a | 12.05 | 5.81 | 59.51 | 0.88 | 18.71 | 3.05 |
| b | 6.01 | 2.76 | 76.73 | 1.11 | 10.64 | 2.75 |

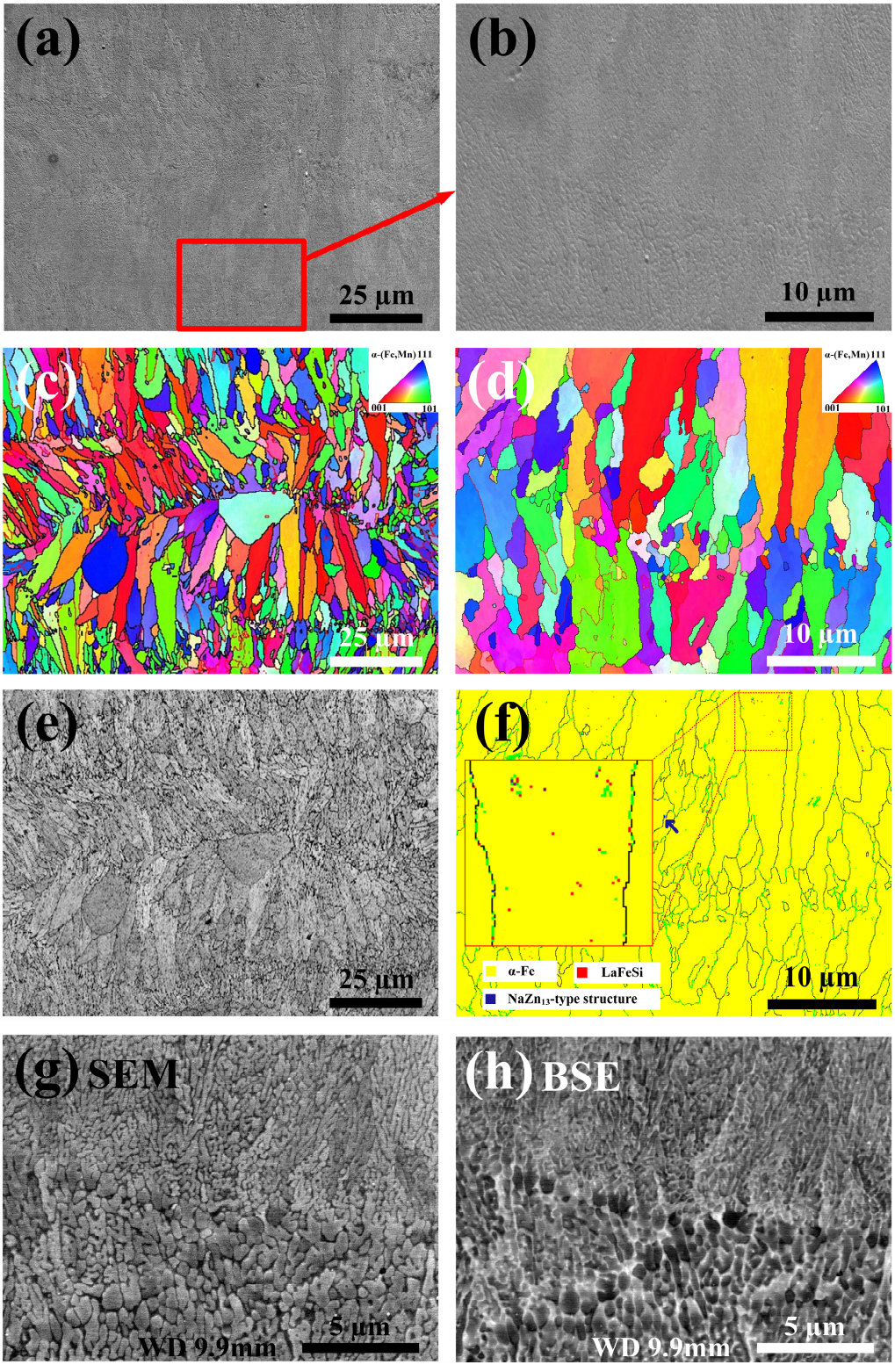



**Fig. 6.7. The microstructure of the AF sample (a and b) SEM images, (c and d) Euler EBSD image of the microstructure, (e) EBSD band contrast (BC) map, (f) EBSD phases map, (g) SEM image, and (h) the SEM-BSE image.**

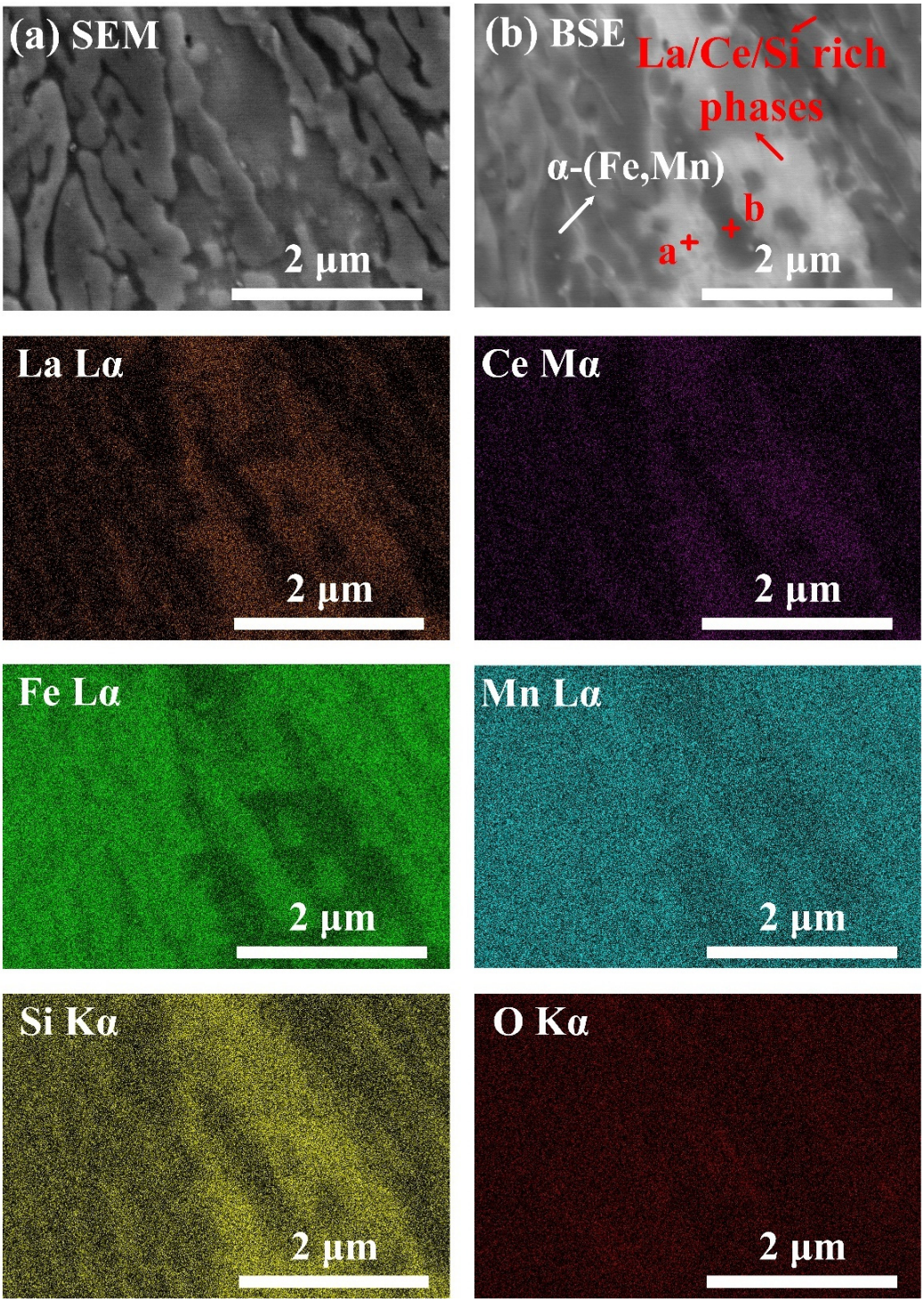



**Fig. 6.8. The microstructure of #90-4 with high magnification (a and b) SEM and BSE images, and EDX map, including La, Ce, Fe, Mn, Si, and O elements.**

### 6.4.3.2 The Microstructure of the heat-treated sample

Fig. 6.9 presents the microstructure of the HTH sample. As shown in Fig. 6.9 c, d, and e, and EDX maps, the black phases in the BSE map (the phases present a dark grey colour in the SEM image) are the α-Fe type phases mainly containing the Fe element. The white phases in the BSE map (the phases also present a white colour in the SEM image) are La/Ce/O segregations mainly containing La, Ce, and O elements. The grey phases in the BSE map (the phases also present a light grey colour in the SEM image) are $NaZn_{13}$-type $LaCe(Fe,Mn,Si)_{13}$ phases, which contain all elements and a little of the O element. The EDX-point (a, b, c, and d) results also prove the conclusion, as shown in Table 6.5.

Although the crack did not disappear after a long heat-treatment process, the α-Fe phases prefer to gather along all longitudinal cracks, as shown in Fig. 6.9 b and c. The eutectic reaction prefers to happen on one side of the α-Fe dendrites away from the crack. As these α-Fe phases close to the matrix have better external conditions for the eutectic reaction, such as the reaction α-Fe type phases+LaFeSi type phases→$La(Fe,Si)_{13}$ type phases can fully occur [6, 19]. Lots of α-Fe phases close to the crack were preserved during the long heat-treatment process.

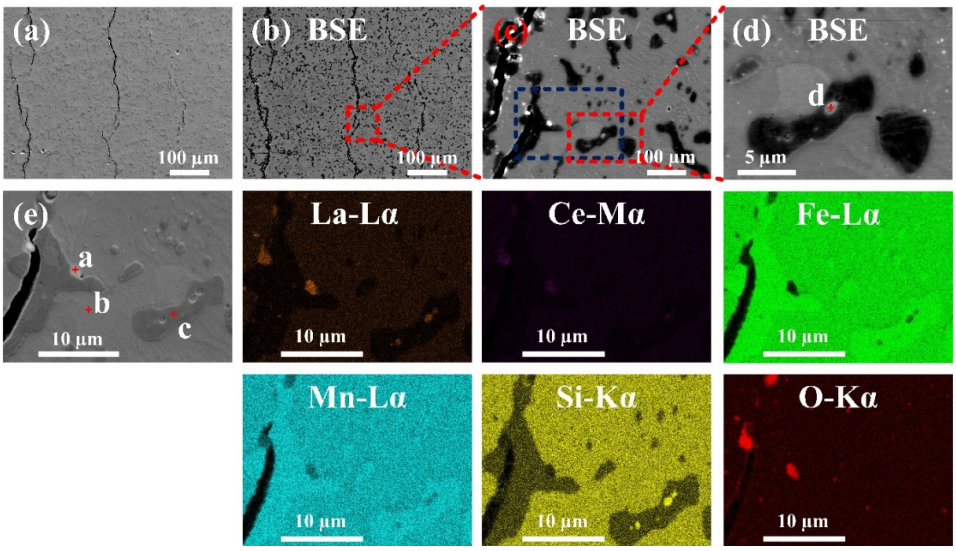



**Fig. 6.9. The microstructure of the HTH sample: (a and b) SEM and BSE images with low magnification, (c and d) BSE images with high magnification, and (e) EDX map for the microstructure.**

**Table 6.5. The composition at points (a-d) shown in Fig. 6.9 was obtained via SEM-EDX.**

| Points | Compositions (at%) | | | | | |
|---|---|---|---|---|---|---|
| | La | Ce | Fe | Mn | Si | O |
| a | 36.9 | 11.2 | 7.9 | 0 | 0 | 44.0 |
| b | 5.1 | 2.3 | 79.5 | 1.3 | 10.9 | 1.0 |
| c | 0.1 | 0.3 | 94.9 | 0.6 | 3.2 | 0.9 |
| d | 41.3 | 10.6 | 8.1 | 0 | 0.2 | 39.8 |

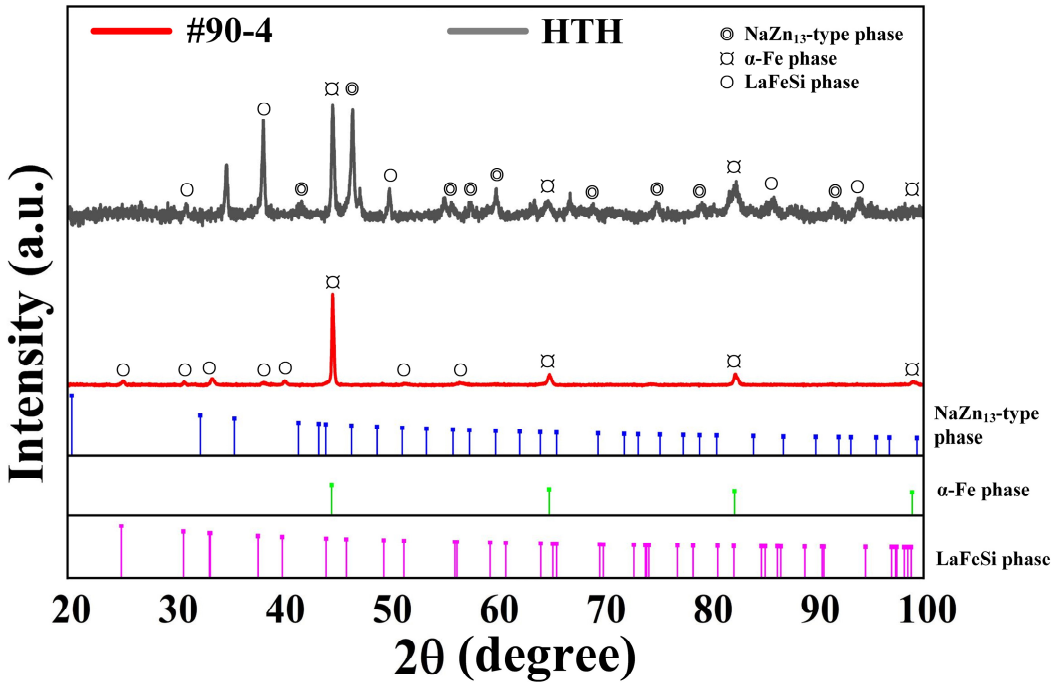



**Fig. 6.10. The XRD pattern of #90-4 and HTH samples.**

The XRD pattern of #90-4 and HTH specimens are presented in Fig. 6.10. The XRD analysis confirmed the AF specimen (#90-4) contains the α-Fe and LaFeSi type phases. The $NaZn_{13}$-type phases ($LaCe(Fe,Mn,Si)_{13}$ phases) cannot be observed in the XRD result of #90-4 as the amount of these phases is a little. However, the EBSD of #90-4 proves the existence of these

phases, as shown in Fig. 6.7 f. The XRD result of the HTH specimen proves the existence of the $NaZn_{13}$ type $LaCe(Fe,Mn,Si)_{13}$ phase, α-Fe type phase, and LaFeSi phases. The long heat-treatment process promoted the formation of the $LaCe(Fe,Mn,Si)_{13}$ phases, where the amount of the α-Fe type phases decreased significantly, as shown in Fig. 6.9.

### 6.4.4 Detailed characterisation of cracking modes

Though parameters were optimised to avoid LOFs, porosity, and crack and to achieve a lower density of defects, it is difficult to fully eliminate the cracking in the microstructure of the best sample, as shown in Fig. 6.3 #90-4. To characterise the cracking behaviour within the AF sample #90-4, it used the phenomenological classification of cracks described in the welding literature [20-23]. The observed bulk cracking is categorised into two types based on the cause of cracking: (i) hot cracking (including solidification cracking and liquation cracking), and (ii) solid-state cracking (cold cracking). In addition, segregation cracking was observed. The following part discusses the detailed fractography characterisation and the cause of cracking.

#### 6.4.4.1 The solidification cracking

Stress and the liquid film, with a lack of feeding, caused the solidification cracking. The liquid film is an essential prerequisite for solidification cracking, while the thermal stress is the driving force for crack initiation and propagation [15, 16, 24].

The morphology of hot cracks, shown in Fig. 6.11, indicated solidification cracking's occurrence. The rough surface of the crack, such as the rounded features of cells and dendrite arms (Fig. 6.11 b), confirmed the crack's occurrence in the liquid phase [25]. During the solidification of $La(Fe,Si)_{13}$-based alloy, the primary α-Fe type phase first formed upon cooling [26-28]. The α-Fe type phases, with a dendrites shape, formed in the PBF-LB process [26]. This

directly affects the distribution and stability of the liquid film. Therefore, the liquid film stability was important in revealing the hot cracking mechanism experienced during the PBF-LB process of the $LaCe(Fe,Mn,Si)_{13}$ alloy.

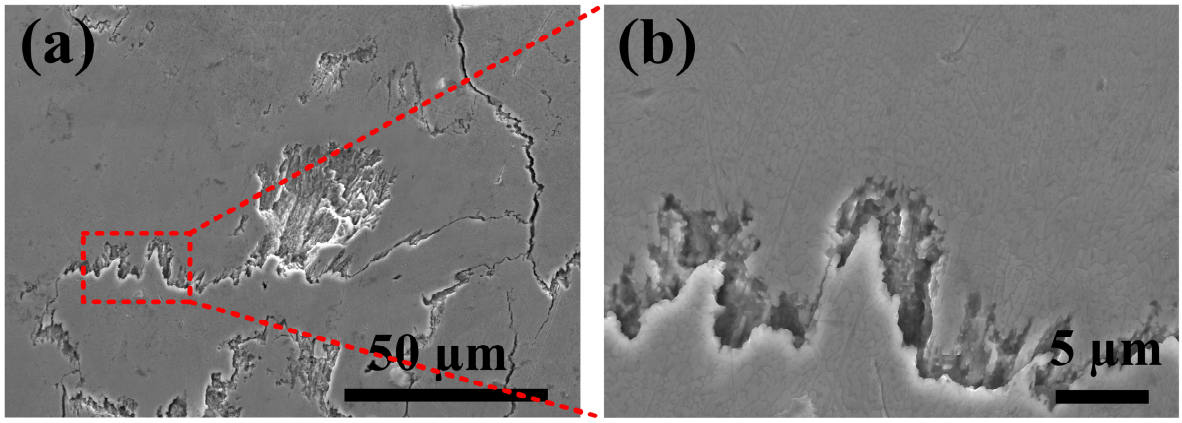



**Fig. 6.11. SEM microscopy of hot cracking in #90-4: (a) Hot crack; and (b) The details of hot cracking.**

The EBSD IPF Map, shown in Fig. 6.12, demonstrated hot cracking's occurrence along the grain boundaries. The misorientation angles of the 1, 2, and 3 adjacent grains at the cracks were 26°, 50.8°, and 48.4° (Fig. 6.12 a). These large misorientation angles suggest that high-angle grain boundaries (HAGB, misorientation > 15°) are sensitive to cracking, whereas low-angle grain boundaries (LAGB, misorientation < 15°) remained insensitive [29, 30].

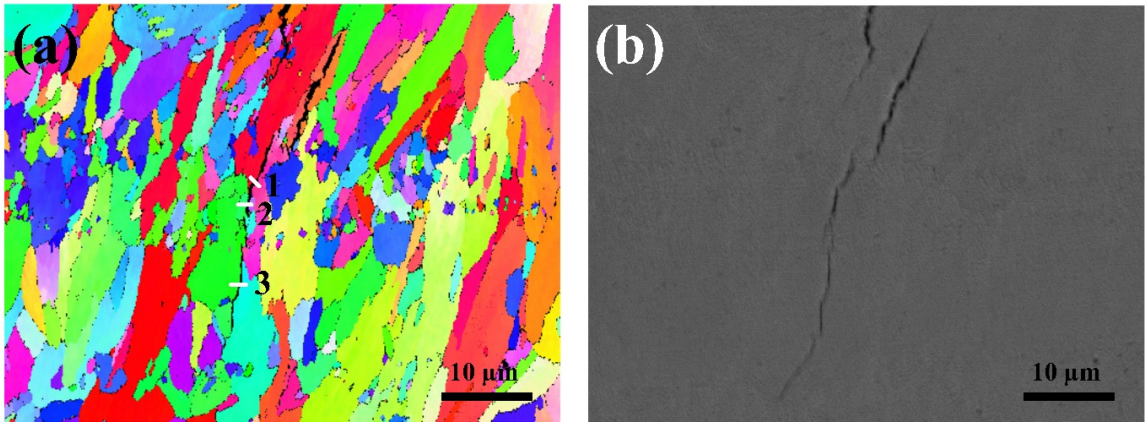



**Fig. 6.12. (a) The inverse pole figure (IPF) along the crack; (b) SEM image showing the crack.**

### 6.4.4.2 Intergranular liquid film

During the solidification, the liquid film is dominated by the undercooling ($\Delta T_b$), as shown in the following formula:

$$\Delta T_b = \frac{\gamma_{gb} - 2\gamma_{sl}}{\Delta S_f \cdot \delta} \quad (6.4)$$

where the $\Delta T_b$ is dendrite coalescence undercooling, $\Delta S_f$ is the fusion entropy, $\delta$ is the isolated solid-liquid interface thickness (about 1 nm), $\gamma_{gb}$ is the GB energy, and $\gamma_{sl}$ is the solid/liquid interfacial energy [15, 16, 31, 32]. The situation where $\gamma_{gb} < 2\gamma_{sl}$ is $\Delta T_b<0$, the liquid film is unstable, and the solid/liquid interfaces are attractive. Otherwise, if the $\gamma_{gb} > 2\gamma_{sl}$, then $\Delta T_b>0$, the boundary is repulsive, where the liquid film is stable. For the $\gamma_{gb} = 2\gamma_{sl}$ and $\Delta T_b=0$, the liquid film is neutral [32]. $\gamma_{gb}$ is calculated based on the theory of dislocations using the following expression [33]:

$$\gamma_{gb} = \frac{Gb\theta}{4\pi(1-\nu)}\left(1 - \ln\frac{\theta}{\theta_m}\right) \quad (6.5)$$

In Eq. 6.5, $\theta$ is the misorientation angle, G is the shear modulus, $\nu$ is the Poisson ratio, b is the Burger vector, and $\theta_m$ is the angle corresponding to the maximum GB energy. When $\theta > \theta_m$, Eq. 6.5 is unsuitable and the GB energy is assumed to be constant, corresponding to the maximum value at $\theta_m$. $\theta_m$ was assumed to be 15° for the calculation [34]. There is a lack of data for G and $\nu$ of $LaCe(FeMnSi)_{13}$ at elevated temperatures. Thus, the data of $La_1Fe_{10.54}Co_{1.43}Si_{1.03}$ at 1,500K was used in the calculation. The Poisson's ratio was assumed to be 0.275 [35]. B. Kaeswurm .et. al [35] reported Young's modulus (E) of the $La_1Fe_{10.54}Co_{1.43}Si_{1.03}$ linearly increases at temperatures above 650 K. Young's modulus (E) at 1,500 K is about 101 GPa [35]. The G can be calculated by using Equation 6.

$$G = \frac{E}{2(1+\nu)} \tag{6.6}$$

Thus, the G of $La_1Fe_{10.54}Co_{1.43}Si_{1.03}$ at 1,500 K is 39.61 GPa. The burger vector is assumed as $11.469 \times 10^{-10}$ m, which is the unit cell size [36]. Similarly, there is a lack of data for $\gamma_{sl}$ of $LaCe(Fe,Mn,Si)_{13}$, and the $\gamma_{sl}$ of pure Iron (336 $mJ/m^2$) approximated calculations [37]. All relevant parameters are shown in Table 6.6. When θ is 15°, the GB energy is maximum, $\gamma_{gb}$ = 1.305 $J/m^2$.

**Table 6.6. The physical parameters are used to calculate the undercooling $\Delta T_b$.**

| Physical parameters | Value |
|---|---|
| Poisson ratio (v) | 0.275 [35] |
| Shear modulus (G) | 39.61 GPa |
| Burgers vectore (b) | $11.469\times10^{-10}$ m [36] |
| Solid/liquid interface energy of Fe | 336 $mJ/m^2$ [37, 38] |
| Young's modulus (E) | 101 GPa [35] |

When the $\gamma_{gb} = 2\gamma_{sl}$=0.672 $J/m^2$, and $\Delta T_b$=0, the critical transition angle (8.77°) is calculated. Thus, the grain boundary is attractive when θ < 8.77° and repulsive when θ > 8.77°. Therefore, it is likelier to form a stable liquid film at HAGBs than LAGBs. And the hot cracks are likelier to occur at HAGBs.

### 6.4.4.3 Driving force for the initiation and propagation of cracks

The residual thermal stress is essential in initiating hot cracking [17]. During the PBF-LB progress' solidification, the solidifying deposit contracts due to solidification shrinkage and thermal contraction [39]. The contraction of the depositing layer is greater than the deposited

layer. The previously deposited layer prevented the solidifying layer's contraction. Therefore, the solidifying layers were subject to tensile stress, which results in hot cracking when the stress exceeds the solidifying metal's strength [39]. As the stress accumulates and increases, the crack propagates to relieve the stress. Thus, thermal stress is the driving force for crack initiation and propagation.

### 6.4.5 The solid-state cracking

#### 6.4.5.1 The longitudinal crack

Fig. 6.13 presents the longitudinal cracks on the XZ plane in the AF specimen's (#90-4) microstructure. The length of the longitudinal cracks normally exceeds 100 μm and propagates through several layers of the melt pool (Fig. 6.13 a). The feature of these cracks cannot see solidifying dendrites or liquation regions. In addition, the IPF map presents the cracks' transgranular and intergranular features (Fig. 6.13 b and c). These typical features proved the cracks are solid-state cracks. Fig. 6.13 d and e show the details of the origin and end of the longitudinal crack. It is obvious the solid-state crack preferred to start in the La/Ce/Si rich phases (the white phases in the SEM-BSE image), and it stopped at the edge of α-(Fe,Mn) phases (the grey phases in the SEM-BSE image). In addition, the huge cracks can tear α-(Fe,Mn) phases through and go through (Fig. 6.13 d and e). It is likely the origin of the longitudinal crack happening in the area with fine grains between two adjacent weld beads (Fig. 6.13 c) and had transgranular and intergranular features. The crack mainly exhibited epitaxial cracking and expansion towards the centre of the melt pool. As the crack grew, its width increased, and it exhibited transgranular features (Fig. 6.13 b) as the internal residual stresses caused elastic-plastic strain on the borders between different grains. The crack appeared to prefer to occur at

the boundaries of the grains as most crystal lattice distortions are concentrated there. The crack can also go through the bodies of the grains in future movements [40].

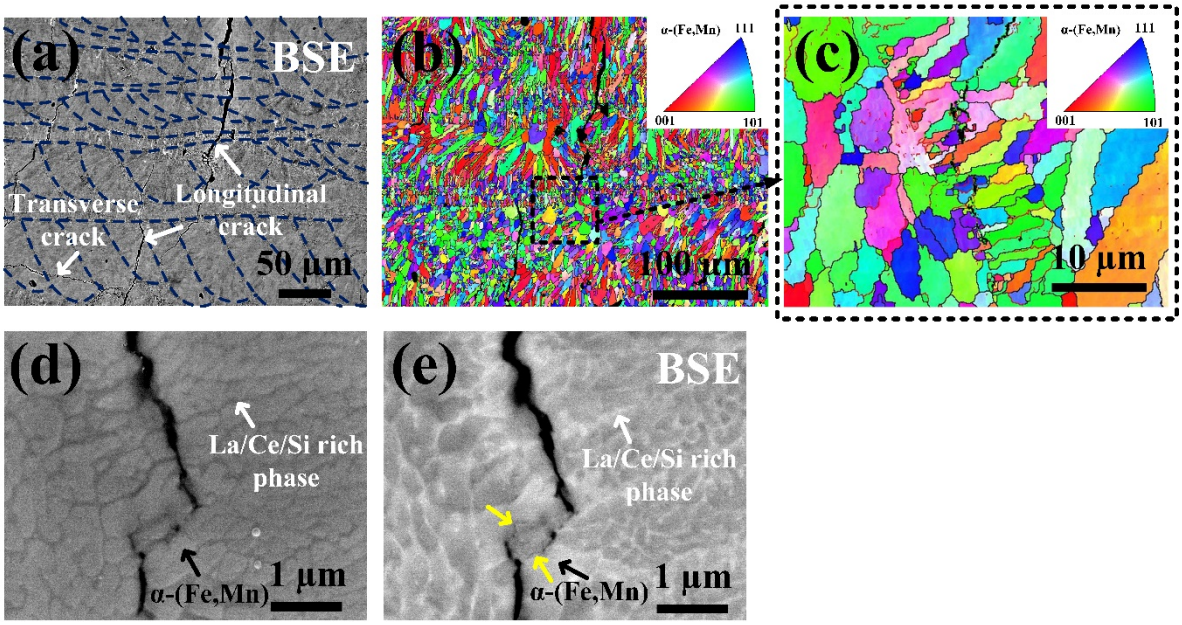



**Fig. 6.13. Solid-state cracks observed in the AF sample (#90-4): (a) the SEM image with low magnification; (b) the IPF map with low magnification; (c) the IPF map with high magnification; (d) the SEM image with high magnification and (e) the SEM-BSE image with high magnification.**

### 6.4.5.2 The transverse crack

Fig. 6.14 and 6.15 present the transverse cracks on the XZ plane in the AF specimen's (#90-4) microstructure. The microcracks first occurred in the La/Ce/Si-rich phases under the effect of residual stress (Fig. 6.14 b). These cracks possibly stop when approaching the α-(Fe,Mn) phases (Fig. 6.14 c) as the toughness of the α-(Fe,Mn) phases is more significant than La/Ce/Si rich phases. The α-(Fe,Mn) phases deform plastically to a large extent when the crack approaches them [41]. The plastic deformation releases the energy required for crack propagation. The further movement of these microcracks would lead to them connecting (Fig. 6.14 c). The cracks could also go through the grain (Fig. 6.14 c and 6.15 b). Lastly, the long transverse crack formed

and even went through several weld beads (Fig. 6.14 a and Fig. 6.15). Fig. 6.15 presents the three transverse cracks' SEM image and IPF map. Transverse crack I began at the defects and went through different weld beads. Transverse crack II is the secondary crack of the longitudinal crack which went through different weld layers or beads. Transverse crack III happened in the transverse La/Ce/Si segregation. It is obvious the transverse crack also had transgranular and intergranular features.

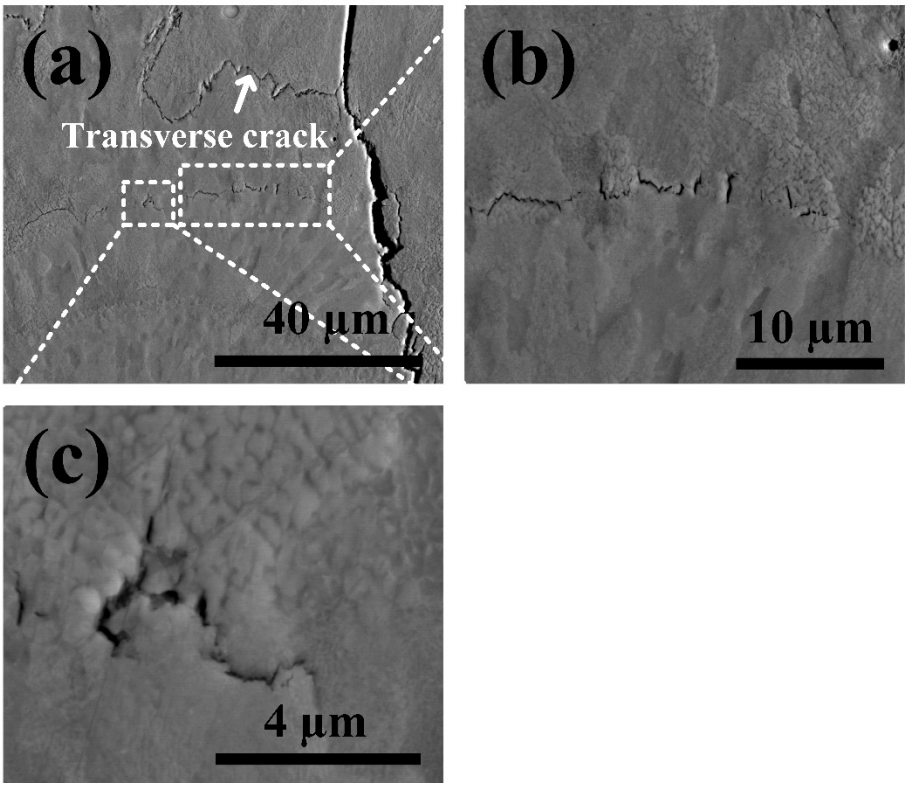



**Fig. 6.14. Transverse solid-state cracks: (a) the SEM image with low magnification; (b and c) the SEM image with high magnification.**

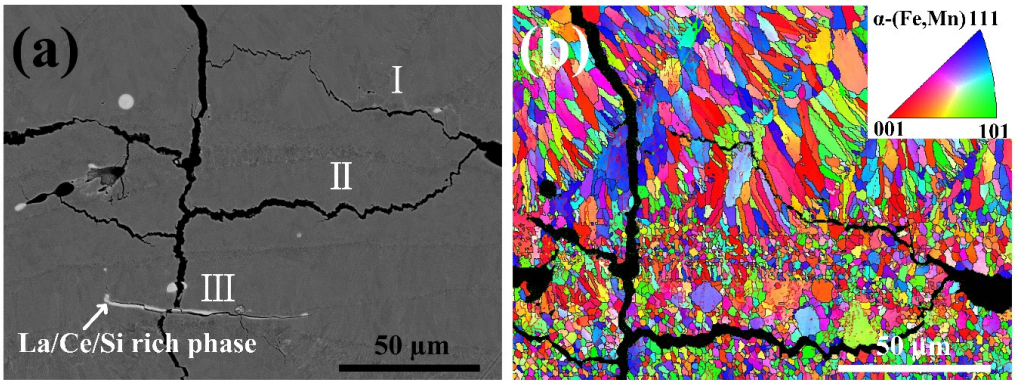



**Fig. 6.15. Transverse solid-state cracks: (a) the SEM image; (b) the corresponding IPF map.**

## 6.4.6 The segregation cracking

Fig. 6.16 presents the crack around the segregations. The crack preferred to expand along the La/Ce/Si segregations (red arrows in Fig. 6.16). When the large longitudinal crack went through segregation, the resulting branch crack preferred to occur along the segregations, as shown in Fig. 6.16 a. This is thought to occur as the La/Ce/Si segregation has a higher hardness and poorer toughness [42]. When the stress transfers to the segregations, it cannot deform plastically and dissipate the stress required from crack propagation. Thus, the La/Ce/Si segregations cracked preferentially. The small gap in Fig. 6.16 d proves the segregation cannot combine well with a base metal. The La/Ce/Si segregations first solidified during the solidification process due to the lower melting temperatures [43]. The subsequent solidification of other phases prevented filling the liquid metal into these small gaps. The small gaps can be the origin of the crack (Fig. 6.16 c). In addition, the small LOFs were also observed in the La/Ce/Si segregations (blue arrows in Fig. 6.16), as there is no filling liquid metal during the rapid solidification progress of the La/Ce/Si segregations.

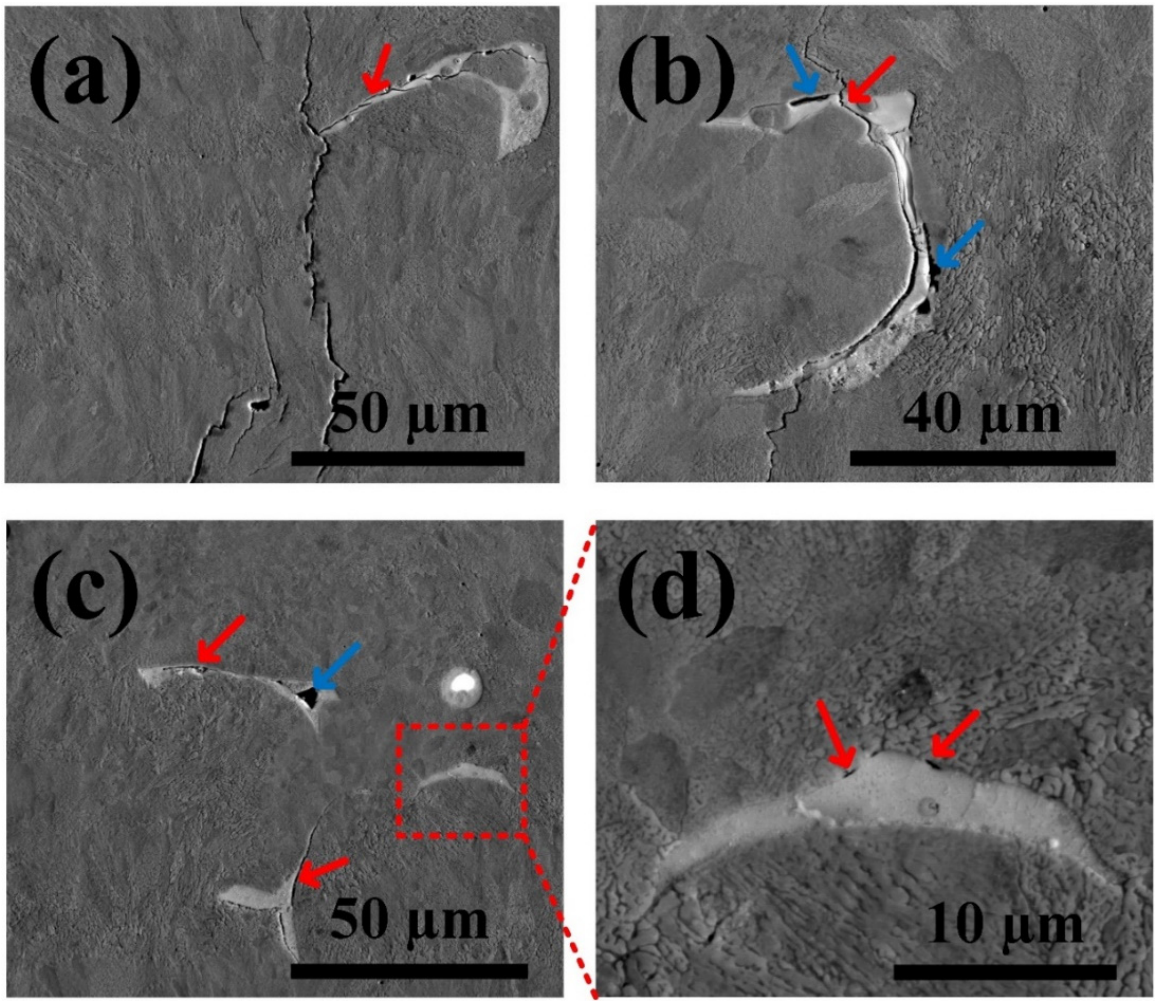



**Fig. 6.16. (a-d) SEM microscopy of the cracking around the La/Ce/Si segregations.**

## 6.4.7 Magnetic property

Fig. 6.17 shows the thermo-magnetisation of the HTH sample built with $E_V$ = 250 J/mm$^3$ (90 W, 600 mm/s, and 0.02 mm). The ferromagnetic-paramagnetic (FM-PM) transition was seen in the thermo-magnetisation curve. However, there are no other magnetic ground state transitions. The magnetisation saw a shape drop from 3.6 to 2.3 emu/g around 298 K, which is the Curie temperature ($T_c$) [44]. The inset picture in Fig. 6.17 also proves the value of $T_c$. The magnetisation was still 2.3 emu/g when the temperature was above the $T_c$ due to the presence of α-(Fe,Mn) phases within the sample. The isothermal magnetisation curves were tested from

280 to 319 K under the external magnetic field of 0-1 T (Fig. 6.17 b). And the temperature step is 3 K. Magnetisation of the sample saw a decreasing trend when the temperature increased due to the spin heat fluctuation of the sample decreased with the temperature [45, 46]. In addition, the field hosting the M-H curve coincides with the field cooling it, which means the hysteresis is very small. The first-order itinerant electron metamagnetic FM-PM transition cannot be found in the M-H curve. This means there is a second-order transition in the HTH sample. An Arrott plot was constructed from the isothermal magnetisation curve to determine the exact properties of magnetic transition. The type of magnetic phase transition is determined by the positive and negative slopes of the H/M-$M^2$ curve [44, 45, 47]. The positive slope suggests the second-order transition (SOPT) occurred, with the negative slope showing the first-order transition's (FOPT) occurrence [45, 47]. The slope of the H/M-$M^2$ curve in Fig. 6.17 c is positive, indicating a second-order transition in the HTH sample.

The maximum magnetic entropy change ($\Delta S_m$) of SOPT is -3.68 $Jkg^{-1}K^{-1}$ at 295 K when applied to the 1 T field. Table 6.7 compares the magnetic entropy of the HTH sample in this work with the pure Gd and La-Fe-Si-based alloys reported in other literature. The $\Delta S_m$ of HTH sample is better than Gd and most La-Fe-Si-based alloys manufactured using arc melting and post-processing treatment. However, the $\Delta S_m$ value achieved by heat treated PBF-LB made $LaCe(Fe,Mn,Si)_{13}$ sample with optimum condition E = 123 $J/mm^3$ is 4.2 J/kg K at ~293 K (Table 6.7) [8]. Although the value is higher than the result of this work, the adiabatic temperature change ($\Delta T_{ad}$) (1.41 K) is lower that this work (1.65 K) (Fig. 6.17 d). The HTH sample in this work just went through 5.5 hours' heat treatment at $H_2$ with 1 MPa pressure, which is energy saving compared with [8]. The $\Delta S_m$ of SOPT in this work is promising, although the FOPT cannot be seen in the HTH sample. While FOPT can cause a sharp magnetic entropy change, it is also accompanied by large magnetic hysteresis [48] and a big volume

change [49]. The cyclic magnetocaloric transition can cause volumetric stresses, leading to a fragmentation of the sample [42]. Although the Δ*S* of SOPT is not as effective as FOPT, it cannot induce volumetric change and large magnetic hysteresis. It is more suitable for the long-term cyclic magnetocaloric transition. In addition, the $T_c$ (room temperature, 298 K) makes the material an ideal choice for realising room temperature magnetic refrigeration.

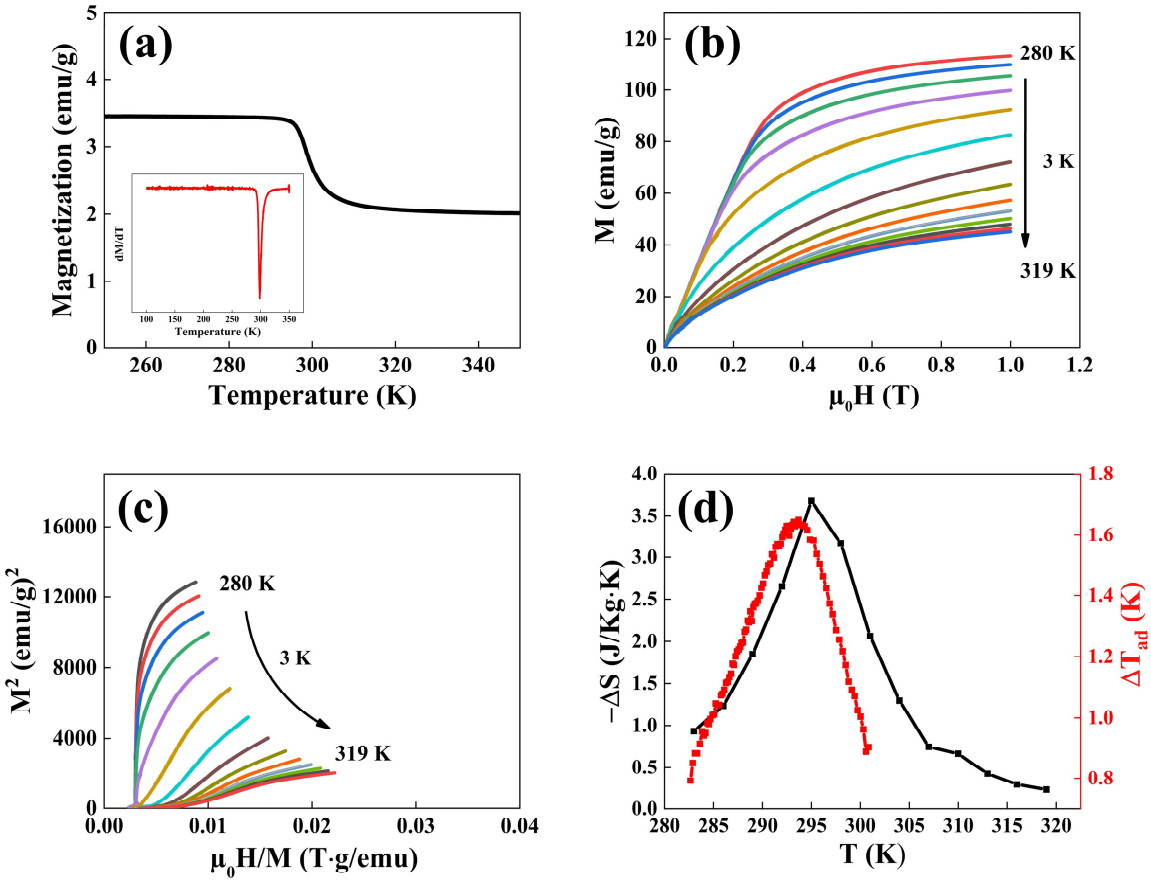



**Fig. 6.17. (a) Thermo-magnetisation curves in an applied field of 0.01 T; (b) Isothermal magnetisation curves of the HTH sample near the $T_c$; (c) the relevant induced Arrott plot; and (d) the Thermal variation of ΔS around the $T_c$ at 1 T.**

**Table 6.7. Comparison of the magnetic entropy of the La-Fe-Si-based alloys with those reported in the literature**

| Alloy | Applied Field (T) | $-\Delta S_m$ of SOPT ($Jkg^{-1}K^{-1}$) | $T_c$ (K) | $\Delta S_m$ of FOPT ( $Jkg^{-1}K^{-1}$) | $T_M$ (K) | Manufactured method | Ref. |
|---|---|---|---|---|---|---|---|
| $LaCe(Fe,Mn,Si)_{13}H_y$ | 1 | 3.68 | 298 | / | / | PBF-LB &1323 K for 7 days & Quench in water & 673 K for 5.5 hours at $H_2$ with 1 MPa pressure. | This work |
| $LaCe(Fe,Mn,Si)_{13}H_y$ | 1 | 4.9 | 292 | / | | PBF-LB &1323 K for 7 days & Quench in water & 673 K for 6 hours at $H_2$ with 1 MPa pressure. | [8] |
| Pure Gd | 2 | 4.5 | 294 | / | / | | [50] |
| $LaFe_{11.4}Si_{1.6}$ | 1 | / | / | 10.5 | 208 | Arc-melting & 1273 K for 30 days & quenched in liquid nitrogen. | [51] |
| $LaFe_{10.4}Si_{2.6}$ | 2 | 3.1 | 243 | / | / | | |
| $La_{1.07}Fe_{11}Si_2$ | 2 | 3.3 | 238 | / | / | Arc melting & suction casting and & 1375 K for 12 hours. | [52] |
| $La_{1.07}Fe_{11.2}Si_{1.8}$ | 2 | / | / | 8.3 | 215 | | |

| | | | | | | | |
|---|---|---|---|---|---|---|---|
| $La_{1.07}Fe_{11.4}Si_{1.6}$ | 2 | / | / | 17 | 202 | | |
| $La_{1.07}Fe_{11.6}Si_{1.4}$ | 2 | / | / | 22.5 | 190 | | |
| $La_{0.8}Ce_{0.2}Fe_{11.4}Si_{1.6}$ | 1 | / | / | 73 | 177 | | |
| $La_{0.8}Ce_{0.2}Fe_{11.3}Mn_{0.1}Si_{1.6}$ | 1 | / | / | 16 | 163 | Arc melting & & 1373 K for 5 days & quenched in cool water. | [53] |
| $La_{0.8}Ce_{0.2}Fe_{11.2}Mn_{0.2}Si_{1.6}$ | 1 | / | / | 26 | 142 | | |
| $La_{0.8}Ce_{0.2}Fe_{11.1}Mn_{0.3}Si_{1.6}$ | 1 | / | / | 15 | 122 | | |
| $La_{0.9}Ce_{0.1}(Fe_{0.99}Mn_{0.01})_{11.6}Si_{1.4}H_{1.6}$ | 1 | / | / | 7.8 | 326 | Arc melting & 1293 K for 15 days & quenched in ice water & 773 K for 3 hours at $H_2$ with 0.5 MPa pressure. | [54] |
| LaFe11.6Si1.4 | 2 | | | 13 | 191 | Arc-melting & 1573 K for an hour & furnace cooling. | [55] |
| $LaFe_{11.5}Co_{0.1}Si_{1.4}$ | 2 | / | / | 19.94 | 205 | | |
| $LaFe_{11.3}Co_{0.3}Si_{1.4}$ | 2 | / | / | 12.5 | 225 | | |
| $LaFe_{11.1}Co_{0.5}Si_{1.4}$ | 2 | / | / | 8 | 247 | Arc-melting & 1523 K for 5 hours & furnace cooling. | [56] |
| $LaFe_{10.9}Co_{0.7}Si_{1.4}$ | 2 | 5.05 | 270 | / | / | | |

| | | | | | | |
|---|---|---|---|---|---|---|
| $LaFe_{10.8}Co_{0.8}Si_{1.4}$ | 2 | 4.57 | 280 | / | / | |
| $LaFe_{8.8}Si_{2.2}$ | 1.5 | 2.0 | 251 | / | / | Arc-melting |

## 6.5 Conclusion

In this work, $LaCe(Fe,Mn,Si)_{13}$ block samples were manufactured by using the PBF-LB technique. The laser processing parameters were optimised for optimal dense blocks. The behaviour and the mechanism of different cracks and defects were revealed. In addition, the effect of the heat-treatment process was also discussed. The following conclusions were made:

1. The condition of $E_V$ = 250 J/mm$^3$ (the laser power is 90 W, the scanning speed is 600 mm/s, and the hatch is 0.02 mm) showed the lowest porosity fraction and crack density, which the authors have been recommended as the optimal condition.
2. The redeposits increased the difficulty of fully melting the next layer using low energy density. The low energy density caused by the high scanning speed and hatch space can result in many LOFs.
3. Solidification cracking was attributed to the stress concentration and a stable liquid film. The PBF-LB of $LaCe(Fe,Mn,Si)_{13}$ demonstrated a strong susceptibility to hot cracking. Hot cracks preferred to form in the high-angle grain boundaries. The estimated value of the critical transition angle was 8.77°.
4. Solid-state cracks were common in the microstructure of the as-fabricated samples. The length of the longitudinal and transverse cracks on average exceeded 100 μm and propagated through several layers of the melt pool. All the solid-state cracks presented transgranular and intergranular features.
5. The maximum $\Delta S$ of the HTH sample was -3.68 Jkg$^{-1}$K$^{-1,}$ and the maximum adiabatic temperature change ($\Delta T_{ad}$) is 1.65 K when applied to the 1 T field. Compared with the pure Gd and La-Fe-Si-based alloys reported in other literature, the MCE of SOPT in this work

was promising. The $T_c$ (room temperature, 298 K) found in this study makes the material ideal for realizing room-temperature magnetic refrigeration.

## 6.6 Reference


[1] M.-H. Phan, S.-C. Yu, Review of the magnetocaloric effect in manganite materials, Journal of Magnetism and Magnetic Materials 308(2) (2007) 325-340.

[2] V. Franco, J.S. Blázquez, B. Ingale, A. Conde, The Magnetocaloric Effect and Magnetic Refrigeration Near Room Temperature: Materials and Models, Annual Review of Materials Research 42(1) (2012) 305-342.

[3] K. Imaizumi, A. Fujita, A. Suzuki, M. Kobashi, K. Ozaki, Improvement of magnetocaloric effect in La(FexSi1-x)13 by dealing with inhibitory microstructures at high Fe concentration, Acta Materialia 227 (2022) 117726.

[4] L. Yang, Z. Zhou, S. Feng, J. Li, J. Liu, J. Li, Q. Hu, J. Li, Microstructure and magnetic property of LaFe11.6Si1.4 magnetocaloric alloys by a novel short time heat treatment, Intermetallics 105 (2019) 1-5.

[5] G. Cao, Q. Wang, J. Liu, Y. Zhang, X. Wang, M. Huang, H. Shen, L. Zheng, Enhanced magnetic entropy change and refrigeration capacity of La(Fe,Ni)11.5Si1.5 alloys through vacuum annealing treatment, J Alloy Compd 800 (2019) 363-371.

[6] X.C. Zhong, X.T. Dong, D.R. Peng, S.M. Wu, C.L. Liu, J.H. Huang, H. Zhang, K.W. Long, D.L. Jiao, H. Zhang, W.Q. Qiu, H.Y. Yu, Z.W. Liu, R.V. Ramanujan, Microstructural evolution, magnetocaloric effect, mechanical and thermal properties of hot-pressed LaFe11.6Si1.4/Ce2Co7 composites prepared using strip-cast master alloy flakes, Journal of Magnetism and Magnetic Materials 525 (2021) 167652.

[7] X. Chen, Y. Chen, Y. Tang, The studies of high-temperature and short-time annealing, phase transition process, and magnetic property for LaFe11.7Si1.3 compound, Phase Transitions 85(1-2) (2012) 27-40.

[8] A.E.-M.A. Mohamed, M. Jeong, R.S. Sheridan, M.M. Attallah, Enabling high efficiency magnetic refrigeration using laser powder bed fusion of porous LaCe(Fe,Mn,Si)13 structures, Addit Manuf 51 (2022) 102620.

[9] S.L. Sing, S. Huang, G.D. Goh, G.L. Goh, C.F. Tey, J.H.K. Tan, W.Y. Yeong, Emerging metallic systems for additive manufacturing: In-situ alloying and multi-metal processing in laser powder bed fusion, Progress in Materials Science 119 (2021) 100795.

[10] C. Chang, H. Liao, L. Yi, Y. Dai, S.C. Cox, M. Yan, M. Liu, X. Yan, Achieving ultra-high strength and ductility in Mg–9Al–1Zn-0.5Mn alloy via selective laser melting, Advanced Powder Materials (2022) 100097.

[11] X. Hou, C. Liu, Y. Xue, N. Han, H. Xu, C. Ma, M.H. Phan, Formation of NaZn13-type phase in LaFe11.5Si1.5 alloy during solidification process, MRS Proceedings 1708 (2014) mrss14-1708-vv04-23.

[12] J.D. Moore, D. Klemm, D. Lindackers, S. Grasemann, R. Träger, J. Eckert, L. Löber, S. Scudino, M. Katter, A. Barcza, K.P. Skokov, O. Gutfleisch, Selective laser melting of La(Fe,Co,Si)13 geometries for magnetic refrigeration, J Appl Phys 114(4) (2013) 043907.

[13] K.G. Prashanth, S. Scudino, T. Maity, J. Das, J. Eckert, Is the energy density a reliable parameter for materials synthesis by selective laser melting?, Materials Research Letters 5(6) (2017) 386-390.

[14] H. Zhang, Y. Sun, E. Niu, F. Hu, J. Sun, B. Shen, Enhanced mechanical properties and large magnetocaloric effects in bonded La(Fe, Si)13-based magnetic refrigeration materials, Appl Phys Lett 104(6) (2014) 062407.

[15] N. Lu, Z. Lei, K. Hu, X. Yu, P. Li, J. Bi, S. Wu, Y. Chen, Hot cracking behavior and mechanism of a third-generation Ni-based single-crystal superalloy during directed energy deposition, Addit Manuf 34 (2020) 101228.

[16] S. Wu, Z. Lei, B. Li, J. Liang, Y. Chen, Hot cracking evolution and formation mechanism in 2195 Al-Li alloy printed by laser powder bed fusion, Addit Manuf 54 (2022) 102762.

[17] D. Gu, L. Du, D. Dai, K. Lin, M. Xia, S. Li, J. He, Influence of thermal behavior along deposition direction on microstructure and microhardness of laser melting deposited metallic parts, Applied Physics A 125(7) (2019) 455.

[18] J.U. Rakhmonov, D. Weiss, D.C. Dunand, Solidification microstructure, aging evolution and creep resistance of laser powder-bed fused Al-7Ce-8Mg (wt%), Additive Manufacturing 55 (2022) 102862.

[19] K. Niitsu, R. Kainuma, Phase equilibria in the Fe–La–Si ternary system, Intermetallics 20(1) (2012) 160-169.

[20] Y.T. Tang, C. Panwisawas, J.N. Ghoussoub, Y. Gong, J.W.G. Clark, A.A.N. Németh, D.G. McCartney, R.C. Reed, Alloys-by-design: Application to new superalloys for additive manufacturing, Acta Mater 202 (2021) 417-436.

[21] Library, MRS Bulletin 28(9) (2003) 674-675.

[22] D. Dye, O. Hunziker, R.C. Reed, Numerical analysis of the weldability of superalloys, Acta Materialia 49(4) (2001) 683-697.

[23] J.C. Lippold, Welding metallurgy and weldability, John Wiley & Sons2014.

[24] G. Liu, D. Du, K. Wang, Z. Pu, B. Chang, Hot cracking behavior and mechanism of the IC10 directionally solidified superalloy during laser re-melting, Vacuum 181 (2020) 109563.

[25] S. Griffiths, H. Ghasemi Tabasi, T. Ivas, X. Maeder, A. De Luca, K. Zweiacker, R. Wróbel, J. Jhabvala, R.E. Logé, C. Leinenbach, Combining alloy and process modification for micro-crack mitigation in an additively manufactured Ni-base superalloy, Additive Manufacturing 36 (2020) 101443.

[26] J. Kagathara, S. Wieland, E. Gärtner, V. Uhlenwinkel, M. Steinbacher, Heat Treatment and Formation of Magnetocaloric 1:13 Phase in LaFe11.4Si1.2Co0.4 Processed by Laser Beam Melting, Materials 13(3) (2020) 773.

[27] P. Jin, Y. Li, Y. Dai, Z. Xu, C. Song, Z. Luo, Q. Zhai, K. Han, H. Zheng, Zn and P Alloying Effect in Sub-Rapidly Solidified LaFe11.6Si1.4 Magnetocaloric Plates, Metals 9(4) (2019) 432.

[28] X. Hou, C. Liu, Y. Xue, N. Han, H. Xu, C. Ma, M.H. Phan, Formation of NaZn13-type phase in LaFe11.5S1.5 alloy during solidification process, MRS Online Proceedings Library 1708(1) (2014) 75-82.

[29] E. Chauvet, P. Kontis, E.A. Jägle, B. Gault, D. Raabe, C. Tassin, J.-J. Blandin, R. Dendievel, B. Vayre, S. Abed, G. Martin, Hot cracking mechanism affecting a non-weldable Ni-based superalloy produced by selective electron Beam Melting, Acta Materialia 142 (2018) 82-94.

[30] W. Zhang, F. Liu, F. Liu, C. Huang, H. Zheng, Q. Zhang, Y. Zheng, J. Gao, Microstructural evolution and cracking behavior of Hastelloy X superalloy fabricated by laser directed energy deposition, Journal of Alloys and Compounds 905 (2022) 164179.

[31] M. Rappaz, J.M. Drezet, M. Gremaud, A new hot-tearing criterion, Metallurgical and Materials Transactions A 30(2) (1999) 449-455.

[32] M. Rappaz, A. Jacot, W.J. Boettinger, Last-stage solidification of alloys: Theoretical model of dendrite-arm and grain coalescence, Metallurgical and Materials Transactions A 34(3) (2003) 467-479.

[33] P.M. Anderson, J.P. Hirth, J. Lothe, Theory of dislocations, Cambridge University Press2017.

[34] J.A. Dantzig, M. Rappaz, Solidification: Revised & Expanded, EPFL press2016.

[35] B. Kaeswurm, A. Barcza, M. Vögler, P.T. Geiger, M. Katter, O. Gutfleisch, L.F. Cohen, Behaviour of the Young's modulus at the magnetocaloric transition in La(Fe,Co,Si)13, J Alloy Compd 697 (2017) 427-433.

[36] S. Fujieda, A. Fujita, K. Fukamichi, Y. Yamaguchi, K. Ohoyama, Neutron diffraction and isotropic volume expansion caused by deuterium absorption into La (Fe0. 88Si0. 12) 13, Journal of the Physical Society of Japan 77(7) (2008) 074722-074722.

[37] L. Gránásy, M. Tegze, Crystal-melt interfacial free energy of elements and alloys, Materials Science Forum, Trans Tech Publ, 1991, pp. 243-256.

[38] X. Jiang, B. Xiao, R. Lan, X. Gu, X. Zhang, H. Sheng, Estimation of the solid-liquid interface energy for metal elements, Computational Materials Science 170 (2019) 109174.

[39] T. DebRoy, H.L. Wei, J.S. Zuback, T. Mukherjee, J.W. Elmer, J.O. Milewski, A.M. Beese, A. Wilson-Heid, A. De, W. Zhang, Additive manufacturing of metallic components – Process, structure and properties, Progress in Materials Science 92 (2018) 112-224.

[40] K. Makarenko, O. Dubinin, I. Shishkovsky, Direct Energy Deposition of Cu-Fe System Functionally Graded Materials: Miscibility Aspects, Cracking Sources, and Methods of Assisted Manufacturing, (2022).

[41] R.N. Gardner, H.G.F. Wilsdorf, Ductile fracture initiation in pure α-Fe: Part I. Macroscopic observations of the deformation history and failure of crystals, Metallurgical Transactions A 11(4) (1980) 653-658.

[42] O. Glushko, A. Funk, V. Maier-Kiener, P. Kraker, M. Krautz, J. Eckert, A. Waske, Mechanical properties of the magnetocaloric intermetallic LaFe11.2Si1.8 alloy at different length scales, Acta Materialia 165 (2019) 40-50.

[43] J.R. Chelikowsky, K.E. Anderson, Melting point trends in intermetallic alloys, Journal of Physics and Chemistry of Solids 48(2) (1987) 197-205.

[44] Y. Hu, X. Zhao, X. Wang, S. Wang, Effects of Nd doping on the magnetocaloric properties of double perovskite Sr2FeMoO6, Journal of Magnetism and Magnetic Materials 499 (2020) 166212.

[45] Y. Hu, W. Li, X. Wang, Y. Cui, Y. Wei, L. Sun, T. Guo, X. Zhao, Enhanced magnetocaloric effect of Sr1.8Eu0.13Ba0.07FeMoO6 perovskite compound, Ceramics International 44(3) (2018) 2761-2767.

[46] I. Hussain, M.S. Anwar, J.W. Kim, K.C. Chung, B.H. Koo, Influence of La addition on the structural, magnetic and magnetocaloric properties in Sr2−xLaxFeMoO6 ($0 \leq x \leq 0.3$) double perovskite, Ceramics International 42(11) (2016) 13098-13103.

[47] B. Banerjee, On a generalised approach to first and second order magnetic transitions, Physics letters 12(1) (1964) 16-17.

[48] J. Liu, C. He, M.X. Zhang, A.R. Yan, A systematic study of the microstructure, phase formation and magnetocaloric properties in off-stoichiometric La-Fe-Si alloys, Acta Mater 118 (2016) 44-53.

[49] S. Fujieda, A. Fujita, K. Fukamichi, Y. Yamazaki, Y. Iijima, Giant isotropic magnetostriction of itinerant-electron metamagnetic La(Fe0.88Si0.12)13Hy compounds, Applied Physics Letters 79(5) (2001) 653-655.

[50] V. Chaudhary, X. Chen, R.V. Ramanujan, Iron and manganese based magnetocaloric materials for near room temperature thermal management, Prog Mater Sci 100 (2019) 64-98.

[51] F.-x. Hu, B.-g. Shen, J.-r. Sun, Z.-h. Cheng, G.-h. Rao, X.-x. Zhang, Influence of negative lattice expansion and metamagnetic transition on magnetic entropy change in the compound LaFe11.4Si1.6, Appl Phys Lett 78(23) (2001) 3675-3677.

[52] V. Franco, J.Y. Law, A. Conde, V. Brabander, D.Y. Karpenkov, I. Radulov, K. Skokov, O. Gutfleisch, Predicting the tricritical point composition of a series of LaFeSi magnetocaloric alloys via universal scaling, Journal of Physics D: Applied Physics 50(41) (2017) 414004.

[53] Z. Lin, S. Li, M. Liu, J.-G. Duh, K. Peng, X. Mao, Magnetocaloric effect of La0.8Ce0.2Fe11.4−xMnxSi1.6 compounds, Journal of Alloys and Compounds 489(1) (2010) 1-3.

[54] C. Wang, Y. Long, T. Ma, H. Zhang, Magnetocaloric effect and magnetic properties of La0.9Ce0.1(Fe0.99Mn0.01)11.6Si1.4H1.6 compound, Journal of Rare Earths 29(5) (2011) 474-476.

[55] T. Liu, Y. Chen, Y. Tang, S. Xiao, E. Zhang, J. Wang, Structure and magnetic properties of shortly high temperature annealing LaFe11.6Si1.4 compound, J Alloy Compd 475(1) (2009) 672-675.

[56] X. Chen, Y. Chen, Y. Tang, Phase relation of LaFe11·6Si1·4compounds annealed at different high-temperature and the magnetic property of LaFe11·6–xCoxSi1·4compounds, Bulletin of Materials Science 35(2) (2012) 175-182.

# CHAPTER 7: Conclusion & Future Work

## 7.1 Summary and conclusion

The environmentally friendly Magnetic refrigeration is based on the MCE of the magnetocaloric material. However, magnetocaloric materials have limited uses due to poor mechanical properties. This study set out to use PBF-LB technology to overcome the disadvantages of difficult-to-machine these alloys (including NiMnSn alloy and $LaCe(Fe,Mn,Si)_{13}$) and directly produce parts with complex shapes, especially the porous magnetocaloric materials with predefined external bodies and internal architecture. In addition, we studied the post-treatment processes' effects on microstructural development and magnetocaloric performance.

### 7.1.1 Parametrical studies for densification

We can use the PBF-LB technology to build NiMnSn-based Heusler alloys with different shapes, in particular blocks, MC cylinders, and lattices. We optimised the PBF-LB processing parameters to minimise these samples' defects, cracks, and maximum densification. Setting the condition at $E_V$ = 53.33 J/mm$^3$ showed the lowest defects and cracks fraction, with suitable densification, and was recommended as the optimum condition for block samples. It has demonstrated that PBF-LB technology can create a fully dense NiMnSn block and lattice strut magnetic refrigerant with a competitive MCE. The low laser powers (60, 70, and 80 W) with low energy density (< 53.33 J/mm$^3$) can manufacture MC cylinders and lattices with suitable microstructure.

During the PBF-LB processing of $LaCe(Fe,Mn,Si)_{13}$ alloy, the low energy density caused by

the high scanning speed and hatch space can result in many lack-of-fusions. The redeposited powders (unmelted powders connected and gathered together) increase the difficulty of fully melting during the next layer. It is found that suitable energy density with low laser power, low scanning speed, and low hatch is good for building $LaCe(Fe,Mn,Si)_{13}$ block samples with the lowest porosity fraction and crack formation.

### 7.1.2 Influence of solution heat treatments

We explored different heat treatments, homogenising NiMnSn alloy's chemical composition and obtaining good MCE. The chemical composition is more uniform when increasing the heat treatment time. Although the long heat treatment process did not significantly affect MCE around the curie temperature, it improved MCE around the martensitic transition.

Two different heat treatment processes were performed to improve the MCE and change the transition temperature of PBF-LBed $LaCe(Fe,Mn,Si)_{13}$. Firstly, the heat treatment in an argon atmosphere at 1323 K for 168 hours before water quenching. Then the heat treatment in a hydrogen atmosphere with one-bar pressure. The heat treatment processes improve the form of $NaZn_{13}$-type $LaCe(Fe,Mn,Si)_{13}$ phases and improve the MCE. The heat treatment in a hydrogen atmosphere incorporates hydrogen atoms into $NaZn_{13}$-type $LaCe(Fe,Mn,Si)_{13}$ phases interstitially. This treatment improves the MCE and increases the curie temperature. Moreover, the heat treatment in a hydrogen atmosphere can decrease oxides volume, improving the magnetic properties.

### 7.1.3 The cracking mechanisms

The observed bulk cracking is categorised into three types based on the cause of cracking: (i) hot cracking (including solidification cracking and liquation cracking), (ii) solid-state cracking (cold cracking); and (iii) new types of cracks that were observed: segregation cracking.

Solidification cracking was attributed to the stress concentration and a stable liquid film. The PBF-LB of $LaCe(Fe,Mn,Si)_{13}$ demonstrated susceptibility to hot cracking. Solid-state cracks were common in the microstructure of the as-fabricated sample. The length of the longitudinal and transverse cracks, on average, exceeded 100 μm and propagated through several layers of the melt pool. All the solid-state cracks presented transgranular and intergranular features. Some cracks preferred to expand along the La/Ce segregations.

### 7.1.4 The magnetocaloric effect

Thermo-magnetisation curves and M-H curves proved that the FOPT (M-A structural transformation) and SOPT (magnetic transformation around the $T_C^A$) existed in the HT PBF-LB NiMnSn Heusler alloy. The $\Delta S_m$ value was 0.53 $Jkg^{-1}K^{-1}$ (with a field change of 10 kOe) for the FOPT of the sample built with optimum condition E = 53.33 $J/mm^3$. Compared with the NiMnSn alloy manufactured using arc melting, the $\Delta S_m$ of the PBF-LB NiMnSn alloy was lower. The different PBF-LB process parameters did not significantly affect the $\Delta S_m$ value around $T_C^A$. The $\Delta S_m$ for the three PBF-LB samples around $T_C^A$ is approximately 1.0 $Jkg^{-1}K^{-1}$ when applied to the 1 T field.

The $\Delta S_m$ of HTH $LaCe(Fe,Mn,Si)_{13}$ sample was -3.68 $Jkg^{-1}K^{-1}$ when applied to the 1 T field, achieved at a $T_c$ value of 298 K. Compared with the pure Gd and LaFeSi-based alloys reported in other literature, the $\Delta S_m$ of SOPT in this work was promising $T_c$ (room temperature, 298 K) found in this study makes the material an ideal choice for realising room-temperature magnetic refrigeration.

## 7.2 Future work

This work has explored the PBF-LB processing of NiMnSn alloy and $LaCe(Fe,Mn,Si)_{13}$ alloy. This work optimised parameters during the two different alloys' PBF-LB processing. Different lattice structures were designed and built to increase heat exchange efficiency. In addition, it reveals the microstructural development and related properties in PBF-LBed NiMnSn-based alloy and $LaCe(Fe,Mn,Si)_{13}$ alloy. Future works will focus on more fundamental research topics. In addition, future work will also explore the actual applications in magnetic refrigeration by using the PBF-LB processing.

a. This work has observed many cracks in PBF-LBed in-situ NiMnSn alloy and $LaCe(Fe,Mn,Si)_{13}$ alloy. To disappear the cracks, the PBF-LB of NiMnSn parts using pre-alloy NiMnSn powder should be built, especially the lattice structures with smaller unit cells. HIPing technology can be used to close the defects within the PBF-LBed in-situ NiMnSn alloy and $LaCe(Fe,Mn,Si)_{13}$ alloy parts. If HIPing does not work because of too many cracks inside, the coating can be used to cover the surface of PBF-LBed samples before HIPing.

b. This work has studied the relationship between the PBF-LBed specimens' microstructure and magnetic properties. It did not study the effect of different scanning strategies on the microstructure and magnetic properties. Future work will focus on the impact of varying scanning strategies on composition uniformity, microstructure, crystal structure, grain orientation, and magnetic property.

c. This work has designed and built different kinds of lattice structures. It just explores the possibility of making these lattice structures by using PBF-LB. The heat exchange

efficiency of different structures is not studied. Thus, future works will focus on improving heat exchange efficiency by optimising the lattice structures within the heat exchangers.

d. In the application process of magnetic refrigeration materials, the heat exchange medium, such as water, oil, and so on, plays an essential role in transferring heat. Thus, the interaction between magnetic refrigeration materials and these media, especially the materials' corrosion resistance, deserves further study.